Imaging Transport Resonances in the Quantum Hall Effect

by

Gary Alexander Steele

Submitted to the Department of Physics
in partial fulfillment of the requirements for the degree of

Doctor of Philosophy

at the

MASSACHUSETTS INSTITUTE OF TECHNOLOGY

February 2006

Author .....
Department of Physics
January 19, 2006

Certified by .....
Raymond C. Ashoori
Professor
Thesis Supervisor

Accepted by .....
Thomas J. Greytak
Professor, Associate Department Head for Education

Imaging Transport Resonances in the Quantum Hall Effect

by

Gary Alexander Steele

Submitted to the Department of Physics
on January 19, 2006, in partial fulfillment of the
requirements for the degree of
Doctor of Philosophy

Abstract

We image charge transport in the quantum Hall effect using a scanning charge accumulation microscope. Applying a DC bias voltage to the tip induces a highly resistive ring-shaped incompressible strip (IS) in a very high mobility 2D electron system (2DES). The IS moves with the tip as it is scanned, and acts as a barrier that prevents charging of the region under the tip. At certain tip positions, short-range disorder in the 2DES creates a quantum dot island inside the IS that enables breaching of the IS barrier by means of resonant tunneling through the island. Striking ring shapes appear in the images that directly reflect the shape of the IS created in the 2DES by the tip.

Through the measurements of leakage across the IS, we extract information about energy gaps in the quantum Hall system. Varying the magnetic field, the tunneling resistance of the IS varies significantly, and takes on drastically different values at different filling factors. Measuring this tunneling resistance provides a unique *microscopic* probe of energy gaps in the quantum Hall system.

Simulations of the interaction of the tip with the quantum Hall liquid show that native disorder from remote ionized donors can create the islands. The simulations predict the shape of the IS created in the 2DES in the presence of disorder, and comparison of the images with simulation results provides a direct and quantitative view of the disorder potential of a very high mobility 2DES.

We also draw a connection to bulk transport. At quantum Hall plateaus, electrons in the bulk are localized by a network of ISs. We have observed that the conductance across one IS is drastically enhanced by resonant tunneling through quantum dot islands. Similarly, this resonant tunneling process will dramatically enhance the conductance of certain hopping paths in the localized bulk and could play an important role in dissipative transport at quantum Hall plateaus.

Thesis Supervisor: Raymond C. Ashoori
Title: Professor

Acknowledgments

First and foremost, I would like to thank my advisor Ray. In my graduate career, I have learned a great deal from Ray: in particular, his openness, his remarkable physical intuition, his enthusiasm for physics, and his creativity are all things that I aspire to. It is these qualities that make him an excellent physicist and teacher. Success in this project would not have been possible without the drive and excitement he brought to the experiment. I would also like to thank my thesis committee, in particular Professor Leonid Levitov for the helpful and insightful discussions we had.

In experimental physics, nothing is accomplished alone. Whether it is borrowing a vacuum fitting, discussing physics on a white board in the hallway, or fixing the liquefier, interacting with a community of people around you is a key to a successful experiment. For me, that community was the people of the second floor of Building 13, including the all the members of our research group as well as the Kastner and Greytak groups. I would like to thank Oliver Dial in particular for his endless help with writing software and building electronics, and even more so for the stimulating physics and non-physics discussions we have had in our time here. I would like to thank all the Ashoori group members who have helped me over the years, in particular Paul Glicofridis who taught me to run the microscope and Nemanja Spasojevic who was instrumental in our simulation work.

Finally, I would like to thank my family for their constant support and encouragement, and Susan Dunne, who was always there for me.

Contents

List of Figures

List of Tables

Chapter 1

Introduction

In the past 25 years, the two-dimensional electron system (2DES) has proven to be a remarkable system for studying fundamental physics. Studies of the behaviour of electrons in the 2DES probe the basic concepts from quantum mechanical theory, and the 2DES is a model system for studying the effects of correlations between interacting electrons. These properties are exhibited most clearly when the 2DES is subjected to a very large magnetic field, which results in a phenomena known as the quantum Hall effect. The 2DES has stimulated an enormous body of experimental and theoretical work, and the quantum Hall effect has been the subject of two Nobel prizes in physics.

The goal of this research is to study the physics of the 2DES on a microscopic scale using a scanning probe microscope. We begin with an overview of the 2DES and the quantum Hall effect. We then descibe the method we have developed for studying transport in the quantum Hall effect on a micrscopic level.

1.1 The 2D Electron System and the Quantum Hall Effect

It was discovered in the 1960s that by squeezing the electrons into a very narrow 10 nm plane strictly restricts the motion of the electrons to two degrees of freedom

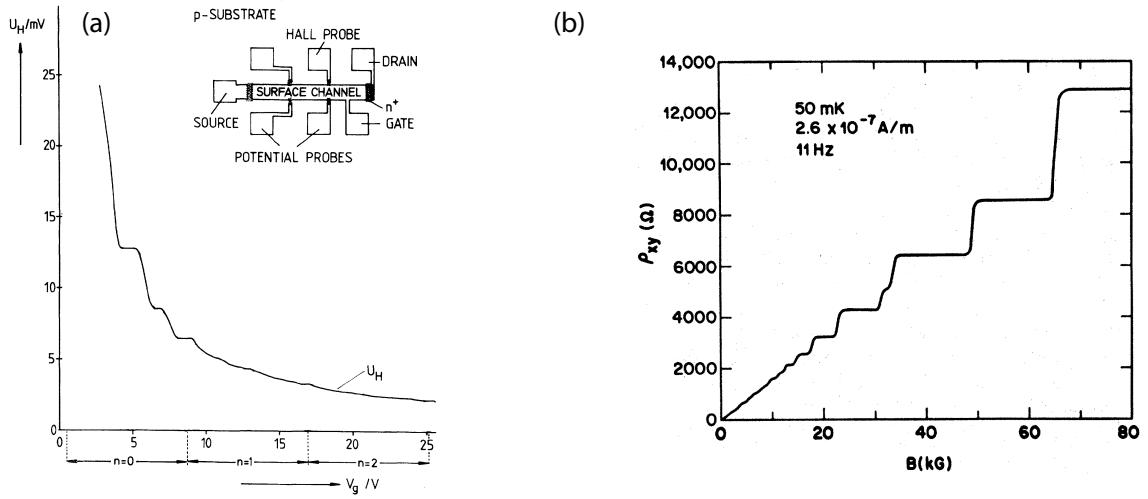

Figure 1-1: (a) Quantized plateaus in the Hall resistance observed as a function gate voltage by von Klitzing in a silicon MOSFET. Adapted from [3]. For this measurement, the gate voltage is swept at constant magnetic field, varying the electron density. (b) Quantized plateaus in a GaAs heterostructure. In experiments in GaAs heterostructures, the electron density is typically kept constant and the magnetic field is swept. Adapted from [4].

associated with motions in the 2D plane [1, 2]. This is acheived due to the effects of quantum mechanics: the tight confinement produces a wavefuntion in the confined direction that is restricted to quantized energy levels. At low temperatures, the spacing between these levels can become smaller than the the thermal energy kT. As a result, electrons will occupy only the lowest energy level. Although the wavefunction itself is 3 dimensional, motion of the electrons is restricted only to the two remaining unconfined directions.

In the late 1970s, a physicist named Klaus von Klitzing had been studying the Hall resistance of a 2DES at low temperatures in very large magnetic fields. Classically, applying a magnetic field perpendicular to the current flow in a metal will exert a Lorentz force on the moving electrons, pushing them to one side of the channel. In equilibrium, a charge accumulation at the edges of the sample results that creates an electric field that balances this force. Attaching a voltmeter to the sides of the sample, we then measure a voltage proportional to the current. The proportionality

constant is called the Hall resistance, and is given by [5]:

$$R_H = \frac{B}{qn_s} \tag{1.1}$$

where q is the charge of the carriers and n_s is the sheet concentration. At low magnetic fields, the Hall resistance of the 2DES showed the expected behaviour from the classical formula. At very large magnetic fields and at low temperatures, however, von Klitzing observed that there the Hall resistance showed deviations from the classical behavior in the form of flat plateaus. This is shown in figure 1-1. Remarkably, von Klitzing noticed that the Hall resistance on the plateaus was quantized to a value that depended only on fundamental physical constants:

$$R_H = \frac{h}{Ne^2} \tag{1.2}$$

where N is an integer, e is the electron charge, and h is Plank's constant. The ratio h/e^2 is the quantum of resistance. The quantization seen in the experiment was extremely accurate: in the paper [3] announcing the discovery, the accuracy was better than 1 part per million. Since then, the accuracy has been improved to better than 1 part per billion. The quantum Hall effect is now used as the official international resistance standard [6], and plays a fundamental role in the quantum metrology triangle [7]. For this discovery, von Klitzing was awarded the Nobel prize in 1985 [8].

Two years before von Klitzing's discovery, another significant change to the field of semiconductor physics had occurred. This was the development of the modulation doping technique by Horst Störmer and collaborators at Bell Labs [9]. It turns out that this development would have an equally large impact on semiconductor physics. One of the problems that plagued semiconductors was that they intrinsically have no free charge carriers, and consequently are insulators at zero temperature. In order to conduct at low temperatures, they must be "doped" with impurity atoms that carry an excess electron. The difficulty is that once the dopant atoms release their electron, they act as charged scattering sites. These charged impurities scatter electrons quite

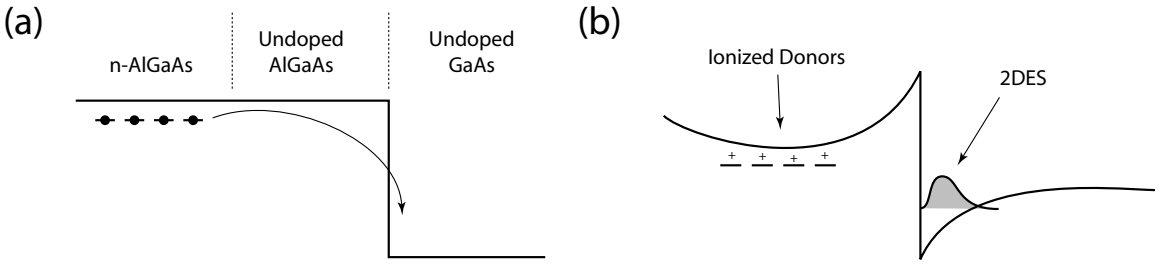

Figure 1-2: The 2DES in GaAs. (a) Using molecular beam epitaxy, layers of semiconductors with different chemical composition can be grown on top of each other, a single crystalline layer at a time. This is used to create structure that has a GaAs layer below an AlGaAs layer. The AlGaAs layer has a larger band gap, leading to a step in the effective potential electrons see. (b) Electrons from dopants in the AlGaAs layer fall into the more energetically favorable undoped GaAs layer, where they form a 2DES at the interface.

strongly, resulting in very poor mobility.

The group at Bell labs used a new crystal growth technique called Molecular Beam Epitaxy (MBE) [10] to get around this problem. In MBE, a semiconductor crystal can be grown a single atomic layer at a time. By varying the chemical composition, epitaxial layers consistent of different semiconductor materials can be grown on top of each other. Furthermore, by selecting lattice matched semiconductors, this can be done in a way that produces a perfect crystal with no defects. Using this technique, the Bell labs group grew a layer of $Al_{1-x}Ga_xAs$ on top of a GaAs layer, as shown in figure 1-2(a). Because $Al_{1-x}Ga_xAs$ has a larger bandgap than GaAs, there is an offset in the effective potential seen by electron in the crystal at the interface. By including dopants in the $Al_{1-x}Ga_xAs$ layer, electrons from the dopants will fall down into the more energetically favorable GaAs layer, forming a 2DES at the interface. The innovation is that electrons are now spatially separated from the charged donors, drastically reducing scattering. In modern GaAs structures like this, mobilities can exceed 30×10^6 cm^2/Vs, corresponding to electron mean free paths on the order of an astonishing 0.1 mm. The increase in sample quality from this technique lead to the discovery of the fractional quantum Hall effect, for which Horst shared the Nobel prize with collaborator Dan Tsui and theorist Robert Laughlin in 1998. The modulation doping technique has opened up a new realm of semiconductor physics

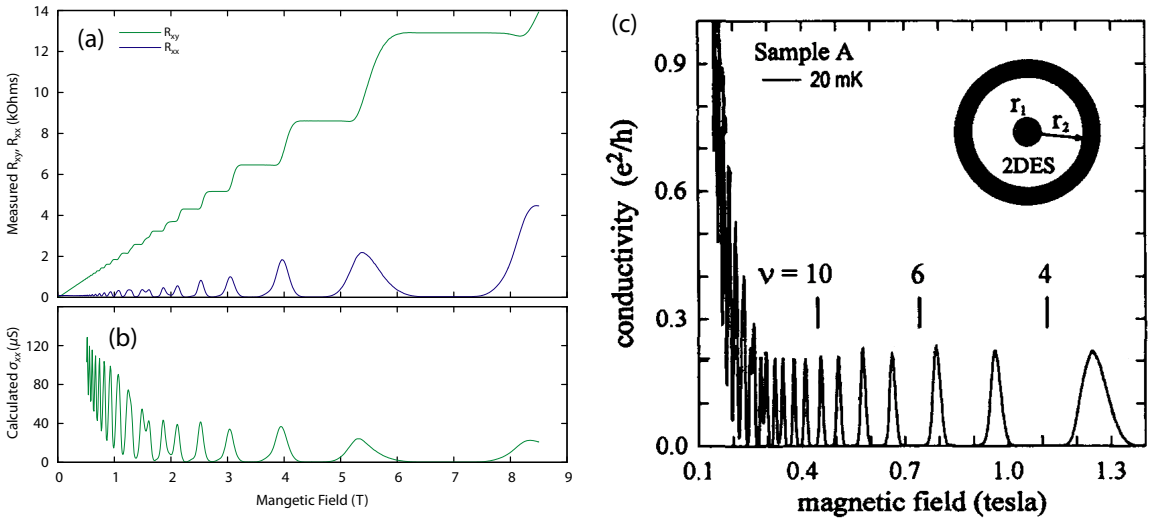

Figure 1-3: (a) The transverse (green) and longitudinal (blue) resistance measured in a GaAs Hall bar at 350 mK. Data taken from [11]. (b) The conductivity σ_{xx} calculated from the data using equation 1.3. At Hall plateaus, the conductivity σ_{xx} becomes extremely small at low temperatures. (c) Direct measurements of the conductivity can be made in a sample design know as the "Corbino Disk" geometry, shown in the inset. The data shows σ_{xx} measured in such a sample at very low temperatures. Adapted from [12].

where many-body correlations between electrons play a central role, and in which the discovery of new many-body states of electrons continues to this day.

1.2 Conductivity in the Quantum Hall Effect

In the previous section, we discussed the remarkable observation that the Hall resistance of a 2DES at large magnetic fields and low temperatures displays plateaus at universal resistance values associated with fundamental physical constants. The Hall resitance is found by measuring the transverse voltage V_{xy} across the sample, and is related to the transverse component of the conductivity tensor σ_{xy}. In order to understand the origin of these plateaus, we will need to take a careful look at the behaviour of the diagonal component of the conductivity tensor σ_{xx}.

In a Hall bar geometry, σ_{xx} can be obtained by measuring both the transverse voltage V_{xy} and the longitudinal voltage V_{xx} in response to an current passed through the sample. These two measurements will give the matrix elements of the resistivity

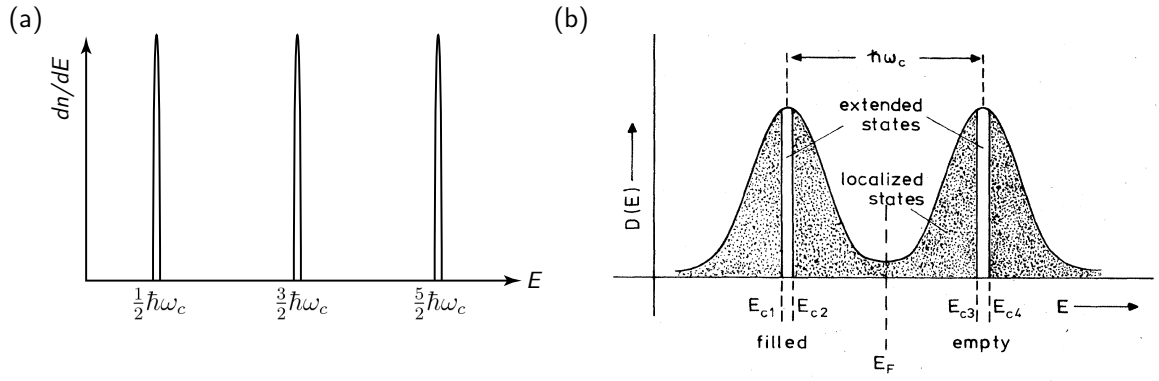

Figure 1-4: (a) In a large magnetic field, electrons occupy quantized energy states known as Landau levels. These Landau levels have fixed energies, resulting in δ-function peaks in the density of states. (b) The plateaus in the Hall resistance seen in the quantum Hall effect can be explained by assuming a disorder-induced broadening of the Landau level peaks. The broadening creates "localized states" in the tails of the broadened Landau levels. When the Fermi energy lies in these localized states, the conductivity σ_{xx} vanishes and the Hall resistance is quantized.

tensor ρ_{ij}. We can calculate the conductivity σ_{xx} by inverting the resistivity matrix[1]:

$$\sigma_{xx} = \frac{\rho_{xx}}{\rho_{xx}^2 + \rho_{xy}^2} \tag{1.3}$$

Figure 1-3 shows the Hall resitance and the logitudinal conductivity in the quantum Hall regime. Particularly striking is that whenever the Hall resistance is on a quantized plateau, the conductivity σ_{xx} goes to zero[2]. The vanishing conductivity plays a fundamental role in the quantum Hall effect: experimentally, there is a one-to-one correspondence between the vanishing conductivity σ_{xx} and the quantization of the Hall resitance R_{xy}. This connection was established on a theoretical basis by Laughlin [13] using very simple, although subtle, gauge invariance arguments, and also using different arguments by Halperin [14]. As long as σ_{xx} vanishes, the Hall resistance will be exactly quantized. This raises the question: what causes σ_{xx} to go to zero?

To understand this, we must consider the effects of quantum mechanics on elec-

[1]Alternatively, the conductivity σ_{xx} can also be measured directly in sample patterned in the Corbino geometry (see figure 1-3(c)).

[2]Note that ρ_{xx} measured in a four-terminal geometry also goes to zero, as can be seen in figure 1-3. At large magnetic fields, $\sigma_{xy} >> \sigma_{xx}$. Inverting the conductivity matrix σ_{ij}, we get ρ_{xx} is linearly proportional to σ_{xx}: $\rho_{xx} \approx \sigma_{xx}/\sigma_{xy}^2$. . This is known as the large Hall angle regime. In this limit, currents are driven predominantly by transverse electric fields.

trons in large magnetic fields. Classically, an electron that is confined to a 2D plane and subjected to a perpendicular magnetic field will circle in a closed loop with a frequency $\omega_c = eB/m$, a motion described as a cyclotron orbit. At high magnetic fields, these orbits become quantized, just as the orbits in an atom are quantized. These quantized cyclotron orbit states are called Landau levels. As a result of this quantization, the density of states of the 2DES in a magnetic field will split into delta-function peaks, as shown in figure 1-4(a). The spacing of the peaks is set by the cyclotron energy $\hbar\omega_c$. When we include disorder, these peaks become broadened, acquiring tails in the the gaps that are associated with localized states, shown in 1-4(b). In the quantum Hall effect, the conductivity σ_{xx} vanishes whenever the Fermi energy lies in this region of localized states. While the quantization is understood, the details of exactly what these localized states are and how they cause the conductivity to vanish are still not well understood.

Some information about the nature of the localized states can be obtained by measuring the temperature dependence of the conductivity σ_{xx}. Such temperature dependent transport measurements in the quantum Hall effect have been the subject of a large number of experimental investigations [4, 15, 16, 17, 18, 19, 20, 21, 22, 23, 24, 25, 26, 27, 28, 29, 30, 31, 32, 33, 34, 35, 36, 37, 38, 39, 40, 41, 42]. Despite this large body of work, a comprehensive understanding of the results, particularly at low temperatures, is still lacking. At high temperatures, σ_{xx} shows an activated behavior, attributed to thermal activation of electrons from the localized states up into the next Landau level. The conductivity in this regime fits well to a function:

$$\sigma_{xx} = \sigma_0 e^{-\frac{E_a}{k_B T}} \tag{1.4}$$

The measured activation energy is usually identified as half of the value of the energy gap separating the two Landau levels: $E_a = \frac{1}{2}\Delta E$. This is based on the assumption that at the center of the Hall plateau, the Fermi energy is pinned halfway between the two levels. The measured ΔE from data at even integer filling factors agrees reasonably well with $\hbar\omega_c$ when the factor of two is included [8]. Such measurements

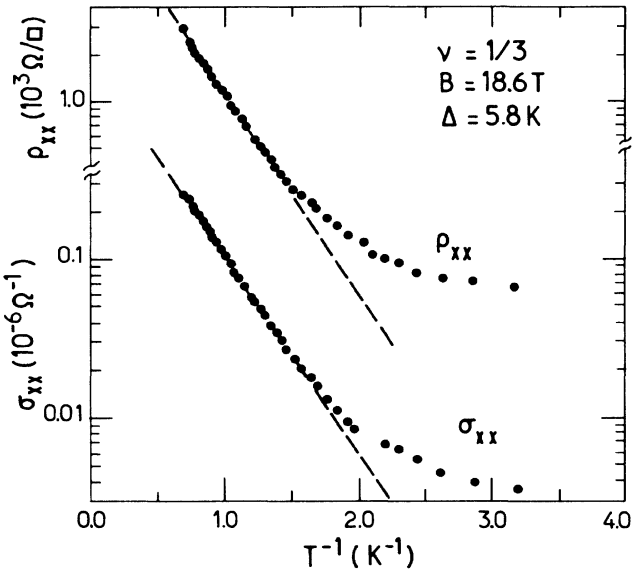

Figure 1-5: Temperature dependence of the conductivity σ_{xx} and the resistivity ρ_{xx} in a fractional quantum Hall plateau. At high temperatures, the data fit well to an activation model, shown by the dashed line. At low temperatures, the conductivity is enhanced, which is usually attributed to variable-range hopping. Data from integer quantum Hall plateaus show similar behavior, but with a deviations from activation starting at about 1K. Reproduced from Boebinger *et al.* [22].

are also often used as a measure of other energy gaps that do not arise from the cyclotron energy splitting, such as the exchange-enhanced spin gap [25] and gaps in the fractional quantum Hall effect [22].

At lower temperatures, the conductivity does not fall as fast as predicted from the activation model. As shown in figure 1-5, the conductivity in the activation plots curves upwards at low temperatures. This deviation is usually attributed to the onset of variable range hopping. In variable range hopping, rather than being activated up to the next Landau level, an electron in a localized state makes a lateral jump to an unoccupied state. These jumps can occur over a very large range of distances, as suggested by the name. Attempts have been made to fit the tail of the conductivity at low temperatures to both 2D Mott variable range hopping [43, 44]:

$$\sigma_{xx} = \sigma_0 e^{-(T_0/T)^{1/3}} \tag{1.5}$$

and to Efros-Shklovskii variable range hopping [45]:

$$\sigma_{xx} = \sigma_0 e^{-(T_0/T)^{1/2}} \tag{1.6}$$

Often, a temperature dependent prefactor $\sigma_0(T)$ is included. Unfortunately the conductivity does not vary significantly in this temperature range, making it difficult to differentiate between the two models, or to reliably extract fit parameters. Because of this, even the phenomenology of transport at low temperatures (< 1K) remains unclear.

Finally, it is important to mention that the analysis of much of bulk transport data [33, 34, 35, 36, 37, 38, 39, 40, 41, 42] is based on a model where electrons are localized in single-particle orbits that fallow trajectories of constant energy obtained from the zero magnetic field disorder potential. These simplifications allow the construction of sophisticated scaling models of the quantum Hall effect [46]. These models agree reasonably well with measurements in low mobility samples, typically InGaP or InGaAs quantum wells where alloy scattering limits mobilities to $\sim 10^4$ cm^2/Vs. One of the problems with these models is that they ignore the modifications to the self consistent potential by the screening properties of 2D electrons in large magnetic fields [47, 48, 49, 50, 51]. Including this screening significantly changes the nature of the localized states [52, 53] and transport [52, 53, 54, 55] in the quantum Hall effect, particularly in the low disorder limit [52].

1.3 Our work

An understanding of the quantum Hall effect is based fundamentally on the localized states that exist in the 2DES when the Hall resistance is quantized. While the quantization is understood, the nature of the localized states remains a mystery: macroscopic transport measurements have failed to draw any clear conclusions as to the exact nature of localization in the quantum Hall effect.

The purpose of our work is to study the localized states of the quantum Hall

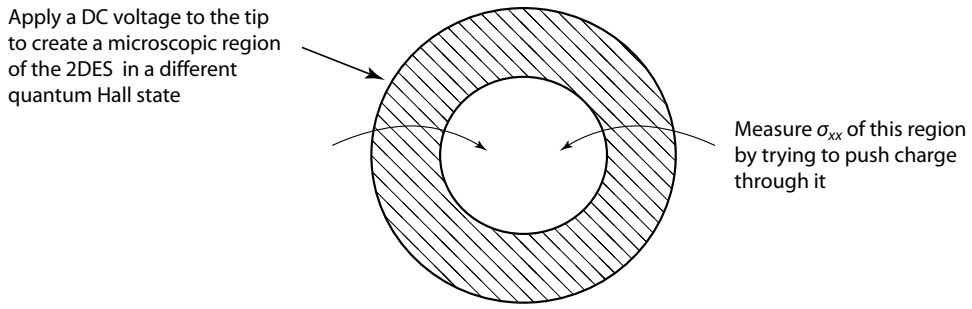

Figure 1-6: By applying a DC bias to the tip, we perturb the local electron density. This can cause a phase transition in parts to the 2DES, creating a ring-shaped region where the electrons are in a different quantum Hall state. We can then probe the conductivity σ_{xx} of this microscopic region by trying to drive charge across it using an AC excitation. By moving the tip, we can probe how σ_{xx} of this microscopic region varies as it is moved to different places in the sample.

effect on a microscopic scale using a novel charge-sensing scanning probe microscope. To do this, we will exploit a unique property of the quantum Hall system: at large magnetic fields, we can create different phases of the 2DES simply by very slightly changing the local electron density. Applying a DC bias voltage to our tip, we create a ring shaped region where the electrons are in a different quantum Hall state than elsewhere in the sample. This is illustrated in figure 1-6. We will then use the same tip to measure the conductivity of this ring shaped region. This is a totally unique experiment in two ways: first, the size of the region we are probing is *microscopic* in scale. Second, because the region we are probing is tied to the position of the tip, by moving the tip we can probe the conductivity σ_{xx} of microscopic rings formed at different positions in the sample.

In this thesis, we use this technique to study transport through such microscopic regions formed from the incompressible states that give rise to localization in the quantum Hall effect. We will discover that transport through the localized states is dramatically enhanced by a new transport mechanism consisting of resonant tunneling through small disorder induced islands. We propose that this resonant transport plays a significant role in the hopping transport seen at low temperatures in the the bulk measurements. The results provide a unique view of the microscopic transport mechanisms in the quantum Hall effect.

In chapter 2 we give a detailed overview of the measurement technique and the operation of the scanning probe microscope. In chapter 3, we present our central results from the scanning probe experiment. Chapter 4 discusses results from a simple experiment motivated by our discoveries in chapter 3, and in chapter 5 we present detailed simulations of the interaction of the scanning probe with the disordered quantum Hall system. We conclude in chapter 6 with a discussion of ideas for future research directions based on our results.

Chapter 2

Scanning Charge Accumulation Imaging

2.1 Scanning Probe Microscope Design

The design of a scanning probe microscope for the study of the 2D electron system presents some significant challenges. The most significant is due to the fact that most of the interesting physics of the 2D electron system occurs at very low temperatures (300 mK and below) and at very large magnetic fields, up to 10T and higher. This requires that the microscope be designed to fit inside the bore of a superconducting magnet in a low temperature cryostat. Another challenge is that the length scales of the 2DES are much larger than the atomic scales studied in STM, and require scan ranges of 10 μm or larger at cryogenic temperatures. It is also essential that the microscope have the ability to translate the sample laterally in-situ. The 2D electron system is easily perturbed by the deposition of charge on the insulating surface of the sample. Having such translational freedom allows us to walk to a new unperturbed location if the area we are scanning is disturbed, and opens up the possibility of studying lithographically defined structures such as quantum dots.

The microscope we use was designed in-house to fit into a top loading Oxford ^{3}He cryostat with a 32 mm sample space bore that is equipped with a 10T superconducting magnet. The microscope consists of a brass body that is mounted at the end of a

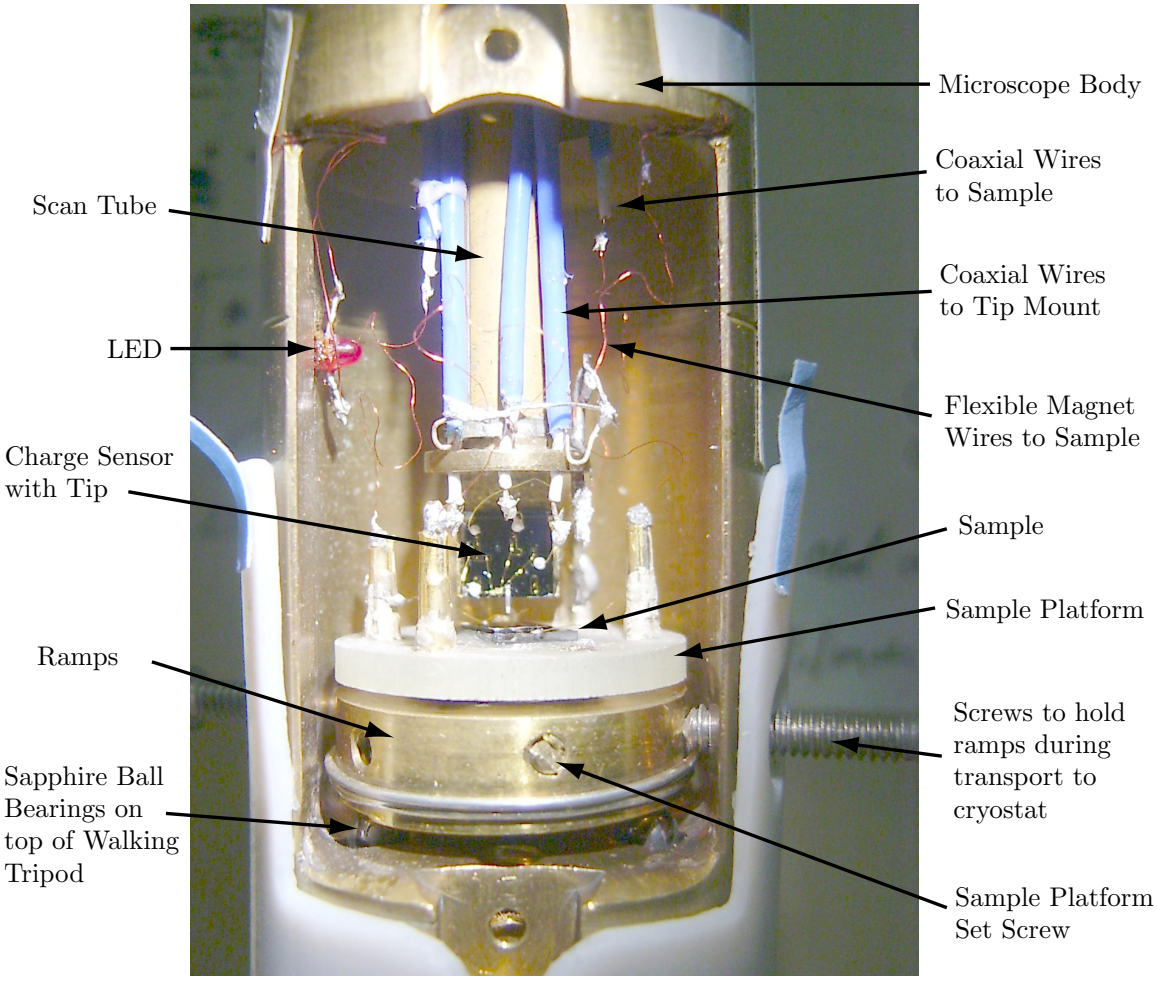

Figure 2-1: A picture of the scanning probe microscope. The sample sits on the sample platform. This platform is attached to a screw that threads into the brass "ramps" used in the Besocke coarse approach motor described in figure 2-2. Once the vertical distance is coarsely adjusted by threading the sample platform in or out of the ramps, the platform is fixed in place using a set screw. Three coaxial cables are provided for the charge sensor. Three additional coaxial wires are provided for the sample, which are connected to the sample platform by 5 cm lengths of 1-mil urethane coated flexible magnet wire.

top-loading probe from Oxford Instruments. A picture of the microscope is shown in figure 2-1.

Fundamentally, a scanning probe microscope consists of three separate parts: a coarse translation motor for large scale movements of the sample, a fine-scale "scanning" translation system that generates small displacements of the tip with respect to the sample, and a sensor to detect the signal from the interaction of the tip with

the sample. Our experiment uses a unique capacitance bridge charge sensor to detect the presence of electrons in the 2DES far below the surface of the sample, and is discussed in detail in section 2.2.

The fine-scale translation in our microscope uses a 3 inch long piezoelectric scan tube. The scan tube consists of a machined tube of piezoelectric ceramic with metalization that defines one electrode on the inner surface of the tube and four quadrant electrodes on the outer surface. Application of a voltage between the inner and outer electrodes causes the piezoelectric material to contract or expand in the radial direction depending on the relative directions of the applied electric field and the fixed polarization of the piezoelectric ceramic. In addition to the radial deformation, the tube also elongates in the vertical direction as it deforms in a way that tries not to change its total volume. The net deformation involves both a compression and a shear. It is this vertical elongation and contraction that produces the Z-direction scanning motion in our microscope. X and Y motion are produced by applying opposite voltages on opposing quadrant electrodes: this causes one side of the tube to elongate while the other size contracts, resulting in a bending of the tube producing lateral motion [56]. The amount of vertical and lateral motion achieved depends on the piezoelectric coefficients and the geometry of the tube [57, 58]. The piezoelectric coefficients also depend on temperature, and are typically reduced by a factor of 5 from room temperature to 4K. The geometry of our tube is chosen to give us a 15 μm lateral scan range and a 2.4 μm vertical range at 300 mK.

The coarse translation mechanism is required in order to bring the tip from an initial distance positioned by eye on the order of $\sim$ 1mm from the surface to within a distance comparable to the fine Z-range of the scan tube. Room temperature microscopes often accomplish this using a stepper motor. In cryogenic applications, this is impractical due to the limited space available in the cryostat and the low temperatures. Most cryogenic microscopes use a "stick-slip" translation motor driven by piezoelectric actuators [59, 60, 61, 62, 63, 64, 65, 66]. The coarse approach motor we have chosen is a Besocke "beetle" [67, 68] design. Here, the sample is mounted on a platform threaded into a brass disc that has three "ramps" machined onto the

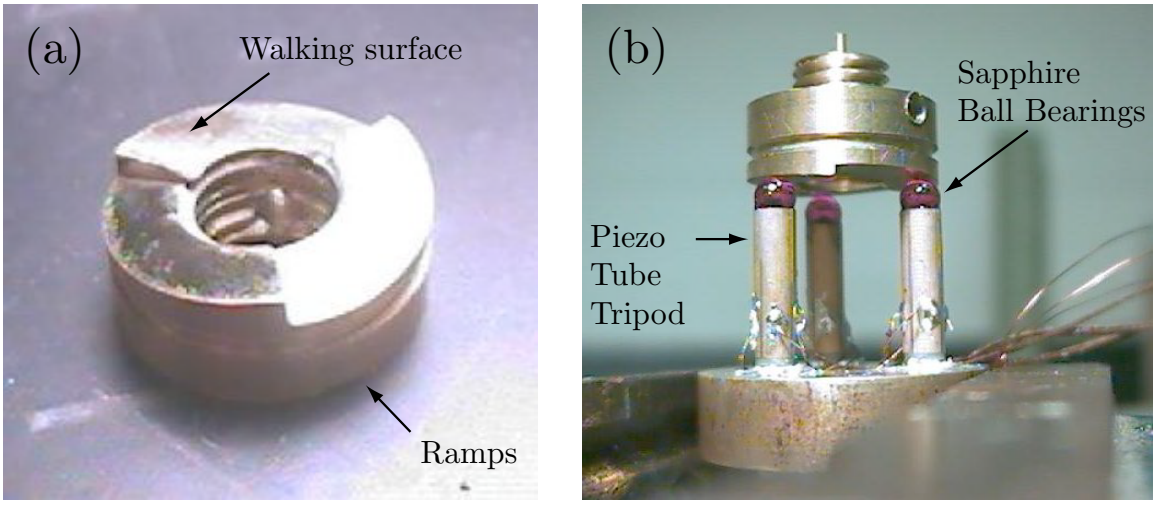

Figure 2-2: Pictures of a Besocke coarse approach motor. This motor was built for a smaller bore microscope than the one used in our experiments. (a) The sample holder disc with the three ramps machined into the bottom. (b) The sample holder placed on top of the tripod of piezo tubes. In the experiment, the sample is mounted on top of the sample holder, and the scan tube comes down from the top.

bottom, as shown in figure 2-2. The ramps are placed on top of a tripod of scan tubes. The bottom surface of the ramps is polished brass, which sits in contact with sapphire balls attached to the ends of the tripod tubes. To generate motion, a sawtooth waveform is applied to the scan tubes. During the slow rising edge of the sawtooth, the friction force between the sapphire and the brass allows the tubes to translate their motion to the ramps. On the fast falling edge of the sawtooth, the friction force is less that the force required to accelerate the inertia of the ramps, and the two surfaces slip relative to each other. This stick-slip motion allows a net linear translation of the ramps to be generated from an oscillating motion of the tubes. By moving the tubes in a tangential direction, a rotation of the sample is achieved with a vertical translation as the tubes "walk up" the ramps. By applying voltages to move all three tubes in the same direction, the same motor can be used to achieve a lateral X-Y translation.

In the Besocke design, the ramps are held in place on the tripod only by gravity. The normal force between the friction surfaces is determined by the weight of the ramps, and is generally quite small. As a result of this, the falling edge of the

sawtooth waveform does not need to be very sharp: typically, a fall time of ∼1-2 ms from 200V works fine. In contrast, the normal forces in clamped designs (for example in reference [59]) are much higher. These designs need fall times on the order of 1 μs from 200V, and require much faster electronics, typically employing a high power FET switching circuit rather than an op-amp to create the falling edge. One advantage of the of the Besocke design is that the longer fall time produces much less high-frequency interference noise: in FET switching design, unshielded cables and capacitive coupling can lead to high frequency transients that can damage static sensitive devices and even reduce the mobility of the 2D electron system [69]. One significant disadvantage of the Besocke design is that the sample is completely "loose", held lightly in place only by gravity. Extreme care must be taken not to bump the microscope or cryostat at any time to avoid crashing the sample into the tip.

2.2 Capacitance Bridge Charge Sensor

In order to sense the effects of electrons 1000 Å below the surface of the sample, we have developed an AC charge sensing technique based on a capacitance bridge [11, 70, 71]. In a capacitance bridge, the capacitance of a unknown capacitor is measured against a standard reference. In our experiment, the sample capacitance is formed between our scanning probe tip and the 2D electron system. The basic operation of a capacitance bridge is shown in figure 2-3.

For a voltage V_s applied to the sample capacitor and a voltage V_r applied to the reference capacitor, the voltage V generated at the "center point" of the bridge is given by

$$C_T V = C_s V_s + C_r V_r \tag{2.1}$$

where C is the total capacitance at the center point of the bridge, and is given by

$$C_T = C_s + C_r + C_g \tag{2.2}$$

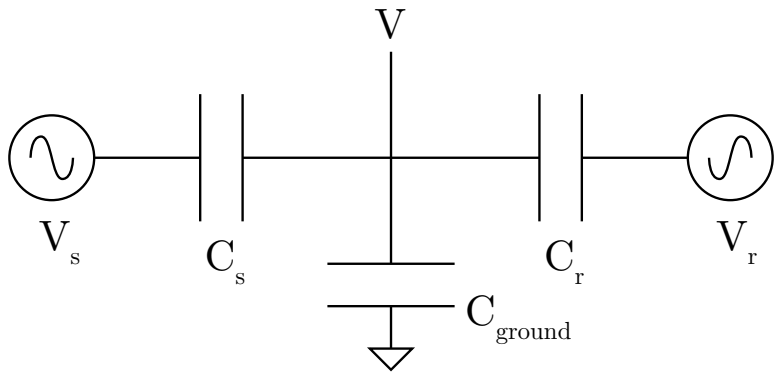

Figure 2-3: Schematic of a capacitance bridge. Balancing the bridge involves adjusting the amplitude and phase of V_r so that the voltage V at the center of the bridge is zero.

where C_g is total stray capacitance to ground. A precise measure of the value of the sample capacitance can be made by choosing a voltage V_r that is of the opposite sign (or 180 degrees out of phase, for an AC signal), and of a magnitude such that the voltage V at the center of the bridge is nulled. Balancing the bridge in this way, the sample capacitance is given by:

$$C_s = \frac{C_r V_r}{V_s} \tag{2.3}$$

A significant advantage of the capacitance bridge is that it allows a precise measure of the sample capacitance without needing an independent measurement of the shunt capacitance or of the gain of any amplifiers used to measure V.

In our experiments, we are generally interested in small changes of the sample capacitance in response to changes in experimental parameters, such as bias voltage, magnetic field, or tip position. These changes are often very small (≈ 30 aF) compared to the total capacitance between the tip and the 2D electron system (typically ≈ 40 fF). For these measurements we do not balance the bridge at each point, but instead use the bridge to null the large background signal. This affords us a significant technical advantage, since we are now measuring small changes in a small signal instead of small changes in a very large signal. The remaining out of balance signal can be directly related to the change in the sample capacitance. Assuming that these changes ΔC_s are small compared to the total capacitance C_T, then equation

2.1 becomes:

$$C_T(V + \Delta V) = (C_s + \Delta C_s)V_s + C_r V_r \tag{2.4}$$

If the bridge was initially balanced, the out of balance signal then becomes:

$$\Delta V = \frac{V_s}{C_T}\Delta C_s \tag{2.5}$$

This allows us to directly convert out of balance voltage readings into changes in the sample capacitance.

This also illustrates a very important consideration for the capacitance bridge technique: as can be seen in the above expression, the out of balance signal of the capacitance bridge is inversely proportional to the total capacitance at the center of the bridge. In order to maximize the sensitivity of the bridge, the stray capacitance to ground C_g should be minimized. Since the cables running to the top of the cryostat have a shunt capacitance of at least 200 pF, using a room temperature amplifier to measure the voltage when working with a 40 fF sample capacitance would result in significant signal loss. For this reason, we have designed a cryogenic amplifier that is mounted ≈ 1 mm from the tip, which allows us to reduce the total bridge capacitance C_T to a value of around 800 fF. A picture of the tip mount with the cryogenic amplifier is shown in figure 2-4.

The cryogenic amplifier is based on a commercial low input capacitance High Electron Mobility Transistor (HEMT). The transistors we use are Fujitsu model FHX35X, chosen for their low input capacitance, high transconductance, and their availability in an unpackaged format. The schematic of the amplifier is shown in figure 2-5. The design incorporates two FHX35X transistors. The measurement transistor is in a common-source configuration, and is used to amplify the signal at the center point of the bridge. The second transistor, labeled the "bias" transistor, is used in a very unconventional way: by pinching off the channel, we use it as both a high impedance (> 100 MΩ) resistor to provide the DC bias voltage to the gate of the measurement transistor, and also as a reference capacitor for our AC capacitance bridge.

The use of the bias transistor offers several advantages. In order to work cold,

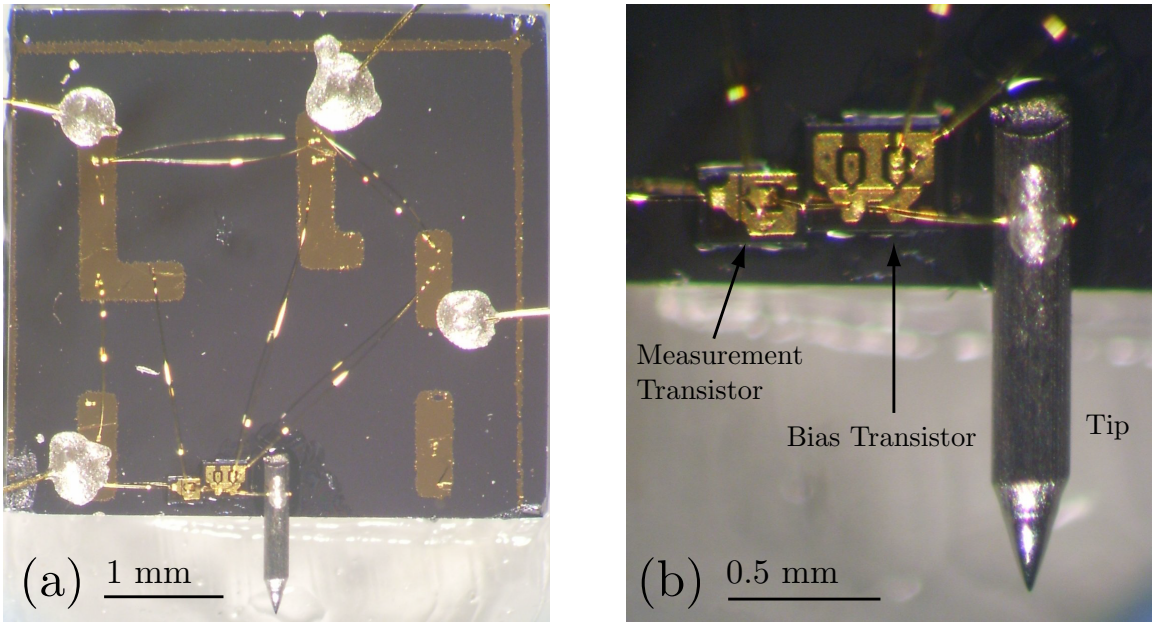

Figure 2-4: Pictures showing the layout of the SCA charge sensor. In this sensor, the measurement transistor has been cleaved. The tip is attached to the GaAs carrier using non-conductive Stycast 1266 epoxy, and has been cut as short as possible to minimize the shunt capacitance. In order to keep the wire bond from the tip to the gate of the measurement transistor as short as possible, the transistors are lined up as shown and the bond wire is glued directly to the tip. The extra wire bonds shown in (a) connecting all of the bond pads are to protect the gates of the transistors from static charge. They are removed once the wires are soldered to coaxial cables on the microscope.

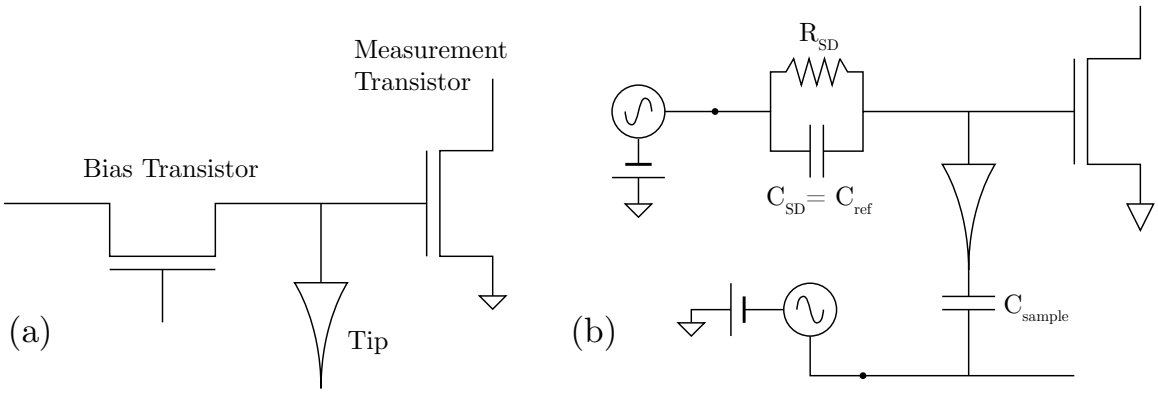

Figure 2-5: (a) Schematic of the cryogenic amplifier. The measurement transistor acts as a common-source amplifier. (b) Effective circuit during operation. Once pinched off, the bias transistor acts as both a reference capacitor for the bridge and a high impedance resistor for DC biasing the gate of the measurement transistor. A DC bias applied to the sample allows us to adjust the DC voltage between the sample and the tip.

conventional resistors must be of the metal film variety, as "thick chip" ceramic and carbon composition resistors have exponential temperature dependence in the cryogenic range. In order to produce a metal film resistor with a sufficiently high resistance (> 10 MΩ), a long meander line pattern must be used as the sheet resistance of the metal film is relatively small. These long meander line resistors result in an increased shunt capacitance to ground, which would reduce our sensitivity. (Measurements showed an increase of about 700 fF for a 10 MΩ commercial meander line resistor from Mini-Systems Inc. as compared to an uncleaved FHX35X bias transistor.) A second advantage of the bias transistor is that by opening up the channel, we can obtain a direct measure of the gain of the measurement transistors. Knowledge of the gain allows us to directly measure our shunt capacitance and the input noise of our cryogenic amplifier (see appendix A). Quantitative measurements of both of these is required to properly optimize the sensor design.

In addition to the gain stage at 300 mK, a second common-source amplifier stage is used at the 1K Pot of the cryostat. The purpose of this second stage is to increase the bandwidth of the cryogenic amplifier. In a common-source configuration with a fixed drain resistor and a voltage readout, the bandwidth of the amplifier will be limited by the RC charging time formed from the differential resistance of the HEMT with the capacitance of the cable leading to the next voltage amplification stage. This second stage is biased to give some amplification, but more importantly to give smaller source-drain resistance than the first stage so that it can drive the capacitive load of the cables to the top of the cryostat. With a typical setup, this gives an overall corner frequency of about 300 kHz. At 1 MHz, the gain drops to about 2, and the input noise of the room temperature amplifiers begins to become important. The bandwidth can be increased by using a custom designed current amplifier to read out the signal from the second stage (see section B.3). This increased the corner frequency to about 1.5 MHz, which was likely limited by the differential resistance of the first stage transistor charging the length of cable to the 1K pot. In the end, however, the experiment suffered from significant electrical interference noise at these high frequencies, possibly due to radio station signals. The signal to noise ratio was

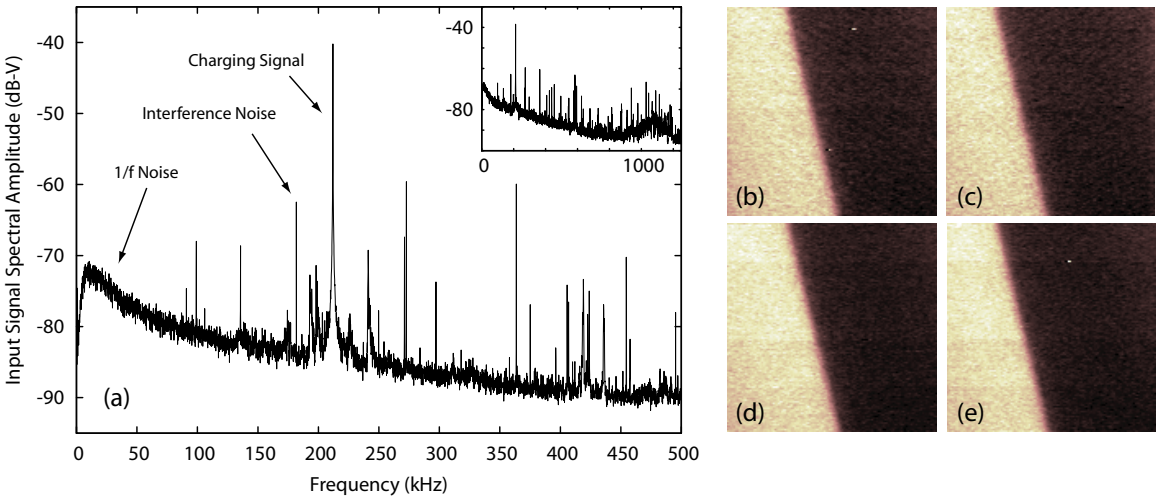

Figure 2-6: (a) The frequency spectrum of the broadband signal at the input of the lock-in amplifier, recorded using the Tektronix TDS744 digital oscilloscope in FFT mode. The noise consists of two components: a 1/f noise power spectrum inherent to the transistors and interference noise that couples in as narrow band spikes. The charging signal can be seen in the frequency spectrum as a peak at 212 khz. As long as the density of noise spikes is relatively sparse, interference noise can be avoided by selecting a measurement frequency inside a 1 kHz range where there are no spikes. The SR560 preamplifier was configured to give a 2-pole high-pass filter at 10 kHz for this measurement. The inset shows the same signal spectrum recorded to 1.25 Mhz, showing the significant increase in interference noise at high frequencies. (b),(c) Forward and reverse scans showing an example of the influence of narrow-band interference noise on the images. The noise produces a slow oscillation of the lock-in output leading to opposing diagonal lines in the forward and reverse scans. (d),(e) The same scan taken with the frequency shifted by 3kHz so that the interference noise is now outside of the output filter bandwidth.

still poor at MHz frequencies despite the increased cryogenic amplifier bandwidth.

Noise in the experiment comes mostly from two sources: the interference noise mentioned above, and the intrinsic noise of the HEMT transistors. Both of these contributions can be seen clearly in the frequency spectrum shown in figure 2-6. The units of the noise measurement using the FFT mode of the scope are in units of the amplitude of the output voltage, but can be calibrated by measuring the noise using the lock-in amplifier noise mode at a given frequency (see appendix A for a detailed discussion). Interference noise is electrical noise that consists of sharp spikes in the frequency spectrum where an external sinusoidal signal is coupling into the experiment and is being amplified. The most common way this type of noise can

couple in is through ground loops or unshielded cables. It can often be eliminated by improving grounding, shielding, or both (see section X in [72] for an excellent discussion of sources of interference noise and how to eliminate them). When looking at the output of the lock-in amplifier, this interference noise will only appear if there is a noise spike separated from the measurement frequency by an amount smaller than the bandwidth of the output filter time constant (typically ∼40 Hz). The noise spikes can easily be seen by looking at the frequency spectrum of the broadband signal after amplification (see appendix A). If the density of spikes is not too high, they can be eliminated by shifting the frequency by a small amount (∼100 Hz) to pick part of the noise spectrum that is free of spikes.

The HEMT transistors also have an intrinsic noise spectrum that has a 1/f character, and that is characterized as fluctuations in the channel conductance[73]. Because the noise diverges at low frequencies, there is a significant advantage to working at high frequencies. The noise becomes qualitatively "very bad" below about 10 kHz, and makes it impractical to measure below this frequency. At 200 kHz, with a well optimized setup, we have achieved input noises as small as 5 nV/$\sqrt{\text{Hz}}$. As a technical detail, although the large low frequency noise will not couple in directly to the output of the lock-in as it is well outside of the output filter bandwidth, it can limit the gain that can be used on the room temperature amplifiers. For this reason, a Stanford Research SR560 preamplifier is used with a 2 pole High pass input filter at 10 kHz at after the second stage of the cryogenic amplifiers. This allows the gain of the room-temperature amplifiers to be set quite high giving better overall noise performance. (Typically, we were able to use 40 dB on the SR560 and 34 dB on the 7280 input amplifier.)

Ultimately, the most important noise figure for the measurement setup is the equivalent input charge noise. The capacitance signal can always be made larger by increasing the magnitude of the AC excitation applied to the 2D electron system. However, due to the small energy scales in the experiment, it is important to use a small excitation voltage. Thus it is the charge sensitivity that will ultimately limit our ability to reduce the amplitude of the AC excitation. Given an input voltage

noise for the cryogenic amplifier, the charge noise can be calculated by multiplying the voltage noise by the total center point capacitance:

$$e^* = C_T v^* \approx 5 \text{ nV}/\sqrt{\text{Hz}} \times 800 \text{ fF} \approx 0.04 \text{ e}/\sqrt{\text{Hz}} \tag{2.6}$$

One can see that reducing the shunt capacitance will lead to a lower charge noise for the same input voltage noise. Since the averaging time needed to remove noise goes as the square of the signal to noise ratio, every possible care should be taken to minimize the shunt capacitance: a factor of two increase in the signal to noise ratio results in a factor of four reduction of the averaging time.

As a final note, one has to be careful about how the center point capacitance is minimized. In particular, an analysis of gain of the HEMT amplifier (see appendix B) shows that reducing the shunt capacitance by cleaving the measurement transistor will not necessarily increase the charge sensitivity, and in fact will likely only decrease it. The reason is quite simple: the transconductance of the measurement transistor is proportional to its width, and thus cleaving the transistor in half will cut the gain in half. The input capacitance of the measurement transistor is about 300 fF, which means that by cleaving the transistor we have reduced the total capacitance from $\sim$ 800 fF to $\sim$ 650 fF. This 20% reduction of the shunt capacitance does not make up for the 50% decrease in the transistor gain, and thus our overall sensitivity is reduced by 30%. This would suggest the optimal sensitivity would be achieved when the input capacitance of the measurement transistor dominates over the unavoidable shunt capacitance, although the details will also depend on how the input noise of the HEMT varies with the channel width. (For more details, see the discussion in appendix B). In practice, these considerations suggests that the measurement transistor should not be cleaved, and that some benefit may be achieved by combining multiple FHX35Xs in parallel.

2.3 What does SCA measure?

Fundamentally, SCA directly measures the amplitude and phase of the AC charge induced on the tip due to the AC excitation applied to the ohmic contacts at the corners of the 2D electron system. To understand what this tells us about the physics of the 2D electron system, consider the schematic model of the system as shown in figure 2-7. The bulk 2D electron system can be thought of as a distributed RC network formed from the sheet resistance of the 2D electron system and the self capacitance of the 2D electron system to ground.

We will first consider the effect of varying the sample-tip capacitance. If the conductivity of the 2DES is large then all of the resistors in this model will be irrelevantly small and variations in the charging signal will tell you directly about the local capacitance between the sample and the tip. Variations of the sample-tip capacitance will result in a change in the amount of charge induced on the tip for a given excitation voltage. Variations of this nature can arise due to geometric changes in the sample-tip capacitance, for example if the tip is moved closer or further from the surface of the sample. They can also arise due to changes in the electrochemical (or "quantum") contributions to the capacitance. Such quantum contributions occur when one of the plates of the capacitor is not a perfect metal, but instead a material with a finite density of states dn/dE such as a semiconductor. In this case, the measured capacitance is reduced from the purely geometric capacitance [74, 75, 76]: for a parallel plate geometry C_{meas} is given by

$$\frac{1}{C_{\text{meas}}} = \frac{1}{C_{\text{geom}}} + \frac{1}{e^2 A \; dn/dE} \tag{2.7}$$

where e is the electron charge and A is the area of the capacitor. Physically, this can be understood as due to a change in the work function of the semiconductor due to a change in the Fermi energy. By applying an external voltage V to the capacitor using a battery, we do not set the electrostatic potential difference between the capacitor plates, but instead impose an electrochemical potential difference. If the chemical potential of the semiconductor varies by an amount $\Delta\mu$ due to a change

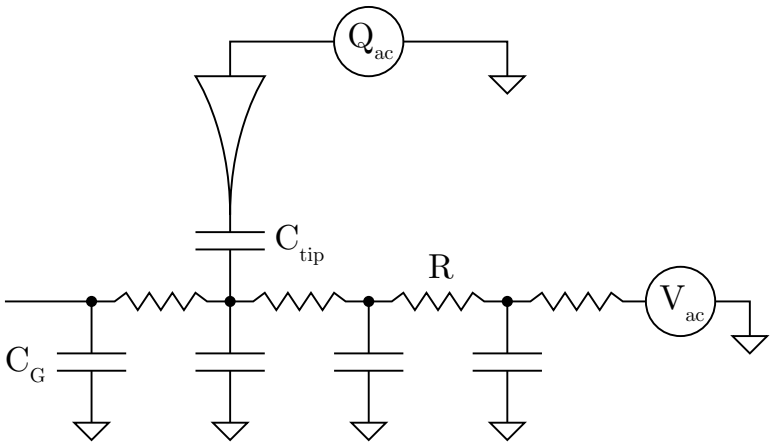

Figure 2-7: Schematic showing a distributed RC model of charging in the 2D layer.

in its electron density, then the electrostatic potential difference between the plates is $\Delta U = V - \Delta\mu$. Measuring the charge on the plates, we would find a charge $Q = C_{geom}(V - \Delta\mu)$, leading to a reduction of the measured capacitance. Through this electrochemical contribution to the capacitance, SCA can in principle be used to image local changes in the density of states of the 2D electron system.

Another way in which the charging signal can change is through variations of the resistance of the path from the ohmic contact where the AC excitation is applied to the position of the tip. If the resistance of the 2D electron system becomes large, then the rate at which the network of resistors can charge and discharge the capacitors in figure 2-7 can become slower than the frequency of our AC excitation. As this happens, the amplitude of the charging signal will also decrease. An important distinction, however, is that this drop of signal will also be associated with a phase change: this provides a clear signature that allows the differentiation between signal changes due to capacitive effects and resistive effects.

The difference between the changes in the charging signal from these two effects can be illustrated by considering the simple RC model shown in figure 2-8. Here, the region under the tip is treated as having some self capacitance to ground given by C_g. It is connected to the AC excitation by a resistor R. The sensor in our circuit directly measures the in-phase and 90-degree lagging phase components of the AC charge induced on C_{tip}. The resulting signal as a function of the measurement

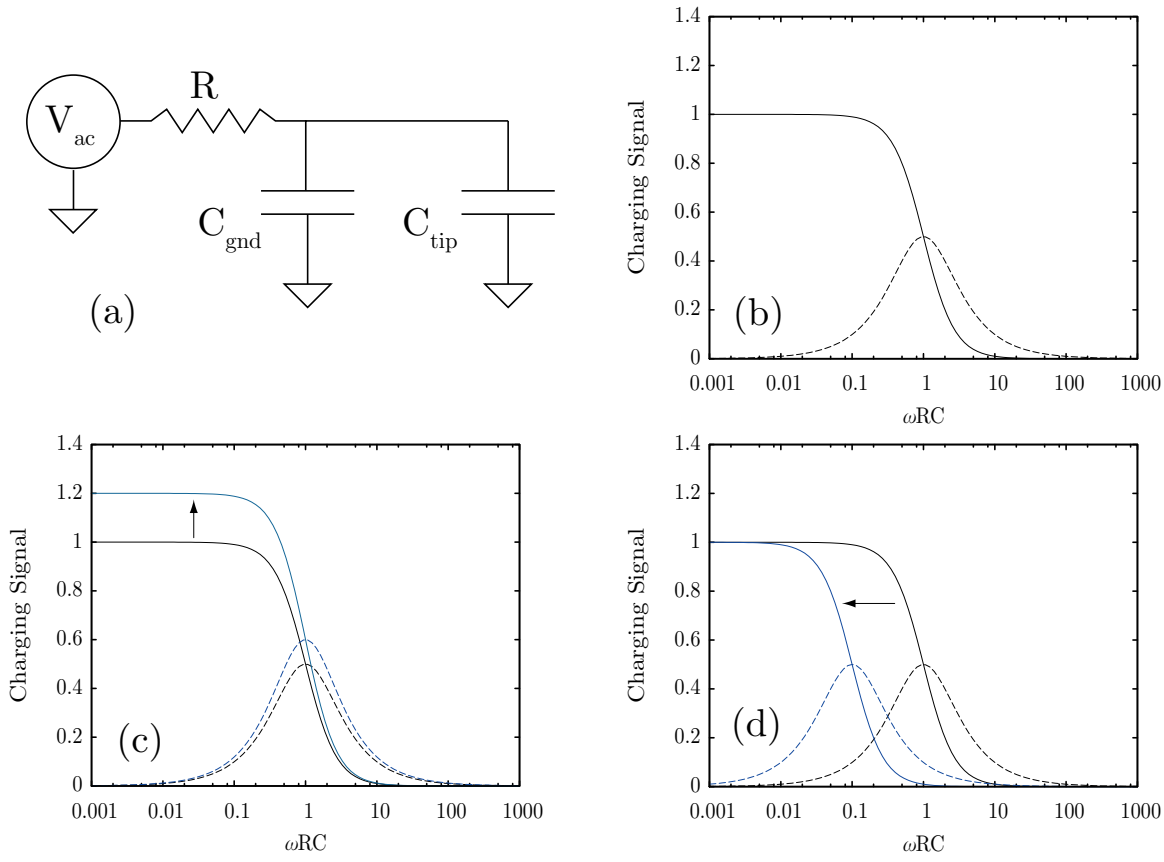

Figure 2-8: Simple RC charging model. (a) A model for the charging signal in the experiment. A resistance R from the resistivity of the 2DES charges up local the capacitances of the 2DES C_{tip} and C_{ground}. The charge sensor directly measures the charge induced on C_{tip}. (b) The in-phase and lagging-phase charging signals as a function of frequency. As the frequency is increased, the capacitor does not have time to charge and discharge during the cycle of the excitation. As we pass through $\omega = 1/RC$, the in-phase signal rolls off while the lagging-phase signal goes through a peak. (c) A change in the sample capacitance C_{tip} results to first order in only a vertical scaling of the whole curve, since more charge is being distributed on C_{tip}. (b) Changes in the resistance R shifts the curve to lower frequencies but does not change the height.

frequency ω and the RC charging time τ is shown in figure 2-8. A change of the sample to tip capacitance will result to first order in a constant scaling of the curve. Changes of the resistance R, however, will cause the entire curve to shift laterally. As it does so, we will see a roll off in the in-phase charging signal and a peak in the lagging-phase signal. It is also interesting to note that for small resistances ($\omega RC << 1$), the in-phase signal will begin to change as:

$$X \propto 1 - (\omega\tau)^2 \tag{2.8}$$

while the lagging phase signal will be linear in $\omega\tau$:

$$Y \propto \omega\tau \tag{2.9}$$

Thus, small changes in the sheet resistance will show up stronger in the lagging phase signal than in the in-phase signal. This effect is seen clearly in magnetocapacitance curves at low magnetic fields, where Shubnikov-de-Haas oscillations appear first in the lagging-phase data (see, for example, figure 2-18).

2.4 Understanding the influence of the measurement on the 2D electron system

Charge accumulation imaging has a significant advantage over many other techniques because the DC electric fields between the sample and the tip from the work function difference can be completely nulled if desired. This is in stark contrast to STM: in STM, there are large electric fields between the sample and the tip even when no current is flowing. They cannot be eliminated because applying a bias voltage results in current flow. These large electric fields will lead to a significant change in the local electron density and Fermi energy under the tip. Another common technique that is often used to study the 2D electron system is electrostatic force microscopy (EFM) (or similar variants with different names that are based on measuring an electrostatic

force, such as "scanning potential microscopy" [77, 78] or "Kelvin-probe" force microscopy). EFM is also capacitively coupled, but in EFM, the force is proportional to the square of the image charge on the tip. This allows the sensitivity to be enhanced by applying a DC voltage between the tip and the sample [77]. Using such a technique, EFM has the capability to achieve single-electron sensitivity [79, 80]. However, the sensitivity is significantly degraded if the DC electric fields are nulled (see figure 2 in [80]). Because the SCA sensor is capacitively coupled and the sensitivity does not depend on the DC fields between the tip and the sample, we can eliminate the DC electric fields by applying a DC voltage to null them, and hence image features of the unperturbed electron density.

While we can eliminate the DC perturbation of the 2D electron system, we will still have a small AC perturbation due to the AC excitation we are using. An important question then becomes: how small should the AC excitation be to avoid perturbing the 2D electron system?

The effect of the AC excitation is relatively easy to analyze if the conductivity of the 2D electron system is large. In this case, there are no lateral voltages in the sample and the sample charges and discharges due to its capacitance to ground and to the tip. This is shown schematically in figure 2-9. In the absence of the tip, the AC excitation would induce a small, uniform modulation of the bulk density due to the 2D layer capacitance to ground. In our case, the nearest ground plane is a metal backgate evaporated on the back of the sample, a distance of ~ 500 μm away. For a 10 mV excitation, this would give a bulk density modulation of:

$$\Delta n_{\text{bulk}} = \frac{\epsilon V}{d} \sim 10^6 e/\text{cm}^2 \sim \frac{n_{\text{typical}}}{100\ 000} \tag{2.10}$$

For typical electron densities of 1.5×10^{11} e/cm^2, this corresponds to a density change of 1 part in 10^5, and is completely negligible. The tip has a more significant effect. In our experiments, we use tips with a large radius of curvature (~ 2 μm). For a typical distance of 50 nm above the surface, we can confidently use a parallel plate capacitor model for the electric fields from the tip. The 2D electron system is 100 nm below

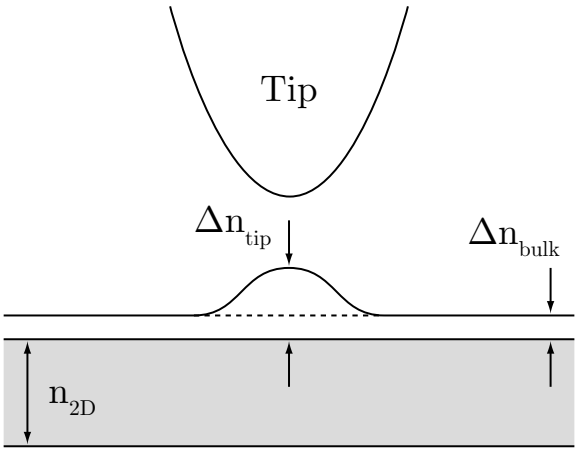

Figure 2-9: Effect of the AC excitation on the fully charging 2D electron system. The AC excitation induces a periodic modulation of the bulk density by an amount Δn_{bulk} due to the self capacitance of the layer. There is an additional AC modulation under the tip due to its local capacitive coupling. Typical numbers for these perturbations are $\Delta n_{\text{bulk}} \sim 10^6$ e/cm^2 and $\Delta n_{\text{tip}} \sim 10^9$ e/cm^2, while $n_{2\text{D}} \sim 1.5 \times 10^{11}$ e/cm^2. Note that the charge induced on the tip (ie. our signal) is equal to the total integrated charge in the area above the dashed line in the figure.

the surface of the GaAs semiconductor, giving:

$$\Delta n_{\text{tip}} = \frac{V}{\frac{100 \text{ nm}}{\epsilon_{\text{GaAs}}} + \frac{50 \text{ nm}}{\epsilon_0}} = \frac{\epsilon_0 V}{60 \text{ nm}} \sim 10^9 \text{ e/cm}^2 \sim 1\% \tag{2.11}$$

For a sample density of $1.5{\times}10^{11}$, the Fermi energy is about 54K, thus a 10 mV excitation in this case produces variations of the local Fermi energy comparable to our temperature of 300 mK, and can be considered a small perturbation. Note also that, as shown in figure 2-9, the amount of AC charge induced on the tip is exactly equal and opposite to the extra AC charge induced in the 2DES due to the presence of the tip. Thus, in some sense, our signal is always proportional to the magnitude of the tip's AC perturbation of the 2D electron system.

Things become considerably more complicated if the 2D electron system, or portions of it, become highly resistive. In particular, we will consider the case of an isolated metallic region that is positioned under the tip. This island will be separated from the metallic bulk by a highly resistive ring, as illustrated in figure 2-10. This model has particular relevance for our experiment, where the inner disc represents a

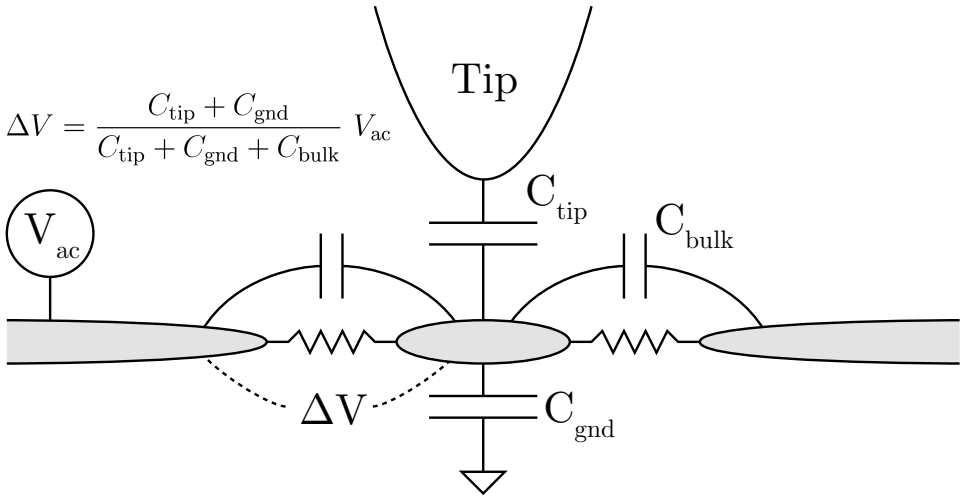

Figure 2-10: Model of an island in the 2D electron system that is isolated from the bulk by a resistive ring. In the high resistance limit $R >> 1/\omega C$, there will be a voltage drop ΔV across the ring given by V_{ac} divided by a capacitive "lever arm". This lever arm factor is given by the ratio of the island's capacitance to ground and the tip to its self capacitance.

region of $\nu > 1$ induced by a DC tip bias, the resistive ring represents the incompressible strip formed at $\nu = 1$, and the magnetic field is chosen such that the bulk is in the $\nu < 1$ compressible state. If the resistance is large enough that the RC charging time of the island is much longer than the period of the AC excitation, then the island will not charge and there will be a voltage drop across the resistive region. For a completely non-charging island, the voltage on the island will be determined by a capacitive divider:

$$V_{\text{island}} = \frac{C_{\text{bulk}}}{C_{\text{tip}} + C_{\text{gnd}} + C_{\text{bulk}}} V_{\text{ac}} \tag{2.12}$$

and the voltage drop ΔV across the resistive region will be:

$$\Delta V = \frac{C_{\text{tip}} + C_{\text{gnd}}}{C_{\text{tip}} + C_{\text{gnd}} + C_{\text{bulk}}} V_{\text{ac}} \tag{2.13}$$

As long as the island's capacitance to the bulk dominates its capacitance to ground and the tip ($C_{\text{bulk}} >> C_{\text{tip}} + C_{\text{gnd}}$), the voltage on the island will float up and down with the AC excitation, and the voltage drop will be small. If the island's

capacitance to ground and to the tip become significant, the voltage dropped across the strip will increase. Estimates of this "lever arm" reduction depend sensitively on the size and shape of the tip, the width of the strip, and the distance from the tip to the surface. To obtain good estimates, we have calculated the lever arm using a numerical electrostatic model (see chapter 5). From the simulations, we obtain numbers on the order of ∼800 aF for $C_{\rm bulk}$ and ∼50 aF for $C_{\rm tip}$ and $C_{\rm gnd}$. The calculated lever arms vary from about 5 to 10, depending on the size of the tip its height above the surface, the size of island, and the width of the resistive strip. Note also that equation 2.13 gives only the maximum voltage drop possible: when the resistive ring becomes leaky, the bubble can begin to charge again, and the voltage drop across it decreases. When the resistance is low enough that the bubble fully charges, the voltage drop goes to zero.

Ideally, the excitation should be chosen such that the maximum voltage drop across the strip is small compared to other relevant energy scales in the experiment, such as the Landau level energy gaps or the temperature. What are the magnitudes of these energy gaps? The orbital energy gap for the GaAs 2D electron system is $\hbar\omega_c = \hbar eB/m = 1.7$ meV/T, giving a gap energy of 10.2 mV at 6T for even integer filling factors. At odd integer filling factors, the energy gap is not given by the cyclotron energy, but instead by a spin subband splitting. In 2D systems at large magnetic fields, this spin splitting is much larger that the bare Zeeman splitting that is expected. The enhancement of the spin splitting is due to the exchange interaction, which energetically favors electrons with parallel spin. This exchange enhancement was first considered by Janak in 1969 [81] in non-quantizing magnetic fields . Ando and Uemura [82] extended these ideas to the quantum limit at very large magnetic fields, where only a small number of Landau levels are occupied. In their model, the exchange energy is given by:

$$E_{\rm ex} = E^0_{\rm ex}(n_\uparrow - n_\downarrow) \tag{2.14}$$

where $n_\uparrow$ and $n_\downarrow$ are the relative populations of the two spin states of a given Landau

level. At magnetic fields where an orbital Landau level is half filled, the exchange interaction creates a large energy gap given by $E_{\rm ex}^0$ and the system is spin polarized. As we begin to fill the second spin sub-band, the magnetization is decreased, and the exchange enhancement goes to zero as when the net spin polarization vanishes. In this model, the relevant energy scale for us is $E_{\rm ex}^0$, as our tunnel barrier is formed by the energy gap in the incompressible strip region, which is fully spin polarized.

In recent years, much more sophisticated models of the exchange interaction have been introduced [83, 84, 85, 86, 87]. In particular, the possibility that the electron spin does not have to lie along the magnetic field direction [85, 86] led to a remarkable prediction that quasiparticles around odd integer filling factors are not simply single spin up electrons, but instead consist of a charged, localized spin wave with a curling topological ordering of the spin orientation. These quasiparticles were described as "skyrmions" [85]. Nonetheless, from our point of view, the exact nature of the quasiparticles is not so important: whatever they are, there is still an energy gap for creating them. These gaps can be calculated theoretically [85], and it is this energy gap that will form the tunnel barrier in our incompressible strip.

From an experimental standpoint, a measure of the exchange-enhanced spin gap can obtained from thermally activated transport measurements [24, 88, 25, 27, 30]. At quantum Hall plateaus, the conductivity σ_{xx} shows an activated behavior as a function of temperature:

$$\sigma_{xx} = \sigma_{xx}^0 \exp\left[-\frac{\Delta E}{2k_B T}\right] \tag{2.15}$$

over as much as two decades in conductivity. Measuring the temperature dependent activated conductivity yields an energy scale energy ΔE for the energy gap[1]. From thermally activated transport measurements of σ_{xx} in odd integer quantum Hall plateaus, Nicholas et al. [24] measured an activation energy gap at odd filling factors of:

$$E_{ex}^0 = 1.73 \text{ meV}/\sqrt{\text{T}} \tag{2.16}$$

At 6T, this would give an exchange enhanced gap of 4.2 mV for integer filling. In

[1]See section 1.2 for a discussion of the factor of two.

subsequent works, measurements at lower fields showed that the activation energy at low fields fit better to a linear function of B [25, 89, 30], and was attributed to the effects of disorder. One has to be careful, however, in interpreting these numbers. The connection between the activation energy obtained from transport through the bulk sample and a microscopic energy gap must be made through a model of the localization in the quantum Hall effect, and a model of exactly how this localization affects the diagonal conductivity. Since localization and transport mechanisms in the 2D electron system at quantum Hall plateaus are still not well understood, the exact connection between the bulk measurements and microscopic energy scales is not clear. These numbers should only considered as a guideline as to what the *microscopic* energy gap could be at high fields.

It would be nice to use an AC excitation small enough that any voltage drops in the sample is smaller than all of these energies. In practice, however, the AC excitation cannot be made arbitrarily small. Furthermore, without a detailed model of the capacitive lever arm, it is even difficult to say *a priori* how to relate the magnitude of the excitation to voltage drops in the sample. The practical limitation is that reducing the excitation amplitude has a quadratic effect on the required averaging time: reducing it by a factor of two requires four times as much signal averaging. At some point, instability in the tip position and other factors make it impractical to spend more time averaging. It is mostly this signal-to-noise limitation that influenced the choice of the amplitude of the AC excitation we have used in our measurements. It is important, however, to keep in mind the ways in which the amplitude of the excitation can influence the experiment, and to carefully study the effect that changing the excitation has on the results.

2.5 Sample Design

In our experiments, we study high mobility 2D electron and hole systems produced in AlGaAs/GaAs heterostructures. These are grown by molecular beam epitaxy by our collaborators. In order to perform SCA microscopy on these samples, as a minimum

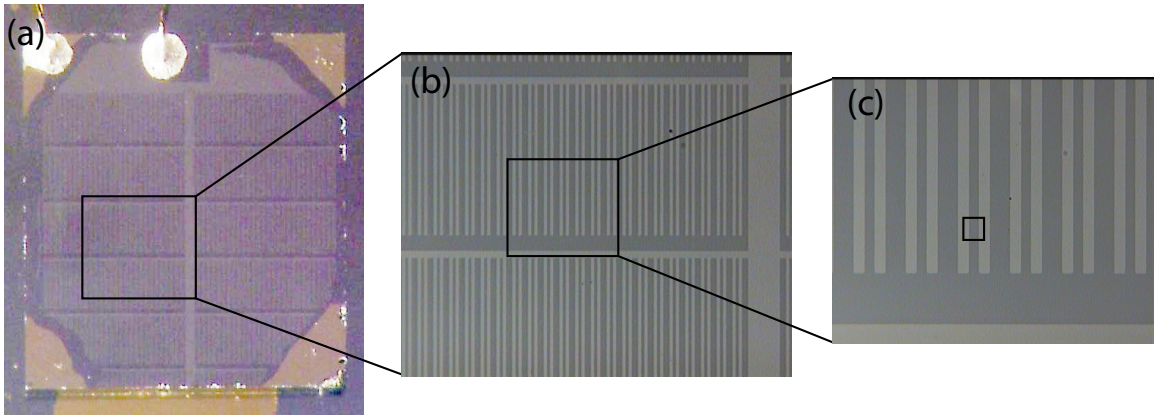

Figure 2-11: Optical images of the sample after processing. Four ohmic contacts are patterned in the corners using photoresist drawn with a toothpick. The metal topgate is patterned with optical lithography and is made from a 10 nm thick chromium layer. The gate bars are 10 μm wide and have alternating 10 and 20 μm gaps. The back of the sample is polished on a wafer polishing machine and a 200 nm Ti/Au layer is deposited to act as a backgate. In (c), the small black box indicates the maximum size of the scan window of the SCA microscope.

we need to make ohmic contacts to the 2D electron layer. This is achieved using standard annealed NiAuGe contacts for electron systems. The sample processing techniques we have used are the same as outlined in [11].

While ohmic contacts are the only necessary sample processing for SCA studies, the majority of our samples also include a metal topgate patterned on the sample surface. This topgate is defined using optical lithography after making the ohmic contacts. The pattern consists of a repeating set of "combs" that are 10 μm wide and have alternating 10 and 20 μm gaps. Optical pictures of a sample with a topgate are shown in figure 2-11. The metalization is made from a 10 nm thick later of Cr, made as thin as possible while maintaining a conducting continuous metal film. AFM images of the gate are shown in figure 2-12, and show a height of 10 nm. The gaps in the comb fingers are chosen to match the maximum scan range of our microscope. This, combined with the repeating pattern, means that we do not have to walk laterally after the initial coarse approach, as all points on the 5 mm area are equivalent. The gates also prevent the diffusion of surface charge between adjacent gaps, allowing us to always be near a fresh unperturbed region of 2D electron system should the tip touch the surface.

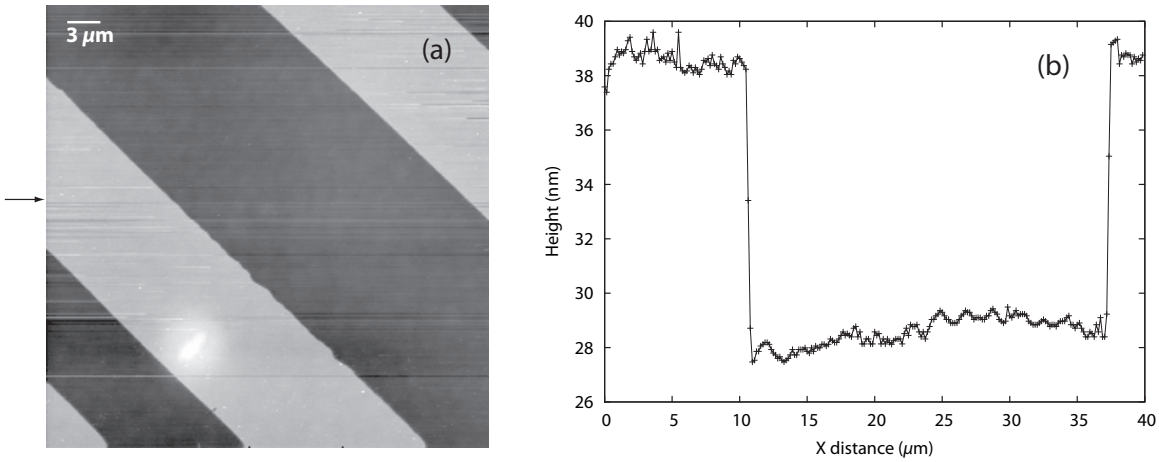

Figure 2-12: (a) A 40x40 μm AFM image of the sample after processing, taken with the Digital Instruments AFM in the CMSE shared facility. The surface of the sample shows islands approximately 1 nm tall and 1 μm in size. These islands are formed naturally as part of the epitaxial growth. Also shown in the bottom left is an example of an oval growth defect: it is about 5 μm in diameter and is 20 nm tall. (b) A horizontal line cut of the AFM image, taken at the position indicated by the arrow in (a). The gate is relatively flat, and shows a measured thickness of 10 nm.

The original idea behind the topgate was to allow us to locally deplete the electron layer and image the spatial structure at the edge of the 2D electron system. However, in every sample we have tested, applying a topgate voltage has led to instability and spreading of charge into either the surface states or the donor layer. (This was also observed in scanning probe measurements by other groups [90]). In all of our results, we have been careful never to apply a DC voltage to the topgate. While it does not serve its original intended purpose, the topgate has proven to have many useful properties: it aids charging of the bulk of the sample at high magnetic fields, it greatly simplifies finding the surface without damaging the tip, and it provides a method of measuring the size of the tip in-situ. For these reasons, we have continued to use samples with a patterned topgate.

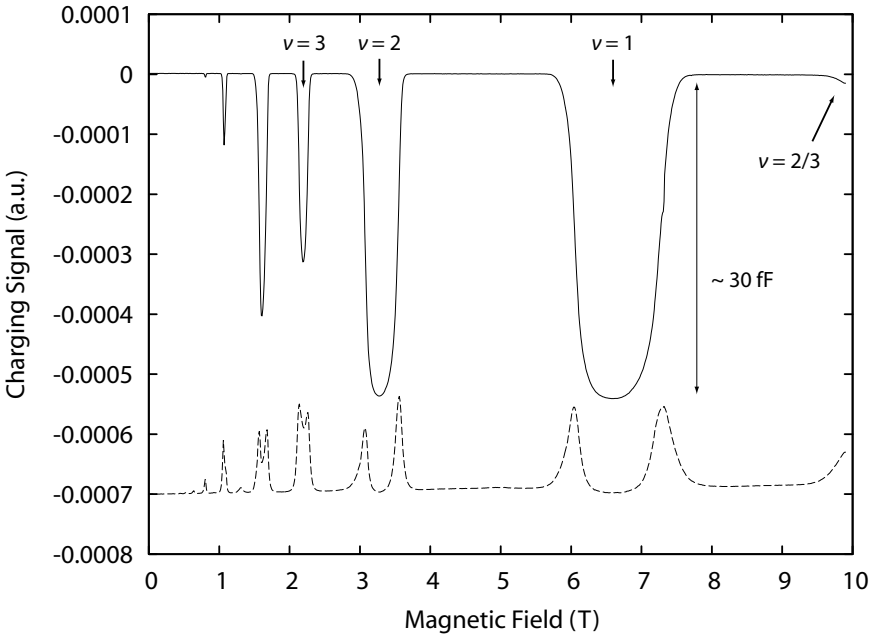

Figure 2-13: A magnetocapacitance trace taken with sample from wafer M226 with no gate. The solid and dashed lines show the in-phase and lagging-phase charging signal respectively. With a filled Landau level in the bulk, the in-phase charging signal shows a deep minimum. Note also that the lagging-phase charging signal has gone entirely through the dissipation peak. Although a bridge calibration was not recorded, the signal level at the minima correspond to a capacitance change comparable to the full out-of-balance signal (about 30 fF).

2.6 Characterizing the sample using Magnetocapacitance

An important measurement we can perform using the SCA microscope is of the charging signal as a function of the magnetic field. We will refer to such a measurement as a "magnetocapacitance" trace. Such a measurement allows us to quantitatively measure the sample density as well as qualitatively assess the mobility of the sample. It has also proven useful at times for identifying sample instability due to effects such as parallel conduction in the donor layer or in the surface states.

An example of the results of such a measurement is shown in figure 2-13. The data was taken using a sample from wafer M226, which had a mobility of $\sim 1 \times 10^6$ cm^2/Vs and a density of 1.5×10^{11} cm^{-2}. The sample was fabricated without a topgate. The charging signal shows strong dips at positions of integer filling factor.

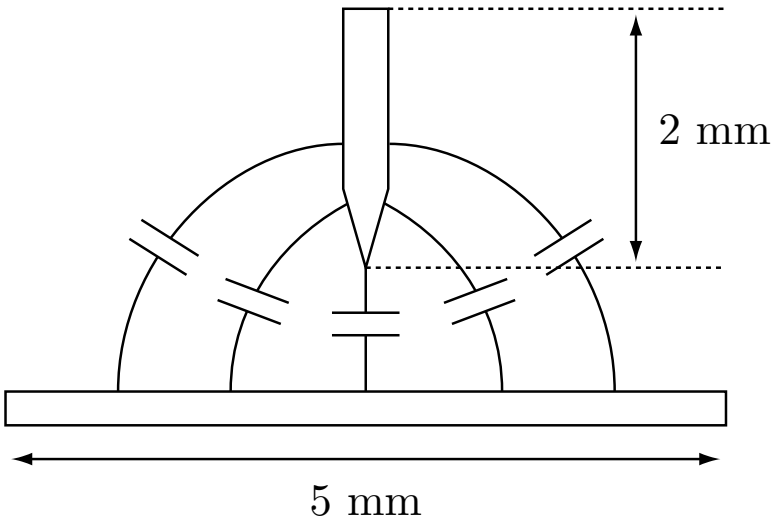

Figure 2-14: Contributions from the sample-tip capacitance include contributions from the local region of the 2D layer under the tip as well global contributions from the entire sample to the full length of the tip. Out of the total sample-tip capacitance of ∼40 fF, the local contribution from the last micron length of the tip is typically ∼1 fF for blunt tips, and local contributions from its very end are comparable to ∼100 aF.

Note, however, that these dips in the in-phase charging signal are also associated with peaks in the lagging phase signal. As discussed in section 2.3, this is an indication that the signal change is not due to a change in the sample capacitance, as would be the case for a quantum density of states contribution, but instead associated with a drop in the longitudinal conductivity σ_{xx} of the 2D electron system. In order to charge and discharge the self capacitance of the 2D electron layer, charge must move in and out laterally from the ohmic contacts. Lateral movements of charge are controlled by the diagonal conductivity σ_{xx}, and thus measuring the charging signal is the same as measuring the diagonal conductivity in a transport experiment in the Corbino geometry (see reference [91], where a model is described for quantitatively extracting the conductivity from the charging signal for a simple topgate geometry. This technique was also used in a recent paper [92] for measuring conductivities at low carrier density.)

Measurements such as those shown in figure 2-13 represent changes in the tip to sample capacitance due to an elimination of charging of the entire bulk of the sample: the signal drop is not associated with a local change in the 2D electron system. Since

the tip is very long, the total capacitance from the tip to the sample is very large (~ 10 fF) compared to the local contribution from the very end of the tip (~ 100 aF). This is illustrated in figure 2-14. Thus, measuring the charging signal while sweeping the magnetic fields results in large background changes that are not associated with the local properties of the 2D electron system. A significant advantage of this, however, is that these magnetocapacitance traces can be taken with the tip very far away, even with the tip millimeters from the sample. This is very convenient, as it allows us to characterize the sample before beginning the coarse approach.

As described in section 2.5, most of the samples we have used include a metal "finger" gate patterned on the surface, to which we apply no DC voltages, but to which we do apply the same AC voltage as to the ohmic contacts. The presence of this topgate significantly changes the charging of the sample. Magnetocapacitance traces from two samples with topgates are shown in figure 2-15. In figure 2-15, the dips in the charging signal are much narrower, meaning the bulk of the sample is continuing to charge even though the 2D electron system is entering a Hall plateau. Also, for the trace shown in figure2-15(b), the lagging phase signal does not go completely to zero, indicating that much of the sample may still be partially charging.

The presence of the topgate has two important effects. Due to the work function difference between the Cr metal and the 2D electron system, the density under the gate is different from that of the bulk. Previous work estimated a density depletion of about 20%. The magnitude and even the sign of this density change depends on the specific heterostructure: while depletion has typically been observed, one wafer (12-16-03.2) showed a density enhancement under the gate. Either way, having a different density under the gate means that at magnetic fields where the bulk 2D electron system is at filling factor $\nu = 1$ and is highly resistive, the 2D electron system under the gate will not be at $\nu = 1$ and could still be compressible. This compressible region under the gate would provide an alternate low resistance path for moving charge into the middle of the sample from the edge, resulting in an increase in the bulk charging.

Another way that the topgate can increase the bulk charging is through its ca-

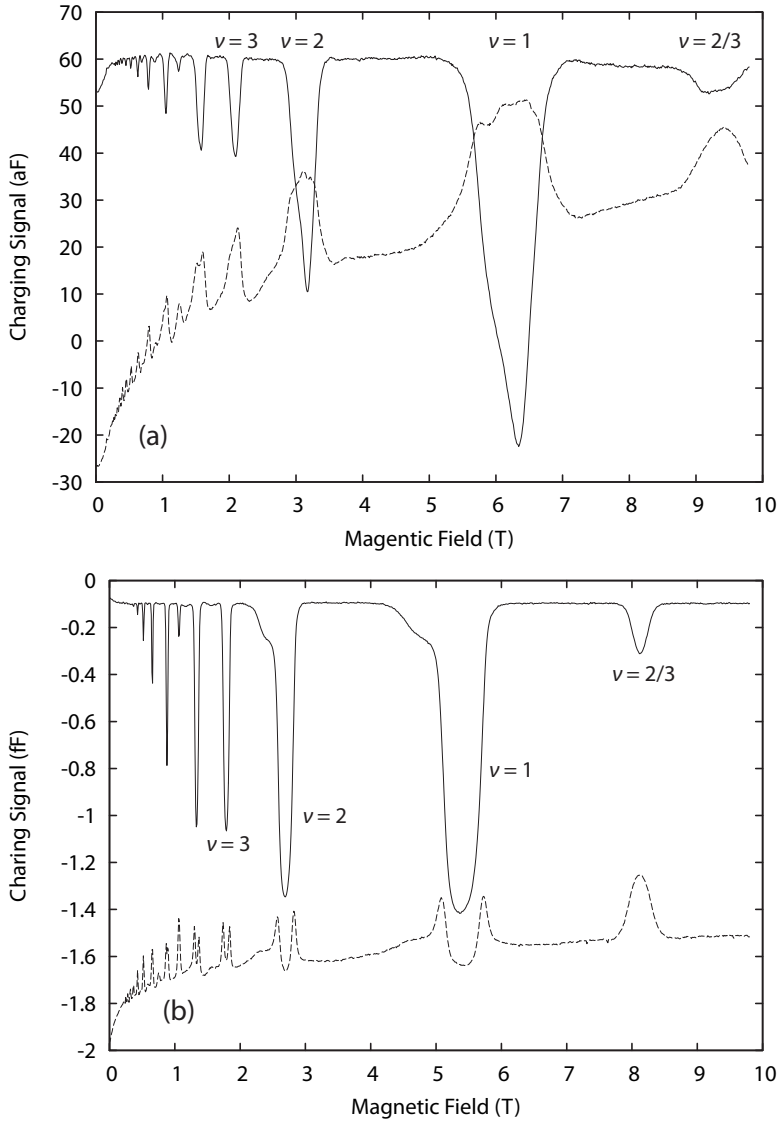

Figure 2-15: Magnetocapacitance traces taken on sample with a topgate. (a) A magnetocapacitance trace taken on sample 12-1-03.2, which was patterned with a topgate. In the sample, the density under the gate was slightly depleted. The solid and dashed lines show the in-phase and lagging-phase charging signal respectively. The total drop in the charging signal is much smaller that in samples without a topgate: this trace shows a capacitance change of about 100 aF, compared to 30 fF for the sample without a topgate. The dips at quantum Hall plateaus are also much narrower, and the lagging-phase signal does not go entirely through the dissipation peak. This trace was taken at 212 kHz. (b) A magnetocapacitance trace on sample 12-16-03.2. This sample differed from all other samples with topgates in that the density under the gate was enhanced. This significantly changed the bulk charging: the in-phase signal shows a larger dip, and the lagging phase signal goes through the dissipation peak.

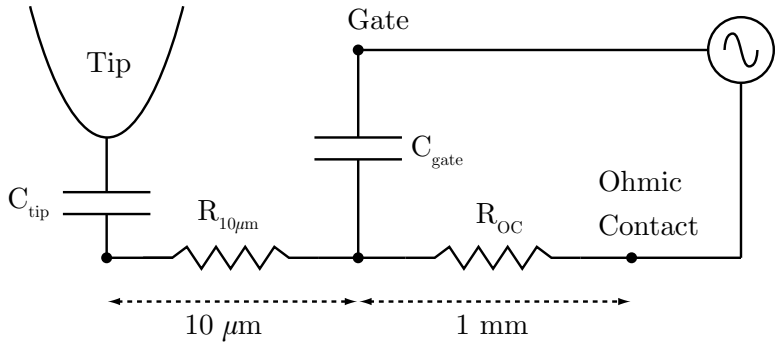

Figure 2-16: Schematic illustration of charging of the 2D layer in a sample with a topgate. At Hall plateaus, the resistance to the ohmic contact $R_{\rm OC}$ diverges. The presence of the gate allows us to still drive AC charge onto the tip capacitor through the capacitive coupling of the gate to the 2D layer.

pacitive coupling to the 2D layer. As the topgate has a large capacitance to the 2D layer ($\sim$ nF), applying an AC excitation to it can also drive charge in and out of the 2D electron system purely capacitively. This is shown schematically in figure 2-16. Essentially, if $R_{\rm oc}$ diverges, the capacitance $C_{\rm tip}$ can still charge, but now through a current path provided by $C_{\rm gate}$.

In the end, the experiments we will describe will mostly be performed at magnetic fields where the bulk 2D electron system is highly conductive, and thus these bulk charging issues are not so important. Nonetheless, the gate plays a crucial practical role in the experiment, allowing us to reliably find the surface and calibrate the size of the tip. These procedures will be described in detail in later sections.

We have also observed effects on the magnetocapacitance traces that are not well understood. In particular, magnetocapacitance traces on samples with topgates show a smooth "shoulder". In some samples, this smooth should shows a very reproducible hysteresis on a forward and reverse magnetic field sweep, shown in figure 2-17(a). On an up sweep, the in-phase charging signal has as deep minimum with a low field shoulder, while on the down sweep it shows two peaks. Figure 2-17(b) shows the signal as a function of time after the magnetic field was swept up to 6.25 T and stopped abruptly. The signal shows a slow relaxation from the lower curve in 2-17(a) to the upper curve with a time scale of $\sim$ 100s. While the exact origin of this behavior is not understood, it may be related to effects from quantum Hall persistent eddy

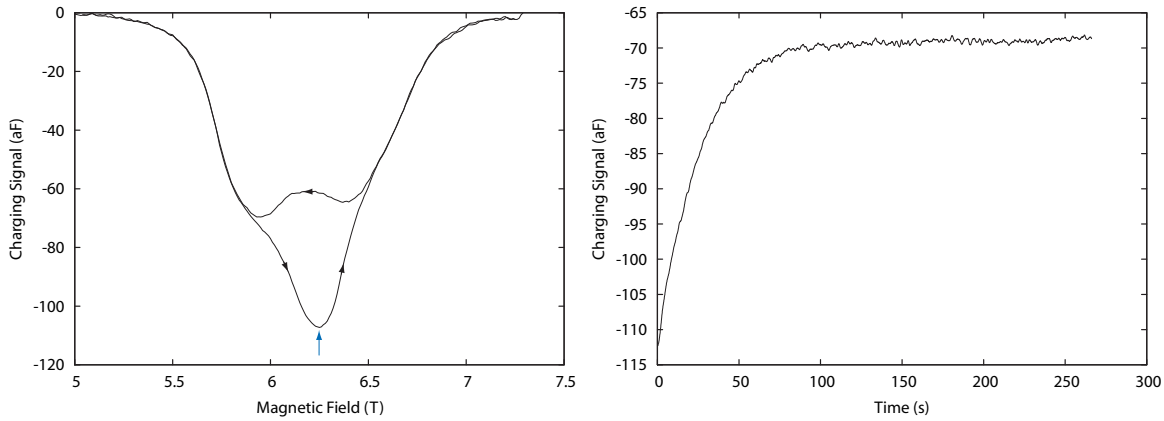

Figure 2-17: (a) The in phase charging signal for a forward and reverse sweep through $\nu = 1$. On the up sweep, the signal shows one deep minimum, while on the down sweep, it shows two shallower dips. (b) Charging signal versus time after the magnetic field was swept up to 6.25T, shown by the blue arrow in (a). The signal shows a slow relaxation from the signal level in the lower curve to that in the upper curve in (a). The origin of this relaxation is not understood, but may be related to slow movement of incompressible strips, and may have relevance to persistent quantum Hall currents.

currents [93, 94, 95, 96, 97]. When sweeping the magnetic field, an EMF is induced that creates eddy currents in the sample. In the quantum Hall regime, these currents can be carried as dissipationless currents in incompressible regions, which take a very long time to decay. The origin of these eddy currents can also be thought of in another way: sweeping the magnetic field at integer filling factor causes the outer edge of the incompressible region to move towards or away from the center of the sample. Since incompressible regions are associated with charge re-distributions, this must also be accompanied with the lateral motion of charge across an incompressible strip. If this charge transfer is slow, then before the charge relaxes, an excess voltage will be present across the strip. Currents in the incompressible regions are driven only by transverse voltages, and so this transverse voltage will result in a excess current[2]. This also leads to a very simple understanding of the dissipative processes that cause quantum Hall eddy currents to decay: these are processes that transfer charge across the incompressible regions, relaxing the excess transverse voltage, allowing the

[2]This relationship between the positions of the edges of incompressible regions and non-equilibrium quantum Hall eddy currents has recently been confirmed in an experiment where eddy currents were induced in a sample in a *fixed* magnetic field by sweeping the carrier density using a backgate [98].

incompressible edge to relax to its equilibrium position. The data in figure 2-17 could also have a similar explanation: such a slow moving incompressible edge could result in a capacitance change as it moves from under the gate to the region of ungated 2D electron system, and could be responsible for the observed hysteresis.

As mentioned above, a magnetocapacitance trace can be used to qualitatively asses sample mobility. In high quality samples, σ_{xx} becomes very small at the Hall plateaus even at high LL index. In transport this leads to good Hall voltage quantization down to very low fields, and is an indication of the high mobility of the sample. In a similar way, the depth of the capacitance dips at low fields can also be used to qualitatively asses sample mobility. Figure 2-18 shows a magnetocapacitance trace from a sample from wafer 12-16-03.2, whcih had a mobility of 7.0 $\times 10^6$ cm^2/Vs. Dips in the charging signal are seen down to very low magnetic fields, with signatures in the lagging phase signal being visible up to a Landau level index of $\sim$40. The sample also shows a small dip at $\nu = 2/3$, indicating the presence of fractional quantum Hall states. Both of these are experimental indications of the sample mobility.

Magnetocapacitance traces can also sometimes be used to asses the stability of the donor and/or surface states in the sample. In many of our experiments, we will be interested in gating the 2D electron system using DC electric fields from the tip. If there is instability in the surface states or the donor layer of the sample, then charge in the unstable layer can move around to screen the DC electric fields from the tip. In one sample, we observed that the donor layer was marginally stable. If the sample was cooled down too slowly, it would exhibit parallel conduction, and we would not be able to gate it reliably. On these cooldowns, the magnetocapacitance traces also showed a broad, unstable shoulder on the low-field side of the capacitance dips, as shown in figure 2-19. On subsequent cooldowns at a faster cooling rate, this shoulder was absent as shown in figure 2-15(a), and the sample was stable. Examining the magnetocapacitance curve before we began the coarse approach saved considerable time compared to walking in and then back out again.

An even more extreme example of parallel conduction was seen in the same sample after cryogenic illumination with a red LED. Cryogenic illumination results in an effect

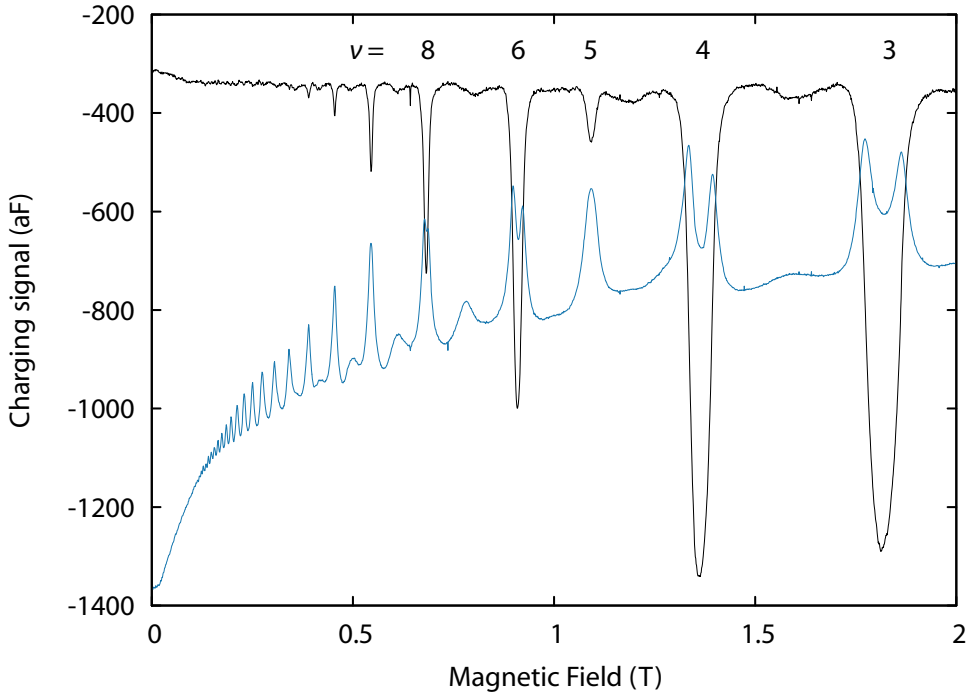

Figure 2-18: A high mobility sample (wafer 12-16-03.2) showing charging signal oscillations down to very low magnetic fields. Oscillations at even filling factors are seen up to Landau level index >40 in the lagging phase.

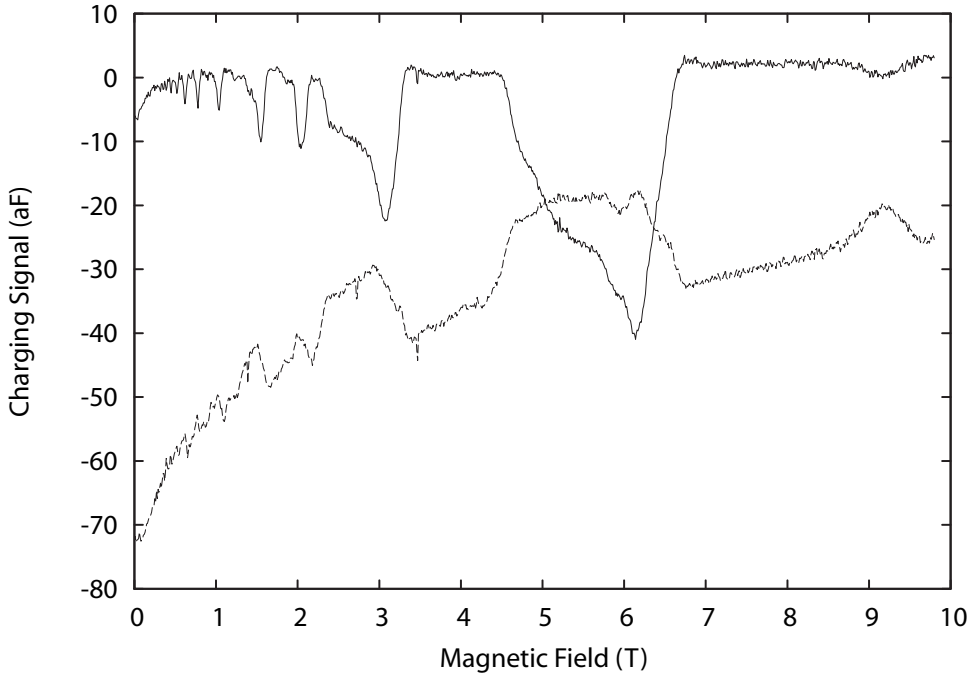

Figure 2-19: The broad low-field shoulder in this magnetocapacitance trace was an indication of instability in the donor layer in this sample.

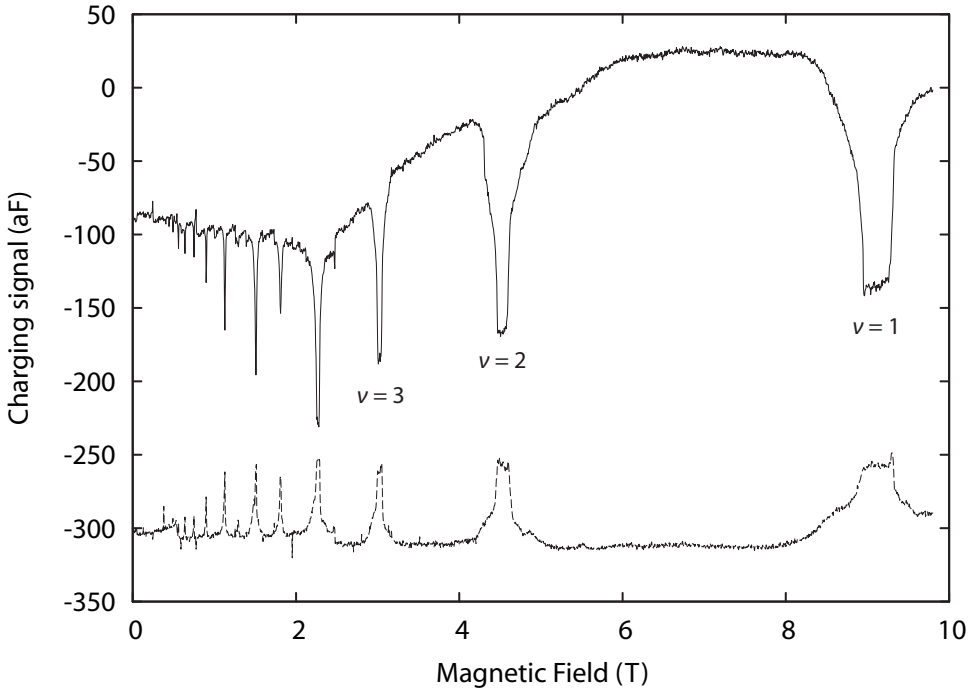

Figure 2-20: Magnetocapacitance in a sample that showed bad parallel conduction after illumination with a red LED. The dips at integer filling were "cut off" all at the same depth once the 2D electron layer became more resistive than the donor layer.

called persistent photoconductivity [99, 100, 101], which is commonly used (see, for example, ref [102]) to increase the 2D electron layer carrier density and the mobility. In our experiment, after illumination of the marginally stable sample, the conductivity in the donor layer became so high that it was also able to screen the AC electric fields from the 2D layer to the tip. This manifested itself in the magnetocapacitance traces as dips in the charging signal that were all "cut off" at the same signal level, as shown in figure 2-20. Our interpretation is that outside of the charging dips, the 2D electron system has a higher conductivity than the donor layer, and thus charge moves in and out of the 2D electron system in response to the AC excitation. As we approach integer filling, σ_{xx}^{2D} drops, and the charging signal starts to drop. However, once σ_{xx}^{2D} is less than $\sigma_{xx}^{donorlayer}$, AC charge then begins to move instead through the donor layer, and the charging signal stops dropping. While the effect is not always as extreme as this, in our experience LED illumination has lead to parallel conduction that is strong enough to prevent at least DC gating in all of the samples we have tested.

2.7 The shape of the tip

As in any scanning probe experiment, the shape of the tip can dramatically influence the measurement, and in particular, the interpretation of the data. Experiments such as AFM and STM have an advantage in this respect in that the interaction between the tip and the surface is very short range: in AFM, it is typically the van der Waals potential with a $1/r^6$ term in the attractive regime and a strong repulsive term $\sim 1/r^{12}$ in the repulsive regime. In STM, the signal is even more strongly distance dependant, with the tunnel current falling off exponentially with distance. For our measurement, the Coulomb interaction falls off only as $1/r$, and thus we expect that we will be more sensitive to the overall shape of the tip than STM or AFM measurements.

For charge accumulation measurements, it turns out that there is a significant advantage to using a large tip. A tip with a blunt end has a much larger local capacitance to the 2D electron system, and thus for the same AC excitation, a much larger amount of charge is induced on the tip. This leads to a dramatic increase of our signal. One of the difficulties of scanning probe microscopy is that it can be very difficult to assess the shape of the tip in-situ. One of the most important things I have achieved in my Ph. D. research is a method for systematically determining the size of the tip from SCA measurements using a combination of a well calibrated capacitance bridge, a careful inspection and analysis of the gate images, numerical modelling, and systematic experimentation with tips of various sizes. This work has allowed us to determine that in all previous SCA work [11], the tip had been blunted by crashing into the sample surface. Estimates show that the tips used ranged in size from ~ 1 μm to ~ 10 μm. The most useful data for the determination of the tip size are the shape and amplitude of the capacitance change curve as a function of the distance from the surface (which we will call the capactiance "tip approach" curve), and the shape and the magnitude of the capacitance change between areas covered with gate and ares with the exposed 2D electron system in images taken at zero magnetic field. We will discuss each of these in the following sections.

2.7.1 Analysis of the capacitance tip approach curve

A useful type of measurement involves measuring the charging signal as a function of the distance between the sample and the tip. This is performed after the coarse approach so that the sample is within the Z range of the scan tube (2.4 μm at 300 mK). A typical curve is shown in figure 2-21. In general, for distances far from the surface, the curve is roughly linear, but as the tip gets closer to the surface, there is a strong "upturn" in the capacitance. One remarkable feature of the curve is that it is very difficult to fit with any reasonable function over the full 2 μm range. Attempts to fit it to a parallel plate capacitor model even in only the "upturn" region are unreliable, and more complicated models that attempt to fit the entire range, such as a linear term plus a $1/d$ term introduce too many degrees of freedom to the fit.

This may not seem surprising since it seems unlikely that our tip would be modelled well by a parallel plate capacitor. When the tip is far from the surface, it can be thought of as a semi-infinite cone. Since the electric fields around the apex of the cone drop off as a power law, the capacitance far away will vary more slowly than a parallel plate model. As the tip gets closer and the radius of curvature of the tip becomes comparable to the distance from the tip to the 2D electron system, the electric fields no longer fall of as a power law, and we begin to approach the parallel plate limit. Thus the distance scale of the strong "upturn" in the capacitance curve will occur when the radius of curvature of the tip is comparable to its separation from the surface.

More quantitative information can be obtained from the magnitude of the capacitance upturn $\Delta C_{\mathrm{upturn}}$. In order to perform accurate comparisons of tip approaches with different tips, a carefully calibrated bridge is required in order to convert the lock-in readings into absolute capacitances. This conversion factor will depend on the shunt capacitance, the amplitude of the excitation, and the gain of the amplifiers:

$$\Delta V_{\mathrm{lock-in}} = \frac{\Delta V_{\mathrm{center}}}{G} = \frac{V_{\mathrm{s}}}{G C_{\mathrm{total}}} \Delta C \tag{2.17}$$

where G is the total gain of the amplifiers and V_{s} is the amplitude of the AC voltage

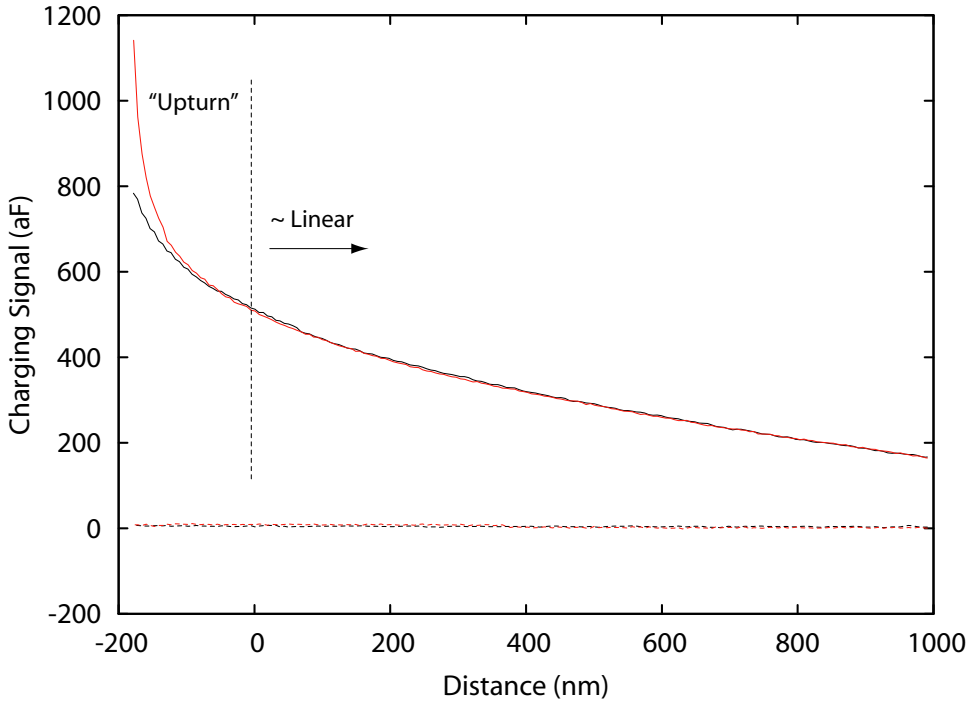

Figure 2-21: The in-phase (solid lines) and lagging-phase (dashed lines) charging signal as a function of the z-position of the tip. The black curves are for a position over the 2DES and the red curves are over a metal gate. The x axis shows the vertical displacement of the scan tube from its equilibrium position. Curves have been truncated at the position where the tip touched the surface. Since the lagging phase signal is flat, the in-phase signal can be interpreted directly as a capacitance. These curves were taken with a custom etched tip with a 3 μm radius of curvature that had not been crashed. The curve can be qualitatively divided into a roughly linear section with a strong "upturn" close to the surface.

applied to the sample. Note that if the value of the reference capacitor is known, it is not necessary to directly measure G and C_{total} in order to calibrate the bridge. Instead, the product GC_{total} can be measured by measuring the change in the output signal is response to a change in the AC amplitude V_{ref} applied to the reference capacitor. In this case, we will have:

$$\Delta V_{\text{lock-in}} = \frac{\Delta V_{\text{ref}} C_{\text{ref}}}{G C_{\text{total}}} \tag{2.18}$$

Thus if we know the value of the reference capacitor, performing this measurement will allow us to calibrate our out of balance capacitance signal. In our experiment, we use a pinched off FHX35X transistor as our reference capacitor. The source-drain capacitance of and uncleaved FHX35X was measured against a fixed 500 fF reference capacitor, which was independently calibrated using the General Radio manual capacitance bridge. The results of these measurements showed that after pinch off, the source-drain capacitance of an uncleaved FHX35X including the wire bonds was 100 fF, and was independent of the gate voltage. By using a computer controlled signal generator, we perform the above calibration measurement for the sensor on our SCA microscope several times a day in order to keep a reliable record of the conversion factor from lock-in units to absolute capacitance units. (For details, see appendix A).

Figure 2-22 shows calibrated tip approaches for several different tips. Of particular interest is a curve from a cool-down where I managed to come into range without smashing the tip too badly. (This is quite difficult with a sharp tip: see section 2.8 for a discussion of the coarse approach procedure with the SCA microscope.) The capacitance curve shows only a very small linear slope and exhibits no measurable "upturn" even when the tip was moved close enough that it touched the surface of a metal gate. The position of the surface in this case was easily determined because once the tip touches the metal gate, the DC bias on the measurement transistor is shorted out and the signal drops immediately to zero. The fact that the tip was sharp was also confirmed by images of the gate (see next section). The other capacitance

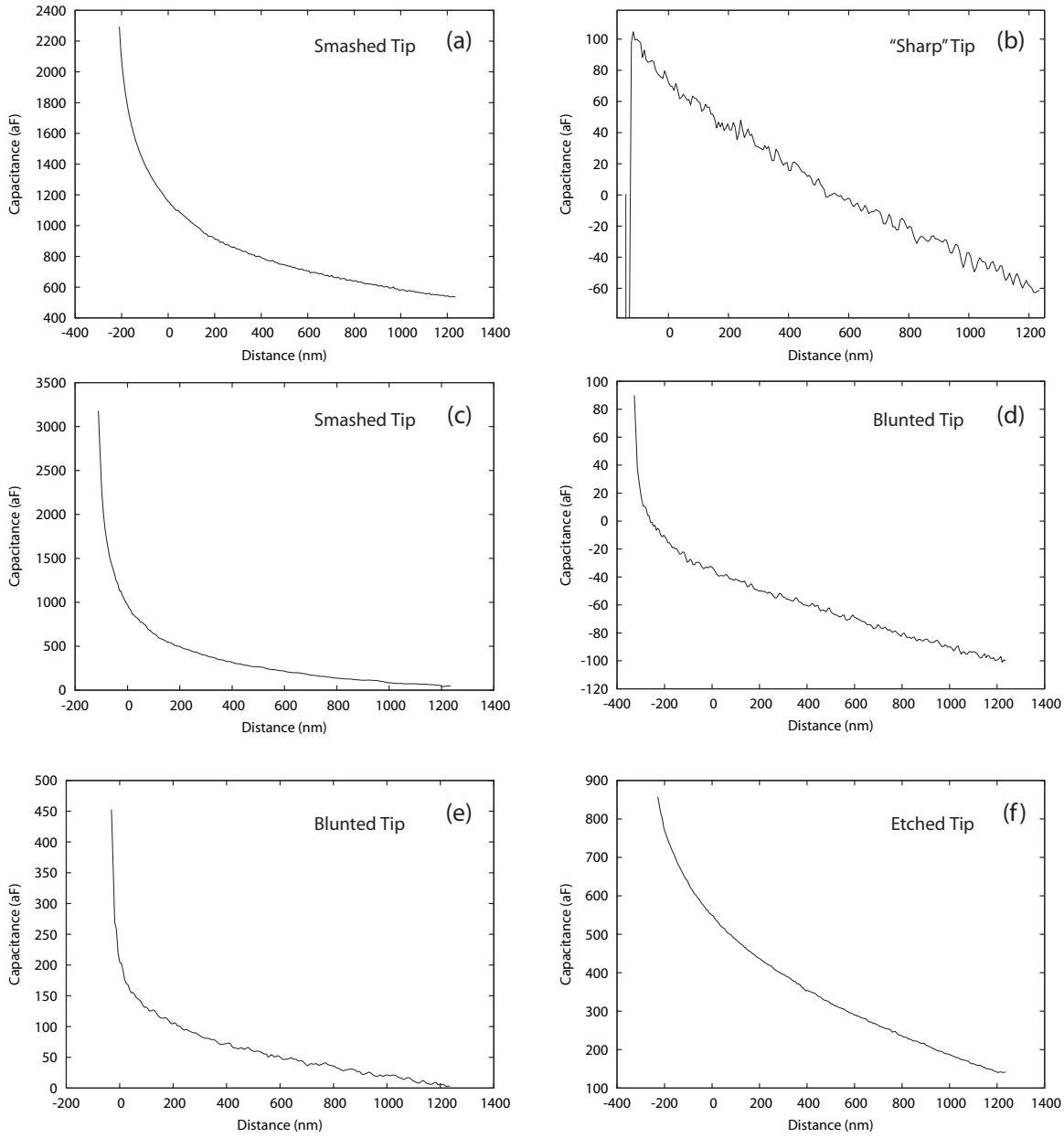

Figure 2-22: Capacitance vs. distance for tips of various sizes. (a) A PtIr tip smashed in-situ. A later inspection under an optical microscope showed a flat end of about 3 μm. (b) Tip approach for a nominally sharp tip PtIr tip. It does not show any measurable upturn. The tip shorted to the gate at the closest position, demonstrating that we had reached the surface. (c) The same tip 1 day later after it had been smashed in-situ when the cryostat swung. (d) Tip approach for a moderately damaged tungsten tip. The tip was initially sharp, but was likely damaged during coarse approach. (e) The same tip after attempts to enlarge it by smashing the surface. Further smashing did not enlarge the tip. SEM images showed it had buckled, but would not smash as easily as the PtIr tips. (f) A capacitance approach curve for a undamaged etched tip with a 3 μm radius.

traces in figure 2-22 show upturns of difference magnitudes, ranging from no upturn for the sharp tip to 2.5 fF for the bluntest. The magnitudes of these upturns are an indication of the effective "area" presented by the end of the tip in the parallel plate capacitor model.

If a tip can be retrieved from the experiment after a run without damage, then the capacitance tip approach curves can be correlated with the tip size through an examination of the tip in an optical or scanning electron microscope. Alternatively, tip approach curves can be compared with the results from the numerical simulations discussed in Chapter 5.

One of the difficulties in using tip approach curves to determine the tip size is that it requires knowledge of the calibration of the bridge, which is not always available. A more robust method of determining tip size involves an analysis of the SCA images of the gates. From this measurement, discussed in the next section, a measure of the size of the tip can be obtained that is independent of the bridge calibration.

2.7.2 Analysis of the SCA gate images

In addition to increasing the charging rate to the bulk of the sample (see section 2.6), the topgate on the sample has proved to be of indispensable use in calibrating the shape of the tip, as well as in finding the surface of the sample (see section 2.8).

Images of the gate can be used to calibrate the tip size in two ways. First, the magnitude of the capacitance change ΔC in the image as the tip is moved from over the gate to over the 2D electron system will yield information about the size of the tip. Similar to the tip approach curves, quantitative comparisons of different images requires a calibrated bridge. Another way to gauge the size of the tip is from the "smear" of the edge of the gate in the SCA images. Since this involves only a distance scale, it can be used even when the bridge calibration is not known. For a simple tip with a flat end, the edge of the gate in a line cut of the SCA image will be smeared over a distance scale comparable to the diameter of the flat face of the tip. Although there will also be contributions from portions of the tip that are further away, we will see that these die off quite quickly. The exact shape of the line cut for arbitrary tip

shapes can be obtained from numerical simulations (see chapter 5).

A complicating factor is that both the capacitance change and the smearing will also depend on the z height of the tip above the sample surface. For quantitative comparisons, images should be taken at the same sample-tip separations. In practice, the separation is chosen to be as small as possible such that the tip does not short to the gate metalization, either by touching or by tunnel current. This is part of a standard procedure for selecting the scan height (see section 2.8). While this height will strongly affect the magnitude of the capacitance change, it is not critical for estimates of the tip size from the gate smear. The reason for this is that when the tip is retracted to such a distance that it is no longer in a parallel plate capacitor limit, then there is a significant loss in the signal to noise. On the other hand, if it is in the parallel plate limit, the distance from the tip to the surface is small compared to the radius of curvature of the tip, and thus the smear will be dominated by the tip radius and not the tip height. Thus, as long as an image of the gate shows a good signal to noise ratio, it can be used to obtain an estimate of the tip size from the gate smear. This can be confirmed by comparing gate images for a known tip at different heights.

Figure 2-23 shows capacitance images of the gate taken with several different tips. Also shown in the figure is the magnitude of the capacitance change ΔC, the magnitude of the AC excitation, and the averaging time. The capacitance change varies between 3 aF for the sharpest tip to 200 aF for the largest tips. The figure also demonstrates the dramatic enhancement of the signal with a blunt tip: the image taken with the sharp tip was averaged for more than 12 hours, while that with the etched tip was averaged for 1 minute. Figure 2-24 shows line cuts from the scans taken in a direction perpendicular to the gate. As can be seen in the line cuts, larger tips result in an increased smearing of the capacitance step between the gate and the 2D electron system. The length scale of this smearing is a direct measure of the maximum capacitive (electrostatic) spatial resolution of the experiment. For non-perturbative measurements, no feature should exist in the images that is sharper than this smearing. As we shall see, for measurements where the interaction of the tip with the 2D electron system is significant, much sharper features can be seen in

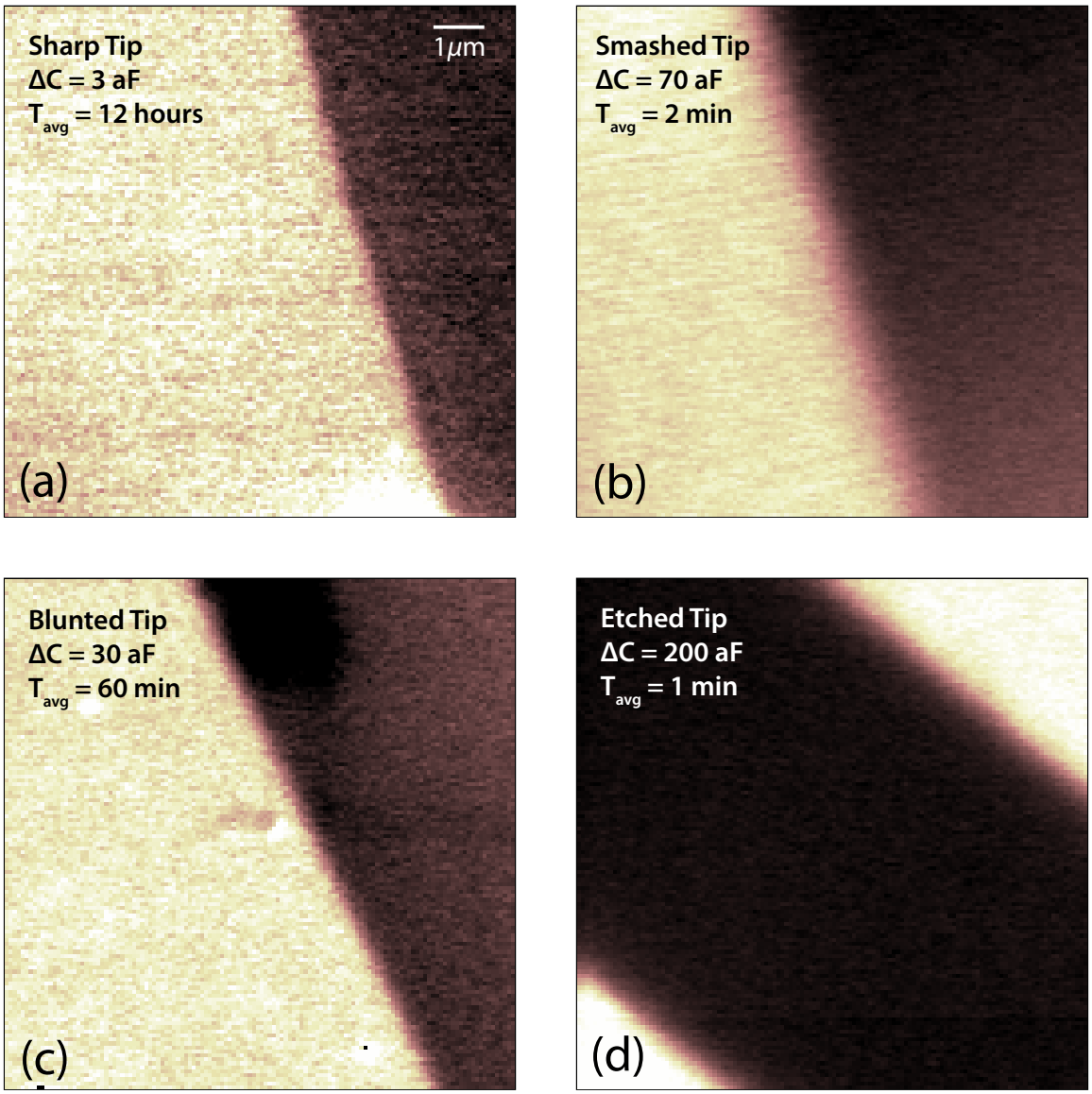

Figure 2-23: 10x10 μm images of the edge of the gate taken with different tips. (a) Image taken with the sharp tip. Note the very long averaging time required for the image. The tip approach curve for this tip is shown in figure 2-22(b). (b) An image taken with the same tip after it had been smashed into the surface, with the approach curve shown in figure 2-22(c). (c) An image taken with the blunted tip from the approach curve shown in figure 2-22(e). The black square over the electron system near the top center is a region where the tip was intentionally crushed into the surface during a small scan in an effort to blunt it. (d) An image taken with an etched tip. Note the exceptional signal to noise ratio for such a small averaging time.

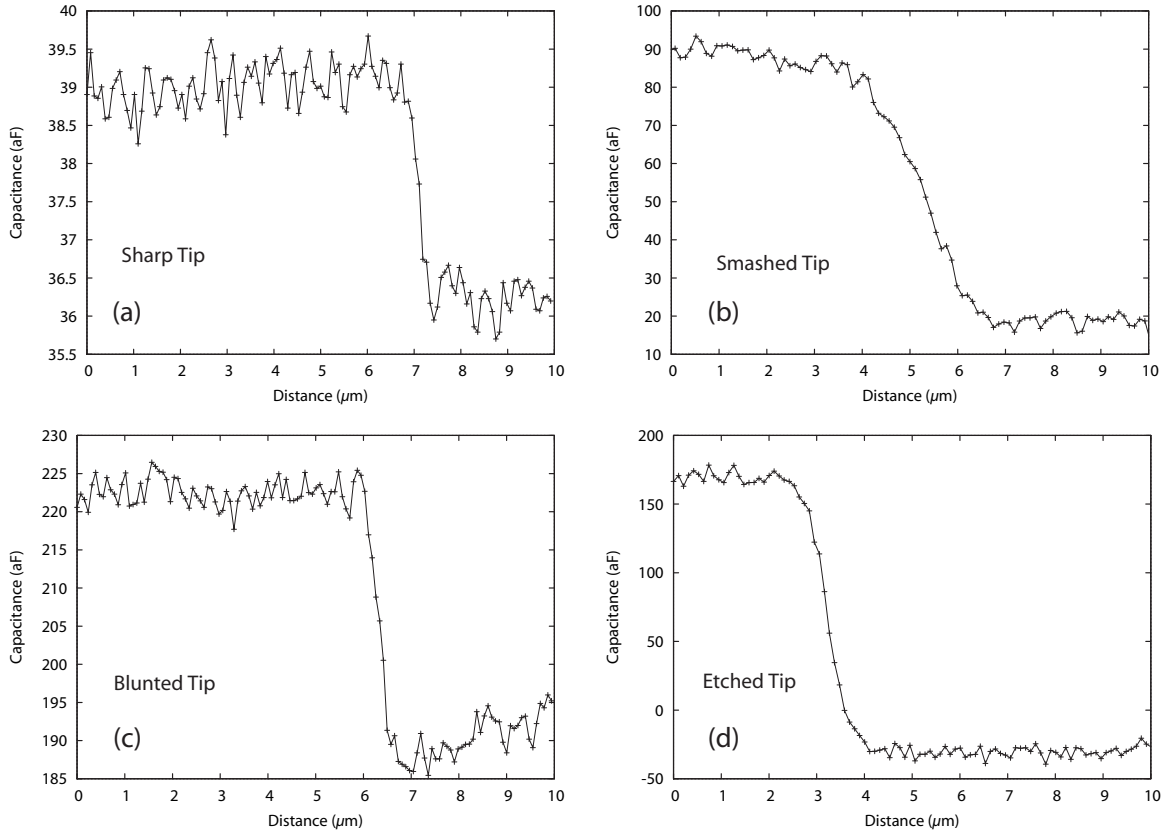

Figure 2-24: Line cuts from the images of gate taken from the corresponding panels in 2-23. The line cut direction was oriented perpendicular to the gate edge. Note in panel (d) that although the tip is etched to give a 3 μm radius of curvature, the electrostatic resolution is about 700 nm.

the charging images. Finally, it is interesting to note that the line cut show in figure 2-24(d) was taken with an etched tip with a ~ 3 μm radius of curvature, but shows a gate smearing of ~ 700 nm. Thus, even though the Coulomb interaction falls off only as $1/r$, the measurement is still mostly sensitive to the region at the very end of the tip.

2.8 Finding the surface of the sample

During cool-down from room temperature, the sample is separated from the tip by ~ 1 mm. In order to be able to image, the surface of the sample must be moved to within 30 nm of the end tip. To do this, the coarse approach motor is used (see section 2.1). In most scanning probe measurements, this is performed in an automated way by the SPM controller electronics. The controller is designed to automatically take steps using the coarse approach motor until a feedback signal from the surface, such as a cantilever deflection in AFM or a tunnel current in STM, is detected. Unfortunately, in charge accumulation imaging, there is no reliable feedback signal for detecting the surface. Because the sample to tip capacitance is dominated by the stray capacitance from the entire length of the tip to the sample, even the sample-tip capacitance value cannot be used as a reliable indication of the sample-tip separation due to variations in the length of the tip. (Typically, the total sample-tip capacitance when in range has varied between 30 to 40 fF.) The only real indication of the surface that we have is the "upturn" in the capacitance discussed in the previous section. Unfortunately, this is too qualitatively defined to allow a computer-controlled approach.

The method we have adopted for finding the surface during coarse approach is a non-automated procedure that involves looking for the onset of non-linearity in the capacitance vs. distance curves while we walk in. This is described in figure 2-25. When the tip is far away, performing a capacitance vs. distance trace by moving the scan tube gives a linearly increasing capacitance, as shown in figure 2-25(a). During the coarse approach, the capacitance vs. time is measured, as shown in figure 2-25(b). The capacitance vs. time during operation of the motor generally shows a

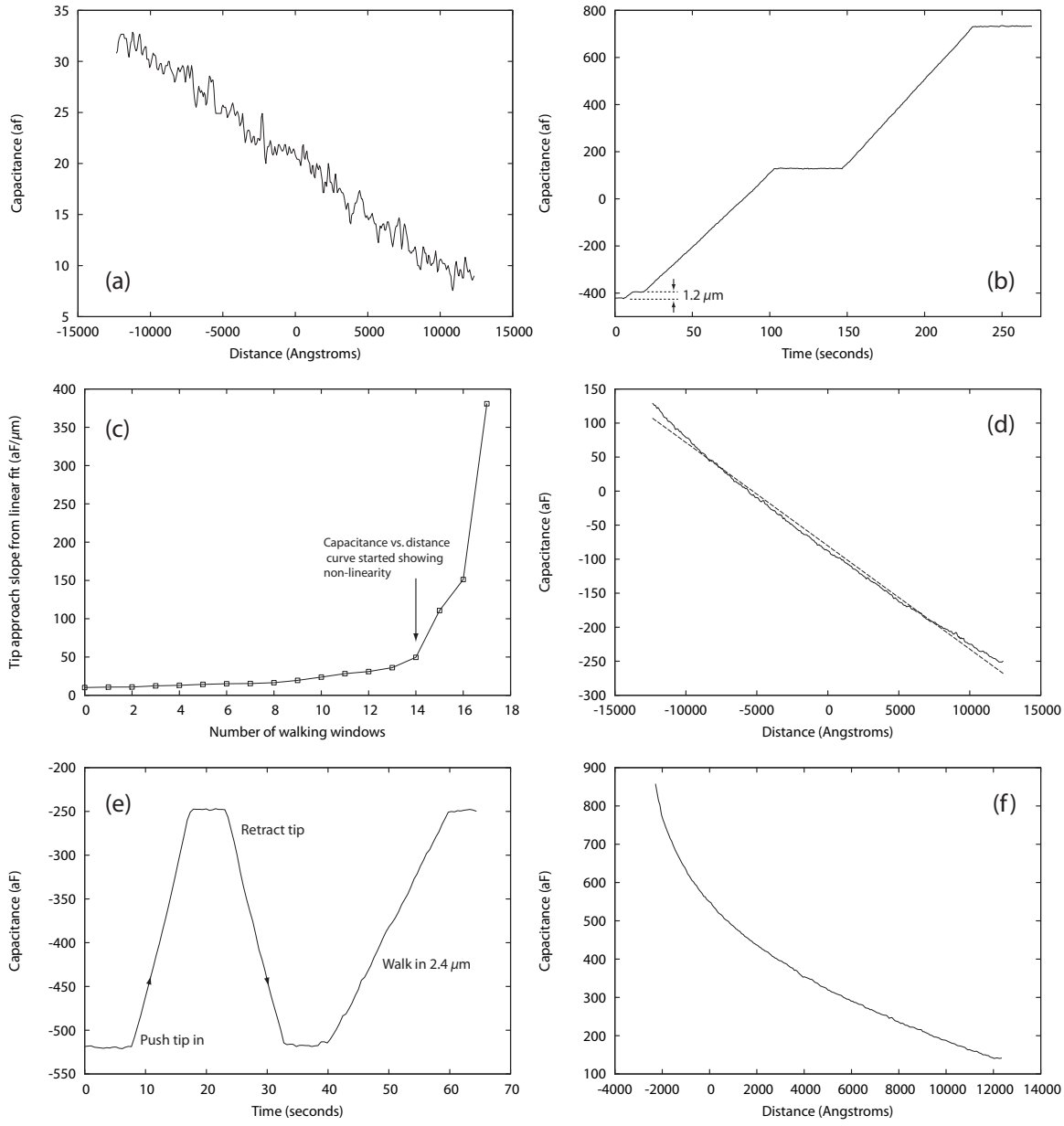

Figure 2-25: Coarse approach procedure. From far away, the capacitance vs. distance measured by moving the scan tube is linear, as shown in (a). The curve is fitted with a line and the slope is recorded. (b) The coarse approach motor is used to walk the sample towards the tip, and the capacitance signal is monitored as a function of time. At the beginning of the recording, the tip is moved in by 1.2 μm, allowing the distance walked to be read off from the capacitance change. (c) As the sample moves closer, the slope in the tip approach curves becomes steeper. (d) Once the slope has increased by about a factor of 5, the tip approach curves start to show some non-linearity. (e) At this point, the coarse approach motor is operated manually to move the sample in exact increments of the Z scan range (2.4 μm) (f) Eventually, the tip approach curve shows a "very steep" upturn. The software is stopped manually so that the tip does not crash into the surface.

linear slope if the coarse approach motor is working properly. As the sample gets closer, the capacitance begins to rise faster as a function of distance. However, since the pitch of the ramps is not constant as a function of rotation angle, we cannot use the capacitance vs. time during walking as a gauge of this. Instead, we stop walking every 500-1000 steps and perform a capacitance vs. distance measurement using the scan tube to move the tip, and fit this to find a slope in aF/μm. These slopes for a typical approach are plotted in figure 2-25(c) as a function of the total number of walking windows taken. Once the slope has increased by a factor of ~ 5, the capacitance vs. distance curves begin to show a noticeable non-linearity. At this point, the walking is performed manually in increments of the maximum scan tube range of 2.4 μm, and capacitance vs. distance curves are remeasured. Eventually, the capacitance vs. distance curve will show a sharp upturn, as shown in figure 2-25(f). This sharp upturn is an indication that the tip is within about 100 nm of the surface. The software should be stopped when this curve gets "really steep" to avoid crashing the tip into the surface. At this point the sample is then moved such that the sharpest portion of the upturn is at an absolute position of Z = -2000 Å.

The next step is to adjust the plane compensation. The RHK SPM controller has two plane compensation settings that allow the tip to be scanned in a tilted plane to compensate for any small tilt on the sample. This functionality is crucial for scanning probe experiments such as ours where we operate without surface feedback. These settings should be adjusted to level a 10x10 μm capacitance image taken initially with the tip at Z = 3000 Å (5000 Å from the position of the sharpest part of the upturn). The tip should then be moved towards the sample initially in 500 Å increments, readjusting the plane compensation as necessary. As the tip is moved closer, a gate should appear in the image. (If it does not, the scan range may be increased if possible, or you may need to walk laterally.) Once the gate becomes clear in the signal to noise of the image, the steps in Z should be decreased to 200 and then 100 Å. Eventually, the tip will short to a tall point in the area over the gate, unbiasing the measurement transistor and leaving a clear signature in the image, as shown in figure 2-26(f). At this point, the tip should be retracted by 100 Å so that the tip no longer

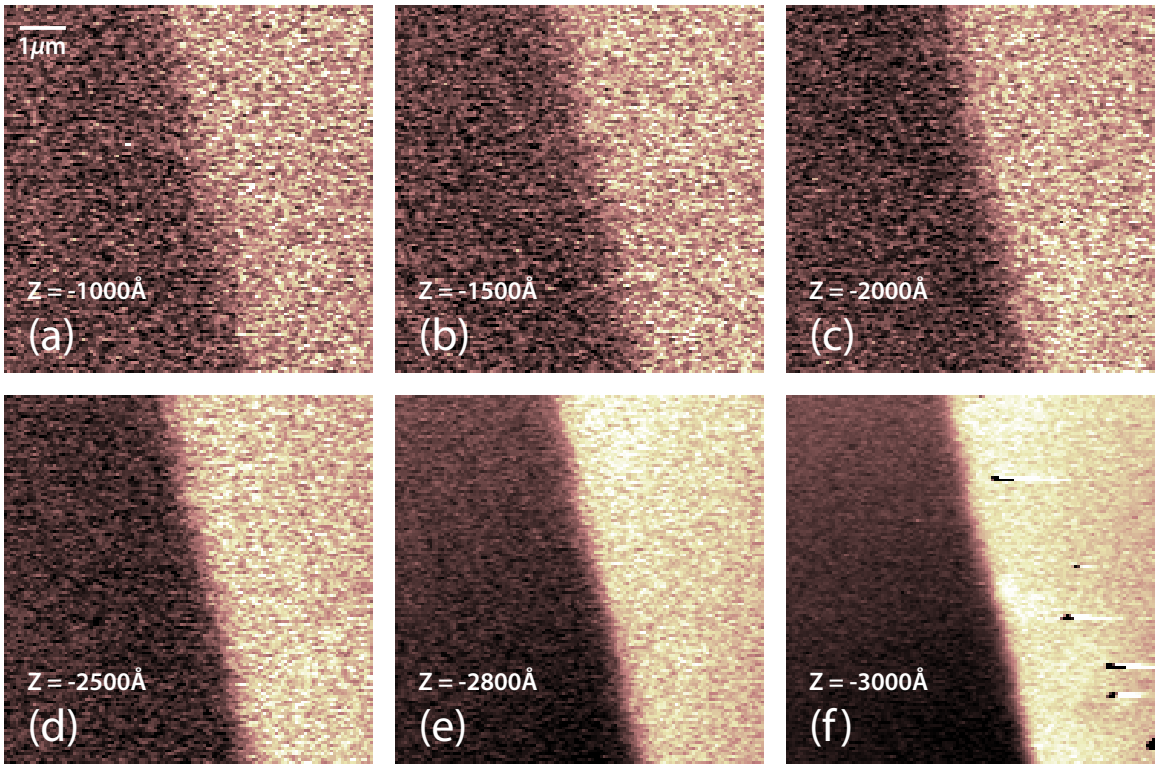

Figure 2-26: Once the approximate position of the surface is found from the tip approach curve, the "closest" scanning distance is found by watching images of the gate as the tip is moved closer. Panels (a)-(f) show 10x10 μm images as a function of the Z position of the tip. As the signal to noise ratio improves, smaller steps are taken. Eventually, tunnel current from the tip to the gate shorts out the measurement transistor bias as the tip "brushes" tall spots over the gate, as shown in (f). At this point, the tip is retracted 100 Å. The tip is now in scanning range.

shorts to the gate. The gate has a nominal thickness of 10 nm, but has high points that are as tall as ∼20 nm. Thus, this distance should correspond to 30 nm from the sample surface. In my experience, the sample-tip separation will drift up and down by ∼10-20 nm during normal operation over the period of a couple of hours. If scanning continuously, the absolute sample-tip capacitance should be monitored by plotting image histograms, and the z height should be adjusted accordingly to compensate for drift. Ultimately, this drift of unknown origin makes it impractical to scan closer than 30 nm from the sample surface. After leaving the microscope overnight or after changing the magnetic field, the position of the surfaced should be checked again using this gate-shorting technique.

One limitation of the coarse approach procedure discussed above is that it relies

heavily on the capacitive upturn seen with blunt tips. With sharp tips, the upturn is very small or even non-existent (see figure 2-22(b)), and thus it is impossible to get into range without smashing them. (For figure 2-22(b), the tip was only mildly smashed during coarse approach because the tip happened to come in contact with the metal gate during walking, and the coarse approach was immediately stopped and the tip retracted.) Thus to perform experiments with a sharp tip, integration of our capacitive sensor with another type of surface detection, such as a tuning fork AFM sensor [103, 104, 105, 62, 106], would be needed.

2.9 Producing blunt tips with a controlled geometry

During the course of our investigation of the 2D electron system using SCA, it became clear that it was very advantageous to work with large tips. While sharp tips would in theory allow a higher electrostatic resolution, the charging signal was much too weak due to their smaller capacitive coupling, and images suffered from poor signal to noise ratios. Furthermore, during one cool-down, images taken with a tip that was blunted in-situ showed an intricate and reproducible charging pattern in the quantum Hall regime after applying a DC bias voltage (see data in appendix C). The patterns showed a very systematic dependence on the bias voltage and the magnetic field, suggesting a link to the physics of the 2D electron system. Patterns like these were never seen with sharp tips, and were so striking and reproducible that we were determined to understand them.

It became clear that what was needed was a method for producing very large, blunted tips in a controlled and reproducible fashion. Experimentation with evaporative coating of sharp tips failed to produce tips that were blunt enough for our needs. An extensive literature search turned up a journal article [107] describing an electrochemical etching procedure for producing a tungsten tip with a large radius of curvature for nanoindentation studies of soft polymers. This method work well, and

was adopted and modified to suit our needs.

The procedure is very similar to etching methods used to produce sharp tips [108, 109, 110, 111]. A length of tungsten wire is lowered ∼2-3 mm into a 1M NaOH solution. The wire is attached to a Variac AC power supply, and a tungsten evaporation boat is placed in the solution as a counter-electrode. A voltmeter is used to measure the AC current during the etch, which is recorded by a computer through a serial interface. The Variac is configured to give a 30 VAC voltage and is then turned on. At this point, hydrogen bubbles begin to evolve at the surface of the tip. Over time, the current decreases as the tip metal is removed, and eventually the current goes to zero, indicating that the etching is complete.

Figure 2-27(a) shows a recording of the current versus time during the etching. The current trace shows several abrupt drops, which are likely a result of sudden movements of the meniscus of the NaOH solution. Figure 2-27(b) shows an SEM image of a tip produced by this type of etch. The tips produced by this etch are generally too sharp for our needs, typically with $r_{\max} \sim 500$ nm. In order to reliably produce blunter tips, a second "polishing" etch was performed. Here, the Variac voltage is lowered to 5 VAC, and the tip is lowered again into the solution ~ 3 mm. The Variac is then switched on and the tip is allowed to etch for another 30 seconds. Before the current drops to zero, the power is shut off and the tip is removed and rinsed in deionized water. (This last step is quite important: without it, the tips will be contaminated with NaOH crystals, which are clearly visible in the SEM.) After this second polishing etch, the tips show a reproducible ∼2-3 μm radius of curvature with a very smooth and shiny surface, as shown in the optical and scanning electron microscope images in figure 2-27(c) and 2-27(d).

Before use, all tips were imaged in a scanning electron microscope. Knowing the exact shape of the tip was crucial for understanding our remarkable results, and allows us to compare our experimental data quantitatively with results from simulations we have developed of the interaction of the tip with the disordered quantum Hall liquid.

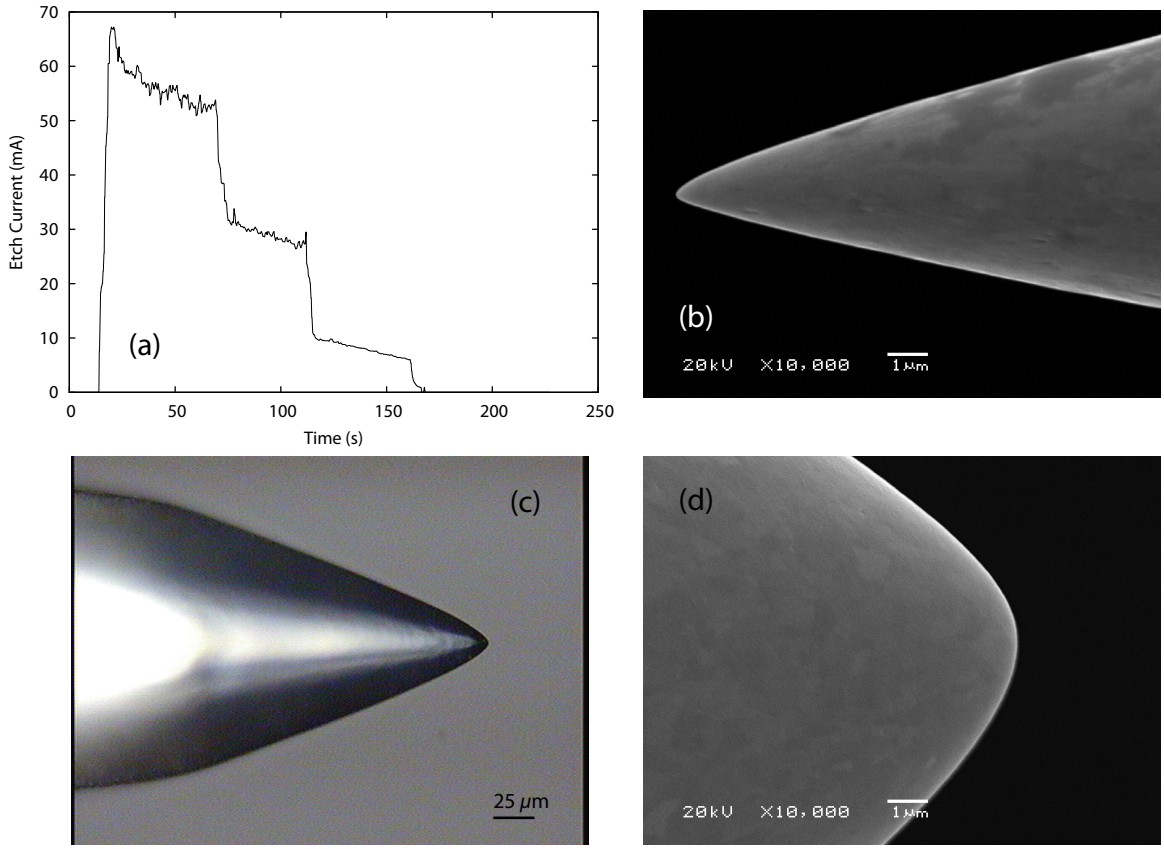

Figure 2-27: (a) A recording of the AC current during the electrochemical tip etch. Sudden movements of the meniscus of the etchant down the tip result in sharp drops in the etching current. (b) An SEM image of a tip after the etching. The radius of curvature ranges from as small as 90 nm to as large as 500 nm. In order to produce blunter tips, a second "polishing" etch is performed. After this second etch, the tip has a very smooth surface and a typical radius of curvature of 3 μm, as shown in the optical microscope and SEM images in (c) and (d).

Chapter 3

Imaging Transport Resonances in the Quantum Hall Effect

In this chapter, we describe the central result of our research: the experimental observation of transport resonances in the quantum Hall effect [112]. In this work, we have discovered a fundamental mechanism for transporting charge in the localized quantum Hall fluid. This transport mechanism consists of single-electron resonant tunneling through small quantum dot islands. Our observations show that this resonant transport dominates all other ways to move charge through the localized quantum Hall liquid, and likely plays a significant role in transport at quantum Hall plateaus.

We begin with a brief background on localization and incompressible strips in the quantum Hall effect. We then present our experimental data, and show how the images we observe point to this resonant tunneling mechanism. We conclude with a discussion of how this resonant tunneling mechanism impacts transport and localization in the quantum Hall effect.

3.1 Background

Electrons confined to move in 2 dimensions that are placed in a very large perpendicular magnetic field have a remarkable property: the Hall resistance becomes quantized to a value that depends only on fundamental physical constants [113]. This quanti-

zation of the Hall resistance is remarkably robust: it is insensitive to all properties of the system used to create the 2D electron gas, including the size of the sample, the properties of the host semiconductor crystal, and even the level of disorder. The origin of this robust quantization stems from the localization of electrons in high magnetic fields. Laughlin [13] showed that as long as the electrons in the bulk of the sample are localized so that their diagonal conductivity σ_{xx} vanishes, the Hall resistance will always be exactly quantized. While the quantization is understood, there is no consensus on a microscopic picture of this localization. The models of localization can be broadly separated into two categories: those that do not account for electron interactions [46] in which electrons are localized in single-particle drift trajectories around the disorder potential, and those that include the first order corrections due to electron interactions in the form of non linear screening [52, 53].

The model of localization that we will consider is one that arose from the non-linear screening theory proposed by Efros [47, 48, 49] to describe the quantum Hall effect. The non-linear screening theory is based on a very simple idea: when a Landau level is only partially filled, the density of states is very large. This large density of states means the system is compressible and very effectively screens potential fluctuations, acting as a "perfect" metal. In contrast, when a Landau level is full, there is a gap at the Fermi surface: the system cannot screen at all, and acts as an insulator. Chklovskii *et al.* [51] applied this theory to a depleted edge of the 2D electron system and found that the density gradients found there produced regions of compressible electrons where a Landau level was locally partially filled, separated by "incompressible strips" where a Landau level was locally full, as shown in figure 3-1. In the non-linear screening models [52, 53], localization occurs when one of these incompressible strips spreads to the center of the sample, forming a percolating network that localizes electrons in the bulk, as shown in figure 3-2. In this picture, the strong localization that results in the quantized Hall resistance arises from the large resistance to transporting charge across this network of incompressible strips.

Relatively few experiments have been designed to directly probe the resistance of incompressible strips. In one such experiment[114], sharp resonances were seen in

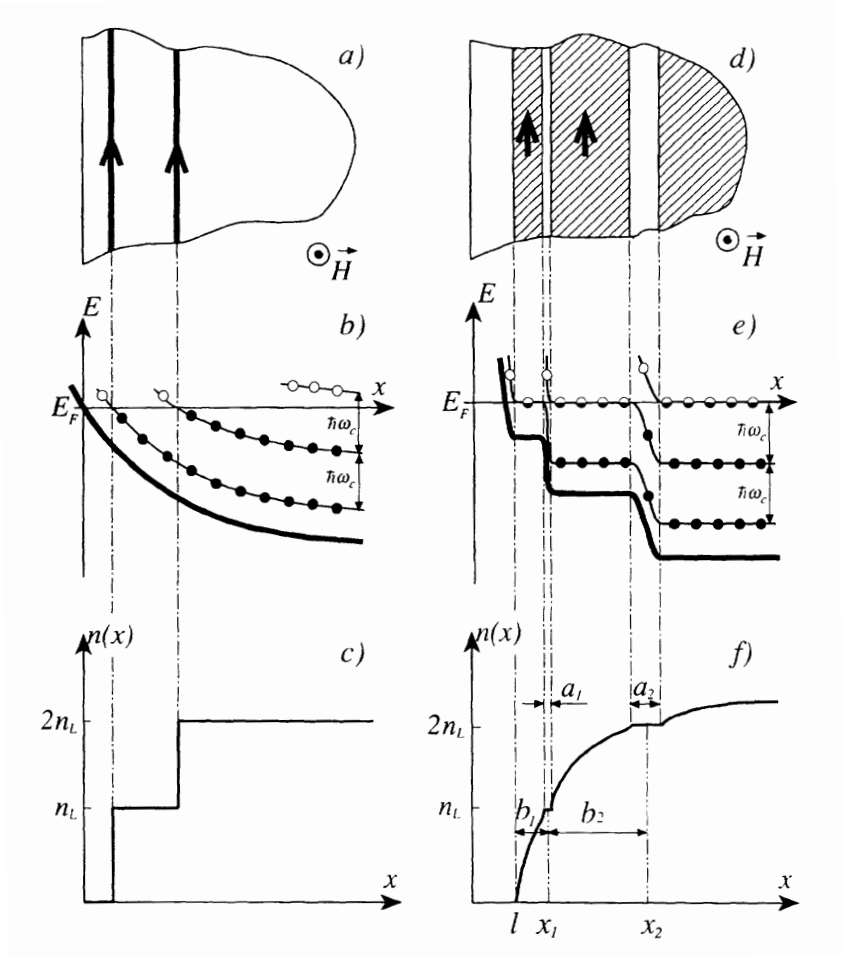

Figure 3-1: Non linear screening at a depleted edge of the 2DES producing an alternating pattern of metallic-like compressible strips and insulating incompressible strips. Panels (a), (b) and (c) on the left shows the "single particle" model of the edge of the quantum Hall liquid. The potential is taken to be the same as obtained from the self-consistent potential at zero magnetic field,and Landau levels are simply filled up to the Fermi energy. This leads to infinitely narrow compressible regions where the LL energies pass through the Fermi energy, which are referred to as "edge states". The majority of the sample is incompressible, and locally there is exactly one Landau level filled. When the self-consistent screening modifications due to a quantizing magnetic field are included, shown in panels (d), (e), and (f), the picture is changed dramatically. The compressible regions now acquire finite width due to the higher degree of screening provided by a partially filled Landau Level. These wide compressible regions are now separated by narrower incompressible regions. This transition is driven by electrostatic forces that are associated with trying to create the density profile shown in (c), which would involve a significant electrostatic energy penalty. After this reconstruction, the density profile follows as closely as possible the density profile at zero magnetic field in order to minimize the electrostatic energy. Figure taken from Chklovskii, Shklovskii, and Glazman [51].

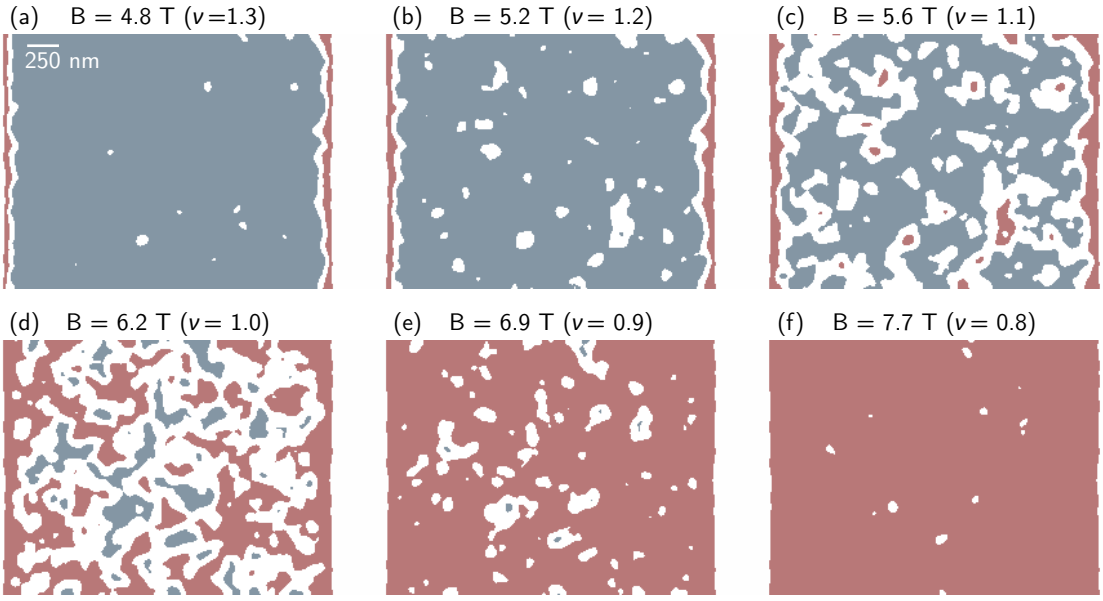

Figure 3-2: Localization of electrons in the bulk by a percolating incompressible strip. Figure shows simulations of the electron density in a 3 μm wide etched Hall bar at high magnetic fields. The average electron density is 1.5×10^{11} e/cm^2, and the disorder model includes 1.5×10^{11} cm^{-2} randomly ionized donors with a 50 nm setback. (For details of the simulation, see chapter 5.) In panels (a) through (f), metallic regions where the local filling factor is $\nu_{\rm local} < 1$ are shown in pink, incompressible regions of $\nu_{\rm local} = 1$ are shown in white, and metallic regions of $\nu_{\rm local} > 1$ are shown blue. (a) At low magnetic fields, a relatively narrow incompressible strip separates metallic states at the edge from the bulk. As we increase the magnetic field, this incompressible strip spreads to the center of the sample forming a percolating network that localizes electrons when $\nu_{\rm bulk}$ is close to an integer. At these fields, the Hall resistance becomes quantized. As we increase the magnetic field further, shown in (e) and (f), the metallic $\nu < 1$ state begins to percolate and the Hall voltage quantization is lost.

transport across the strip as a function of a local gate voltage that modulated the electron density. The resonances appears as sharp peaks in the IS conductance at certain magnetic fields and gate bias voltages. The exact origin of the resonances were not understood. Based on an observation that the conductance peaks followed trajectories in a magnetic field vs. electron density plot that ran parallel to integer filling factors, Chklovskii [115] argued that the resonances were the signature of single-electron tunneling through a Coulomb blockaded island in the incompressible strip. The reasoning is quite simple: consider a density fluctuation creating a small island inside the incompressible strip, as shown in figure 3-3(b). If this island is small and only weakly coupled to its surroundings, the number of excess charges on the island will be quantized. According to the Coulomb blockade picture, the island will then show resonances whenever the charge on this island is changed by one electron. In the non-linear screening model, the excess charge on the island is set only by the difference in the local density from integer filling, as illustrated by the hatched area in figure 3-3(b). In this way, the Coulomb blockade model predicts that trajectory of the resonance peaks in a magnetic field vs. electron density plot will be quantized and run parallel to integer filling factor[1].

A similar phenomenon arises in narrow Hall bars. In a narrow Hall bar, the network of ISs that produces localization in wide Hall bars is replaced by a single IS that separates the two sides of the sample. Any transport that occurs across this IS will destroy the quantization of the Hall resistance. Thus, indirectly, transport in narrow Hall bars also probes the resistance of an IS. In contrast to the smooth transitions between Hall plateaus seen in large samples, narrow Hall bars show sharp, reproducible fluctuations (see [118] for a comprehensive list of references). Of particular interest is the work of Cobden *et al.* [119], which was performed on a gated device. By mapping the trajectory of the the fluctuation peaks as a function of both magnetic field and density, the fluctuations were seen to distinct come in groups that ran exactly parallel to integer filling factor. This behavior was not consistent with

[1]The same argument was presented in [116] as evidence for the nature of localized states at quantum Hall plateaus.

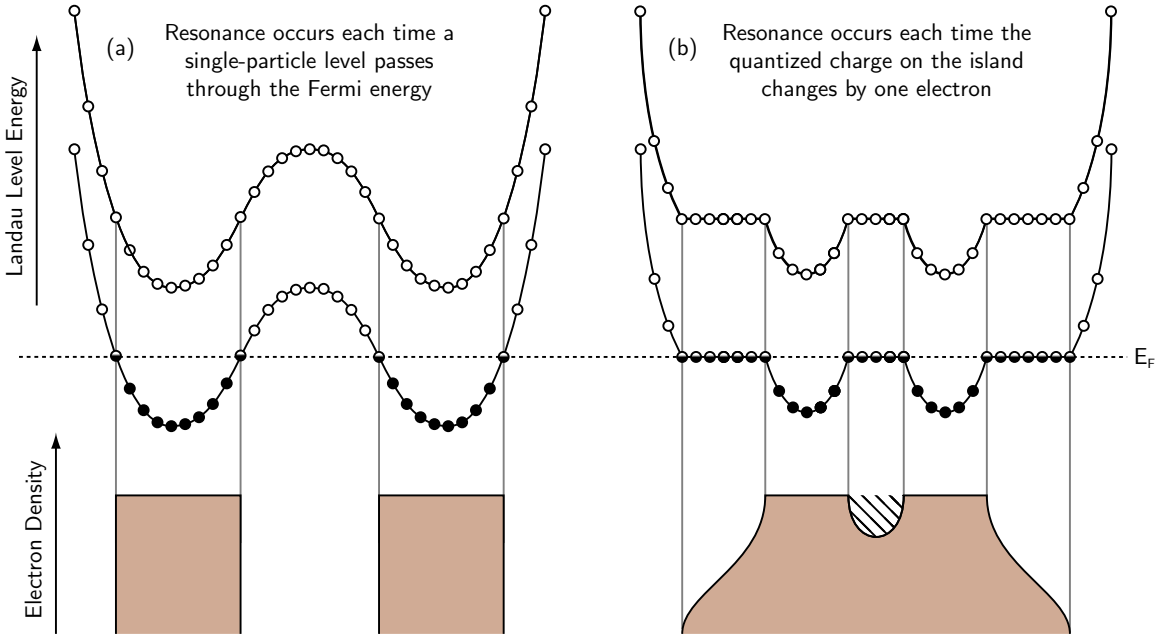

Figure 3-3: Models of a localized state inside a narrow Hall bar. Panel (a) shows the localized state in the single-particle picture, as described in [117]. In this picture, the potential is assumed to have the same form as in zero magnetic field. The localized states always take the form of rings that encircle hills and valleys in the potential. Resonances occur each time a single-particle orbital passes through the Fermi energy. Including non-linear screening, as shown in (b), the self consistent potential is modified, acquiring flat regions where a Landau level is partially filled. In this case, a new type of localized state can occur in the form of a small Coulomb-blockaded island. This localized state has the shape of a disc, not a ring, and resonant tunneling through it is governed by the total charge on the island, not the number of single-particle orbitals it encloses. This charge is determined only by the difference in the local density from integer filling, shown by the hatched area in (b). This leads to resonance peaks that follow trajectories parallel to integer filling factor in a magnetic field vs. density plot.

previous single particle models [117], which predict localized states of the form shown in figure 3-3(a). In analogy with Chklovskii's ideas, Cobden *et al.* suggested that the results demonstrated a different type of localization in the quantum Hall effect, driven by Coulomb blockade of small compressible islands inside incompressible strips.

While many of the narrow Hall bar experiments were performed on relatively low mobility samples (see [118] and references therein), fluctuations in both the integer and fractional quantum Hall regimes were seen in high mobility samples in earlier experiments by Simmons *et al.* [120, 121]. In the 1/3 and 2/3 fractional plateaus, they observed that the quasi-periodicity of the fluctuations was triple that of those at integer plateaus. Interpreting the results in the context of the single-particle model [117], the authors suggested that these were evidence of h/e^* Aharonov-Bohm type oscillations of the magnetic bound states, where e^* is the fractional charge of the quasiparticles at fractional filling factors. However, it was later pointed out [122] that fractionally charged quasiparticles must also be treated with fractional statistics: including this effect, the Aharonov-Bohm type oscillations will have a periodicity of h/e, not h/e^*. It is interesting to note that if we re-interpret these early results in the context of the Coulomb blockaded island model, they constitute the first true experimental observation of fractional charge.

Finally, recent remarkable experiments [116] measuring chemical potential fluctuations at Hall plateaus using fixed and scanning single-electron transistors have conclusively demonstrated the existence of such Coulomb blockaded islands in both the integer [116] and fractional [123] quantum Hall regimes, but do not address their influence on transport.

3.2 Imaging the resistance of an Incompressible Strip

The works discussed in the previous section concerning transport across incompressible strips all relied on "bulk" probes, such as measuring the resistance between two

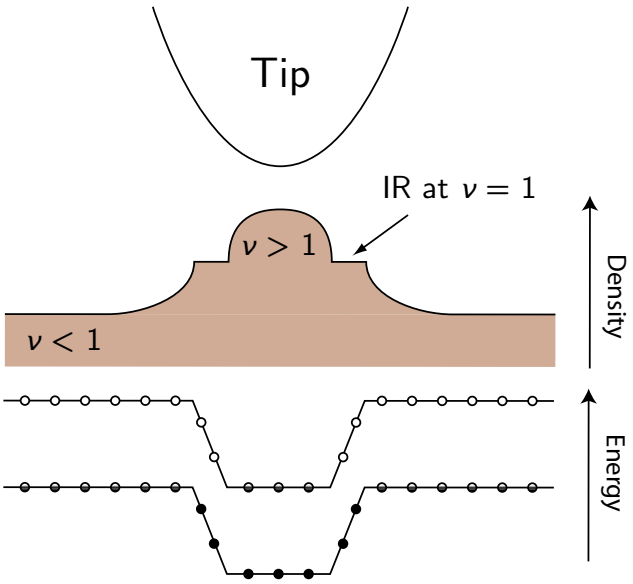

Figure 3-4: For bulk filling factors less than one, applying a positive DC bias voltage attracts electrons to the region under the tip, creating a bubble of compressible electrons in the $\nu > 1$ state, separated from the bulk by an incompressible ring (IR) at $\nu = 1$. In order to move across the incompressible strip, electrons from the bulk must tunnel across a triangular tunnel barrier formed from the energy gap between the two Landau levels, which presents a large resistance to charging the central bubble.

terminals of a Hall bar or measuring the capacitance of a large metal pad to the 2D layer. As such, it is difficult for these experiments to determine the microscopic origin of the observed behavior, and only speculation can be made as to what is really happening on a microscopic scale.

In this section, we introduce a new technique that images transport across incompressible strips directly on a microscopic scale. We use a scanning charge accumulation microscope to probe the resistance of a tip-induced mobile incompressible strip. By applying a DC bias voltage to our tip, we can create the situation shown in figure 3-4. When the bulk filling factor is less than integer ($\nu = 1 - \epsilon$), applying a positive voltage to the tip attracts electrons to the region under the tip. For a sufficiently large positive voltage, a "bubble" of electrons is in the $\nu = 1 + \epsilon$ state in the region under the tip. The bubble is separated from the surrounding 2DES by a ring shaped incompressible strip that we will refer to as an "incompressible ring" (IR). By detecting the charging of the bubble in response to an AC excitation applied to the sample,

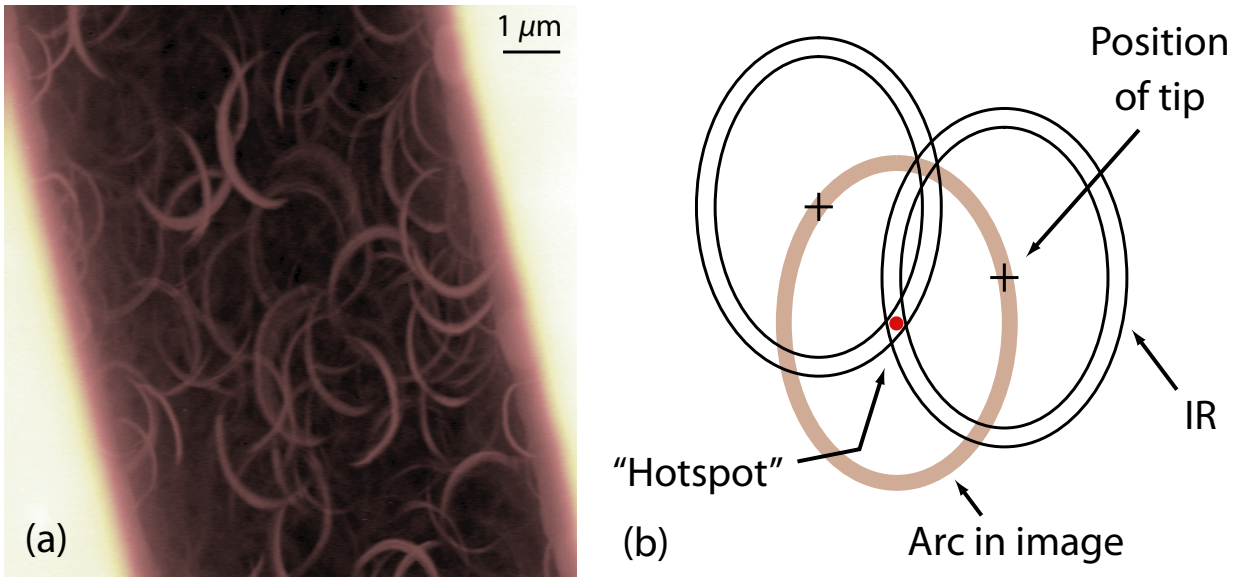

Figure 3-5: (a) A 10×10 μm in-phase charging image taken at $\nu_{\text{bulk}} = 0.89$ ($B = 7.0$T) with a bias of +1.5V applied to the tip. The image is generally dark, but is penetrated by bright arcs at positions where the IR becomes leaky. (b) Intersection of the IR with hotspot of fixed position in the 2DES creates the arc patterns shown in the image in (a) that reproduce the shape of the IR inverted through the hotspot.

we directly measure the resistance of the IR. Moving the tip, the bubble and ring translate together, producing an image that is a map of the resistance of IRs formed at different locations in the sample.

Figure 3-5(a) displays an image of the in-phase component of the charging signal, taken with the 2DES at filling factor $\nu_{bulk} = 0.89$ and a positive bias voltage applied to the tip. The gates appear as regions of high capacitance in the top right and bottom left areas of the image. In the region of the image where the tip is over the 2DES, a bubble forms from a local accumulation of electrons in the $\nu > 1$ state. The image is generally dark due to the large resistance of the surrounding IR, with the exception of sharp, bright elliptical arcs. The patterns repeat at uncorrelated positions in the image. In the absence of a magnetic field, the images are completely featureless. The observed arcs appear only at magnetic fields near integer filling factors and upon applying a bias voltage of an appropriate polarity for the formation of a bubble.

We interpret the arcs that we see in the image with the following model. The arcs in the images correspond to the locus of points at which the IR intersects a "hotspot"

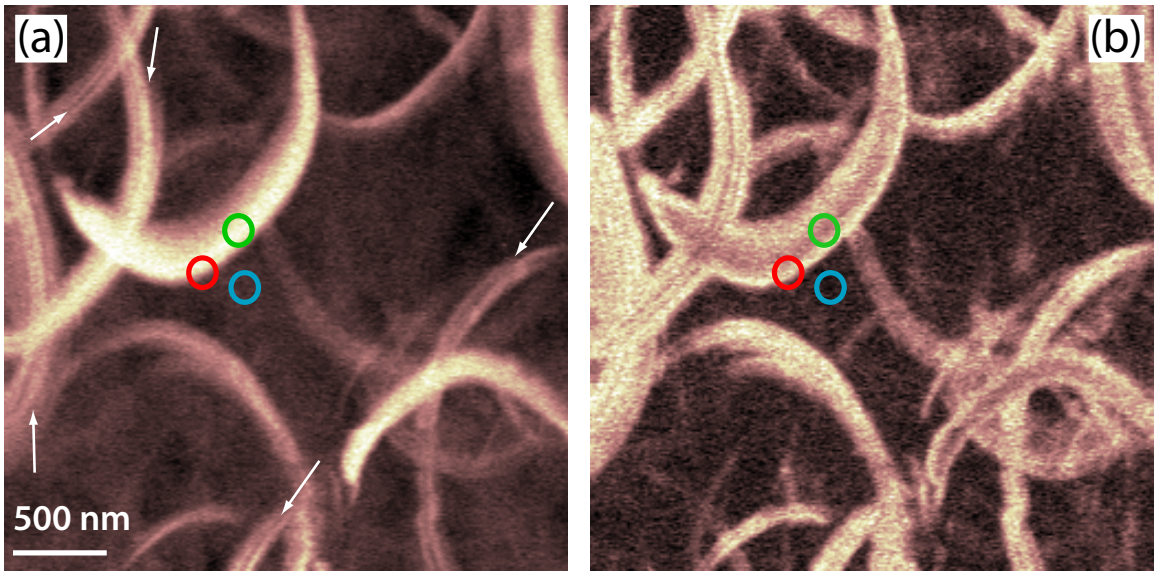

Figure 3-6: (a), (b) 3×3 μm charging images taken at $\nu_{\text{bulk}} = 0.83$ (7.5 T) and $V_{\text{tip}} = +1.5$V. Note the inversion of the contrast in the lagging-phase images at the center of the filaments. Circles in the drawn in the images show tip positions where the IR resistance varies to result in the in-phase and lagging-phase signals shown by the matching colored arrows in the RC model shown in 3-7. The white arrows show narrow sub-filament fringes seen in many of the arcs.

in the 2DES, as shown in figure 3-5(b). The arcs in the images directly reflect the shape of the tip, and the hotspots are located at the centers of the ellipses suggested by the arcs. The size of the IR created by the tip depends on the magnetic field and the bias voltage, and can be directly measured from the size of the arcs in the image. The elliptical shape of the arcs is most likely a result of asymmetry in the tip etching procedure[2].

3.3 What are the hotspots?

The hotspot model explains very well the shape of the arcs seen in the image, but is does not say anything about what the hotspots are or how they cause the IR resistance to drop. In order to answer these questions, we need to take a closer look at the data.

Figure 3-6(a) and (b) show in phase and 90° lagging-phase charging images at

[2]Miscalibration of the lateral scan tube coefficients may also play a role

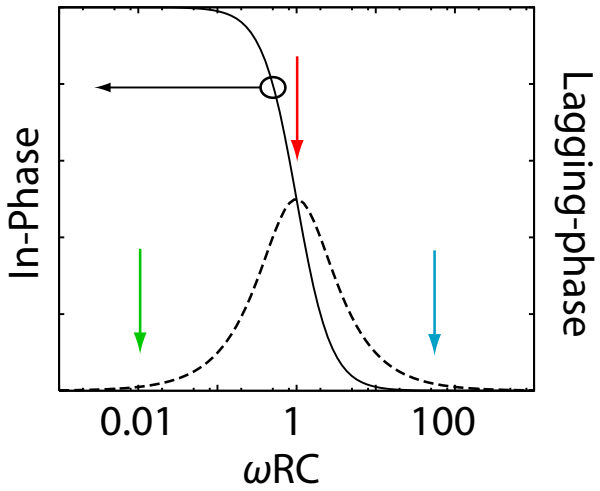

Figure 3-7: In-phase and lagging phase signals are shown for a simple RC model where the bubble's self capacitance to its surroundings charges through the resistance of the IR. Colored arrows indicate the places on the RC curve marked by the matching circles in figure 3-6.

$\nu = 0.83$ (7.5T) with a tip bias of +1.5V taken at a high spatial resolution. There are two remarkable features revealed in these scans: the first is that the lagging phase signal inverts contrast at the center of the arcs. The second is that on small length-scales, the arcs show a fine structure consisting of striation-like oscillations. These two observations will lead us to a model for the origin of the hotspots.

The inversion of the contrast in the y-phase data gives us quantitative information about the magnitude of the drop in the IR resistance. We can consider the charging of the bubble in a simple RC model where the capacitance of the bubble to its surroundings charges through the resistance of the IR. Figure 3-7 shows the expected behavior in this model of the in-phase and lagging-phase signals as a function of the RC charging time of the bubble. Our measurements are performed at fixed frequency: any changes in the charging signal must arise from changes in the product RC. The area of the bubble is fixed only by the tip voltage and the magnetic field, and as can be seen from the uniform radius of the arcs in the images, can be taken to be approximately constant. This allows us to directly relate changes in the charging signal to changes in the IR resistance.

Three positions are marked by colored circles in figures 3-6(a) and (b). At these

positions, the IR resistance varies to result in the in-phase and lagging phase signals shown by matching colored arrows in 3-7. In the green circles, the IR has a low resistance and the bubble nearly fully charges and discharges during the cycle of the excitation. The blue circles correspond to at least 10,000 times higher resistance and the bubble does not charge at all. Remarkably, displacing the IR by 100 nm causes its resistance to change by more than four orders of magnitude.

We can also use this data to estimate the absolute value of the IR resistance. The lagging phase data in figure 3-6(b) demonstrates that the positions where the bubble does not charge correspond to RC charging times that are far in excess of the period of the AC measurement. We can roughly estimate the self-capacitance of the bubble from its size: a 2 μm bubble in GaAs gives a self capacitance of 1 fF[3]. Estimating the product ωRC to be at least 100 from the data gives a value of at least 100 GΩ for the resistance of a pristine IR. The intersection of the IR with a hotspot can cause this resistance to drop abruptly to $\sim$ 10 MΩ.

The second clue to the origin of the hotspots is our observation of radial oscillations of the charging signal inside the arcs. Upon magnification, many of the filaments show these remarkable striations down to astonishingly small length scales. Figure 3-8 shows images where spacings as small as 10 nm were seen. This length scale is both smaller than the Bohr radius in GaAs and the magnetic length.

Motivated by these two observations, along with the fact that the hotspots appear at uncorrelated positions in the images, we propose the following model. A hotspot arises from a short length-scale density fluctuation in the 2DES, which creates a small quantum dot (or anti-dot) island embedded in the IR as shown in figure 3-9. Electrons can then resonantly tunnel across the IR through the dot, causing the IR resistance to drop dramatically. This model also explains explains the observed striations. Since the island is small and is only weakly coupled to its surroundings, the charge on the island will be quantized. The fringes results from Coulomb blockade of transport through the dot. The dot combined with the bubble acts as a single-electron transistor

[3]We can calculate this number more accurately from our electrostatic simulations in chapter 5. From these, we also obtain bubble self-capacitances on the order of 1 fF.

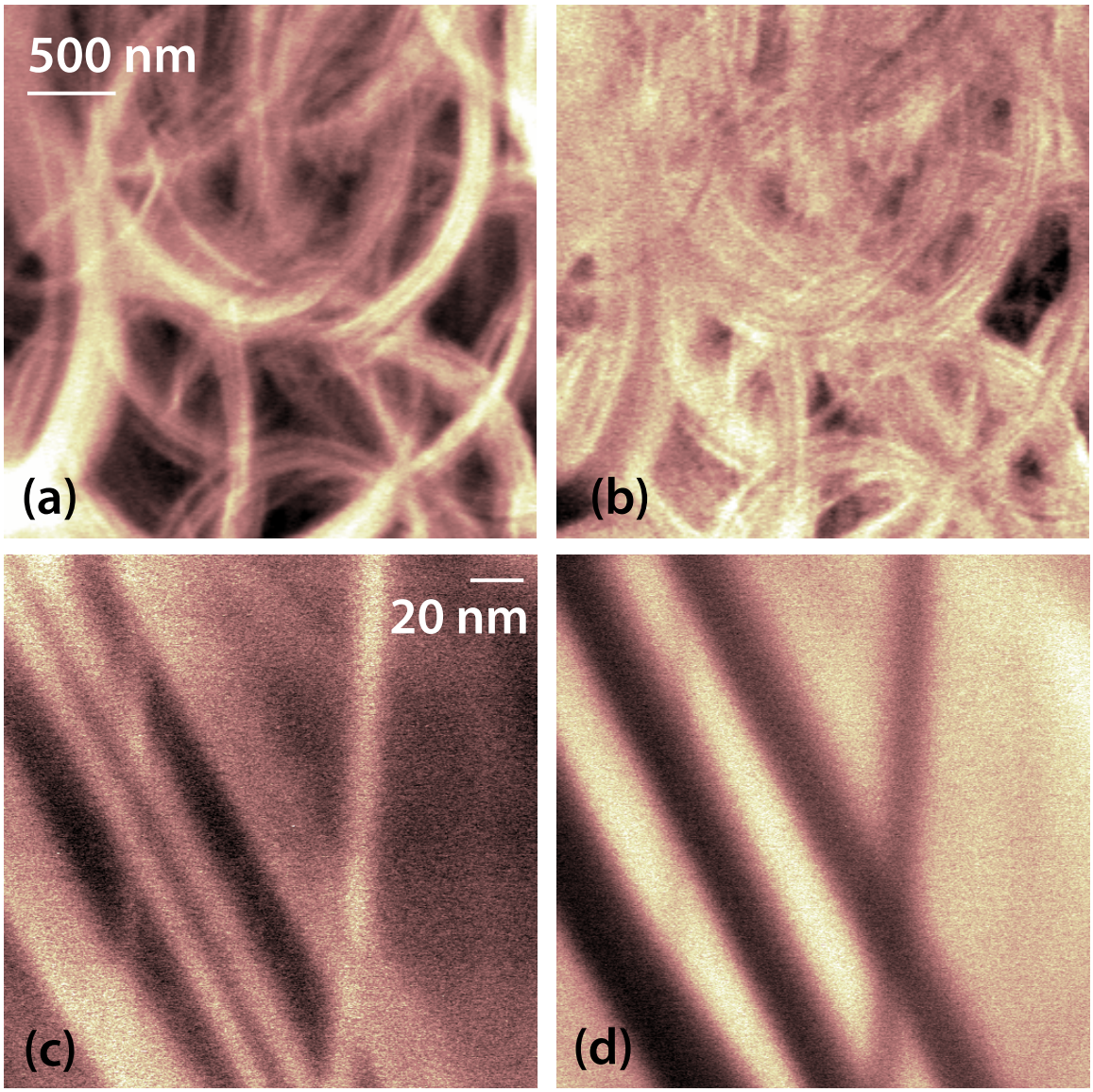

Figure 3-8: (a), (b) 3×3 μm in-phase and lagging phase images taken at $\nu_{\text{bulk}} = 1.1$ (5.5 T) and $V_{\text{tip}} = -1.5$V. Many narrow oscillations are visible in these arcs in these images. (c), (d) Ultra-high resolution scans (200x200 nm) showing oscillation structures down to length scales comparable to and smaller than the magnetic length.

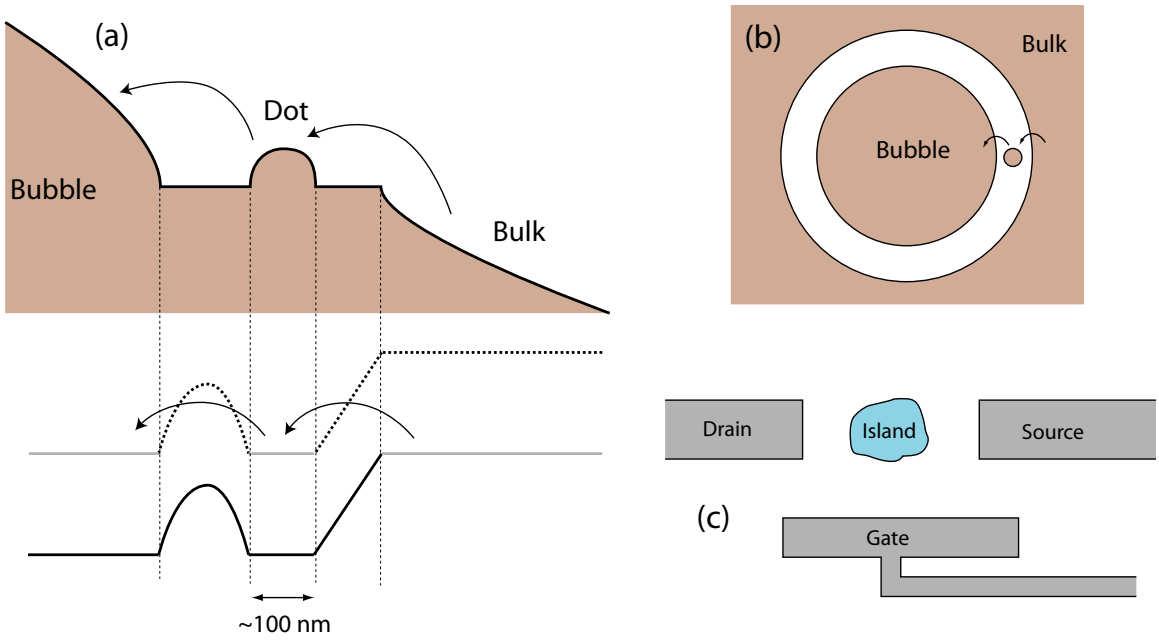

Figure 3-9: (a) Density profile (top) and Landau level energy profile (bottom) of a short length-scale fluctuation creating a quantum dot island inside the IR. Dotted, gray, and solid lines (bottom) depict empty, partially filled, and filled Landau levels respectively. Resonant tunneling through this dot leads to a dramatic reduction of the IR resistance. (b) Top view of the island inside the IR. (c) The charge on the island is quantized, and can only change in increments of one electron. The bubble, island, and bulk act as a single-electron transistor.

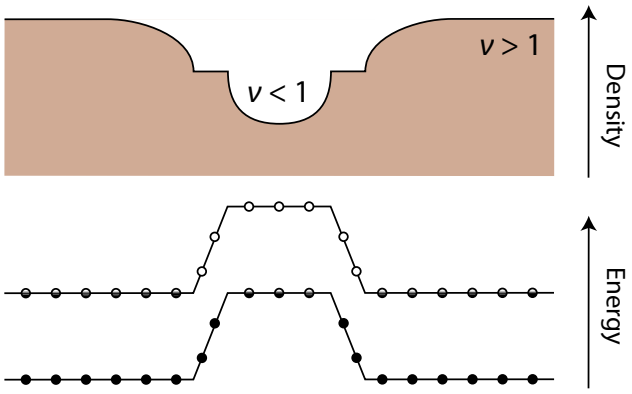

Figure 3-10: Starting with $\nu_{\text{bulk}} > 1$ and applying a negative bias voltage to the tip, we can create a bubble from an accumulation of holes in a lower filled Landau level.

(SET), with the bulk 2DES as the source contact and the bubble as the drain contact. The SET island is embedded in the IR, and is gated by electric fields from the tip, leading to discrete changes in its occupancy as the tip is moved, or as the DC bias is changed with the tip at a fixed position. Note that the fact that we observe a conductance enhancement implies that this single-electron resonant tunneling is a coherent process, as Coulomb blockade with incoherent tunneling, such as seen in metal SETs, results only in a conductance suppression.

3.4 Imaging the resistance of a $\nu = 1$ IR at lower magnetic fields: Creating a hole-bubble

We can also probe the resistance of a $\nu = 1$ IR by moving to a magnetic field with $\nu_{\text{bulk}} > 1$ and reversing the polarity of the bias voltage on the tip. This will deplete locally under the tip to produce an accumulation of holes in a lower filled Landau level (a "hole bubble"), as shown in figure 3-10. Similarly to an electron bubble, this hole bubble is isolated from the bulk by a $\nu = 1$ incompressible strip. This allows us to image the resistance of an incompressible strip formed at lower magnetic fields.

Figure 3-11 shows in-phase and lagging phase hole bubble images taken at $\nu = 1.1$ (B = 5.5T). As can be seen from the images, the hole bubble IR has a much lower resistance on average, suggesting a significantly reduced tunnel barrier formed from

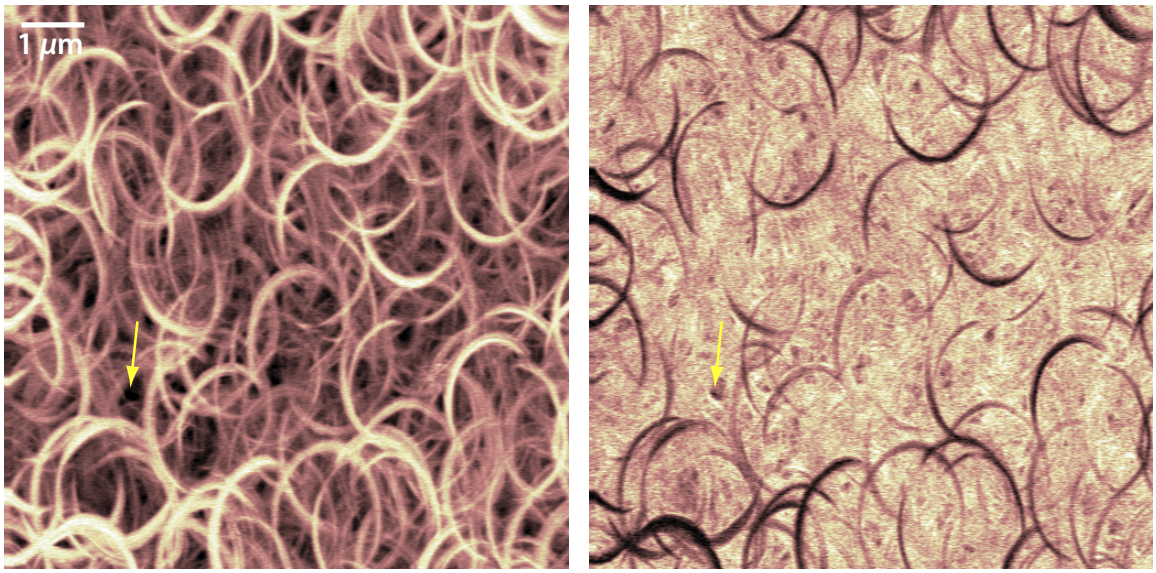

Figure 3-11: 9×9 μm high resolution hole bubble images. Hole bubble images display a spectacular tangle of arcs, implying a very high density of active hotspots. Arrows denote a place in the image where the IR does not intersect any hotspots. The IR has a high resistance at this position, producing a dark signal in both the in-phase and lagging-phase images.

the exchange-enhanced spin gap at these magnetic fields. A careful examination of the lagging phase data shows that this is not simply on overall reduction of direct tunneling across the IR: in particular, there are still places where both the in-phase and lagging-phase signals are dark, indicating that the IR resistance is still $\sim$ 100 GΩ. The increase in the brightness of the lagging-phase signal in the hole bubble data occurs instead as the superposition of a very high density of hotspot arcs. Thus, it seems that the reduction of the energy gap has resulted in an increased susceptibility of the IR to the formation of active quantum dot islands. Note also that the arcs in the hole-bubble images typically show many more Coulomb blockade oscillations, suggesting that the islands in the hole-bubble IR are larger in size.

To confirm that the difference between the electron and hole bubble images is due to the magnetic field and not associated with depleting vs. enhancing under the tip, we have used a global backgate to deplete the sample and compare hole bubble and electron bubble images taken at the same magnetic field.. Figure 3-12 (a), (b) and (c), (d) show in-phase and lagging-phase electron and hole bubble images with a

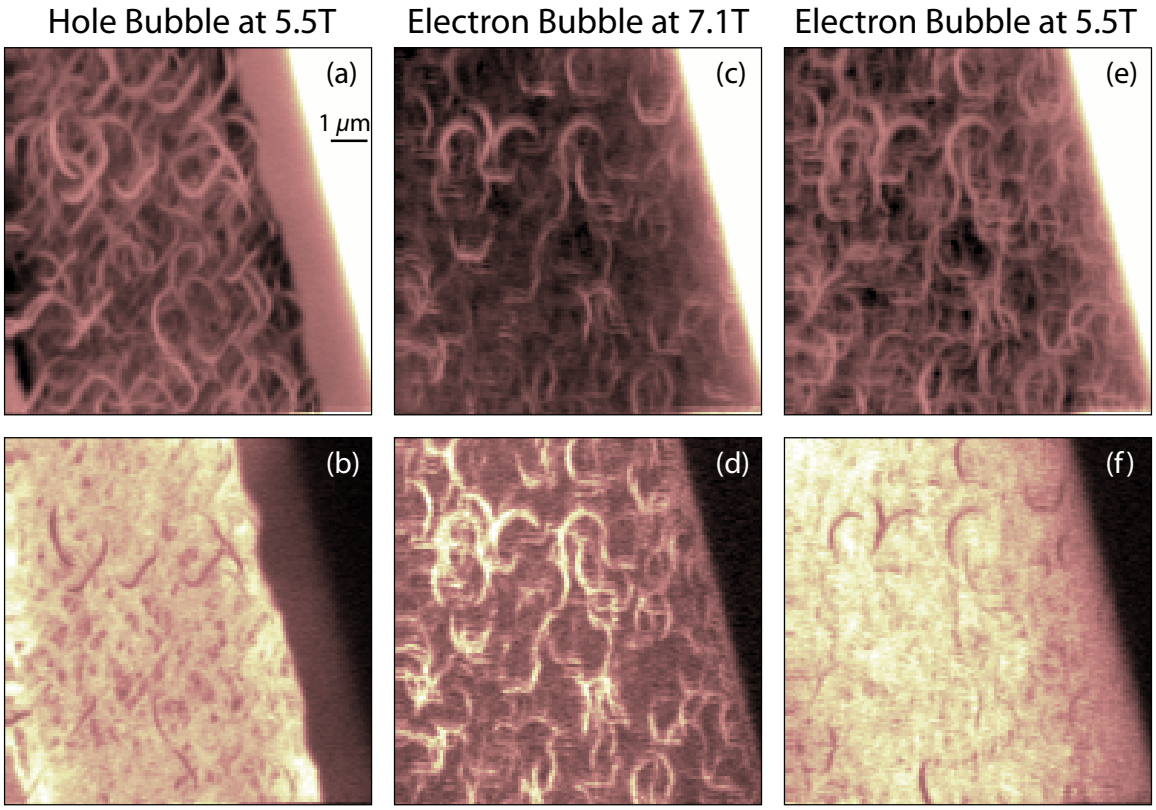

Figure 3-12: Comparing electron and hole bubble images at the same magnetic field. (a),(b) In-phase and lagging-phase hole bubble images at 5.5T at an electron density of 1.5×10^{11} cm^{-2}. (c), (d) Electron bubble images at 7.12T at the same density. In (e) and (f), the sample density was lowered to 1.16×10^{11} cm^{-2} to allow electron bubble images to be taken at the same magnetic field as the hole bubble images in (a) and (b).

density of 1.5×10^{11} e/cm^2 at 5.5T ($\nu = 1.1$) and 7.12T ($\nu = 0.87$). As usual, the hole bubble data shows many more resonances, as can be seen by the overall brightness in the lagging-phase images. In (c), we have lowered the electron density globally to 1.16×10^{11} so that $\nu = 0.87$ occurs at 5.5T. Upon doing this, the electron bubbles images show a number of resonances comparable to in 3-12(a), as can be seen by the brightness of the lagging-phase image, demonstrating that the difference in the hole bubble images is due only to the lower magnetic field.

Another feature that is prevalent in the hole bubble data is a bright, fully charging region that runs parallel to the gate, as can be seen in figure 3-12(a). In this area of the image, the charging signal recovers to the full value seen at zero bias, and no arcs are seen. The interpretation of this feature is quite straightforward: due to the work

function difference between the metal topgate and the 2DES, the density under the gate is slightly depleted. The "bright edge" in the image corresponds to the position where the $\nu < 1$ hole bubble merges with the $\nu < 1$ region under the gate. Once this happens, we no longer have to traverse an IS to charge the region under the tip. The distance that this region extends out from the gate is given by the radius of the IR, and correlates well with the size of the arcs in the image.

There is also a feature that runs parallel to the gate edge in electron bubble images, visible in figure 3-5(a). In these images, the charging signal is only partially enhanced and arcs frequently penetrate the area. This feature in the electron bubble images results from the screening of the electric fields from the tip by the gate: when the tip is over the center of the sample, the IR is elliptical in shape and has a width set by the density gradient from the tip. As we move close the gate, the DC fields from the tip are screened and the IR takes on a "D" shape. The straight edge of the "D"-shaped IR is formed from the steeper density gradients from the gate, giving a narrower strip. This narrowing of one side of the IR produces the partial enhancement of the charging signal.

3.5 Frequency Dependence

As the IR goes on and off resonance, the charging time of the bubble varies by four orders of magnitude. In our measurement, we will only observe arcs in the charging images if this charging time is varying in a range of values that is near the inverse of our measurement frequency. For the case of a $\nu = 1$ electron bubble IR, we were remarkably lucky: it just so happened that the RC charging time was varying in a range that started from well below to well above the inverse of the measurement frequency at which we have optimal charge sensitivity. The images that resulted showed the maximum possible variation of the charging signal at a measurement frequency where we had the best signal to noise ratio.

In general, we will not be so lucky, and we may have to change our measurement frequency in order to observe IR resonances. Changing the frequency, we can adjust

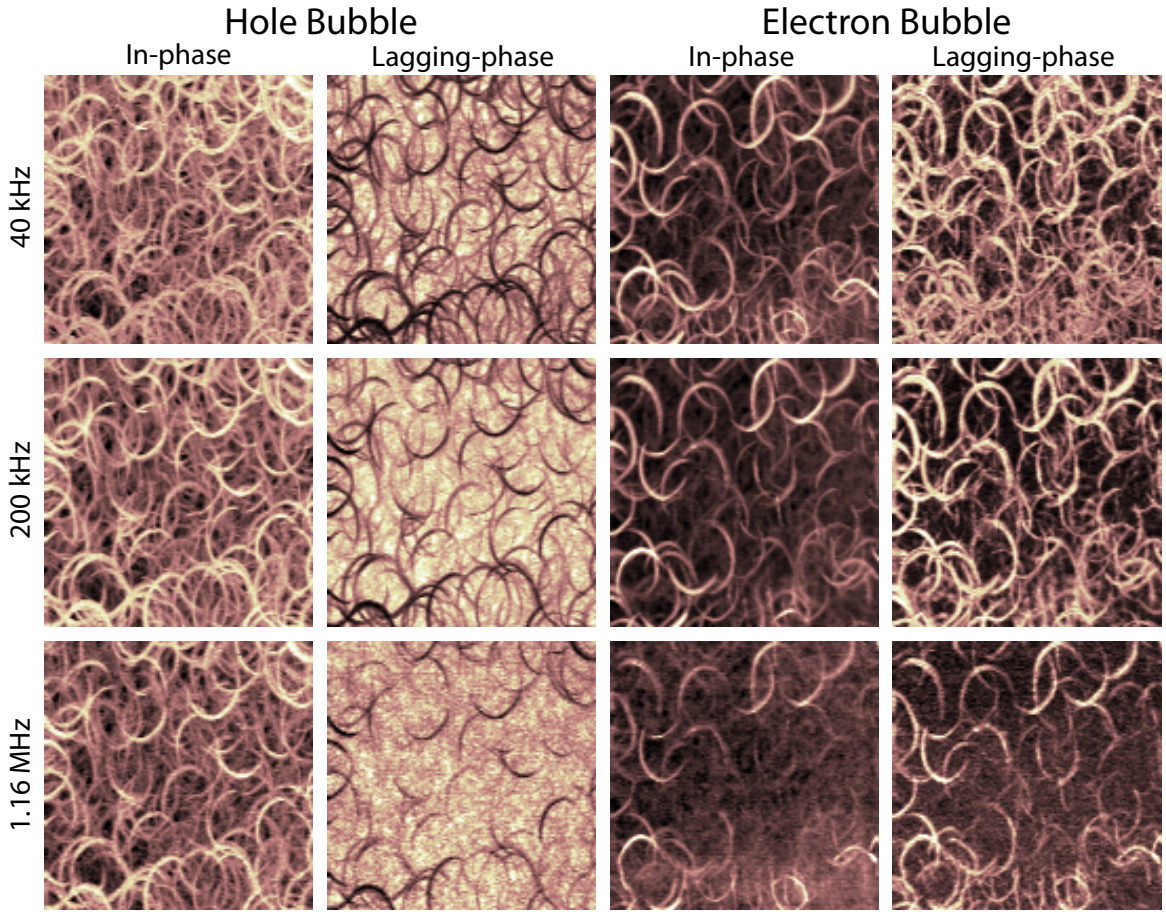

Figure 3-13: Frequency dependence of the resonance images at $\nu = 1$. The left two panels show 9×9 μm in-phase and lagging-phase hole-bubble images taken at 5.0T ($\nu = 1.26$) at +1.75V. Images were taken at 40 kHz, 200 kHz, and 1.16 MHz. The right panel shows the same measurements for an electron bubble at 7.5T ($\nu = 0.83$) with a tip bias of -1.75V.

the range of charging times we are sensitive to, allowing us to observe resonances from greater or fewer hotspots. This is shown in figure 3-13 for both $\nu = 1$ electron and hole bubble IRs. In both sets of images, the charging time is slow, and so by decreasing the measurement frequency we observe more resonances. There are two factors that make such frequency dependent measurements difficult: the first is that although we do have the freedom to change our measurement frequency by two orders of magnitude, this does not significantly change the number of resonances we are sensitive to since the resonances themselves are already modulating the charging rate by four orders of magnitude. The second is that our signal to noise ratio gets worse at both low frequencies due to 1/f noise and at high frequencies due to interference noise (see section 2.2). This limits the practicality of working near the limits of our frequency range.

3.6 Behavior of the imaged arcs with bias voltage and magnetic field

We have discussed the interpretation of our images in the context of a model where we probe the resistance of a ring shaped IS created by electric fields from the tip. This model makes very specific predictions about how the size of the arcs in our images should change with tip bias voltage or with magnetic field. If our interpretation of the data are correct, we should observe that changes in the size of the arcs upon varying magnetic field or tip bias are consistent with these predictions.

Figure 3-14 shows a panel of images from a hole bubble bias voltage sweep taken at a magnetic field of 5.5T ($\nu = 1.1$). As we are starting out with $\nu > 1$ in the bulk, applying a positive bias voltage to the tip does not create a bubble. All scans with positive tip biases at this magnetic field are completely featureless. At null voltage and small negative tip voltages, we also see no structure, as the local depletion is not sufficient to empty the partially filled Landau level. At a particular threshold voltage we start to barely deplete to $\nu = 1$: at this voltage, the image shows weak,

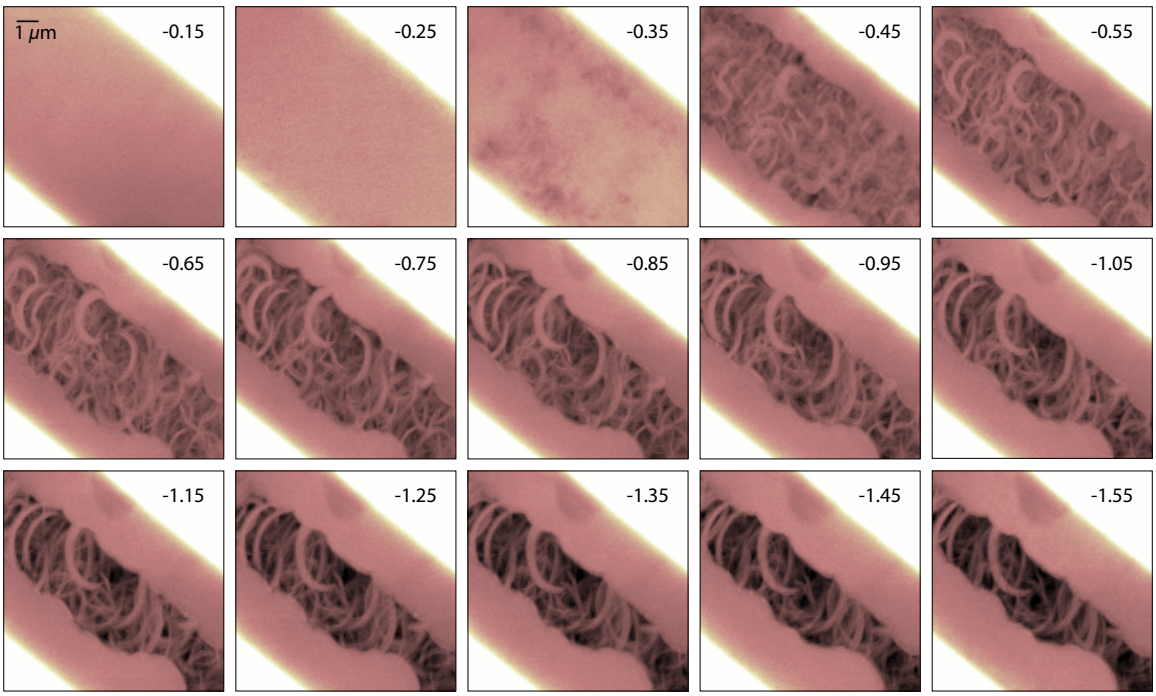

Figure 3-14: A sequence of images from a hole-bubble bias sweep. The 10×10 μm images show the in-phase charging signal at 5.5T for the tip bias voltage indicated in the top right of the images.

patchy dark spots as the $\nu = 1$ region under the tip forms and disappears at different positions in the sample. Beyond this threshold voltage, arcs appear in the image, indicating the formation of a well defined IR. Making the bias voltage more negative repels more electron from under the tip. As a result, the IR ring increases in size, as do the arcs we observe in the images.

In addition to the change in the diameter of the arcs with bias voltage, we also observe a change in the contrast between the charging and uncharging signal levels in the images in figure 3-14. To show this more quantitatively, in figure 3-15 we plot the histograms of the images in 3-14. Below threshold, the histograms show two distinct peaks associated with the signal level over the gate and the signal level over the fully charging 2DES. Once we have formed an IR, a new peak forms at lower signal levels, associated with the drop in capacitance from the uncharging bubble. As we make the tip bias voltage more negative, the diameter of the IR and the area of the hole bubble both increase. Correspondingly, we observe that the peak in the histogram from the

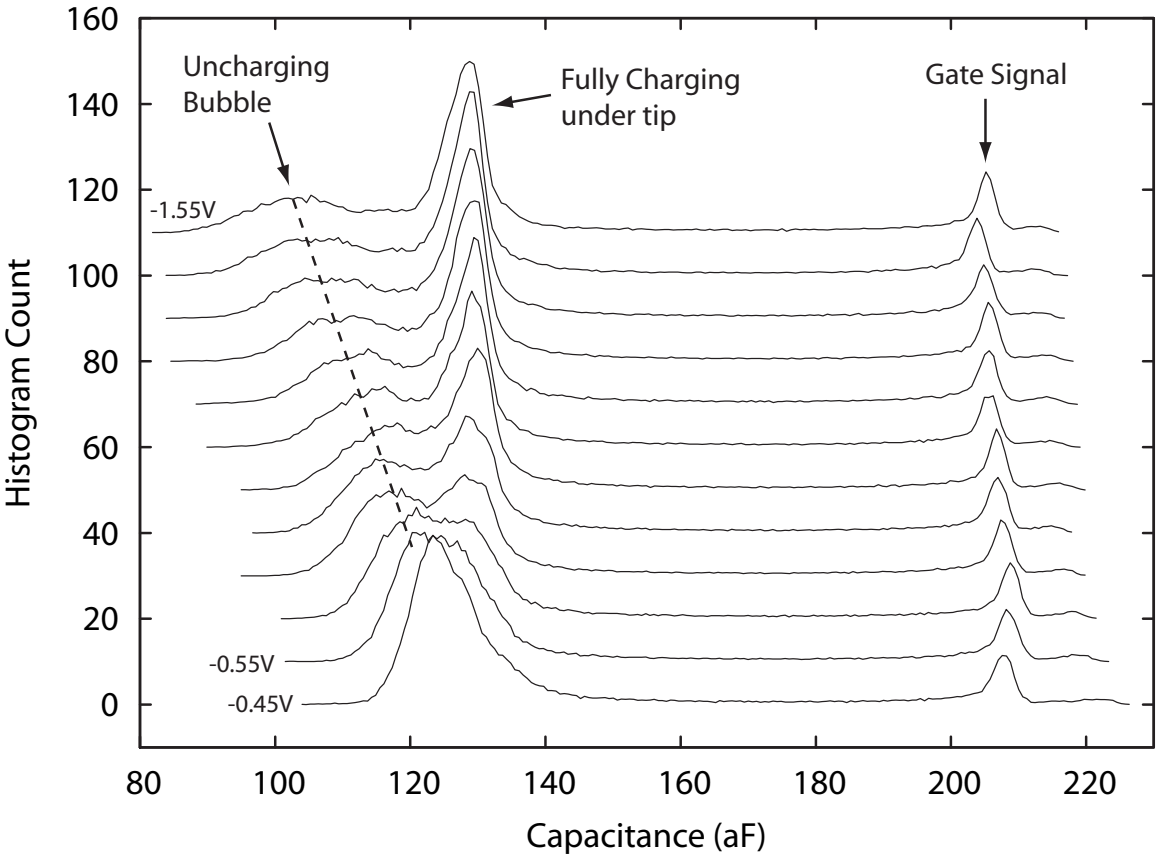

Figure 3-15: The histograms of the images from 3-14, starting at -0.45V. (The tip height drifted too far during the earlier scans to allow quantitative comparison of histograms of these images). The histograms show peaks associated with the gate signal level, the signal level of a fully charging region under the tip, and the signal level of the uncharging bubble. As the IR increases in diameter, the capacitance drop associated with the uncharging bubble increases. Drift of the absolute tip height as a function of time can be seen as variations in the gate signal level.

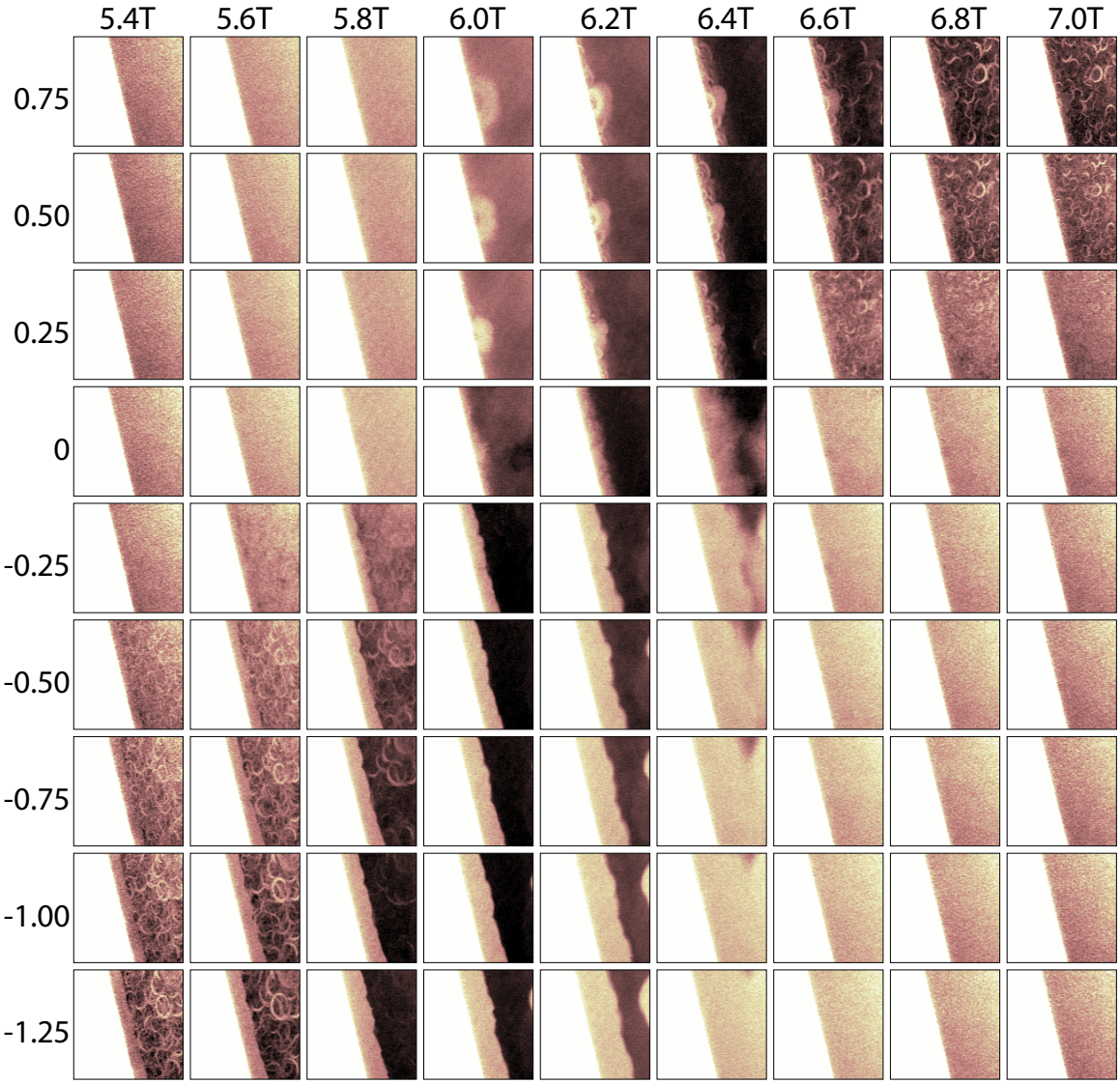

Figure 3-16: A panel of 10×10 μm in-phase charging images as a function of both tip bias voltage (vertical) and magnetic field (horizontal).

uncharging bubble shifts to a lower capacitance value.

By performing bias sweeps at different magnetic fields, we can produce a series of images that map out the full bias and magnetic field dependence of the data. Such a dataset is shown in figure 3-16. For magnetic fields below $B_{\nu=1}$, features only appear for negative bias voltages. For magnetic fields above $B_{\nu=1}$, arcs only appear for positive bias voltages. Near $B_{\nu=1}$, electrons in the 2DES become strongly localized and the region between the gates does not charge. At these fields, we observe features even at null voltage that are associated with charge penetrating the localized $\nu = 1$

state from the compressible regions under the gate. However, even with no DC bias on the tip, it appears that the interaction of the tip with the 2DES is still important, as we observe features that are sharper than our electrostatic resolution. We do not currently understand these results.

In addition to providing a comprehensive overview of the results, figure 3-16 also allows us to accurately find the true null voltage that produces no DC perturbation in the 2DES by finding the horizontal row that shows neither electron nor hole bubble behavior at all fields.

3.7 Measuring the signal with the tip at a fixed position

In addition to using the tip to produce spatial images of the 2DES, we can also use the tip as a local probe of a fixed position in the 2DES, and measure changes in the charging signal as a function of bias voltage or magnetic field. This has the advantage that for this single position, we can spend much more time averaging a measurement for a given bias voltage or magnetic field than if we are imaging a large area. The interpretation of this measurement, however, can be tricky: to be certain of the meaning of the features in the bias or magnetic field sweep, they should be accompanied by an image for at least one bias and mangetic field showing the spatial structure we are probing.

Figure 3-17 shows the in-phase and lagging phase charging signal for a bias sweep taken at 7.0T, corresponding to $\nu = 0.89$ in the bulk. For negative tip bias voltages we do not form an incompressible ring and the charging signal is flat. Once we apply a sufficient positive voltage, an IR forms. The large resistance of the IR prevents charging of the central $\nu > 1$ bubble and we see a drop in the in-phase charging signal with a peak in the lagging-phase signal. As we increase the bias voltage further, the IR grows and eventually intersects a hotspot in the 2DES. The hotspot drastically increases the conductance across the strip, producing a broad peak in the charging

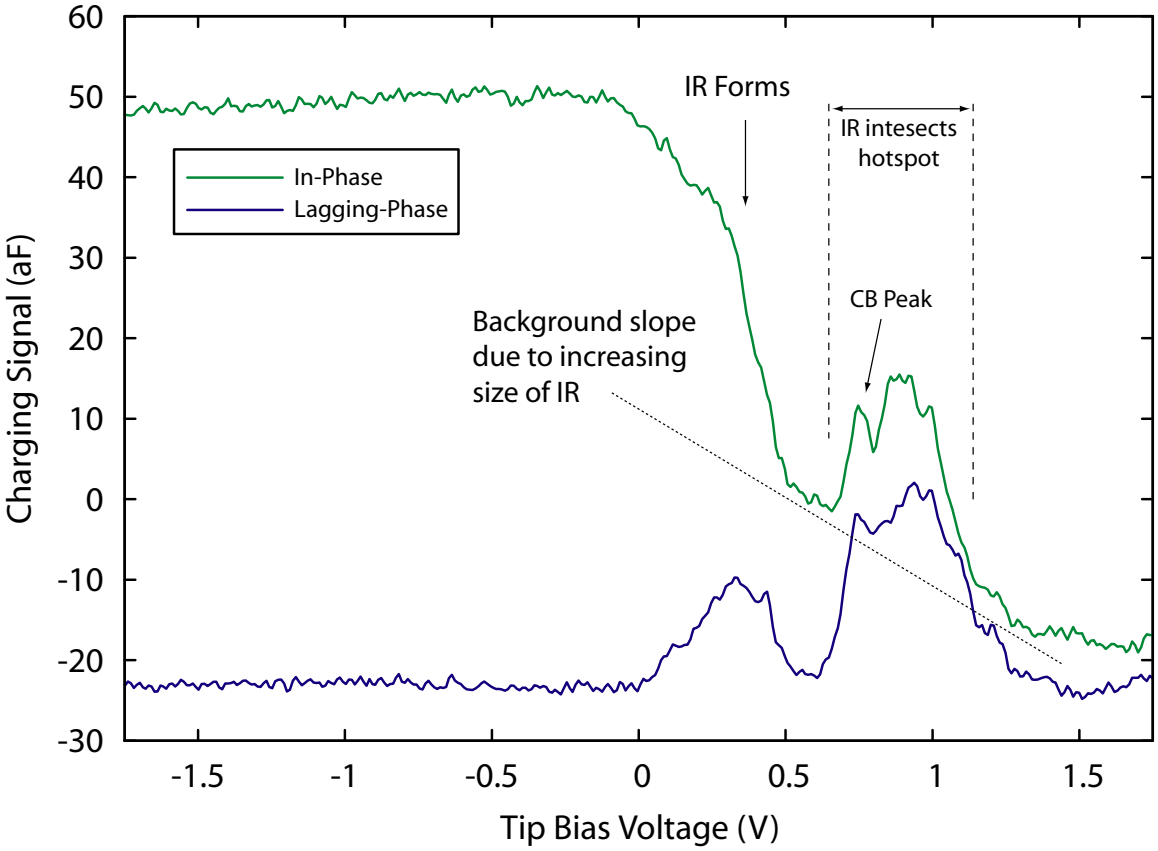

Figure 3-17: Electron bubble bias sweep at $\nu = 0.95$ (6.63T) showing both the in-phase (green) and lagging phase (blue) signals. As the IR forms, there is a drop in the in-phase signal and a peak in the lagging-phase signal. Increasing the bias voltage, there is a broad peak in the charging signal as the IR intersects hotspots in the 2DES. The broad peak shows finer structure associated with Coulomb blockade of the quantum dot island. The charging peak from the hotspot is superimposed on a sloping background in the in-phase signal due to the increasing size of the area enclosed by the IR.

signal as the IR moves through the position of the hotspot. Superimposed on this peak are smaller peaks from Coulomb blockade oscillations of the quantum dot conductance. The hotspot charging peak is superimposed on a sloping background that results from the increased capacitance change from a larger uncharging uncharging bubble.

Repeating this bias sweep with the tip at the same fixed position but at different magnetic fields, we can produce a color scale plot of the charging signal as a function of bias voltage and magnetic field, shown in figure 3-18. Here, we see drops in the charging signal in the lower right (upper left) regions of the plot corresponding to the formation of an electron (hole) bubble IR. Making the bias voltage more positive (negative), the IR grows and intersects hotspots, producing peaks in the charging signal as we saw in figure 3-17. Changing the magnetic field, the hotspot peaks follow sloped lines in the bias-field plot that converge on null voltage when $\nu_{\text{bulk}} = 1$. Near the center of the Hall plateau, the conductivity of the sample vanishes and there is no signal. Applying a bias voltage does create a compressible bubble, but it cannot charge because the bulk 2DES that surrounds it is localized.

By examining spatial images of the area around the position of the tip during the measurement of figure 3-18, we can directly identify features in the color scale plot with individual arcs in the spatial image. Figure 3-18(b) shows a 6x6 um scan taken at 7.0T and +1.5V, corresponding to the lower right corner of the color scale plot. In the image, two arcs are clearly identifiable. The two charging peak lines on the electron bubble side of figure 3-18(a) result from the intersection of the IR with the hotspots of these arcs (see caption of figure 3-18). At the magnetic fields where hole bubbles are formed, the density of active hotspots is much higher (see, for example, figure 3-11), and the charging peaks from individual hotspots cannot be easily identified.

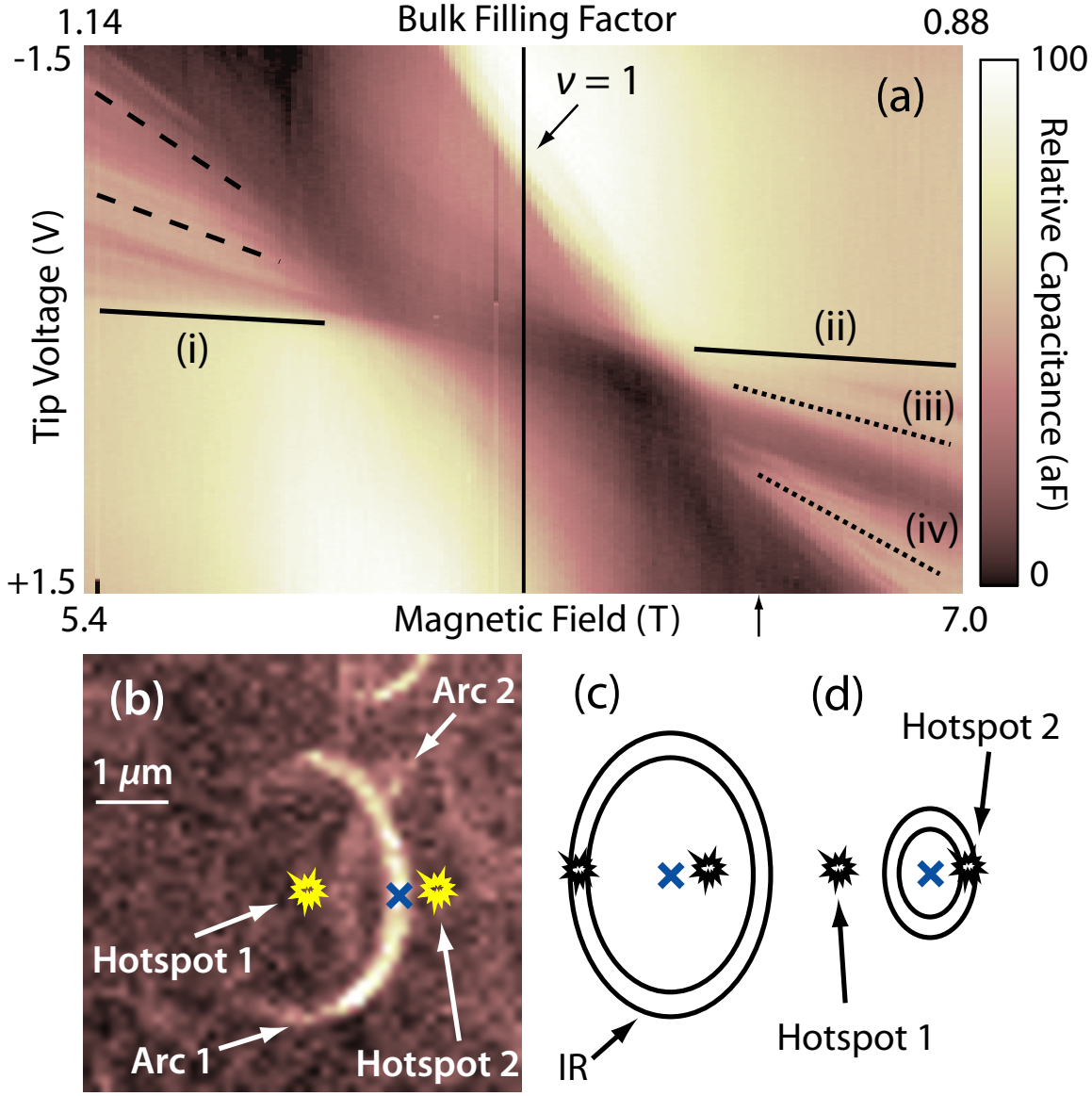

Figure 3-18: (a) Color scale plot of the in-phase charging signal as a function of tip bias voltage and magnetic field with the tip at a fixed position. The arrow on the magnetic field axis shows the magnetic field chosen for the bias sweep shown in figure 3-17. Lines (i) and (ii) display the threshold for forming a hole and electron bubble respectively. Dashed (dotted) lines indicate biases and fields where the IR intersects a hotspot, allowing resonant tunneling into a hole (electron) bubble under the tip. (b) 6x6 μm in-phase electron bubble image at 7.0T and +1.5V. The blue marker shows the position of the tip during the measurement in (a). Two arcs are identified, and the positions of the hotspots responsible for each arc are indicated. (c) The IR intersects hotspot 1 at biases and fields given by line (iv) in (a). (d) At lower biases the IR is smaller, and intersects hotspot 2 at biases and fields given by line (iii).

3.8 Why Partial Rings?

In the hotspot model shown in figure 3-5, we would expect that the arcs in the images would reproduce the entire shape of the IR, forming complete rings. However, in our images, we see only partial rings, and do not seem to see rings that close on themselves. The obvious question then becomes: why not?

An initial clue as to the possible origin of the partial rings comes from their orientations in the images. Like the positions of the centers of the rings that denote the positions of the hotspots, the "direction" that the partial rings point appears to be random and uncorrelated. The uncorrelated positions of the hotspots was one of the factors that led to the disorder-induced quantum dot model. Could disorder also play a role in the reason why we see only partial rings?

The charge fluctuations that produce the quantum dot islands in the IR involve length-scales smaller than the width of the IR. To estimate the IR width, we have completed a series of electrostatic simulations that account for the geometry of the tip as well as the nonlinear screening of the 2DES (see chapter 5. From these, we obtain an IR width of 200–300 nm in the absence of disorder. Density fluctuations on length-scales larger than the IR width appear as an additional local density gradient superimposed on the density gradient from the tip. The width of an IS is inversely proportional to the density gradient creating it [51]. Consequently, the local IR width will vary depending on the relative orientation of the gradients from the tip and the disorder.

Analysis of figure 3-19 explains our observation of only partial ellipses in the context of such local IR width modulations. We compare electron and hole bubble images taken at the same location. In switching from an electron to a hole bubble, the local density gradient from the tip inverts. To obtain the same local IR width at the location of the hotspot, the tip must be moved to the opposite side of the hotspot, as shown in figures 3-19(d) and (e). Figure 3-19(c) shows a composite image formed from an electron bubble image and a hole bubble image taken at the same location. In places where a partial ellipse appears in the electron bubble image, a partial ellipse in

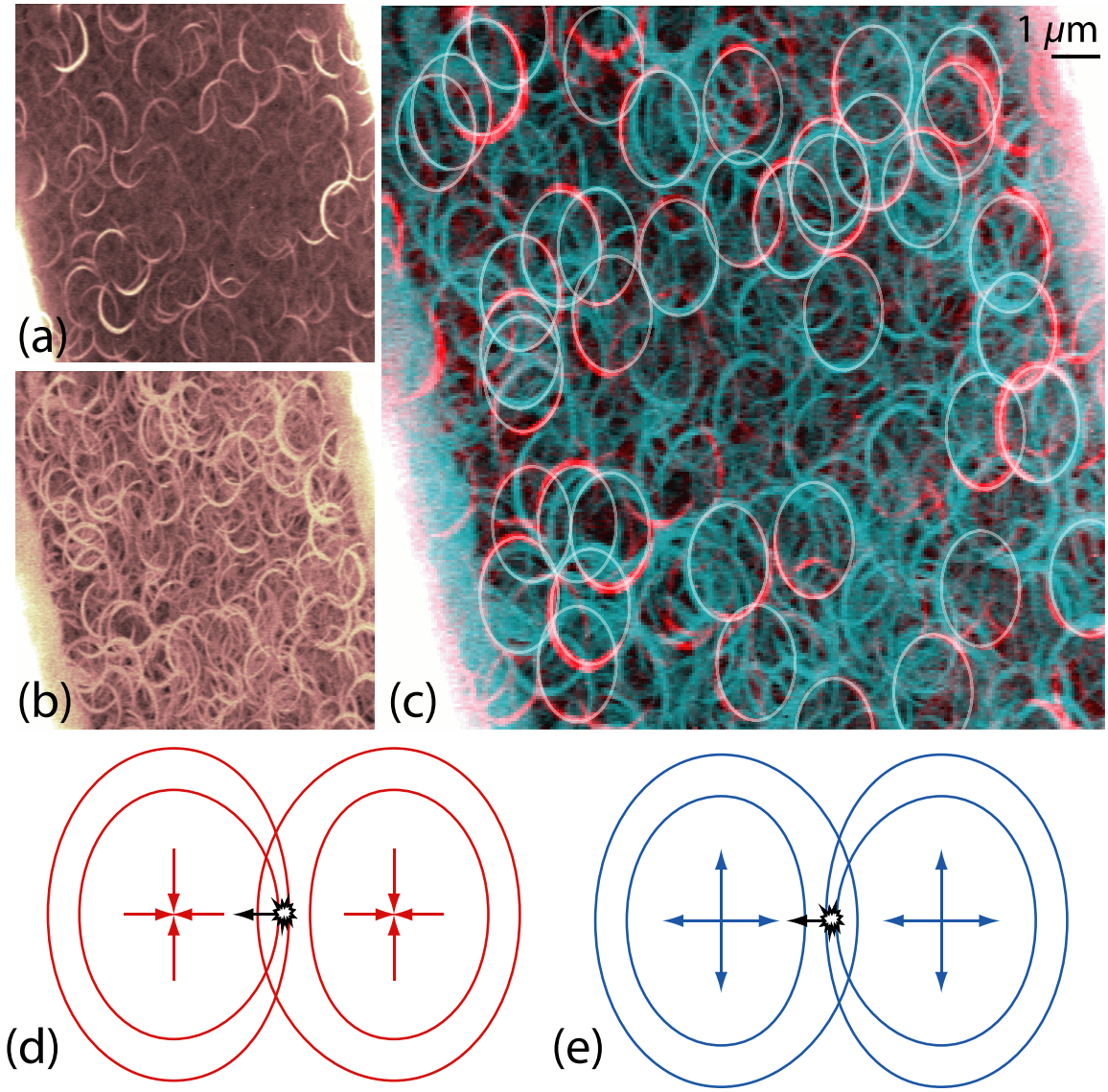

Figure 3-19: (a) 15x15 μm in-phase electron-bubble image, taken at $\nu_{bulk} = 0.83$ (7.5 T), $V_{tip} = +1.75$V. (b) 15x15 μm in-phase hole-bubble image at the same location at $\nu_{bulk} = 1.26$ (5.0T). A tip bias of -1.75V is chosen to produce an IR of the same diameter as in (a). (c) Composite image constructed from (a) and (b) with hole-bubble data in blue and electron-bubble data in red. Semi-transparent repeating ellipses are overlaid as a guide to the eye. (d),(e) Schematics illustrating local IR width modulation from disorder in (d) electron and (e) hole bubbles. The black marker and arrow indicate the location of a hotspot and direction of a fixed local density gradient. Colored arrows indicate the direction of the density gradient from the tip.

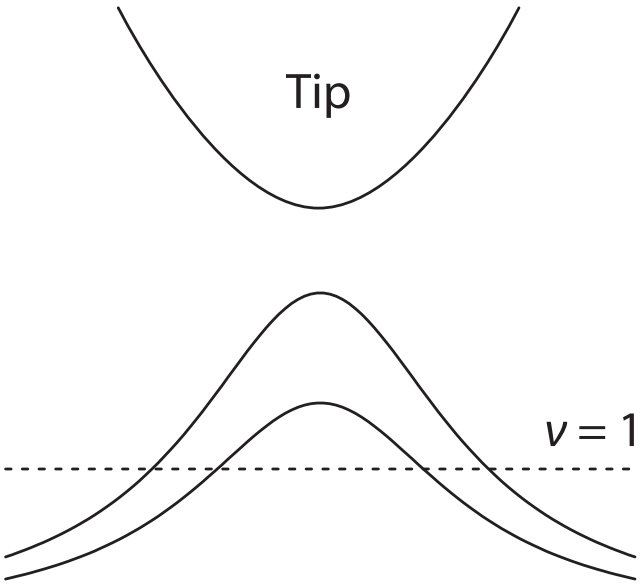

Figure 3-20: Applying a larger DC voltage to the tip does not necessarily increase the density gradient at the position of the strip because the point where the density crosses $\nu = 1$ also moves out to a larger radial position. For this example, we show two Lorentzian density profiles, one of which corresponds to a larger tip voltage than the other by a factor of 1.5.

the hole bubble image appears on the opposite side of the hotspot. This remarkable symmetry between the two images demonstrates that the partial ellipses arise from the influence of longer length-scale disorder.

3.9 Testing the quantum dot island model: Imaging with a large tip-induced density gradient

The evidence we have presented so far for the quantum dot resonance explanation of the hotspots has relied on the magnitude of the conductance enhancement and the observation of the Coulomb-blockade fringes. In the previous section, we showed that the partials rings arose from IR width modulations from disorder. Another possible explanation for the hotspots could involve an abrupt narrowing of the IR from similar density gradients. While this by itself would not explain the fringes, it would be consistent with our observation of partial rings.

One way to differentiate between these two models is to image with a much larger

density gradient from the tip. Experimentally, increasing the density gradient from the tip is not as simple as increasing the bias voltage on the tip. To see this, we examine figure 3-20, which shows the shape of a density profile we may expect from the tip perturbation. The density shown is flat directly under the tip and falls off with Lorentzian tails as we move out in the radial direction. Increasing the bias voltage will scale the entire curve. For any given radial position, this will increase the magnitude of the density gradient, but at the same time, the IR will increase in size, moving further out into the tail of the charge perturbations where the density gradients are shallower. Without a detailed model, we may expect that increasing the bias voltage may not narrow the strip, and could even make it wider. Simulations show that for the tips we use, these two effects cancel to a good approximation, and the width of the IR is independent of bias voltage. We can, however, increase the density gradient by moving to a magnetic field further from $\nu = 1$: to obtain an IR of the same size then requires a larger charge perturbation, leading to larger density gradients. Thus, in practice, the width of the IR is set only by the difference of the bulk filling factor from the integer value at which the IR is formed.

To image the resistance of a $\nu = 1$ IR with a steep density gradient from the tip, we work at a magnetic field that is far from $\nu = 1$. Figure 3-21 shows an in-phase charging image taken at B = 7.9T ($\nu = 0.68$) with a tip bias voltage of -2V. Remarkably, the images show several complete rings. This indicates that the tip gradients at these fields are indeed dominating the disorder gradients that produce the partial rings. It also rules out any explanation of the conductance enhancement that involves a local narrowing of the IR alone, since this would show at most half-rings.

The fact that we still see resonances in the images with such a large tip-induced density gradient also sheds light on the exact way that the disorder gradients affect the resonances. The electron-hole bubble symmetry discussed in section 3.8 demonstrated that the observation of partial rings was a result of local IR width modulations from disorder. It did not, however, determine exactly how these modulations were changing the resonant transport through the dot. In particular, two possible scenarios are shown in figure 3-22. In 3-22(a) and (b), the density gradients from the hotspot

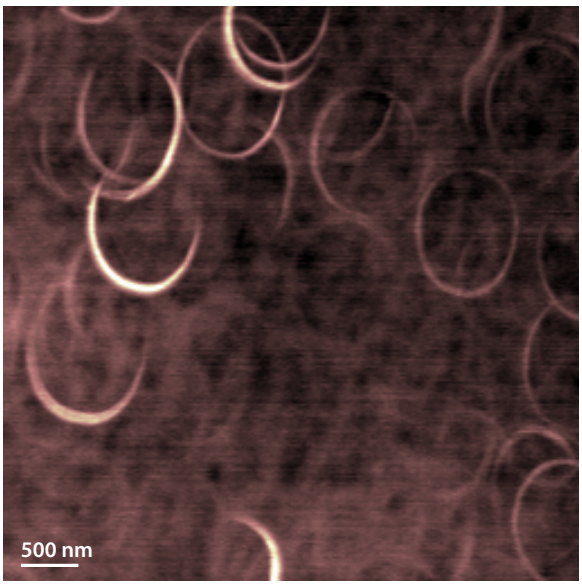

Figure 3-21: A $\nu = 1$ electron bubble image taken at 7.9T ($\nu = 0.68$) with a tip bias voltage of -1.75V. In this data, the density gradient from the tip creating the incompressible strip is large because we are far from integer filling. This large density gradient dominates over disorder gradients, resulting in the appearance of complete rings.

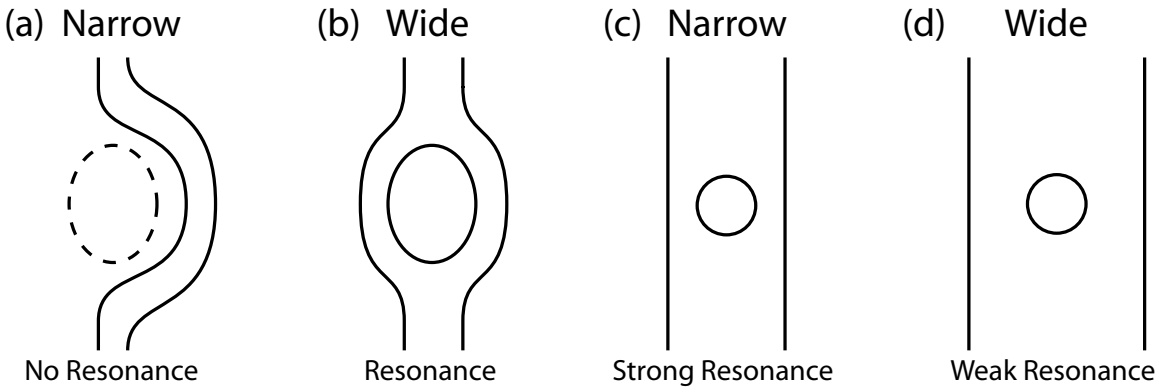

Figure 3-22: Possible ways that modulation of the local strip width could change the resonant conductance. In (a) and (b), the "hotspot" doesn't fit in the narrow strip, and we see resonance after widening of the strip. In (c) and (d), there is always an island inside the strip, but modulating the strip width changes the coupling to the island and the strength of the resonance.

fluctuation are weak compared to those from the tip. With a narrow strip, the fluctuation is too large to create an island that fits inside the strip, and instead only deforms the shape of the strip. With a wider strip and a shallower density gradient, the fluctuation can now create a quantum dot island. In this case, widening of the strip enhances the conductance. In the second scenario shown in (c) and (d), the strip is initially very wide. When the conductance is low, there is a quantum dot island inside the strip, but resonant conductance through the island is small due to the weak coupling. With a narrower strip, the dot is more strongly coupled to the bulk and the bubble leading to more current. In this case, local narrowing of the strip enhanced the conductance. The electron-hole bubble symmetry that we have observed does not distinguish between the two. The fact that we observe complete rings with large tip gradients demonstrates that it is narrowing of the strip that enhances the resonant conductance, suggesting a wide strip scenario such as shown in figure 3-22(c) and (d). Detailed simulations of incompressible rings in the presence of disorder will allow us to determine the microscopic details of how this occurs.

3.10 IRs at other filling factors

In the results presented so far, we have concentrated on the resistance of an IR formed at a local filling factor of $\nu = 1$. We can also study IRs at other filling factors by lowering the magnetic field. Figure 3-23 shows in-phase and lagging-phase images taken with ν =1,2, and 4 IRs at the same position. The IR formed from the $\nu = 2$ orbital Landau gap at 2.7T has a much higher resistance than the IR formed from the $\nu = 1$ exchange-enhanced spin gap at 5.4T. The $\nu = 2$ image shows nearly no signatures of active hotspots and the IR resistance is very high, as can be seen by the dark signal level in the lagging-phase image. Lowering the magnetic field to 1.35T, the IR resistance at $\nu = 4$ drops to a value comparable to but still higher than that at $\nu = 1$, and weak filaments are seen.

Our proposed model for the hotspots considers resonances through small disorder induced islands. Changing the magnetic field will not change the disorder-induced

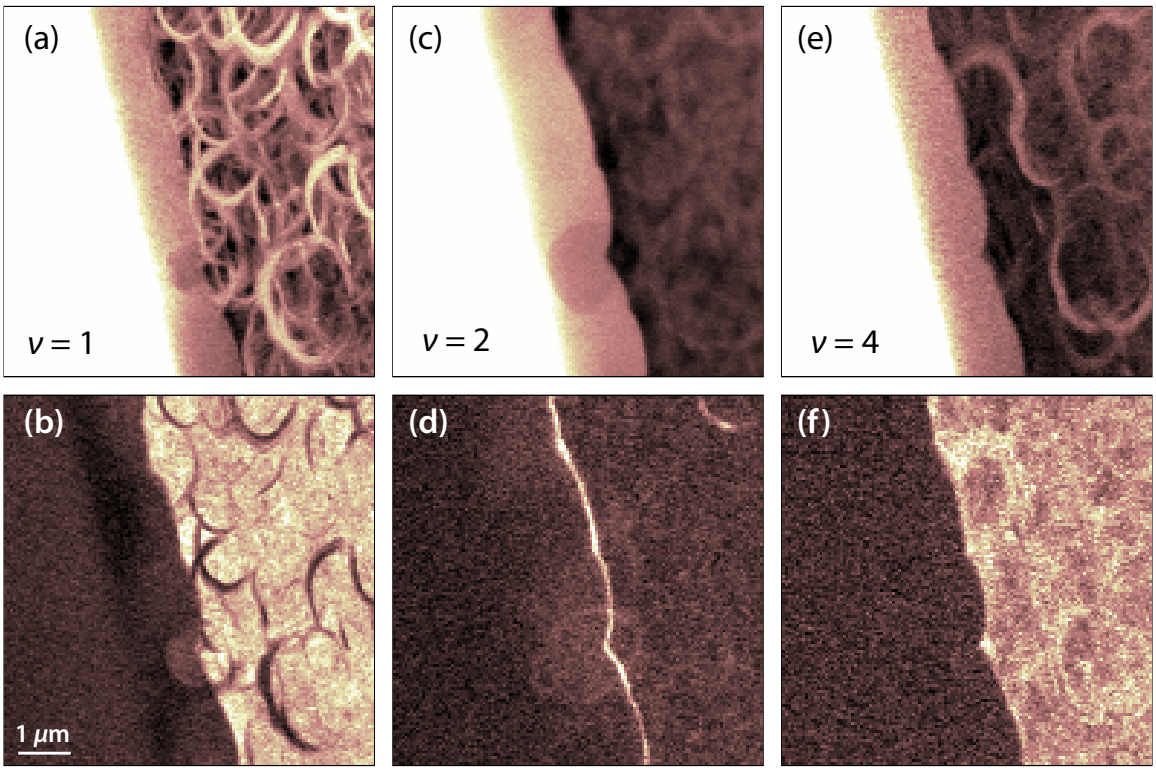

Figure 3-23: $7 \times 7\mu$m images of the IR resistance at different filling fractions taken at the same location. (a), (b) In-phase and lagging-phase charging images for a $\nu = 1$ hole bubble at 5.4T. The image shows many filaments. (c), (d) $\nu = 2$ hole bubble images taken at 2.7T. The IR has a very high resistance and only a faint sign of one resonance is visible in the top left of the lagging-phase image. (d), (e) $\nu = 4$ hole bubble images taken at 1.35T. The image now shows many resonances, although the overall IR resistance is still higher than at $\nu = 1$. In this sample, the IR at $\nu = 3$ was too leaky to be measured.

density profile, which is determined by charge fluctuations in the donor layer. Thus, we should in principle see the same hotspots at different filling factors. This is complicated by the fact that the IR has vastly different resistances at different filling factors, and so the number of "active" hotspots, where the IR resistance drops into our measurable range, varies significantly. This is clearly shown in figure 3-23, where many more arcs are seen in the $\nu = 1$ image. Figure 3-24 shows images taken at $\nu = 1$, 3 and 4 in a different sample, where the IR resistance at $\nu = 3$ was larger, allowing resonances to be resolved. Careful examination of the images shows that there is a good correspondence between the positions of active hotspots at different filling factors, supporting the disorder induced quantum dot model. Interestingly, the strongest hotspots at $\nu = 1$ are not necessarily the strongest seen at $\nu = 3$ and $\nu = 4$.

By measuring the tunneling resistance of the IR, we have a unique probe of the microscopic orbital and exchange-enhanced energy gaps in the quantum Hall system. The technique should also be applicable to IRs formed at filling factors of the fractional quantum Hall effect. Our samples typically show a weak signature of the $\nu = \frac{2}{3}$ state in the bulk magnetocapacitance measurements. Unfortunately, the IR at $\nu = \frac{2}{3}$ was much too leaky to be detected in our experiments. Lower temperatures and higher magnetic fields available in our next-generation microscope for the dilution refrigerator should allow us to study the microscopic energy gaps and transport in the fractional quantum Hall effect.

Another feature to be noted about images at lower filling factors is that the features in the images are generally "softer" (see in particular, figure 3-23(e)). Because of the reduced Landau level degeneracy at low magnetic fields, the magnitude of the density perturbation from the tip is smaller for an IR of the same size. Consequently, the density gradients from the tip creating the IR are much weaker, and are more easily perturbed by disorder, producing the softer images. At these lower fields, with large DC bias voltages we also sometimes observe two concentric arcs in the images that have the same center but very different diameters, indicating the presence of a "double ring" created by the tip where the density perturbation passes through two filling factors.

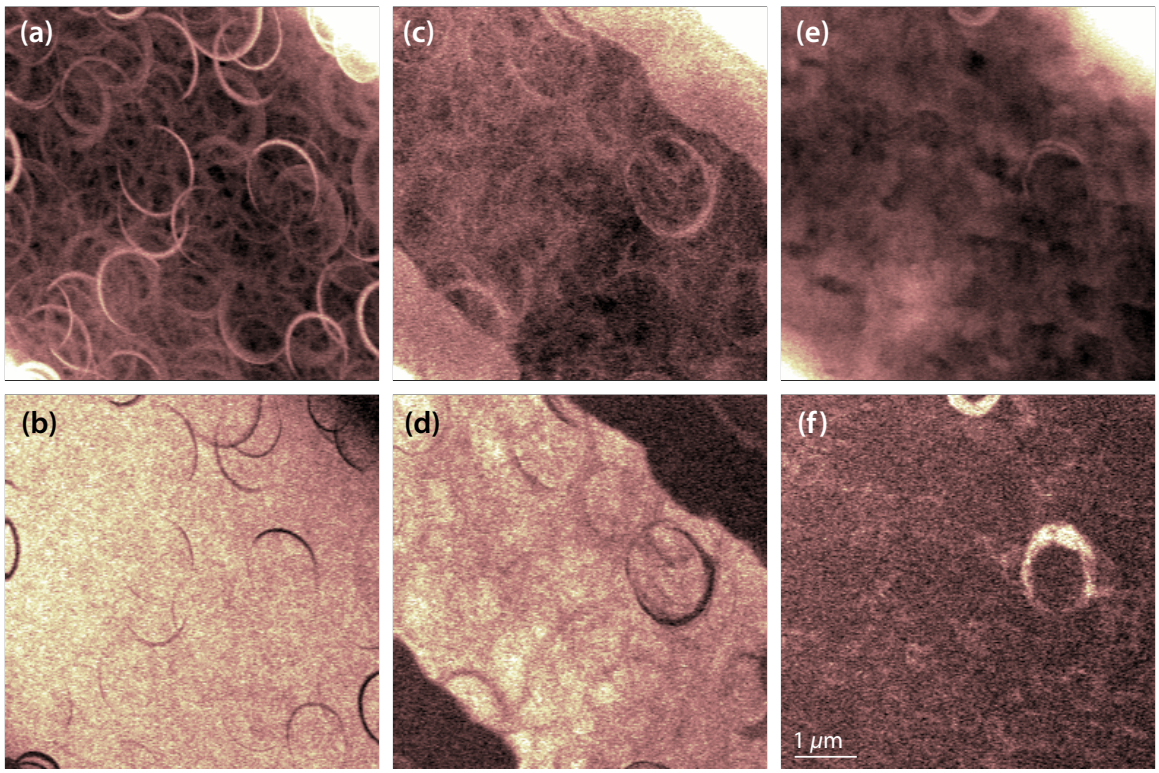

Figure 3-24: 6×6 μm images taken at the same position showing hotspots at the same locations. On this cooldown of a sample from 12-16-03.2, the IR was much more resistive for reasons that we do not understand. This higher resistance, however, allowed us to image at $\nu = 3$ where the IR had previously been too leaky. (a), (b) In-phase and lagging phase $\nu = 1$ hole-bubble images at B = 4.5T ($\nu = 1.2$). (c), (d) $\nu = 3$ electron-bubble images at B = 2.0T ($\nu = 2.75$). (e), (f) $\nu = 4$ hole-bubble images taken at B = 1.27 T ($\nu = 4.4$). The $\nu = 3$ and $\nu = 4$ images show far fewer resonances, but the positions of the hotspots correlate well with those seen in the $\nu = 1$ images.

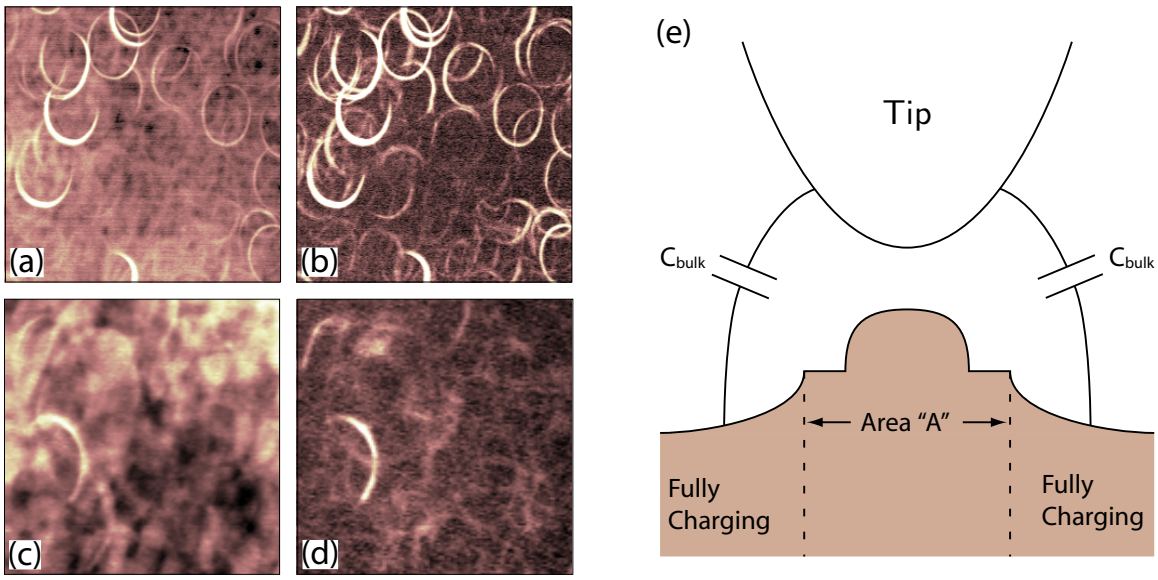

Figure 3-25: Images taken with highly resistive incompressible rings show a bumpy modulation of the in-phase signal with no corresponding change in the lagging phase signal. (a),(b) 5×5 μm in-phase and lagging-phase $\nu = 1$ electron bubble images at high magnetic fields (7.9T, $\nu = 0.68$). (c), (d) 5×5 μm $\nu = 2$ hole-bubble images taken at 2.4T ($\nu = 2.25$). (e) When the bubble is uncharging, the capacitance from the tip to the 2DES is reduced by the area inside the outer edge of the IR. Changes in the shape of the IR will result in changes of the capacitance from the tip to the fully charging region outside the ring, producing the observed bumpy modulation of only the in-phase signal.

3.11 Features of the uncharging bubble

For $\nu = 2$ IRs and the $\nu = 1$ electron bubble IR at high fields, the IR resistance is very large and the bubble does not charge for much of the area in the image. With such uncharging bubbles, two interesting effects are observed. The first is a "bumpy" modulation of the background in-phase charging signal, as shown in figure 3-25. This bumpy modulation is seen only in the in-phase signal: the dark background of the lagging-phase signal is completely flat. This suggests that this modulation is due to changes in the geometric capacitance to the 2D layer and is not associated with resistive effects.

This "bumpy" modulation arises due to changes in the area of the IR as we move it to different places in the sample. A model showing the capacitances of the tip to different regions of the 2DES is shown in figure 3-25(e). When the central bubble is

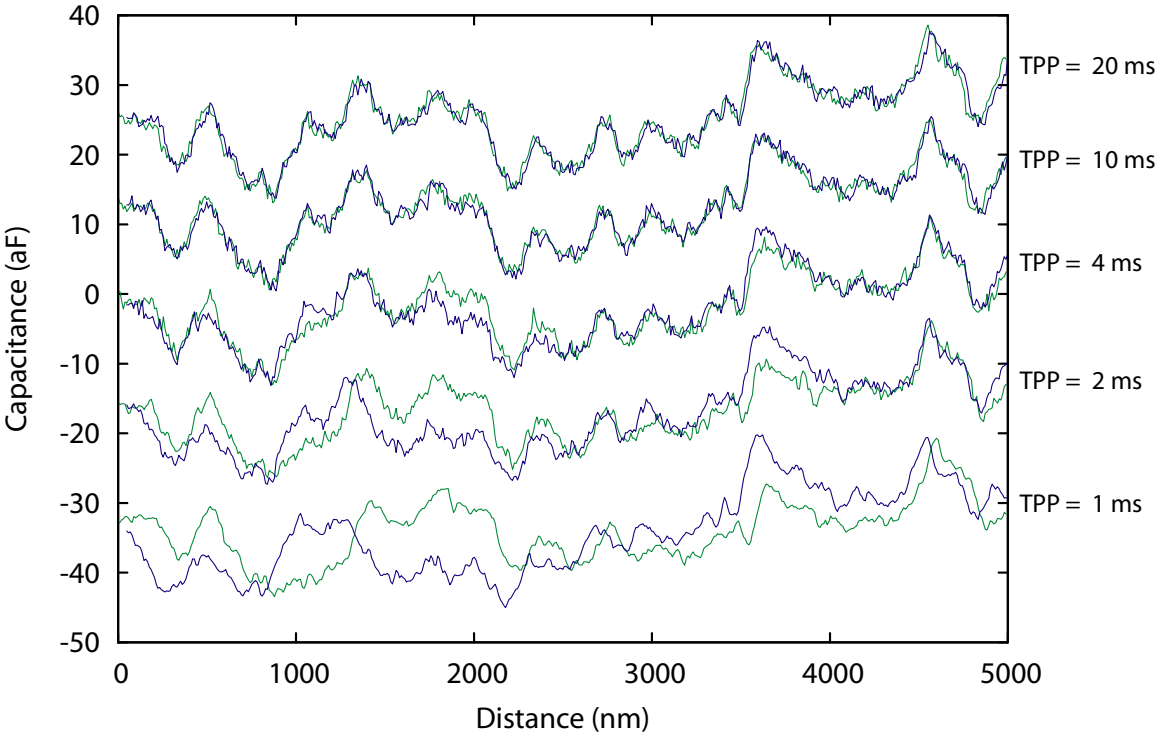

Figure 3-26: Line cuts through the bumpy modulation seen in the in-phase images showing strong hysteresis for a $\nu = 2$ electron bubble at 3.1T ($\nu = 1.68$). The two colors represent forward and reverse scans. The line cut was repeated at several different sweep rates. The sweep rate, in units of time per pixel, is quoted to the right of the plot (line cuts are 512 pixels long). The time constant on the lock-in was set at 500 μs. Curves with different sweep rates are offset for clarity.

uncharging, the capacitance from the tip to the 2D layer is reduced by an amount proportional to the area enclosed by the outer diameter of the IR. As we move the tip to different positions over the 2DES, the IR changes shape. A modulation of the in-phase charging signal results due to a change of the geometric capacitance of the tip to the outer fully charging 2DES.

With the very large IR resistances seen at $\nu = 2$, we also observe hysteresis in the bumpy modulation between the forward and reverse scans, as shown in the line cuts in figure 3-26. While a hysteric lag in the tip position is expected from piezoelectric scan tubes the differences shown in figure 3-26 are more than just a lateral offset, and consist of qualitatively different traces. Lowering the scan speed to 10 ms/pixel, the hysteresis disappears. This hysteresis is also connected to changes in the area of the IR. In order to change the area of the IR, we must transfer charge across it.

While this charge transfer is slow compared to our AC measurement frequency, it is usually fast compared to the scan speed of the tip ($\sim$ Hz). At $\nu = 2$, the IR becomes so resistive that this charge transfer is not fast enough to modulate the area of the bubble even at the slow timescales associated with the tip motion. The data in figure 3-26 show that the charging time of the bubble approaches a timescale of $\sim$ 10 ms. Using a bubble capacitance of 1 fF, this corresponds to a remarkable IR resistance of 10 TΩ. Very large incompressible strip resistances have also been observed in other experiements [124].

It is interesting to note as well that non-equilibrium charge on the bubble will result in an excess DC voltage across the IR. This transverse voltage will in turn induce a large circulating dissipationless current in the incompressible states in the IR. Thus, as we scan a bubble with a highly resistive IR quickly through the 2DES, a large local fluctuating magnetization will be induced.

3.12 Excitation Dependence

Most of the data we have presented so far were taken with AC excitation amplitudes of 10 to 15 mV. In the experiment the central bubble is only capacitively connected to ground, and the voltage appearing across the IR is smaller than the AC excitation through a capacitive "lever arm" reduction (see section 2.4). Our simulations show that the voltage across the strip is about 10 times smaller than the AC excitatino we apply to the 2DES, given a voltage drop of about 1 mV for a excitation 10 mV. We have also taken images using different AC excitation amplitudes, ranging from 2.5 mV to 30 mV. Experimentally, we observe that increasing the amplitude of the AC excitation decreases the resistance of the IR. If the IR has a very high resistance, it is possible that the variations of the IR resistance due to the hotspot resonances modulate the bubble charging times between values that are all outside of our range of sensitivity. In this case, increasing the amplitude of the AC excitation can allow us to decrease the bubble charging time, allowing us to see the effects from a larger number of hotspots. This is shown very dramatically in figure 3-27. The figure shows

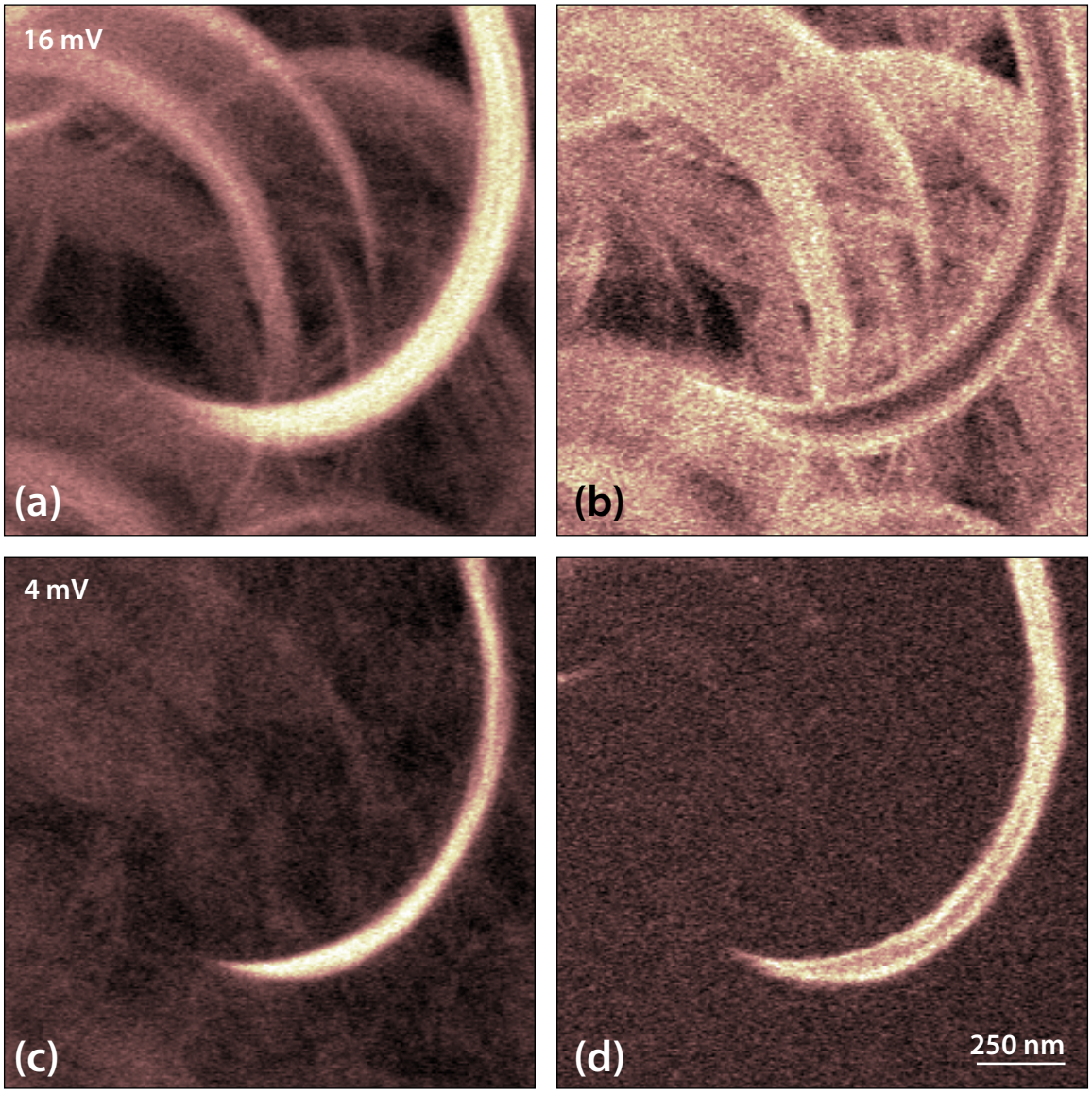

Figure 3-27: 1.5×1.5 μm hole bubble images taken at 4.5T ($\nu = 1.2$) in sample 12-16-03.2 showing an unusually strong excitation dependence. (a), (b) show in-phase and lagging-phase images taken with a 16 mV excitation. The averaging time for the image was 17 minutes. (c), (d) show in-phase and lagging phase images taken with a 4 mV excitation. In order to obtain a signal to noise ratio comparable to the 16 mV images, the 4 mV images were averaged for 5 hours and 52 minutes.

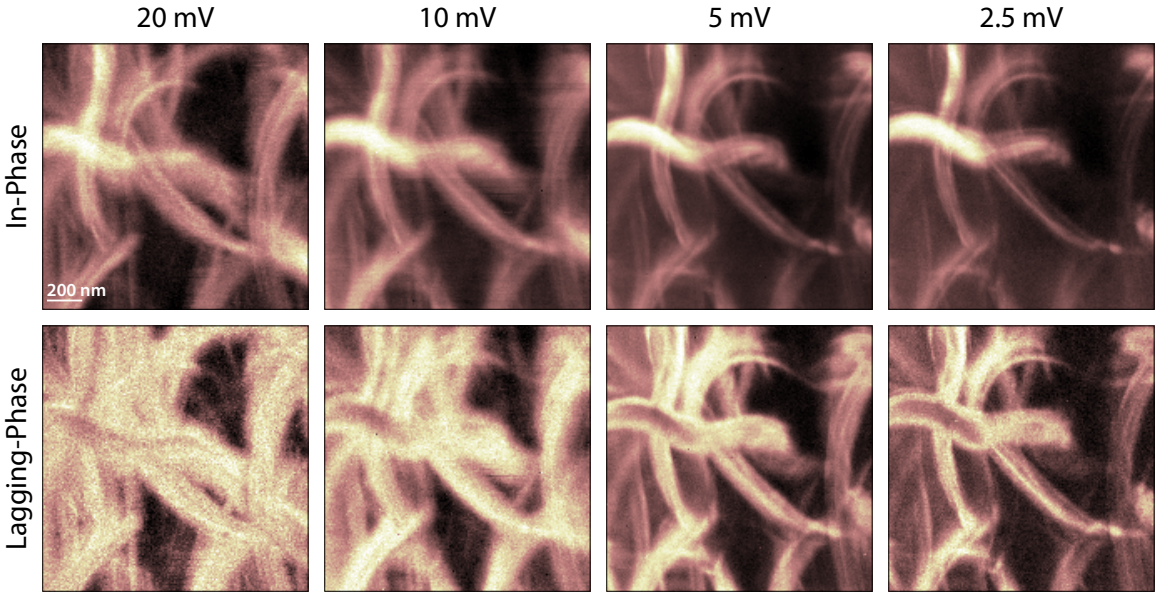

Figure 3-28: 1.5×1.5 μm electron bubble images taken at 6.9T ($\nu = 0.9$) with varying excitation amplitudes. The averaging times for each of the scans was adjusted to give roughly the same signal to noise. These images were taken with a tip that was blunted *in-situ*, resulting in filaments that were irregularly shaped.

the in-phase and lagging-phase images from a $\nu = 1$ hole bubble IR at 4.5T in sample 12-16-03.2. For an unknown reason, the IR in this sample on the second cooldown had an unusually large resistance. Because of this high resistance, the images showed far fewer active hotspots than in the previous sample (12-1-03.2), or even the same sample on a different cooldown. At 16 mV, the hole-bubble images shows a relatively high density of active hotspots. Decreasing the excitation to 4 mV, the images show far fewer resonances. Remarkably, however, the strongest hotspot still shows a strong resonance at 4 mV in which the conductivity is still modulated by four orders of magnitude. A careful inspection of the 4 mV images also shows faint signatures of many of the other resonances seen in the 16 mV images.

The strong excitation dependence shown in figure 3-27 was not seen in all of our cooldowns, and in particular was not seen in earlier experiments where we studied the excitation dependence. Figure 3-28 and 3-29 show the excitation dependence of electron bubble and hole bubble images respectively in sample 12-1-03.2. In these images, decreasing the excitation amplitude did decrease the IR resistance but did not affect the number of resonances that were observed. Since the hole bubble is quite

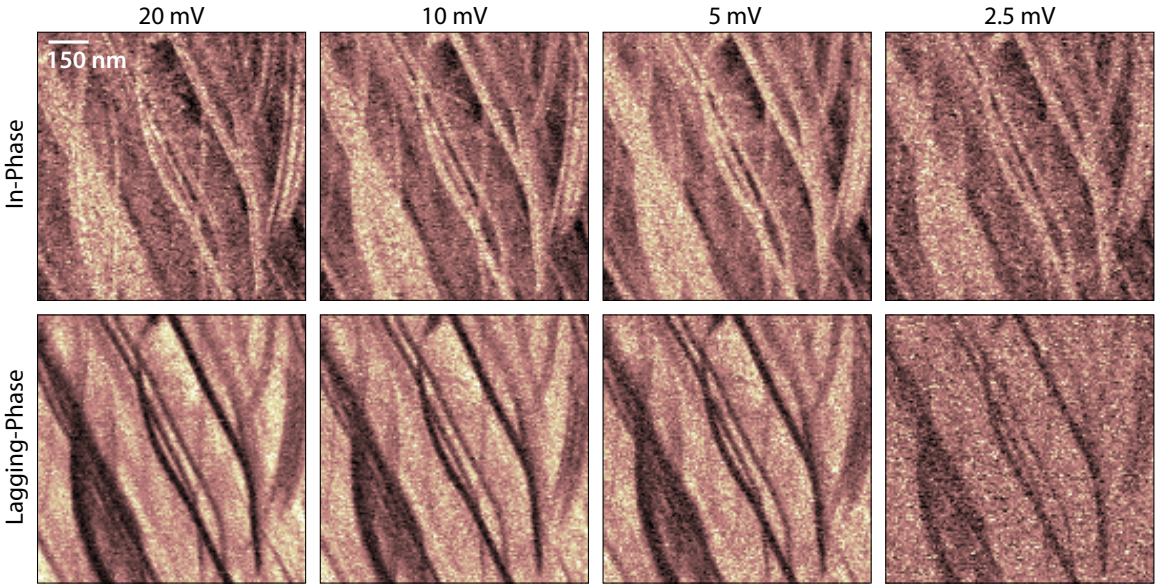

Figure 3-29: 1×1 μm electron bubble images taken at 6.9T ($\nu = 0.9$) with varying excitation amplitudes. For these images, the averaging time at each excitation was the same. These were taken with the same tip as in figure 3-28.

leaky, the resonances in figure 3-29 show up more strongly in the lagging-phase than in the in-phase images. Also, it is interesting to note that the signal to noise does not decrease upon decreasing the excitation until we reach the 2.5 mV images. The reason for this is that in addition to increasing the total amount of charge induced on the bubble, increasing the excitation also decreases the IR resistance, pushing the charging times to lower frequencies. This results in less modulation of the charging signal. This is shown more clearly in bias sweeps with the tip at a fixed position shown in figure 3-30.

The effect of the AC amplitude on the IR resistance is also seen in the uncharging bubble hysteresis discussed in section 3.11. Increasing the amplitude of the AC excitation in these experiments caused the hysteresis to disappear, suggesting that the AC excitation is reducing the IR resistance even when no hotspot resonances are seen.

As discussed in detail in section 2.4, for an uncharging bubble the AC excitation translates into an AC voltage across the IR. The voltage across the IR in the fully uncharging bubble limit is determined by a capacitive divider. Note, however, that

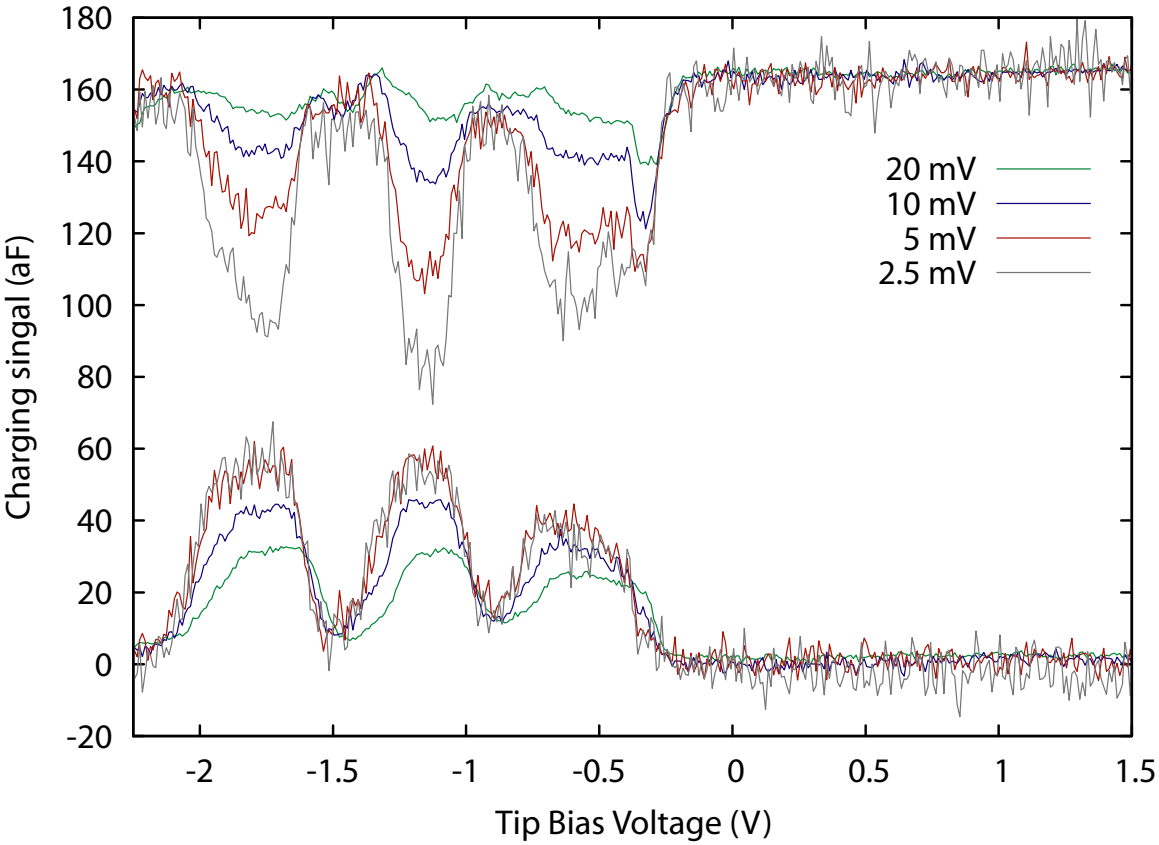

Figure 3-30: Excitation dependence of a hole bubble bias voltage sweep at 5.5T. For the measurement, the tip was positioned at the center of the scans shown in figure 3-29. The three peaks in the bias sweep are associated with the three filaments at the center of the images moving past the fixed position of the tip as we change the bias voltage. The data shows the calibrated signal, where the lock-in signal has been scaled by the sensitivity to account for the varying AC excitation. Increasing the excitation voltage decreases the IR resistance, resulting in different in-phase and lagging-phase signals.

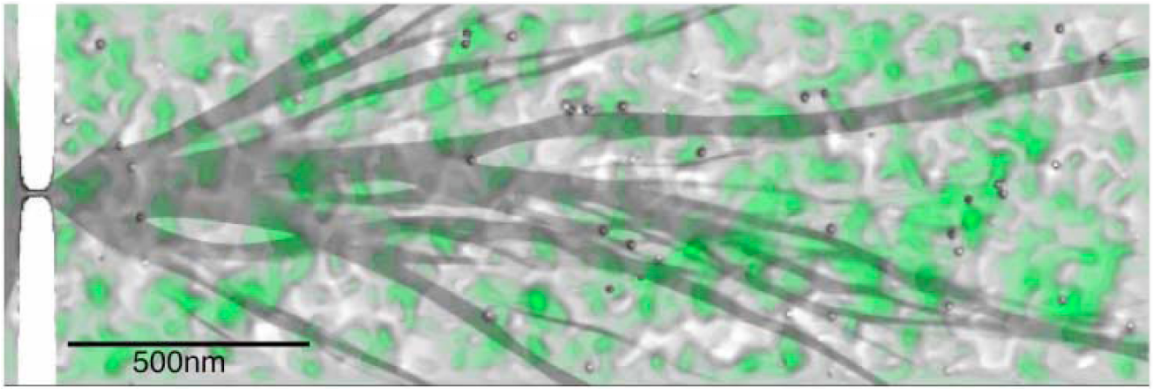

Figure 3-31: A simulation of the electron flow in a high mobility heterostructure. The accumulation of small angle scattering from the weak short length-scale disorder results in caustics in the electron trajectory. Reproduced from Topinka *et al.* in Nature **410** 183 (2001) [125].

if the IR resistance drops, the bubble begins to charge, and the voltage drop across the ring is reduced. In practice, the means that the voltage appearing across the IR due to the AC excitation in our experiment is in some sense "self regulating": on resonance, it automatically adjusts itself, becoming pinned to the value that is required to activate the hotspot. The maximum value it can adjust itself to is set by the capacitive lever arm from the uncharging bubble limit. Thus, the effect of increasing the AC excitation is to increase the maximum range of this self-regulating voltage, allowing us to observe resonances from a larger number of hotspots.

3.13 Hotspots are not "defects"

It is important to emphasize that we believe that the hotspots are not simply "defects" in a 2DES that has an otherwise smooth potential. In particular, the density of hotspots shown in images such as in figure 3-11 is far too high to be associated with impurities arising from background doping in a sample with as high a mobility as ours. Furthermore, different filaments in the images show resonant conductance enhancements that vary over orders of magnitude suggesting they are not associated with an impurity of fixed strength.

We propose that the hotspots arise from length-scale fluctuations that arise natu-

rally in high mobility heterostructures with remote ionized donors. This same disorder was considered recently in the context of experiments mapping electron flow out of a point contact using a scanning gate [125]. The effect of disorder on electron flow at zero magnetic field is illustrated in figure 3-31, which shows a simulation of electron flow out of the point contact in their experiment. The disorder shows both short length-scale fluctuations, on the scale of the setback to the donor layer, as well as longer length-scale hills and valleys, which can be seen as large gray and green areas. Remarkably, the electron flow is dominated by the small angle scattering from the short length-scale disorder: in several places, the electron flow is concentrated over the top of one of these longer length-scale "hills". At zero magnetic field, these short length-scale fluctuations lead only to small angle scattering and smooth branching electron flow [125] because the amplitude of the fluctuations ΔU is small compared to the Fermi energy E_F. In stark contrast, our work shows that at high magnetic fields these weak short length-scale fluctuations have a drastically different effect, creating Coulomb blockaded islands that enable resonant transport of charge across ISs.

3.14 Summary

In summary, we have observed strong resonances in transport across ISs. Using local imaging, we have determined that these resonances arise from the intersection of the strip with fixed positions in the 2DES and are associated with the formation of a small quantum dot island embedded in the incompressible region. These islands are created by disorder, and imaging transport through them allows us to infer the nature of the disorder in the 2DES, as shown in figure 3-32. On small length-scales ($\sim$100 nm), significant disorder exists, creating the islands in the IR. Fluctuations on an intermediate scale are responsible for our observation of only partial rings in the images. On larger length-scales ($\sim$1 um), the amplitude of the disorder fluctuations is relatively small, as evidenced by the uniformity of the size and shape of the rings in the images.

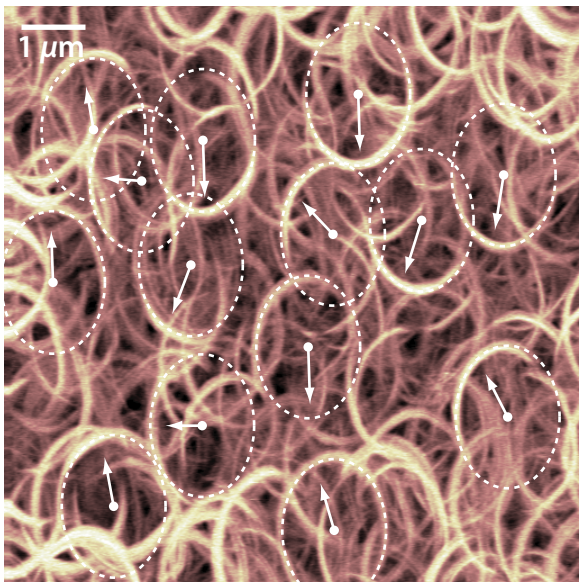

Figure 3-32: The arcs we see in the images can be thought of as a vector feild describing disoder in the 2DES: the centers of each arc shows the position of a hotspot fluctuation and the direction of a longer lenthscale fluctuation is described by an arrow pointing to the strongest portion of the arc. The smooth and repeating shape of the arcs suggests that the amplitude of large lengthscale fluctuations is relatively small.

Finally, the quantum dot islands created by the disorder have a dramatic effect on charge transport across ISs. They provide at least 10 000 times the conductance of tunneling directly across our IR, or equivalently, the same conductance of an ideal IS that is more than 3 cm long. Their presence opens a conduction channel that dominates all transport across narrow incompressible regions. This observation is in agreement with ideas presented by Cobden *et al.* [119] for the origin of fluctuations observed in narrow devices. Moreover, the impressive magnitude of the conductance enhancement suggests that this resonant tunneling may act as the fundamental mechanism for transporting charge through the network of ISs in large samples, mediating hops between larger compressible islands, as illustrated in figure 3-33. Such modifications to hopping transport by resonant states have been considered in the case of the disordered low density electron gas in MOSFETs without a magnetic field by Popović *et al.* [126]. They found that although the number of such resonant hopping paths are orders of magntitude fewer than direct hopping paths, the conductivity of the resonant hopping paths are orders of magnitude higher, suggesting them as an

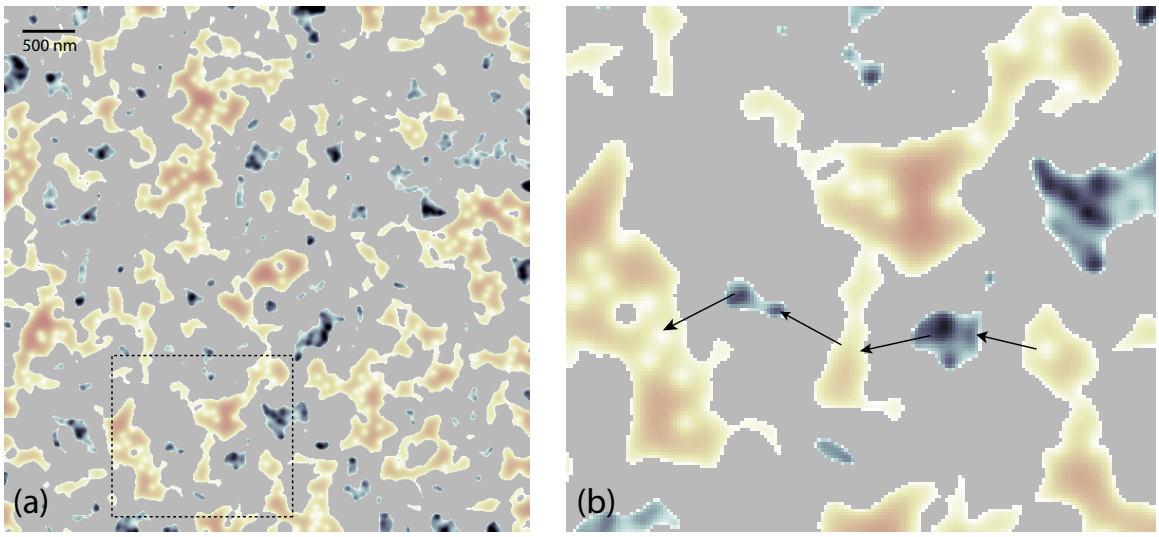

Figure 3-33: (a) The electron density profile at $\nu = 1$, showing the localization of electrons in the bulk by a percolating network of incompressible strips. Blue, gray, and pink areas correspond to local filling factors $\nu > 1$, $\nu = 1$, and $\nu < 1$ respectively. The simulations show large compressible islands that are often separated by small quantum dot sized islands, which could act as stepping stones for transporting charge through the incompressible bulk. (b) A zoom of the area shown in the dashed box in (a). The arrows indicate a preferred hopping path whose conductance could be dramatically enhanced by resonant tunelling.

important part of the transport. To our knowledge, such a resonant tunneling mechanism has not been considered in theories describing transport around ρ_{xx} minima in the quantum Hall effect.

Chapter 4

Measuring the Capacitance of the 2DES to a Fixed Metal Pad

4.1 Motivation

In the experiments discussed in chapter 3, we imaged remarkable resonances in the transport across an incompressible strip by measuring the charging of a central bubble created by a bias voltage on our scanning probe. The ability to move the induced IR by scanning the tip was crucial in determining the microscopic origin of the resonances. The use of the scanning probe microscope, however, places some limitations on the measurements we can perform. Due to arcing between the high voltage quadrants of the piezo tubes at intermediate ^{3}He pressures, it is not possible to run the experiment in the Heliox system at temperatures other than the base temperature of 300 mK, and thus it is not possible to study the temperature dependence of the features. Furthermore, due to the random drift in the sample-tip separation, which can be as large as 20 nm over a period of a few hours, the SCA microscope must be continually interactively monitored to ensure that the tip does not smash into the surface. This is very time intensive, and means that the experiment cannot be left alone to run overnight or for multiple days.

To overcome these problems, we came up with the following idea. In the SCA microscope experiment, the signal to noise ratio in the images increased indefinitely

with the size of the tip: the ultimate signal to noise would be obtained with a very large central bubble, producing an enormous variation in the charging signal. Since we now understand the origin of the resonances, we could replace the movable tip with simply a large metal pad on the surface of the sample. The idea is that this pad would be patterned in the middle of the sample and we would contact it with a wire bond. The experiment would be very similar to those performed by Zhitenev *et al.* [114], except that we would not be measuring charging from the edge of the sample, but instead from the compressible bulk, as we do in the scanning experiment.

Experimentally, the large size of the pads that are required so that we can wire bond to them should not present a problem, as such resonances were observed in the earlier experiments with pad capacitances as large as 1 pF ($7 \times 170\mu$m area). The large capacitance of the central region should also significantly help our ability to measure the lower resistance of weaker incompressible strips, such as those at $\nu = 3$. Since there are no high voltage arcing issues, we will be able to study temperature dependences, and the lack of sample-tip drift will allow unattended operation. Finally, the experiment will be compatible with our dilution refrigerator, allowing us to work at much lower temperatures and much higher magnetic fields, opening up the possibility of studying the resistance of incompressible strips at fractional filling factors.

4.2 Experimental Setup

Because we are using large features, we decided to use a transparency mask that we made using a photoplot process. This process is fast and very inexpensive ($40 for a 8x10 inch sheet). The photoplot process provides a incremental feature resolution as small as 1 micron, but is limited to a minimum feature size of 8 microns. For the pattern, we chose a selection of circular discs of different sizes, as well as a selection of rectangles of different sizes at different orientations. These are shown in figure 4-1(a). The choice of rectangles was chosen in mind of the possibility of observing charging features from anisotropic behavior of the 2DES, such as seen in the stripe phase of

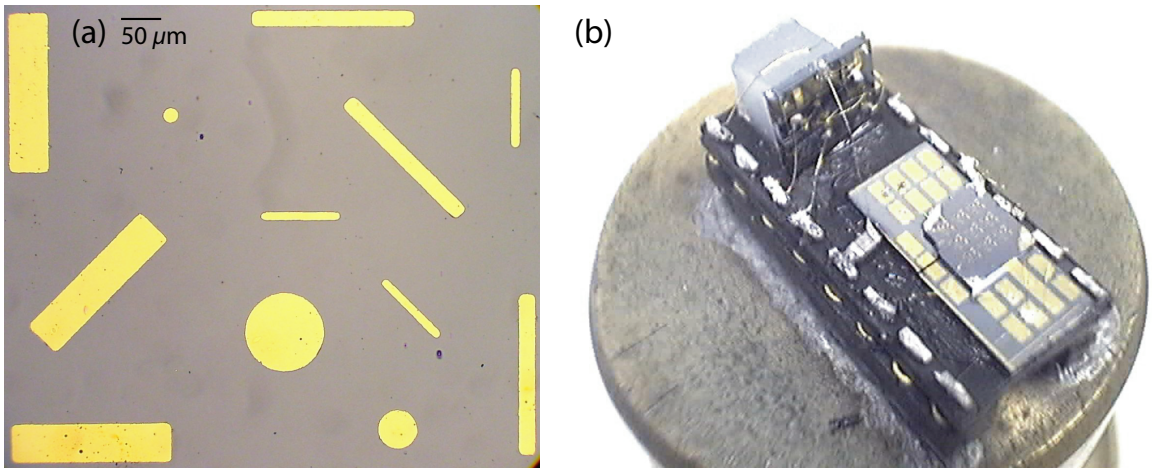

Figure 4-1: Pictures of the sample used for the magnetocapacitance experiment. (a) Pictures of the pads under an optical microscope. We patterned discs with diameters of 20 μm (0.3 pF), 50 μm (2.0 pF), and 100 μm (7.9 pF), as well as 10×100 μm (1 pF) 20×200 μm (4 pF) and 50×200 μm (10 pF) rectangles. (b) A picture of the sample on the DIP socket with the reference capacitor and the vertically oriented transistor mount.

the quantum Hall liquid [127, 128]. The pads ranged in capacitance from 0.3 to 10 pF.

For the amplifier, we used a vertically oriented transistor mount on the dip socket with 3 FHX35X transistors in parallel for amplification. The biasing was provided by an uncleaved FHX35X transistor used as a variable resistor. A 10 pF reference capacitor was included as well, although the background capacitances were small enough that nulling of the capacitance bridge was not necessary. The sample mounted on the DIP socket is shown in figure 4-1(b).

Compared to the scanning experiment, the "central island" in this experiment is much more strongly coupled to ground through the capacitance to the pad. A much smaller excitation was used to prevent the possibility of large voltage across the incompressible strip. Because of the enormous signal to noise provided by the design, this did not prove to be a problem. We measured with excitation voltages ranging from 10 μV to 300 μV. No excitation dependence was observed in this range.

One of the most challenging problems we had was with the adhesion of the pads to the surface of the sample. This has always been proved a problem with GaAs,

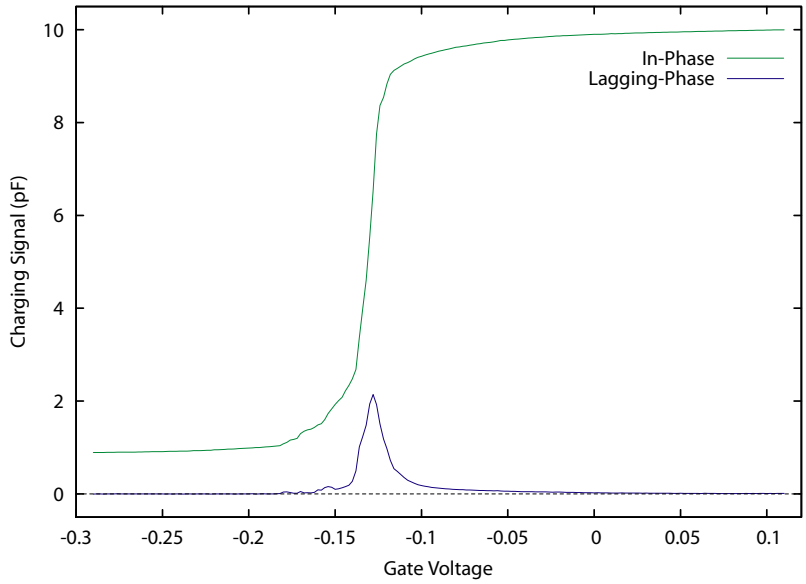

Figure 4-2: Charging signal as the area under the pad is depleted at zero magnetic field. As the sample is depleted, the capacitance to the 2DES drops. At the same time, the resistivity also diverges, leading to a lagging phase signal. The depletion curve is not completely smooth: it contains several steps that are often associated with features in the lagging phase signal. Such features were seen in the depletion curves of multiple pads.

and many of our pads pulled off during the wire bonding process. Fortunately, some of the pads showed good enough adhesion to wire bond to without pulling off the metalization.

4.3 Measuring the Charging Signal

The first measurement we performed was to look at the charging signal as we depleted the region under the pad. Such a measurement taken at zero magnetic field is shown in figure 4-2. As the sample depletes, the capacitance from the pad to the 2DES begins to drop. At the same time, the sheet resistance of the 2DES also increases, producing a lagging-phase component of the charging signal. Interestingly, the lagging phase signal shows a multiple peak structure. Such a multiple peak structure has been observed in all three pads we have measured.

The in-phase charging signal as a function of magnetic field and gate voltage is shown in figure 4-3(a). A cartoon showing the meaning of different regions of the

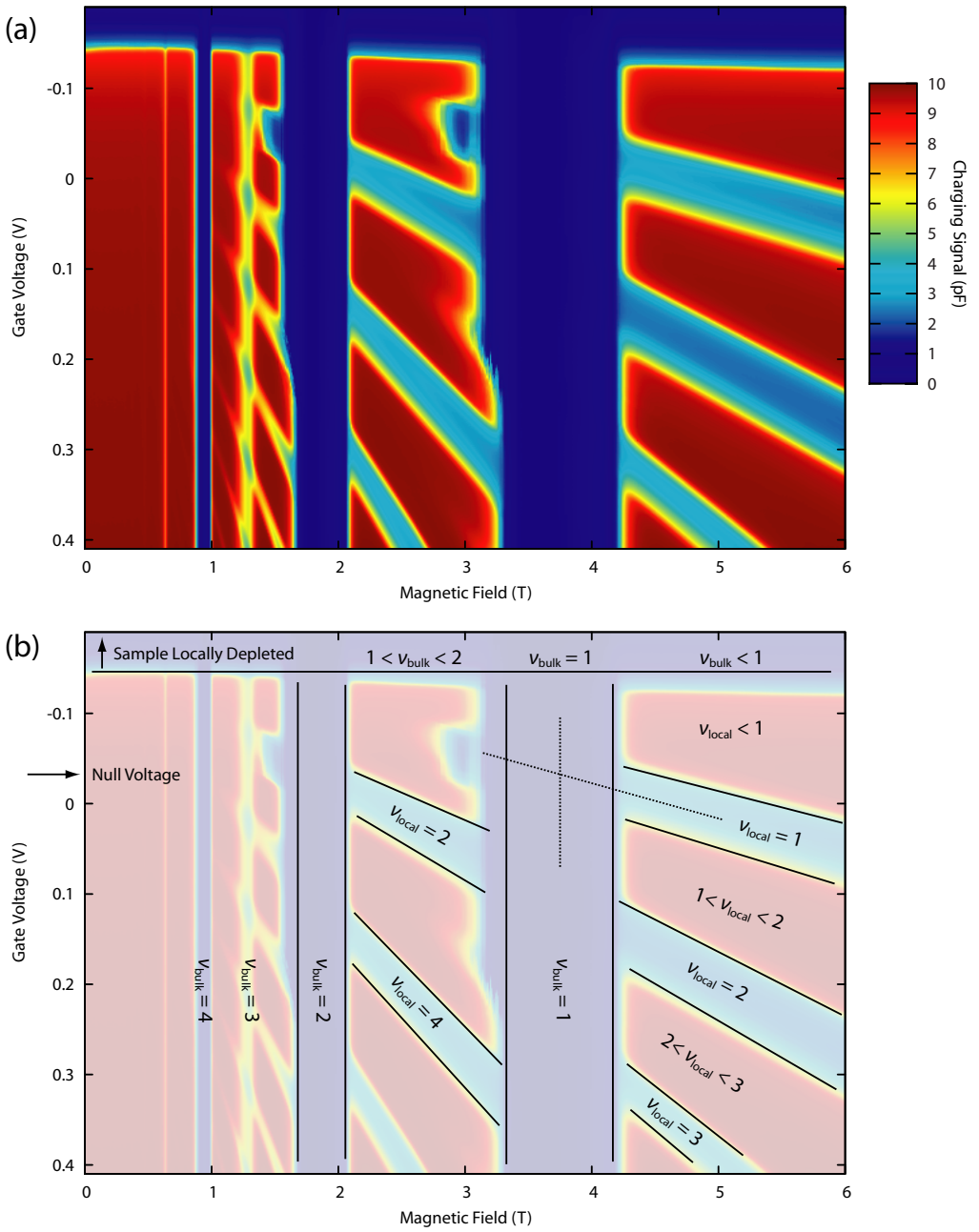

Figure 4-3: (a) A plot of the in-phase charging signal as a function of gate voltage and magnetic field. (b) A cartoon illustrating the meaning of different regions in the plot. The dashed lines intersect indicated the centers of the $\nu_{\rm bulk} = 1$ and $\nu_{\rm local} = 1$ features. They intersect at the gate voltage that nulls the contact potential between the gate and the 2DES. In this sample, the density under the gate is slightly enhanced. Remarkably, the incompressible ring formed around the area under the pad when the local and bulk 2DES are at different filling factors does not present any significant resistance to charging the area under the pad.

bias-field plot is shown in figure 4-3(b). The vertical features in the plot correspond to magnetic fields where there is a filled Landau level in the bulk of the sample. In these regions, the conductivity of the bulk vanishes, and the entire 5x5 mm area of the sample stops charging. Outside of these regions, the bulk of the sample is compressible and its conductivity σ_{xx} is high, allowing charge to travel from the ohmic contacts to the edge of the gate with little resistance.

In the regions where the bulk is compressible, we observe drops in the charging signal that follow sloping lines corresponding to having a filled Landau level in the local gated region under the pad. The voltage that nulls the contact potential between the 2DES and the metal gate can easily be read off the plot from where the ν_{bulk} and ν_{local} intersect, as shown in figure 4-3(b).

One of the remarkable features of the data is that we observe no evidence of a large resistance from the IS strip that separates the gated region under the pad from the bulk when they are at different filling factors. This was initially quite surprising. However, there is a very significant difference between the IS we have created here and that we created in the scanning experiment. Specifically, since the gate metalization is very close to the 2DES, the density gradient created by the gate is much steeper than that created by applying a voltage to the conical tip. This means that the IS created by the gate is much narrower than that produced by the tip. Our observations suggest that such narrow ISs do not show the large resistance we observed in wider strips in the SCA experiments.

As discussed in section 3.9, the IS strip width, to a good approximation, depends only on the magnetic field. Specifically, increasing the bias voltage on the gate at a given field increases the density perturbation, but does not change the strip width because the strip also moves further away from the gate. Thus to measure transport across a wide incompressible strip, we need to measure at a magnetic field closer to where there is a filled Landau level in the bulk. However, since our pad capacitance is so large, the vanishing conductivity of the bulk limits how close we can get to integer filling before we lose the charging signal.

In the experiment of Zhitenev *et al.*, one of the sides of the gated region ran along

the edge of a mesa etched in the sample. This allowed them to charge the gated region from one of the compressible edge channels even when the bulk was incompressible. With this advantage, they were able to probe much wider incompressible strips that displayed a large resistance, and also to observe the effects of the resonant enhancement of transport across the strip from the hotspots we imaged in the scanning experiment.

4.4 Measuring Oscillations of the Density of States

The fact that the incompressible strip around the edge of our pad has a very low resistance turns out to have some interesting consequences. In particular, it happens that our experiment is particularly well suited to measuring the quantum density of states contribution to the capacitance of the 2DES.

Capacitance was recognized very early on as a probe of the density of states in some of the first experiments on the 2DES in silicon MOSFETs [129, 130]. At the time, however, it was not correctly recognized that the charging signal as measured in these AC experiments is also significantly affected by the diagonal conductivity σ_{xx} of the layer. This fact was brought to light later by Goodall *et al.* [91]. Their measurements in a silicon MOSFET showed that in these samples, the drop in the measured charging signal that occurs when there is a filled Landau level could be accounted for entirely by a model that included *only* variations of the conductivity of the layer. The signals they observed were strongly frequency dependent: going to extremely low frequencies (9 Hz), the drops that they observed in the in-phase component of the charging signal showed no observable oscillations above the noise limit of their experiment. So dramatic was this effect that it led them to wrongly conclude that capacitance measurements are incapable of measuring the density of states correction that was suggested by earlier work, and can only be used to probe the conductivity σ_{xx}.

The situation was clarified in an experiment by Smith *et al.* [74]. They pointed out that the quantum density of states correction can indeed be measured in ca-

pacitance measurements provided that the measurement is made at sufficiently low frequencies that conductivity effects can be ignored. In particular, it is important not only to work at lower frequencies, but also to use higher mobility samples with less electron scattering. In order to achieve this, they measured the capacitance of a 2DES in a GaAs/AlGaAs heterostructure that had a much larger mobility than the Si MOSFET devices. By working at very low frequencies (20 Hz) with much higher quality samples, they observed oscillations of the DC capacitance signal at low magnetic fields corresponding to $\nu > 10$. At these fields, the signal showed no lagging phase component, and they were able to directly extract the Landau level density of states from these low field oscillations. At magnetic fields higher than 1.6T, the layer became too resistive and conductivity effects started to dominate over the quantum oscillations. Thus, the observation of quantum oscillations in the density of states is possible using capacitance measurements as long as conductivity effects can be minimized.

It turns out that our experiment is very well suited for the observation of these quantum capacitance oscillations because our sample has exceptionally high mobility and because the area of the pad we are probing is very small. The mobility of our sample is at least 20 times higher than in the experiments of Smith *et al.* (7×10^6 cm^2/Vs vs. 3×10^5 cm^2/Vs), and the capacitance of the pads we are using are at least 20 times smaller. The mobility of the sample likely plays a very important role in our ability to measure these quantum oscillations. Higher mobility samples such as ours display much narrower Hall plateaus, indicating a higher conductivity σ_{xx} in quantizing magnetic fields, and show qualitatively different transport scaling properties than lower mobility samples [42]. At the same time, the lower level of disorder reduces inhomogeneous broadening of the the Landau level density of states [48].

The combination of much higher sample mobility with smaller pad capacitances has allowed us to measure the effects of the density of states contribution to the capacitance in large quantizing magnetic fields. Figure 4-4(a) and (b) show the in-phase and lagging-phase components of the charging signal taken at 1 kHz from 4

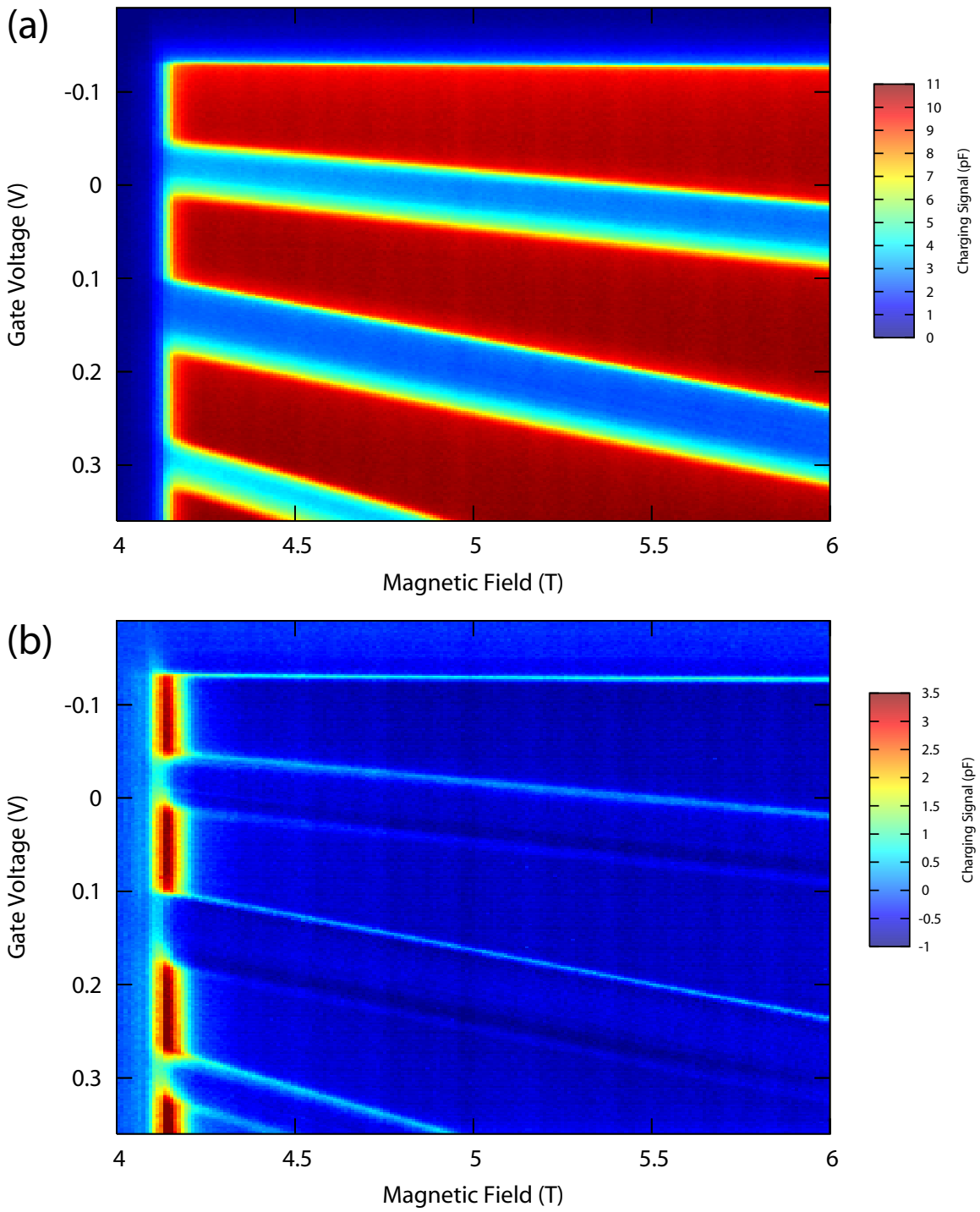

Figure 4-4: In-phase (a) and lagging-phase (b) data taken at 1 kHz. Remarkably, for $\nu_{\text{bulk}} < 1$ ($B > 4.2$T), the lagging phase signal is very small in magnitude when the bias voltage is swept so that the local area under the pad is at integer filling. This small lagging phase signal implies that the large drop seen in the in-phase signal contains a significant contribution from the density of states.

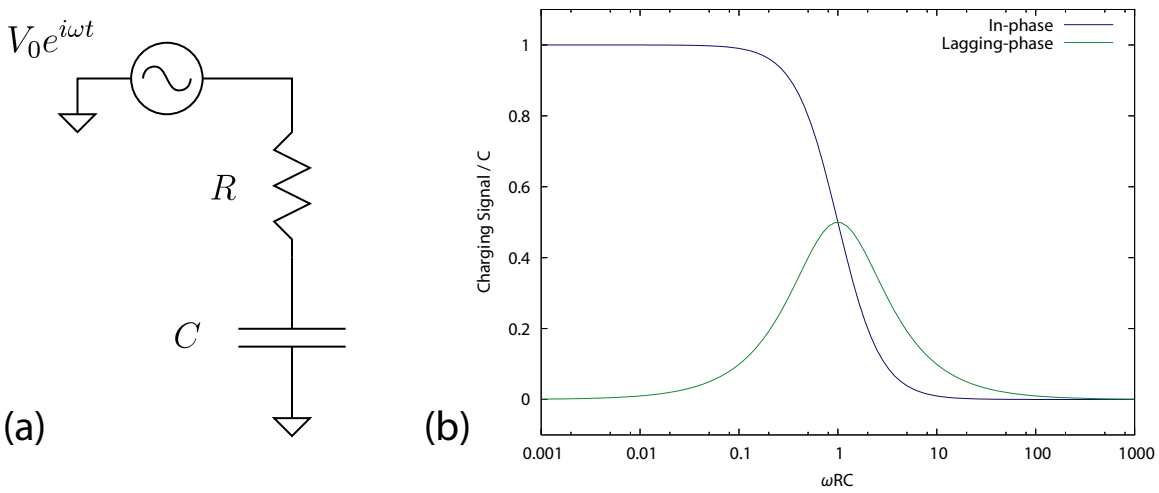

Figure 4-5: (a) RC charging model. (b) In-phase and lagging-phase components of the charging signal. Note that that lagging-phase signal reaches a peak magnitude that is equal to half of the change in the in-phase signal.

to 6T. At fields higher than 4.2T, the bulk is compressible and the features in the plot are associated with the charging of the local area under the pad. As discussed in earlier sections, we observe a large drop in the in-phase charging signal when the local density under the gate corresponds to a filled Landau level. What is quite remarkable, however, is that this drop is *not* associated with a large lagging phase signal. At some places, there is a peak in the lagging-phase signal, but what is notable is that the magnitude of this lagging-phase peak is very small compared to the magnitude of the the change in the in-phase component of the charging signal. This small magnitude of the lagging-phase signal implies that the variation of the charging signal is not purely of resistive origin, but also contains a significant contribution from the quantum density of states correction to the capacitance.

The expected relationship between the in-phase and lagging-phase signals can be demonstrated most easily in an RC model of the charging. In charging a capacitor C through a resistor R, the in-phase and lagging phase components of the charge on the capacitor plate are given by:

$$\mathrm{Re}(Q^*(\omega)) = \frac{CV_0}{1+(\omega RC)^2} \tag{4.1}$$

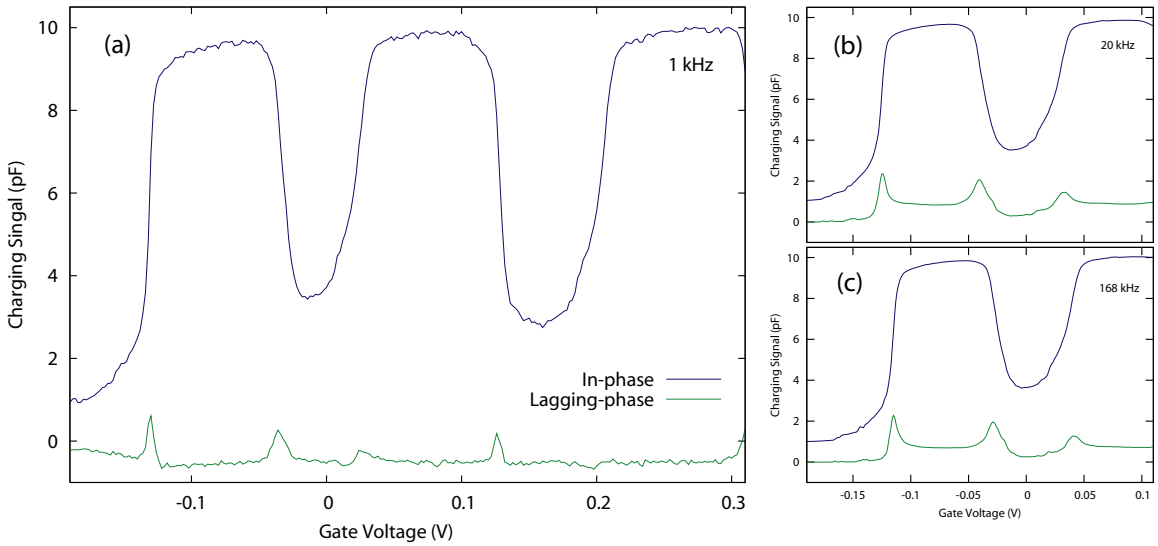

Figure 4-6: Bias sweeps taken at 4.5T. (a) Data taken at 1kHz. The magnitude of the lagging-phase peak is much smaller than would be predicted if the change in the in-phase signal was due entirely to resistive effects. At some voltage, the peak is nearly absent. (b) and (c) show bias sweeps taken at 20 kHz and 168 kHz. In these plots, resistive effects are more significant, although the lagging phase signal is still too small for the in-phase signal drop to be of entirely resistive origin.

$$\mathrm{Im}(Q^*(\omega)) = \frac{CV_0 \cdot \omega RC}{1 + (\omega RC)^2} \tag{4.2}$$

What is particularly notable about these expressions is that if the charging signal is varying *only* due to a change of the resistance R then the magnitude of the peak of the lagging phase signal will always be half of the magnitude of the change in the in-phase signal from the low frequency to the high frequency limit. This is shown in figure 4-5. This RC charging model can also be extended to a continuous distributed RC network such as we have under the metal pad in our experiment (see appendix E). For a circular disc, the charging curve can be calculated analytically. The effect of the distributed nature of the RC charging is a small distortion the RC curve, shifting the peak in the dissipation to a slightly higher frequency and reducing its peak height to 0.42 times the change in the in-phase signal. Qualitatively, however, the curve is very similar to the simple RC charging case. [1]

[1]This relationship between the magnitude of the in-phase and lagging-phase signals can also be thought of in terms of a Kramers-Kronig relationship. If only the resistance is varying, then this is equivalent to changing only the characteristic time $\tau = RC$ of the relaxation. In this case, causality imposes a relationship between the real and imaginary components of the signal, which are not

Figure 4-6(a) shows a bias-sweep line cut of the in-phase and lagging-phase data from figure 4-4 taken at 6.0T. The in-phase signal show a large change of 7 pF, while the peak in the lagging phase signal is at most 1 pF, and often absent altogether. The small magnitude of the lagging phase signal shows that the value of the capacitance C in expressions 4.1 and 4.2 must be varying. This change in the capacitance C arises from the oscillation of the density of states of the 2DES due to the Landau quantization. This can also be seen by comparing traces taken at different frequencies. In contrast to figure 13 of [91], the magnitude of the in-phase charging signal change that we observe does not decrease with decreasing frequency. This further supports the idea that the variations we are observing do involve a significant contribution from the density of states.

Although we can conclude that we are observing effects from the density of states, the presence of small lagging phase signals makes it difficult to quantitatively extract the density of states from our data. To do this unambiguously, the lagging-phase signal should really be zero so that we can safely ignore resistive effects altogether. This could be achieved experimentally by measuring at even lower frequencies and by using pads with smaller areas.

4.5 Density inhomogeneity at the edge of the gate

The magnetocapacitance plots also display some features that are very strange, shown in figure 4-7. In particular, on the low-field side of $\nu_{\text{bulk}} = 1$, the charging signal seems to be suppressed at low bias voltages but then recovers again at sufficiently positive gate biases. During this recovery, the charging signal shows sharp spikes reminiscent of the transport resonances observed in [114]. Also, at slightly lower magnetic fields and at depleting gate bias voltages, it seems that the bias sweeps show a signature of the $\nu_{\text{gate}} = 1$ state that suddenly collapses at lower magnetic fields. What is strange, however, is that the edges of this apparent $\nu_{\text{gate}} = 1$ state do not quite line up with the

independent. Given one component of the signal, a Kramers-Kronig type transformation could be used to obtain the other. These transformations, however, are difficult to implement numerically.

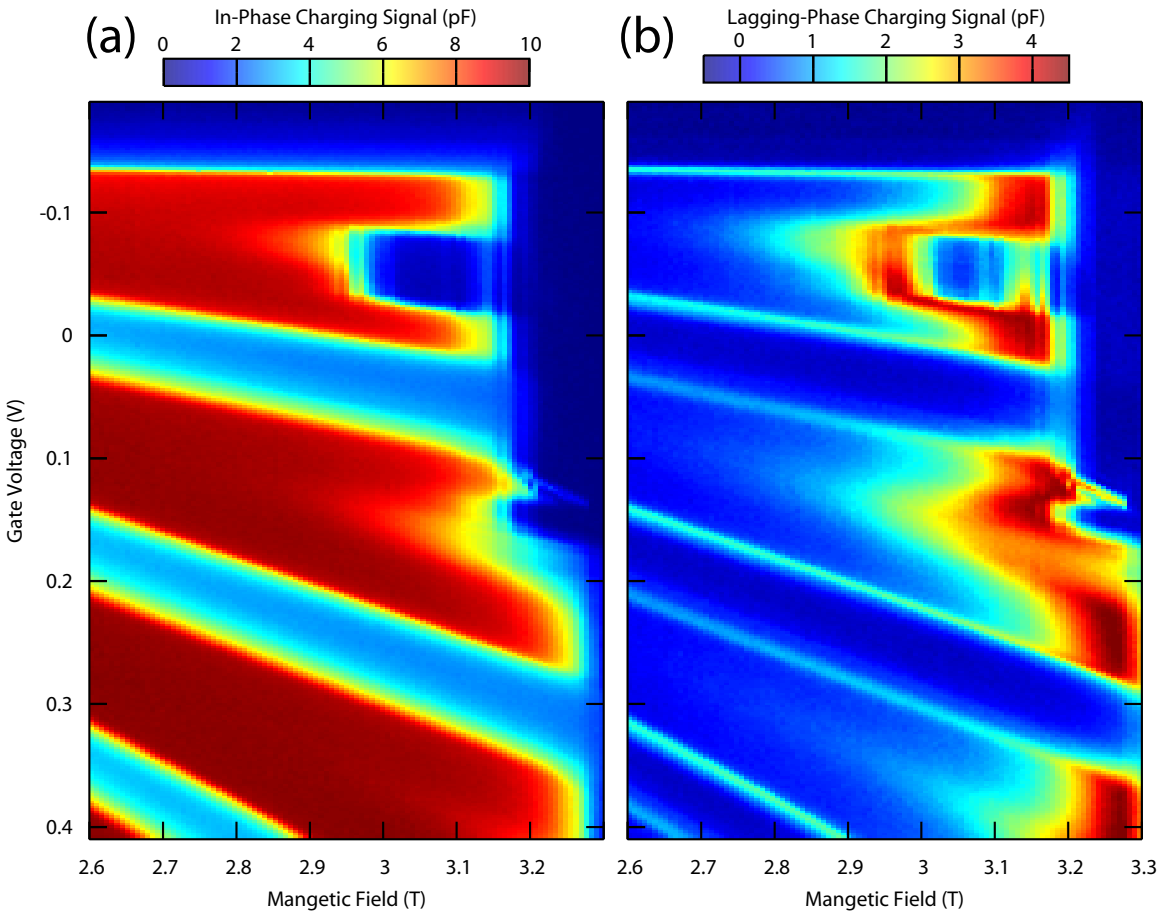

Figure 4-7: In-phase (a) and lagging-phase (b) charging data taken near the low field side of $\nu_{\text{bulk}} = 1$. Near the edge of $\nu_{\text{bulk}} = 1$, the charging signal is suppressed at low densities, but then recovers at higher gate voltages. There is also a strong resistive suppression of the signal at lower magnetic fields at biases that are close to $\nu_{\text{local}} = 1$.

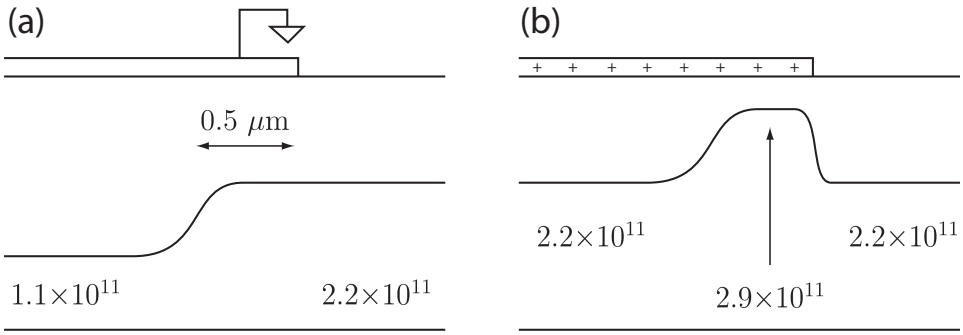

Figure 4-8: After illumination with the LED, the bulk density doubled in our sample. (a) At the edge of the gate, this density enhancement will continue for a distance given by the penetration depth of the red light into the GaAs, about ~ 0.5 μm. (b) Applying a bias voltage to the gate to match the bulk density and the density far under the gate, a density "hump" results.

extrapolation of the data to higher magnetic fields. What is also notable about both of these features is that they are associated with large values of the lagging phase signal, suggesting that they arise from a local resistance somewhere in the 2DES.

A suggestion for the origin of this local resistance comes from observations of the charging plots after cryogenic illumination of the sample with a LED. Exposing heterostructures like the ones we use to light from a red LED while they are cold results in an annealing of the kinetically frozen charge distribution in the donor layer, an effect known as persistent photoconductivity [99, 100]. After exposure to light, both the density and the mobility of the 2DES increase[2]. In order to try to increase the mobility of our sample, we tried illuminating it with a red LED. What had not occurred to us at the time was that because the bandgap of GaAs is in the IR, the penetration depth of the red light into the heterostructure is only ~ 0.5 μm. This means that after illumination, the area under our pad will not be exposed because the light cannot travel far through the GaAs, nor can it penetrate the metal gate. After illumination, with the voltage on the topgate set to null, we will have a significant density mismatch between the area under the pad, which will still be at around

[2]The exact nature of the mobility increase seems to be unclear. In particular, the mobility of a GaAs 2DES scales as $\sim n^{1.5}$ [131, 132, 133], suggesting that the increase in mobility could be a secondary effect that results only from the increase in the electron density. It would be interesting to modify the density of the 2DES with a backgate after illumination to return it to its original density and see if the mobility at the same electron concentration had changed, which would indicate an increase in donor correlations after illumination.

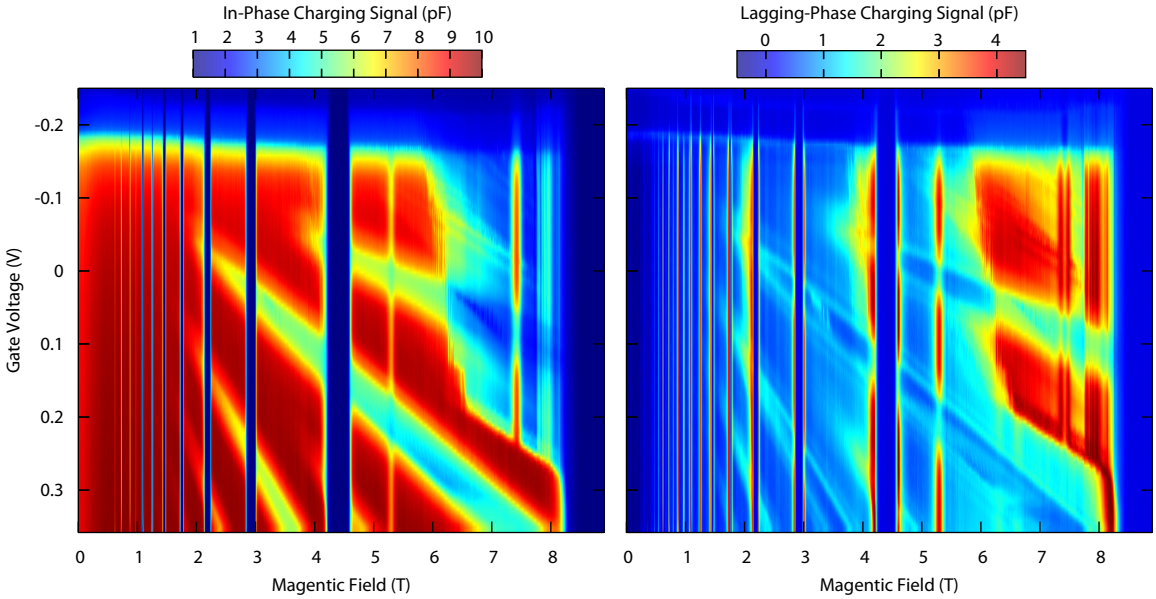

Figure 4-9: In-phase and lagging-phase charging signal after illumination with the LED. After illumination, $\nu_{\text{bulk}} = 1$ occurs at 9T. The data shows a similar resistive suppression of the charging signal at low bias voltage on the low-field side of integer filling factors in the bulk as shown in figure 4-7.

1.2×10^{11} cm^{-2}, and the bulk, which will have increased to about 2.2×10^{11} cm^{-2}. In fact, it is even worse than this: the LED will actually expose a 0.5 μm circumferential ring that is *under* that gate, as illustrated in figure 4-8. Applying a bias voltage to the gate to try to match the density under the pad to that in the bulk will result in a density "hump" that runs around the edge of the gate. At certain biases and magnetic fields, this region could contain a wide incompressible strip that could resistively cut off charging to the entire region under the pad.

Charging signals taken after LED illumination are shown in figures 4-9. The data shows a very similar resistive suppression of charging at low bias voltages. This suggests that such a suppression could arise from a resistive ring formed from density inhomogeneity at the edge of the gate. The sharp spikes seen in the charging signal likely result from resonant tunneling through this resistive ring. In some sense, we have managed to accomplish our original goal of observing transport resonances. However, since we do not have control over the density inhomogeneity created by the illumination, the interpretation is not altogether clear.

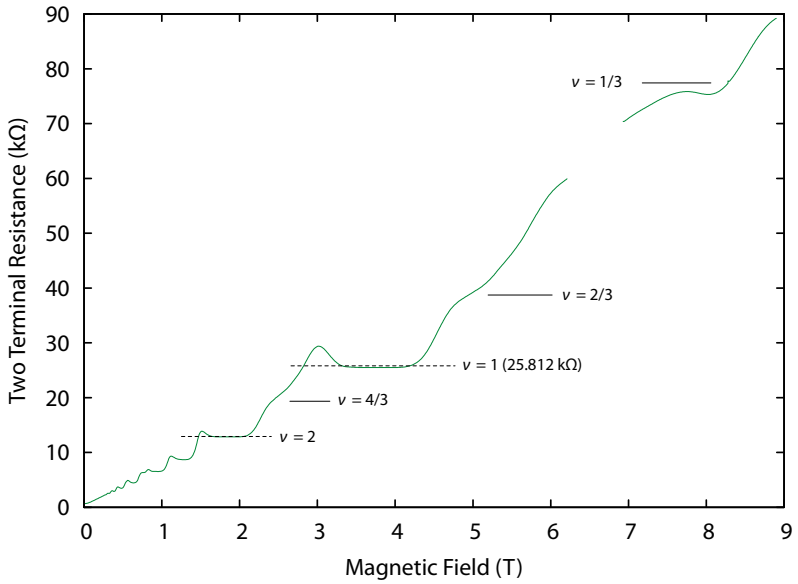

Figure 4-10: Two terminal magnetoresistance of the sample taken on the first cooldown before illumination. The $\nu = 1$ plateau occurs at the same position as the signal from the bulk charging in the magnetocapacitance trace. Weak plateaus from some fractional states are also seen. The measurement was taken at a current bias of 100 nA. (The lock-in amplifier went off scale during the measurement at the positions of the missing data points.)

The data from after LED illumination suggest that similar features shown in figure 4-7 from before illumination could also arise from density inhomogeneity at the edges of the gate. In this case, the inhomogeneity could arise from diffusion of charge into the surface states around the edge of the metal pad. Such instability in surface states has been imaged on several occasions by our group using the SCA microscope, as well as by other groups using different scanning probe techniques [134, 90].

4.6 Sample Density

Another problem we had with this sample was that the density was significantly different from what it was supposed to be, and varied significantly from cooldown to cooldown. This is very different from a sample made for the SCA microscope experiment from the same wafer, which showed the same density to within a couple of percent on three different cooldowns. In order to make sure that we were not misinterpreting the Landau levels seen in the charging signal, we also performed two

terminal magnetoresistance measurements on the sample, shown in figure 4-10 . These clearly show the $\nu = 1$ Hall plateau at 3.8T, and also shows weak plateaus at a few fractional filling factors. Interestingly, we see no sign of any fractional states in the charging signal plots. What is also strange is that below 3T, we observe no evidence in the capacitance measurements of spin split Landau levels in the local area under the pad.

The fact that the density was different from expected suggests that the mobility of the sample on these cooldowns could also be different than expected from measurements on samples from this wafer by our collaborators at Bell Labs. Unfortunately, one of the corners of the sample chipped off during the final stages of processing, preventing us from performing the four terminal measurements necessary to measure the mobility directly. We can qualitatively gauge the mobility by examining the strength of the Shubnikov-de-Hass oscillations of the charging signal at low magnetic fields. In figure 4-3, we do not see nearly as many low field oscillations as observed in a sample taken from the same wafer used in the SCA experiment (see figure 2-18). Applying the LED restores the density to the same value observed by our collaborators after illumination, and we observe much strong low field oscillations in the bulk charging (see figure 4-9). However, as discussed in the previous section, such illumination also leads to undesirable density inhomogeneity at the edge of the gate.

4.7 Conclusions

We started out with an experiment designed for the very specific goal of systematically characterizing the transport resonances we observed in the scanning probe experiment using instead a fixed gate patterned on the sample surface. It turned out, however, that this geometry produces very narrow incompressible strips with very low resistances, and no clear signatures of these resonances were observed.

On the other hand, by probing the capacitance of a relatively small pad on top of a very high mobility 2DES, we unexpectedly managed to observe a strong density of states modulation of the capacitance of the 2DES in strong quantizing magnetic fields

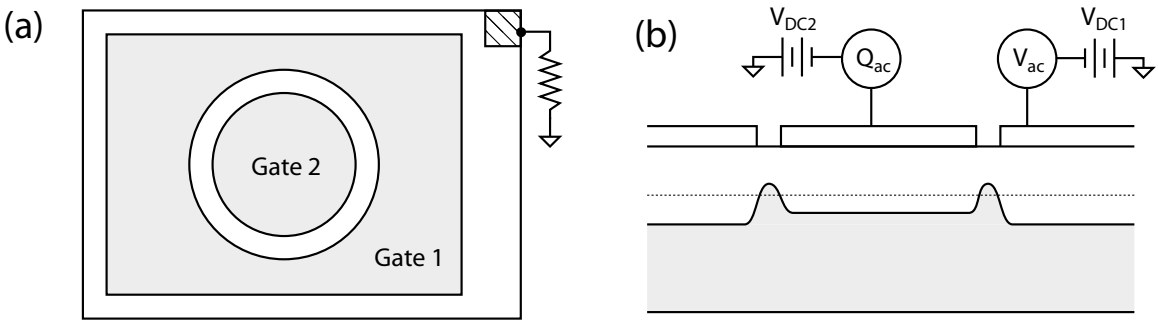

Figure 4-11: A capacitive Corbino ring geometry designed to study transport through a narrow incompressible region with a tuneable density gradient. Two gates are patterned on the surface that are separated by a narrow ring of ungated 2DES, shown in (a). The 2DES is grounded through a large resistor, allowing the voltages applied to the gates to modify the local electron density. By adjusting the DC voltages on the two gate, the regions under each gate can be chosen to be metallic and fully charging. Measuring the capacitance between the two gates with the magnetic field such that integer filling is given by the dashed line directly probes transport through the narrow incompressible region. Because the contact is made only capacitively, we have much more control over the density gradient in the incompressible region.

in a lateral charging experiment. Such an observation had at times been claimed to be impossible by some [91] and was observed by others [74] only at low magnetic fields and very low frequencies. Combining our unique geometry with a smaller pad and a lower measurement frequency should easily allow quantitative extraction of the density of states of the 2DES in large quantizing magnetic fields.

Our experiment has also led to new ideas about how to capacitively probe the resistance of the quantum Hall system in unique ways. One particularly promising idea is that of a capacitive "Corbino ring", shown in figure 4-11. Here, we would measure the capacitance between two metal pads on the surface of the 2DES. The AC voltage driving charge in the 2D layer is contacted only capacitively. An ohmic contact to the 2DES is connected to a DC voltage through a large bias resistor or a bias transistor, which allows us to tune the density under each gate independently. Such a geometry would allow complete control over the density gradients in the resistive region we are probing.

From start to finish, the experiment took only four weeks to complete. Considering the interesting results we were able to obtain in such a short time, repeating this

experiment with a more stable sample would be a relatively easy and fruitful endeavor.

Chapter 5

Simulating the Interaction of a Metallic Scanning Probe with the Quantum Hall Liquid

In this chapter, we discuss simulations we have developed to model the electric fields and charge distributions that result from the interaction of our metallic scanning probe with the 2DES. This work was done is collaboration with Nemanja Spasojevic through the MIT Undergraduate Research Opportunities Program. Many details of the simulations are available in his undergraduate thesis [135].

5.1 Motivation

The conical geometry of the tip and the presence of a dielectric layer covering the 2DES make it very difficult to even estimate the interaction of the probe with the 2DES. In particular, our experiment can directly measure the capacitance from the tip to the 2DES, yet by hand, we cannot even estimate what we expect this capacitance to be.

The effect that voltages on our probe have on the 2DES is also very important. This can become quite complicated in the quantum Hall regime, where the properties of the 2DES are very sensitive to the local electron density, and the 2DES can

become very spatially inhomogeneous. Our experiments often include applying DC bias voltages to the tip in the quantum Hall regime, so understanding how this affects the 2DES is very important in interpreting our results.

These difficulties led us to develop a complete electrostatic simulation of the tip and the 2DES. We initially considered only cylindrically symmetric systems, which significantly reduces the amount of time and computer memory needed. We later extended these to 3 dimensions, allowing us to see effects such as disorder. The 2D simulations have proved to be invaluable in terms of understanding our experiment, and the 3D simulations provide remarkable insight into the effect of disorder on the incompressible ring and the transport resonances we observed discussed in chapter 3.

5.2 Numerical Methods

In order to calculate the charge densities and electric fields between the tip and the 2DES, we need to solve the Poisson equation:

$$\nabla^2\phi(\vec{x}) = -\rho(\vec{x})/\epsilon \tag{5.1}$$

Here, $\rho(\vec{x})$ is an externally imposed charge density and $\phi(\vec{x})$ is the electrostatic potential. There are many ways to implement this numerically. The first step is to divide the region of space we are considering into a discrete grid. This reduces the continuous differential equation above to a set of finite-difference equations describing the potential ϕ_i at the grid points in the simulation. From there, the methods of solving the problem can be divided into two general categories: "direct" and "iterative". In the direct methods, the problem is formulated as a matrix equation:

$$\begin{bmatrix} A_{11} & A_{12} & \dots & A_{1N} \\ A_{21} & A_{22} & \dots & A_{2N} \\ \vdots & \vdots & \vdots & \vdots \\ A_{N1} & A_{N2} & \dots & A_{NN} \end{bmatrix} \begin{bmatrix} \phi_1 \\ \phi_2 \\ \vdots \\ \phi_N \end{bmatrix} = \begin{bmatrix} \rho_1 \\ \rho_2 \\ \vdots \\ \rho_N \end{bmatrix} \tag{5.2}$$

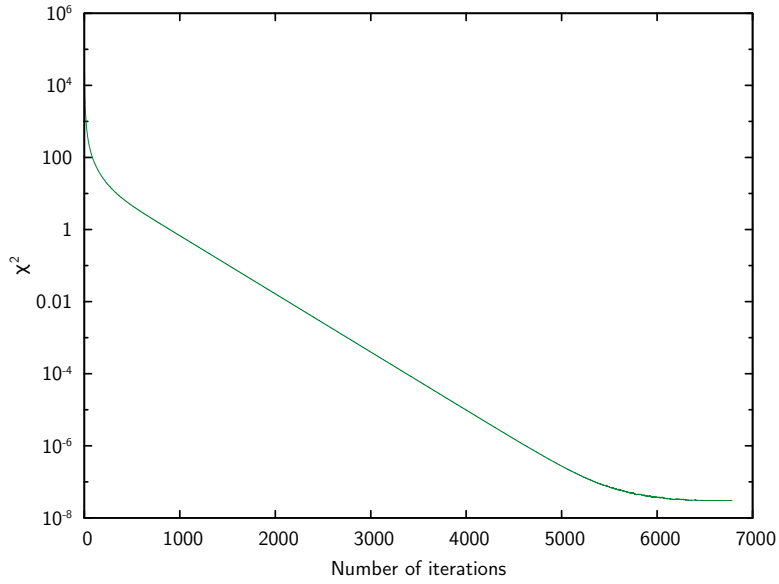

Figure 5-1: A plot of the average squared residual error as a function of the number of relaxations for simple relaxation. χ^2 shows an initial rapid drop as the values of the potential diffuse in from the boundaries. The long tail is associated with the slow damping of long wavelength error in ϕ.

Here A_{ij} is an $N \times N$ matrix that describes the coupling between each of the points on our grid, where $N = L_1 L_2 L_3$ for 3D grid of dimensions $L_1 \times L_2 \times L_3$. At first, this would seem to involve a very large memory requirement $\mathcal{O}(N^2)$. However, because each ϕ_i is only coupled to its nearest neighbors, the matrix A_{ij} is quite sparse: for the 1D case it is band diagonal. In 2D and 3D, it requires some off-diagonal elements, but can still be stored quite efficiently using sparse matrix routines. The memory requirement can be reduced this way to $\mathcal{O}(N \log N)$ (see table 5.1). Solving for the potential involves inverting the matrix A_{ij}, which can be done relatively easily using common math libraries. While there is a larger space requirement needed to store the large A_{ij} matrix compared to the iterative methods we will discuss next, the direct methods can be relatively fast ($\mathcal{O}(N^{3/2})$) and yield and exact solution in one interaction for linear problems.

Iterative methods involve a technique based on relaxation of the potential [136, 137, 138]. Here, we start with an initial guess for the potential ϕ at all points in space and store it in an N element array. We then iterate through the array, replacing ϕ_i at each point with a new value that satisfies equation 5.1 based on the value of

the potential of its neighbors. Over time, the potential "propagates" inwards from the boundary conditions. After sufficient iteration, the potential converges to the correct solution. The process is monitored by examining the residual error after each iteration. At the end of an iteration, for each point we calculate a residual error:

$$F_i = -\nabla^2 \phi_i - \rho_i/\epsilon \tag{5.3}$$

We then define a average residual square error χ^2 as:

$$\chi^2 = \frac{1}{N} \sum_i (F_i)^2 \tag{5.4}$$

F_i has the units of charge, and χ^2 can be though of as the average squared residual charge error per pixel. After sufficient iteration, χ^2 will stop decreasing, indicating that we have reached the limit where the remaining residual charge is due to truncation error in the potential. This is illustrated in figure 5-1. The ultimate value of χ^2 will depend on the physical size of the pixels, the dielectric constant, and the numerical precision used in the code.

Iterative methods have a very good memory requirement, using only $\mathcal{O}(N)$ space, and are more physically intuitive than the direct methods. The disadvantage is that simple relaxation is very slow: each iteration takes an amount of time $\mathcal{O}(N)$, and it can be shown [138] that the number of iterations required to converge is $\mathcal{O}(N)$, giving a total running time $\mathcal{O}(N^2)$. Fortunately, there is a simple procedure called successive over-relaxation (SOR) that can drastically speed up this process. In relaxation, at each iteration n we calculate a $\Delta\phi_i^n$ for each pixel i that will make the new potential ϕ^{n+1} solve the Poisson equation based on the values of its neighbors. In SOR, we multiply $\Delta\phi_i^n$ by a numerical factor ω, making the update to the potential:

$$\phi_i^{n+1} = \phi_i^n + \omega \Delta\phi_i^n \tag{5.5}$$

SOR for a linear problem is guaranteed to converge for $0 < \omega < 2$[1]. For a given

[1]Taking $\omega < 1$ would be called "underrelaxation".

relaxation problem, there is an optimal ω that will cause the problem to converge in $\mathcal{O}(N^{1/2})$ iterations [138].

What is interesting is that it is not the "diffusion" of the boundary values that makes ordinary relaxation slow. This "diffusion" occurs quite quickly, during the steep section of the χ^2 curve shown in figure 5-1. Instead, what makes relaxation slow is the damping of long wavelength fluctuations in ϕ[2]. This is slow because relaxation involves only a short lengthscale "smoothing" since it connects only nearest neighbors. It is this slow damping that produces the long tail in χ^2. SOR helps by creating "waves" in the potential that propagate long wavelength updates more quickly through the simulation than simple relaxation. The value of the optimal ω can be estimated from the simulation size [139]:

$$\omega_{\text{opt}} \approx \frac{2}{1 + \pi/\min(N_x, N_y, N_z)} \tag{5.6}$$

The reason this number is connected with the physics size of the simulation is that for this is that at high ω, SOR gets slower due to the establishment of standing waves in the residual error from reflections from the boundaries. These standing waves can often be seen in plots of the residual error (see figure 2-4 in [135]). From a practical point of view, it is generally better to overestimate ω for the linear Poisson equation, as the convergence rate falls off more quickly for underestimation [138].

Table 5.1, summarizes the memory and time requirements of different methods of solving the Poisson equation. For our simulations, we chose SOR, as it is easy to implement, provides good time and memory performance, and has a nice physical interpretation. It also allows us to deal with the numerical instabilities introduced by the non-linear Poisson equation discussed in the next section in a very natural way.

[2]The damping of these long-wavelength fluctuations is also the basis of the more sophisticated multigrid method. Using the multigrid method, relaxation will converge in $\mathcal{O}(0)$ iterations, achieving the $\mathcal{O}(N)$ theoretical lower time bound for the solution of the Poisson equation.

Method	Serial Time	Space	Direct or Iterative
Dense Cholesky	N^3	N^2	D
Explicit inverse	N^2	N^2	D
Band Choelsky	N^2	$N^{3/2}$	D
Jacobi's	N^2	N	I
Gauss-Seidel	N^2	N	I
Sparse Cholesky	$N^{3/2}$	$N \log N$	D
Conjugate gradients	$N^{3/2}$	N	I
Successive overrelaxation	$N^{3/2}$	N	I
SOR with Chebyshev accel.	$N^{5/4}$	N	I
Fast Fourier transform	$N \log N$	N	D
Block cyclic reduction	$N \log N$	N	D
Multigrid	N	N	I
Lower bound	N	N	

Table 5.1: Comparison of the memory and time complexities of solving Poisson's equation on an $L \times L$ grid ($N = L^2$). Adapted from [138] page 277.

5.3 The Non-Linear Poisson Equation

In the previous section, we discussed solutions of a poisson equation of the form:

$$\nabla^2 \phi(\vec{x}) = -\rho(\vec{x})/\epsilon$$

Each point in space was either an insulator that carried a specific fixed charge $\rho(x)$ (which was zero for free space), or was a metal, which corresponded to a boundary condition of a fixed potential V. Unfortunately, the 2DES that we will want to model corresponds to neither of these situations. The 2DES is similar to a metal in that a 2DES connected to a battery will be held at a fixed electrochemical potential V, and will screen electric fields by adjusting its local charge density. The difference is that the 2DES behaves like a semiconductor and cannot screen these electric fields perfectly because it has a finite density of states. This modifies the Poisson equation in the following way: the local charge density in the semiconductor becomes a function of the local potential:

$$\nabla^2 \phi = -\rho(\phi)/\epsilon \tag{5.7}$$

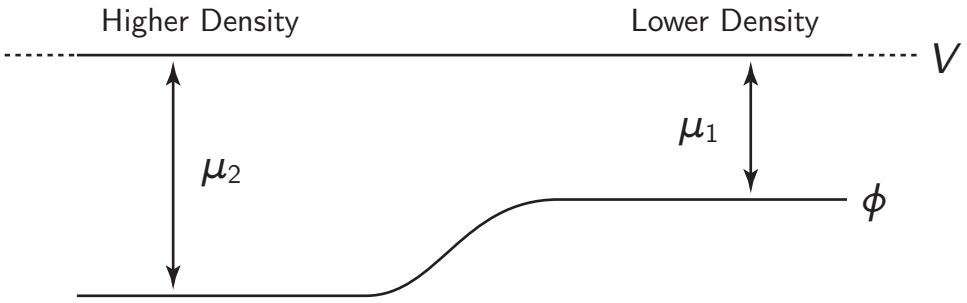

Figure 5-2: A semiconductor held at electrochemical potential V where the electron density is varying with position. The chemical potential μ is larger in regions of higher density. In order to maintain a constant electrochemical potential $V = \phi + e\mu$, the electrostatic potential ϕ must drop.

The function $\rho(\phi)$ describes show the charge density in the semiconductor will vary as a function of the local self-consistent potential. To see what this means physically, consider a semiconductor in equilibrium at an electrochemical potential V in which the local density is varying, as shown in figure 5-2. Due to the change in the electron concentration Δn, the local chemical potential μ changes by an amount $\Delta\mu$. To maintain electrochemical equilibrium, there must also be a change in the electrostatic potential ϕ by an amount $\Delta\phi = -|e|\Delta\mu$. The function $\rho(\phi)$ in 5.7 describes exactly the inverse of this: it tells us the change in the electron concentration Δn that results from a change in the equilibrium electrostatic potential $\Delta\phi$ in the semiconductor. The non-linear Poisson equation 5.7 using a $\rho(\phi)$ derived from the density of states is exactly equivalent to the Thomas-Fermi approximation [131].

The function $\rho(\phi)$ for different types of materials is shown in figure 5-3. For an insulator, $\rho(\phi)$ is constant, independent of ϕ. For a metal, $\rho(\phi)$ is a vertical line: a metal will always adjust its local charge density to keep its potential fixed. The 2DES is a semiconductor, and lies somewhere in between. It shows a slope in the ρ vs. ϕ plane that is given by the thermodynamic density of states $dn/d\mu$ and that intersects zero at the value of of the externally imposed electrochemical potential V. The 2DES also has a finite carrier concentration: for a sufficiently negative ϕ, the local charge density will saturate at $+|e|n_0$.

It is very easy to extend our simulations to model the 2DES in the quantum Hall regime. In a magnetic field, the constant density of states of the 2DES breaks up

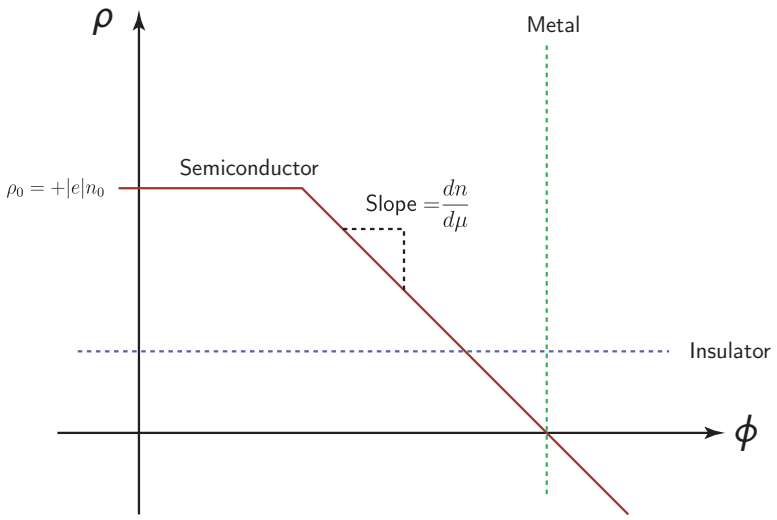

Figure 5-3: $\rho(\phi)$ for a metal (green dashed line), an insulator (blue dashed line) and a semiconductor (red line). Due to the finite density of states, the curve for a semiconductor has a finite slope. A semiconductor with a fixed density of negative carriers n_0 will have a maximum possible space charge density of $\rho_0 = +|e|n_0$, corresponding to full depletion.

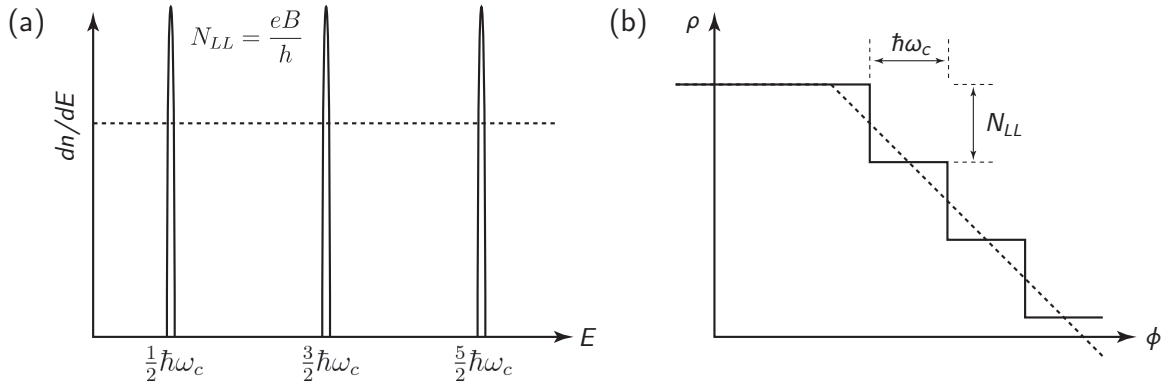

Figure 5-4: (a) In a magnetic field, the zero field density of states (dashed) breaks into δ functions separated by $\hbar\omega_c$. Each Landau level holes eB/m electrons, resulting in a staircase $\rho(\phi)$ shown in (b) that follows the slope of given by the zero field density of states (dashed).

into a set of δ-functions, as shown in figure 5-4(a). These δ-functions are separated in energy by $\hbar\omega_c$, where $\omega_c = eB/m$ is the classical cyclotron frequency. Each Landau level holds $N_{LL} = eB/h$ electrons. The $\rho(\phi)$ curve becomes a staircase that follows the slope of the density of states of the zero field case, as shown in figure 5-4(b). Using such a function $\rho(\phi)$, we can perform calculations of the self-consistent potential in large magnetic fields similar to those in [50, 51, 140] for our exact device geometry. The width of each step is given by $\hbar\omega_c$ and the height of the steps is N_{LL}. Because ideal *delta*-functions lead to numerical instabilities in our relaxation algorithm, we model the ideal δ functions as narrow bars who's integrate area is N_{LL}. The effect of this is to add a finite slope to the vertical "drops" in the staircase.

The function $\rho(\phi)$ is not necessarily linear, and so in introducing it we now have to solve a non-linear differential equation. In the iteration scheme, we expand $\rho(\phi)$ to first order and incorporated the linear term into our update equation [135]. This is equivalent to Newton's method. However, the relaxation of the non-linear Poisson equation can be unstable, and convergence is not guaranteed as it is in the linear case. We have found, however, that most of the non-linear problems we have solved can be "coaxed" into convergence by under-relaxing the pixels of the simulation that have a non-linear $\rho(\phi)$. This is accomplished in the code by having a separate SOR parameter ω_{NL} for the non-linear pixels that has a value $\omega_{NL} < 1$. During the simulation, if a diverging χ^2 is detected, the code will automatically reduce ω_{NL} until χ^2 starts to drop again. This also has the advantage that we can still use a large SOR parameter for the remaining linear pixels.

5.4 Boundary Conditions and Non-Uniform Grids

One of the difficulties in simulating our devices is the decision of what to do at the boundaries of the simulated region. At the edge of the simulation, we have the choice of applied three possible boundary conditions for our problem to be well defined: a "metallic" fixed potential boundary ($\phi_B = C$, Dirichlet condition), a vanishing normal derivative boundary ($\vec{\nabla}\phi \cdot \hat{n} = 0$, Neumann condition), or a periodic boundary

condition ($\phi(x) = \phi(x - L)$). In our experiment, an appropriate boundary condition in many directions is that $\phi(\infty) = 0$. Unfortunately, this is difficult to implement numerically with a finite-sized simulation[3].

One solution that allows us to move the boundaries very far away without increasing the number of grid points is to use non-uniform griding. This can be done in a simple way without resorting to the complications of triangular meshing by using a rectangular grid where the spacing in a given direction depends only on the coordinate in that direction: $\Delta x = f_1(x), \Delta y = f_2(y)$, etc. We have implemented this for our 2D simulations in cylindrical coordinates [135]. In the end, the simulation results were not that sensitive to the boundary conditions anyway, but the non-linear griding does come in handy.

In our work, we have most frequently employed both fixed potential and vanishing normal-derivative boundary conditions at the edges of the simulation. Fixed potential boundary conditions have a very clear physical meaning in electrostatics: they simply correspond to a nearby (rather than infinitely far away) ground plane. Normal boundary conditions are natural at the $r = 0$ side of our simulations in cylindrical symmetry. They also have a simple physical interpretation at other edges: they can be though of as a "mirror" boundary, where we have arranged identical charge distributions on the other side of the plane that cause the electric fields normal to it to cancel. They are similar to periodic boundary conditions in this way. We have tended to use them in place of periodic boundary conditions at the lateral edges of our 3D simulations as we have found that periodic boundary conditions seem to cause instability with the SOR.

[3]There is an interested method for applying such an "open" boundary condition for a 3D Cartesian geometry, where a close form for the Green's function is available [139].

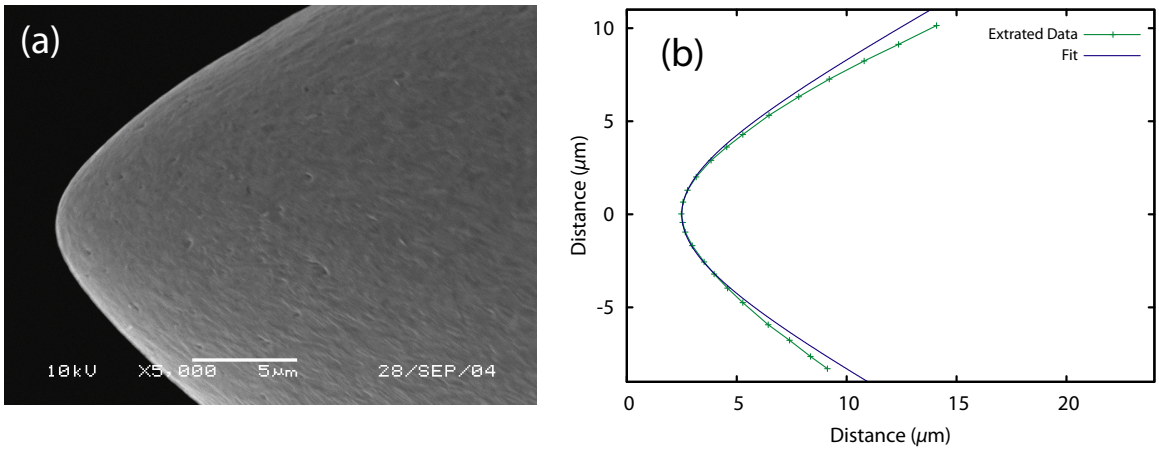

Figure 5-5: (a) An SEM image of an etched tip. The position of the edge of the tip metal was extracted from the image. (b) The position of the Z coordinate of the edge of the tip as a function of the X coordinate is shown in green. The blue line shows the fit to the function 5.8 with a pitch a of 1.6 and a hyperbolic radius R of 5 μm. There is a slight rotation of the tip in the image.

5.5 Results from 2D Simulations Using Cylindrical Symmetry

In the first set of simulations we present, we ignore the effects of disorder and take advantage of the cylindrical symmetry of the tip. This reduces the simulation of the 3D electrostatics to a 2D simulation with cylindrical coordinates that includes only the vertical and radial directions. This allows us to accurately model the exact shape of a large portion of the tip and allows use to use larger simulation sizes to ensure that boundary effects can be neglected.

5.5.1 Tip Approach Curves

The first calculations we performed were to simulate the capacitance "tip approach" curves discussed in section 2.7.1. The first step was to get an accurate fit to the shape of the tip produced by our tip etching procedure. Figure 5-5(a) shows an SEM image of a tip used on one of our cooldowns. The r-z data describing the edge of the metal was extracted from the images using g3data [141], and is plotted in figure 5-5(b). A convenient parametrization of the shape of the tip turned out to be that of

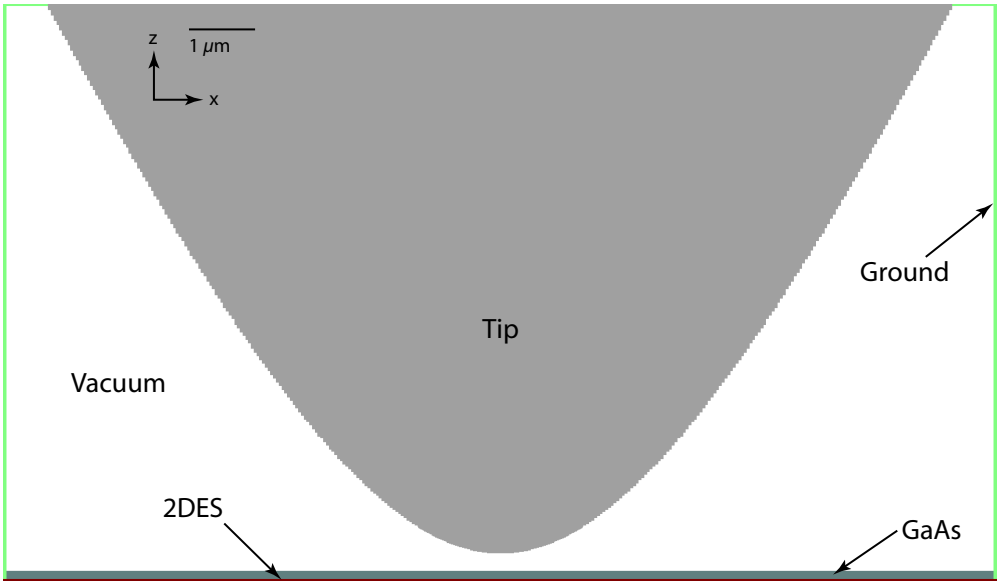

Figure 5-6: Geometry of the simulation. The 2DES is situated 100 nm below a GaAs dielectric layer.

a hyperboloid:

$$z = a\sqrt{R^2 + r^2} \tag{5.8}$$

Here, R is the hyperbolic radius and a describes the asymptotic slope of the hyperboloid, or the "pitch" of the tip. The tip in the SEM in 5-5(a) had a pitch of 1.6 and a hyperbolic radius of 5 μm. The fit is shown in 5-5(b).

For the purposes of the tip approach curves, we modeled the 2DES as a metal layer that is 100 nm below the surface. We used a dielectric constant of 13 for the GaAs layer. Non-linear griding was employed to create a large 9.8×7.5 μm simulation area. The geometry of the simulation is shown in figure 5-6. The capacitance was calculated for tip to surface separations ranging from 10 nm to 1 μm. The calculated curve is shown in figure 5-7. Also shown is the measured tip approach curve from the first approach on the cooldown where a tip with the same form as shown in in figure 5-5 was used. The agreement between the measured and simulated data is remarkably good considering that both of the curves contain *no* adjustable parameters. For the experimental data, the vertical capacitance scale was obtained from an independent calibration of the source-drain capacitance of the bias transistor, and the zero for the sample-tip separation was taken from the kink in the capacitance curve where the tip

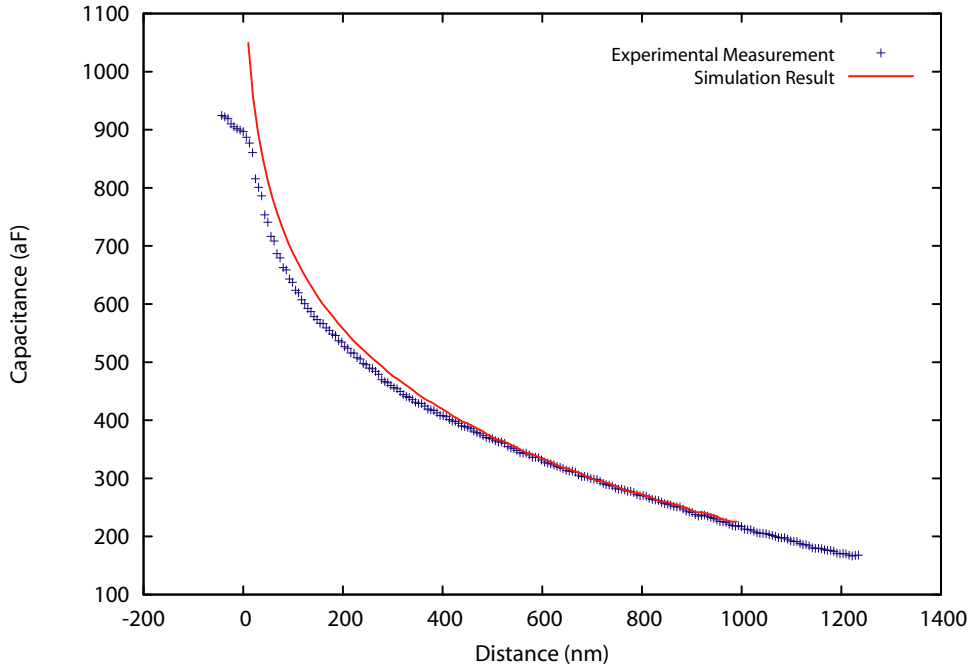

Figure 5-7: A comparison of the experimental and simulated tip approach curves. In this comparison, there are no adjustable parameters. The agreement between the simulated and experimental curves is remarkable.

touched the sample surface. This not only demonstrates the ability of our simulations to accurately model the tip, but also shows the accuracy of the calibration of the capacitance bridge in our experiment.

To demonstrate the correlation between the shape of the tip and the form of the tip approach curve, we have calculated capacitance curves for tips of different shapes. Figure 5-8 shows the curves for the tip shapes shown in the inset. Increasing the tip pitch to 10 with a 5 μm hyperbolic radius, the "upturn" in the capacitance occurs over a shorter distance and is much smaller in magnitude. For an ideally sharp tip (10 nm, corresponding to the pixel size in our simulation), there is no "upturn" at all, and the curve shows only a very small slope from the change in the global capacitance to the 2D layer.

5.5.2 Capacitance Change Seen in Gate Images

Because we are performing a simulation with cylindrical symmetry, we cannot exactly simulate the shape of the line cut across the gate from the capacitance images that

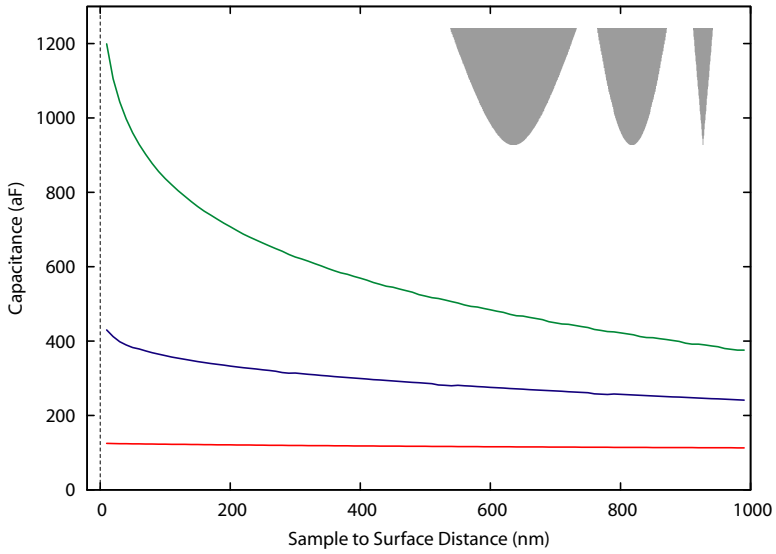

Figure 5-8: Calculated approach curves for different shaped tip, shown at the top right. The curve from figure 5-7 with a pitch of 1.6 and a radius of 5 μm is shown in green. Increasing the tip pitch to 10 with the same radius, shown in blue, decreases the magnitude of the upturn. The curve for a perfectly sharp tip (10 nm) is shown in red. This curve shows no "upturn" at all.

was discussed in section 2.7.2. We can, however, calculate the magnitude of the capacitance change. We can also get a feel for how quickly the signal will fall off as we move away from the gate by chopping a circular "hole" in the gate under the tip. Modeling how the capacitance of the tip to the 2DES and the gate changes as a function of the size of this hole will give us a rough idea of the distance scale to expect from the line cuts of the images.

The results of such a calculation using the same three tip shapes shown in figure 5-8 is shown in figure 5-9. For these simulations, the end of the tip was positioned 30 nm above the surface, and the gate was taken to be 10 nm tall. The largest tip shows a capacitance drop of about 60 aF, in agreement with data from the cooldown with this tip. The tip with the steeper pitch shows a smaller capacitance change of about 10 aF with a faster fall-off. The sharpest tip shows virtually no falloff whatsoever, with the signal changing only by 0.2 aF. This demonstrates the remarkably small local contribution seen in sharp tips, and questions their usefulness in capacitance imaging[4].

[4]The idea that smaller tips do not increase the spatial resolution due to degredation of the signal

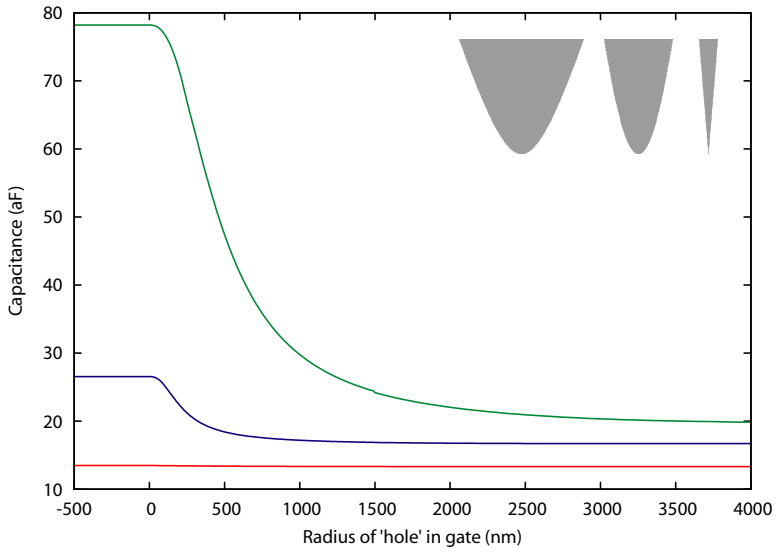

Figure 5-9: A comparison of the gate capacitance curve for the same tips shown in 5-8. The data shows the capacitance to the tip as a function of the size of a circular hole cut in the gate under the tip, as an approximation of how the capacitance falls off with the lateral distance from the gate in the experiment. The $r = 0$ value was extended to negative distances for illustrative purposes. Notably, the curve for the sharp tip is remarkably flat, showing a total capacitance change of only 0.2 aF.

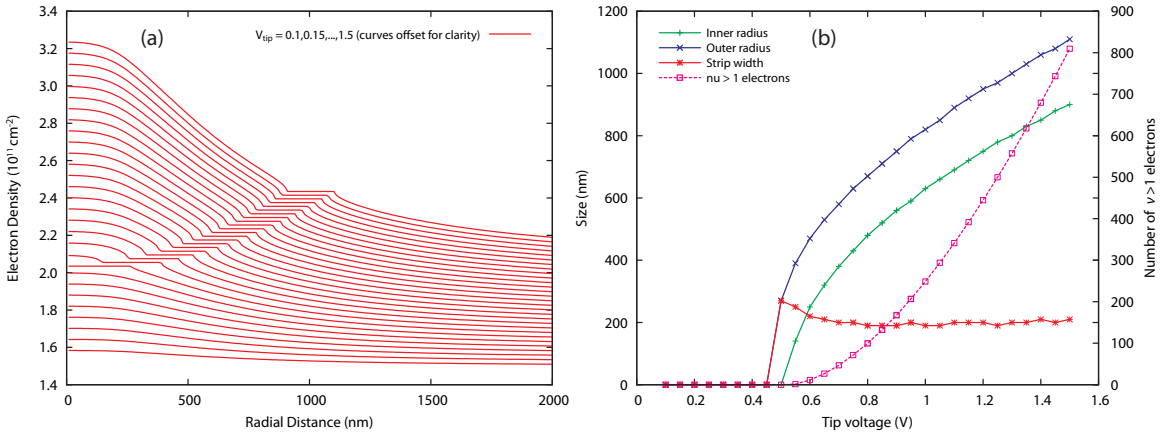

Figure 5-10: (a) Density profile at a magnetic field corresponding to $\nu_{\text{bulk}} = 0.8$ with increasing bias voltage applied to the tip showing the formation of the IR. (b) The dimensions of the IR and the occupation of the central bubble as a function of tip bias voltage. The calculations were performed for a tip with $r = 5$ μm and a pitch of 1.6.

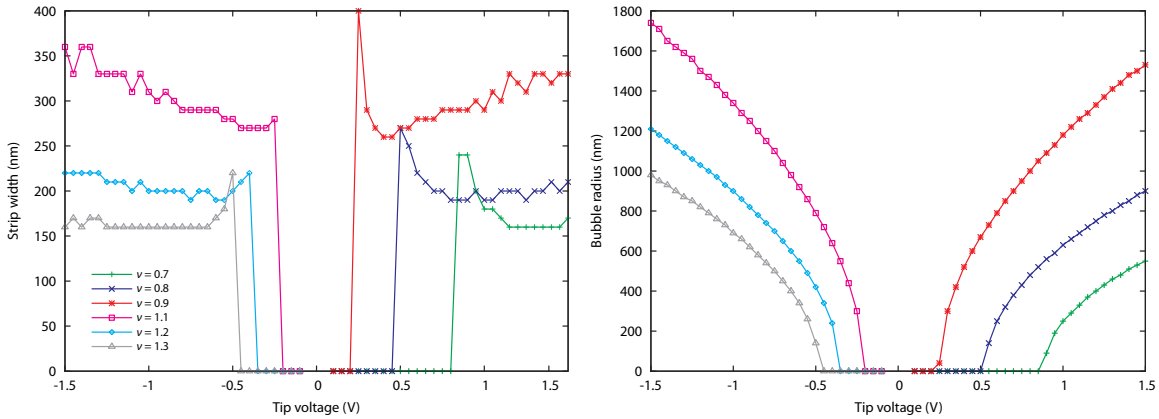

Figure 5-11: The calculated IR width (a) and inner radius (b) as a function of the tip bias voltage for different magnetic fields. Once formed, the IR width is relatively insensitive to the bias voltage, and is determined only by the magnetic field.

5.5.3 Simulating the Incompressible Ring

By using a $\rho(\phi)$ function appropriate for the 2DES as large magnetic fields, we can use our simulations to predict the size and width of the IR in the absence of disorder. Figure 5-10(a) shows the density profile induced by a DC voltage on the tip at a magnetic field corresponding to a filling factor $\nu = 0.8$. Below a threshold voltage, the density perturbation is not large enough to reach $\nu = 1$. As the bias voltage is increased, we reach a point where the local density under the tip reaches $\nu = 1$, and the top of the density mound is "chopped off". Increasing the bias voltage further, a $\nu > 1$ bubble forms. The IR moves to larger radii as this $\nu > 1$ region grows with increasing bias voltage. In figure 5-10(b), we plot the position of the inner and outer edge of the IR as well as the its width as a function of the tip bias voltage. Note that after formation, the IR width does not significantly change as the bias voltage is swept. Also shown is the number of $\nu > 1$ electrons in the bubble. Note that the occupation of the bubble is quite large for this tip. The radius of the IR is in good agreement with the arcs we observe in the experiment.

We have also performed these calculations at several different filling factors. The outer radius and IR width for these filling factors as a function of bias voltage are

was also noted by Lányi *et. al* [142], although their analysis was based on a different experimental setup.

shown in figure 5-11. To a good approximation, the IR width is independent of bias voltage and is set only by the magnetic field, as discussed in section 3.9. Moving to filling factors closer to $\nu = 1$ results in a wider IR, and the IR at the same bias voltage has a larger radius. These observations are also in agreement with what is observed in the experiment.

5.5.4 Calculating the Lever Arm

As discussed in section 2.4, the AC excitation in our experiment will induce an AC voltage across the IR when the IR has a sufficiently high resistance that the central bubble does not charge. The magnitude of the AC voltage appearing across the IR is determined by a capacitive divider formed by the ratio of the bubble's capacitance to its grounded surroundings to the value of its self-capacitance:

$$\frac{\Delta V}{V_{ac}} = \frac{C_{\text{tip}} + C_{\text{gnd}}}{C_{\text{tip}} + C_{\text{gnd}} + C_{\text{bulk}}} \tag{5.9}$$

To calculate these capacitance matrix elements, we will represent each portion of the system as a separate metallic region. The island will be set to a potential of 1V and the bulk 2DES, the tip, and the metal boundary will be grounded. The capacitance of the bubble to each region is found by summing up the charge induced on each region.

Unfortunately, there are many variables that will influence the value of these capacitances. In particular, we will consider the variation of the lever arm with the pitch of the tip, the height of the tip above the surface, the size of the inner bubble, and the width of the IR. For these simulations, we started with a "base" configuration consisting of a tip height of 60 nm above the surface, a tip pitch of 1.6, a bubble size of 1 μm, and a strip width of 100 nm. We then varied each one of these parameters on their own and calculated the lever arms. The results for the island capacitances and the lever arms are shown in figure 5-12(a)-(d). In each, the data points for the base configuration are circled. The typical island self capacitance is ~ 800 aF and the lever arm ranges from about 4 to 12. While some of these parameters we can control,

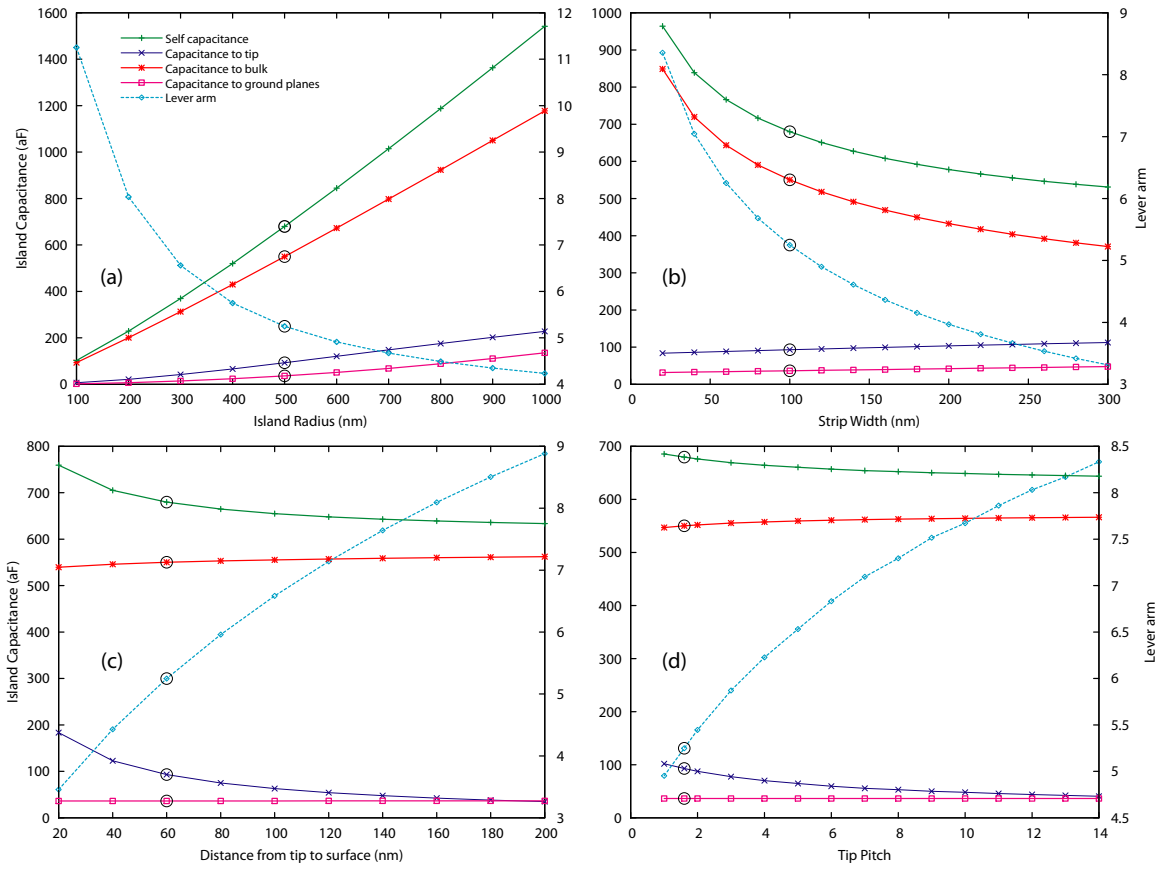

Figure 5-12: Island capacitances and lever arms for varying island radius (a), strip width (b), distance to surface (c), and tip pitch (d). For each, the "base configuration" was a island radius of 500 nm, a strip width of 100 nm, a 60 nm distance from the surface to the tip, and a tip pitch of 1.6. The values for the base configuration in each plot are circled.

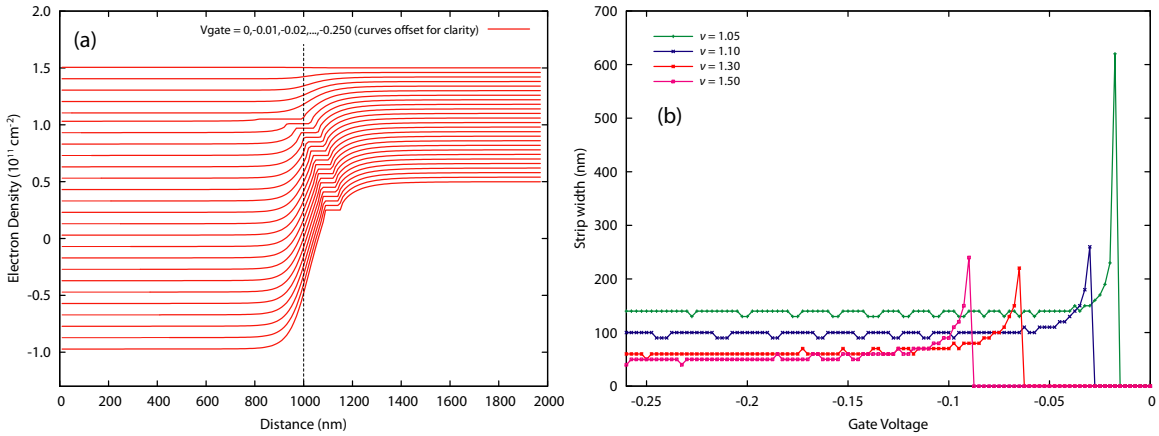

Figure 5-13: (a) Density profile as a function of topgate voltage at $\nu = 1.2$. The dashed line indicates the position of the gate on the surface of the sample. (b) Calculated strip width at a function bias voltage for different magnetic fields corresponding to the indicated bulk filling factor. After the initial formation, the strip width is independent of the the bias voltage.

such as the tip height and pitch and the bubble size, the value of the strip width is difficult to predict accurately, as it will depend sensitively on the microscopic energy gap. It is also influenced by disorder gradients, which will tend to produce a narrower strip than predicted in the absence of disorder.

5.5.5 Incompressible Strip Widths in the Magnetocapacitance Experiment

We can also use our simulations to predict the density profile and IS widths in the experiment discussed in chapter 4 concerning the magnetocapacitance of fixed pads. Since the simulation does not need to include a large tip, these simulations have fewer pixels and run very fast ($\sim$ 11 seconds each on a 1.7 GHz Pentium M).

The density profiles for a magnetic field corresponding to $\nu_{\rm bulk} = 1.1$ for different gate voltages are shown in figure 5-13(a). There are two interesting features to note: first, about 1/3 of the slope in the density gradient is underneath the gate. Second, as we saw with the incompressible strip created by the tip, once the strip has formed, the width of the strip remains nearly constant as we sweep the gate voltage, and is set only by the magnetic field. This is shown clearly in figure 5-13(b), which plots

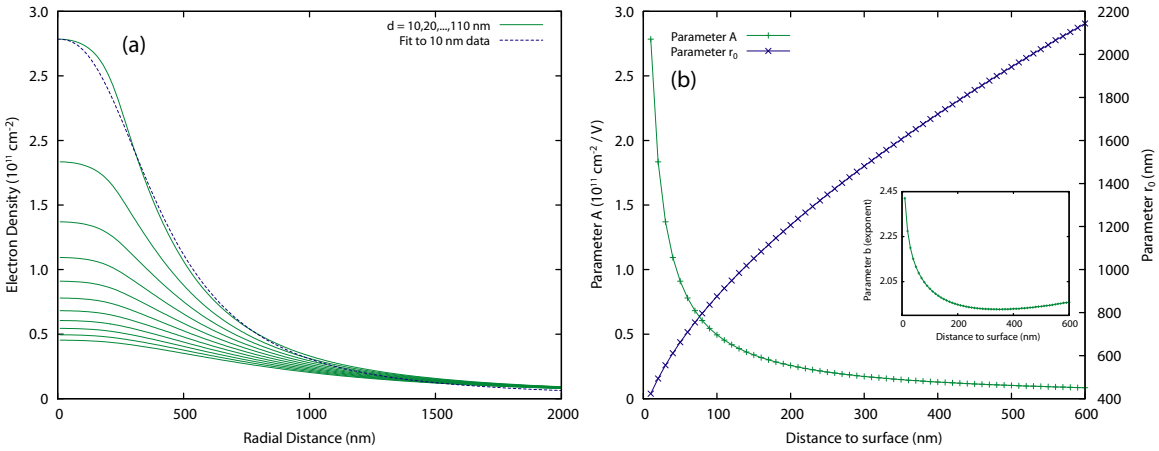

Figure 5-14: (a) Green lines show the density profile for a voltage of 1V applied to the tip at different distances d from the surface. The blue dashed line shows the fit to equation 5.10 for a 10 nm distance from the surface. (b) Parameters obtained from fitting the density profile at different sample-tip separations.

the strip width as a function of gate voltage for several magnetic fields. Also notable is that the incompressible strips are much narrow than those formed by tip due to the increased density gradients due to the proximity of the gate metal to the 2DES.

5.5.6 Jellium Approximation for the Tip Perturbation

In the previous sections we used a full electrostatic model of the tip to predict the size and with of the IR created in our experiment. We will later be interested in extending these results to a 3D simulation that will include disorder from remote ionized donors. In 3D, it would be impractical to include the full geometry of the tip in the simulation, as the size of the arrays we would require would be too large and the simulations would be far too slow.

Fortunately, once we have measured the density profile created by the tip at zero magnetic field, we do not need to include the full metal tip in the simulation to predict the formation of the incompressible ring, as the properties of the strip are controlled only by the local density gradients. By creating a similar situation that imposes the same zero field density perturbation, we can calculate the IS in a magnetic field without needing to include the tip.

To do this, we first characterize the zero field density profile induced by the tip

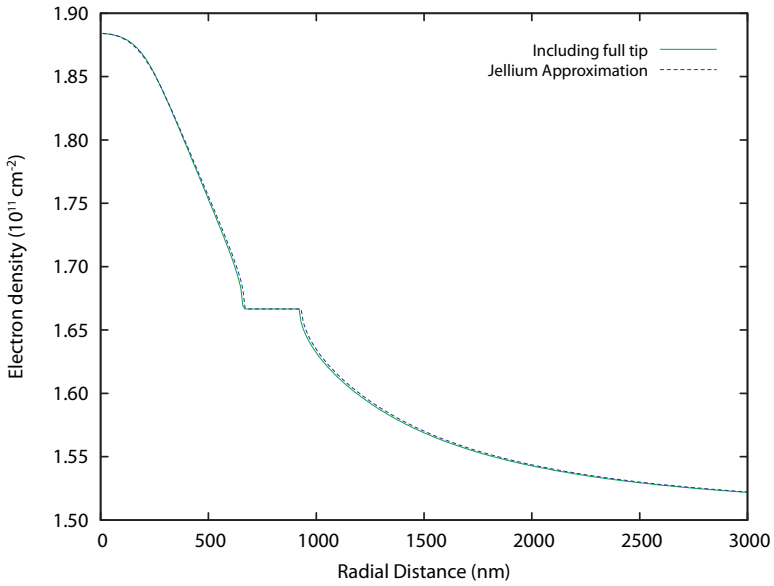

Figure 5-15: Comparing the electron density profile at $\nu = 0.8$ calculated using the full tip (solid green line) to the calculation using the "jellium" approximation to reproduce the density profile from the tip (blue dashed line).

as a function of its height above the surface. Figure 1 shows the density profile for a tip voltage of 1V for various distances above the surface with the tip shown in figure 5-14(a). We fit this profile to an empirical function:

$$n(r) = \frac{A}{1 + (r/r_0)^b} \tag{5.10}$$

Since the capacitance is linear in voltage at zero field, the coefficient A tells us the magnitude of the peak density perturbation per volt applied to the tip. Parameter r_0 describes the half width of the perturbation, and b describes the power law behavior at large r. Figure 5-14(b) shows the fitted value of these parameters as a function of the height of the tip above the surface.

In order to impose this density profile on the 2DES, we include a continuous "jellium" layer in the simulation that has a radial dependence given by 5.10 that is positioned one pixel below the 2DES layer. This induces image charges in the 2DES that exactly mimic those created by the charged tip. In figure 5-15, we show the profile of the $\nu = 1$ IR calculated using this jellium approximation along with the same $\nu = 1$ IR calculated using the tip. The two results show excellent agreement, justifying the

use of this approximation to replace the tip in our 3D simulations. Effectively, using the "jellium" approximation to the tip neglects changes in the charge distribution on the tip that arise due to the dipole formed at the position of the incompressible strip. Since this tip metal is quite far away from this dipole and since the dipole electric fields drop off rapidly with distance, it is reasonable that the jellium approximation should be quite accurate.

5.6 3D simulations

After we began to understand the meaning of our experimental imaging results presented in chapter 3, it became clear that disorder plays a very significant role in the properties of the 2DES. In order to include the effects of disorder in our simulation, we have extended our earlier code to 3 dimensions to allow the modeling of the disordered quantum Hall liquid. We present and discuss these results in the following sections.

5.6.1 Simulating the IR in the Presence of Disorder

In order to simulate the effects of disorder on the IR, we include randomly ionized donors in our simulation. These random donors are displaced vertically from the 2DES layer by a setback distance. The donors are all located in the same 2D plane, describing the δ-doping method used in our samples.

Figure 5-16(a) and (d) show the density profile that results in the 2DES layer from 1.5×10^{11} randomly ionized donors at a 20 nm and 50 nm setback distance respectively. Note that the self-consistent disorder potential has the exact same form: in the Thomas-Fermi approximation, the density and the potential are linearly related through the 2D density of states:

$$n(\vec{x}) \propto \frac{dn}{d\mu} U(\vec{x}) \tag{5.11}$$

Thus at zero field, examining the disorder by looking at the density or the potential

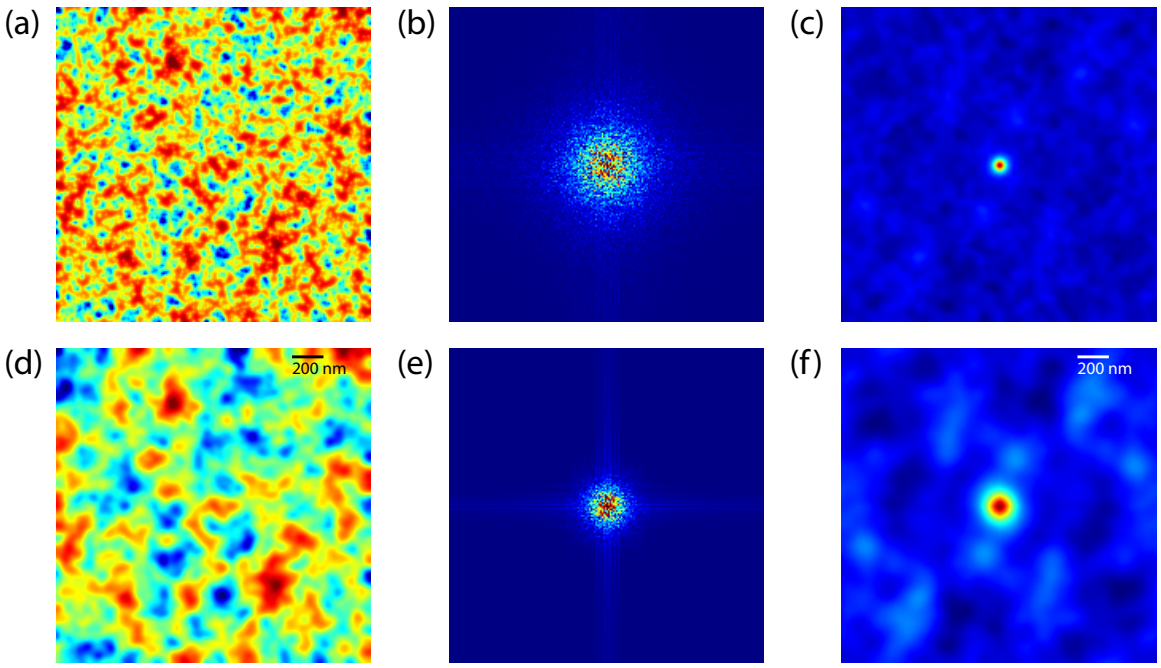

Figure 5-16: Effect of the setback distance on the disorder potential. (a) and (d) show the disorder density profile from the same set of donors at a 20 and 50 nm setback distance respectively. (b) and (e) show the amplitude of the Fourier transform of the density, and (c) and (f) show the autocorrelation function for the density profile. The self consistent disorder potential has the same form as the density profile, as they are linearly related through the density of states at zero magnetic field in the Thomas-Fermi approximation.

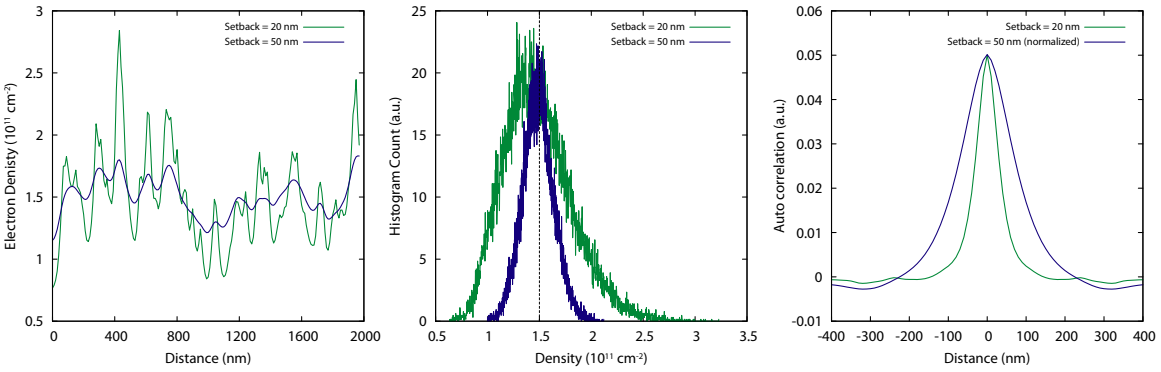

Figure 5-17: (a) A line cut of the disorder density profile for 20 nm (green) and 50 nm (blue) setback distances. (b) Histogram of the simulated density profile for the two setback distances. Note that both density profiles have a high-density tail, caused by the fact that the donors in the simulation are all positively charged. (c) A comparison of line cuts of the autocorrelation function.

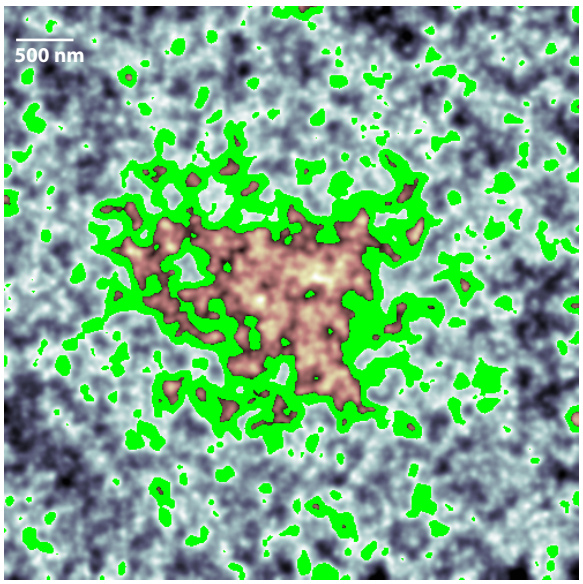

Figure 5-18: Shape of the IR calculated using 1.5×10^{11} cm^{-2} randomly ionized donors with a 50 nm setback. Simulation is for a magnetic field corresponding to $\nu_{\rm bulk} = 0.8$. The perturbation from the tip was included using the jellium model approximation with a tip voltage producing a local density of $\nu = 1.3$ under the tip. The blue color scale shows the density in regions with filling factor $\nu < 1$, the pink color scale shows shown region $\nu > 1$, and incompressible regions of $\nu = 1$ are shown in green. The IR formed with this amplitude of disorder is significantly distorted by disorder, and contains many islands.

are equivalent. In the presence of a large magnetic field, it is more convenient to consider the density profile instead, as the Coulomb interaction of the electrons with the charged donor layer will produce a density profile that follows close that at zero field [51], but results in a drastically different potential profile. As can be seen from figures 5-16(a) and (d), reducing the setback distance results in a smoother disorder potential profile. This can also be seen in the images of the Fourier transform in (b) and (e) and in the autocorrelation images in (c) and (f).

The effect of increasing the setback distance is twofold: it affects both the length-scale of the fluctuations and it reduces the overall amplitude of the fluctuations. This can be seen clearly in the line cuts of the density profile shown in figure 5-17(a), and in the histograms of the 2DES density shown in figure 5-17(b). Figure 5-17(c) shows line cuts of the autocorrelation function for the two setback distances. What is important to note is that although increasing the setback does decrease the amplitude

of the short lengthscale fluctuations, it does *not* create long lengthscale correlations in the potential. In both cases, the correlation length is comparable to the setback distance. The same long wavelength fluctuations are present in both the 20 nm and the 50 nm setback data (see 5-17(a)): however, they are easier to see in the 50 nm data because they are not masked by the larger short lengthscale fluctuations present in the 20 nm setback data.

Figure 5-18 shows a simulation of the IR in the presence of disorder from 1.5×10^{11} cm^{-2} randomly ionized donors with a 50 nm setback. What is quite surprising is that the incompressible strip formed by the tip looks nothing like a ring: its shape has been significantly distorted by disorder. Furthermore, the IR contains a multitude of quantum dot islands. Such a large number of hotspots with such an irregularly shaped IR suggests that the disorder model we have used drastically overestimates the disorder present in our real sample.

5.6.2 Effects of Donor Correlations

During the MBE growth process, the silicon donor atoms are deposited randomly in position in the donor layer. However, in the heterostructures that we use, only a fraction of the donors atoms are ionized. The fact that the donors are only partially ionized allows the system to select the positions of the ionized donors in a way that minimizes the repulsive Coulomb repulsion between them [143, 144, 145, 146, 147, 148] . This is illustrated in figure 5-19. At low temperatures, the non-ionized electrons become trapped into charge neutral DX centers[5], and charge in the donor layer becomes kinetically frozen [143, 145]. If the ionized donors were free to chose any lateral position in the layer, they would form a Wigner crystal. Because they are restricted to the random positions of the silicon donor atoms, they form instead a disordered Wigner glass.

The correlation in the position of the donors can significantly reduce the disorder potential seen by the 2DES. For our simulations, we will use a simpler model for the donor layer than the Monte Carlo simulations of the Wigner glass that captures the

[5]For more information about DX centers, a good starting reference is Davies [131], Chapter 5

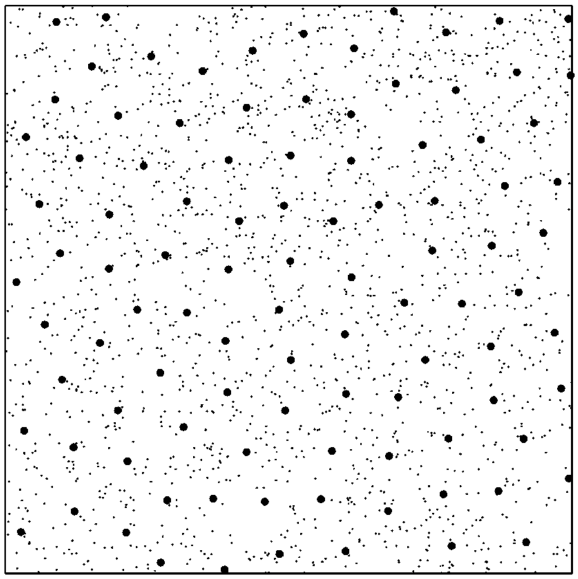

Figure 5-19: The results of Monte Carlo simulations of the formation of a Wigner glass in the donor layer of a GaAs/AlGaAs 2DES heterostructure at an ionization level of 5%. The dots and bullet show the positions of neutral and positive donors, respectively. Figure reproduced from [148].

same basic idea. The model is from Efros [149, 150] and is designed to describe the reduction of the amplitude of disorder fluctuations due to donor correlation. In the non-equilibrium model discussed in [149], the donor layer was treated as a non-degenerate electron plasma at high temperatures. As the system is cooled, the electrons in the plasma become frozen out at a temperature comparable to that required to observe persistent conductivity ($\sim$120 K). Due to this freeze-out, the fluctuations in the donor layer at lower temperatures represent a snapshot of the fluctuations in the electron plasma at the freeze-out temperatures. In this model, the fluctuations as seen from the 2D electron layer can be treated as having the same form as those for randomly ionized donors, but with a reduced amplitude set only by the freezeout temperature:

$$\langle \delta n(r) \delta n(0) \rangle = c_{\text{eff}} = \frac{\epsilon k_B T_0}{4\pi e^2 s} \tag{5.12}$$

where ϵ is the dielectric constant, T_0 is the freezeout temperature and s is the setback to the donor layer. Essentially, the residual fluctuations in this model correspond to

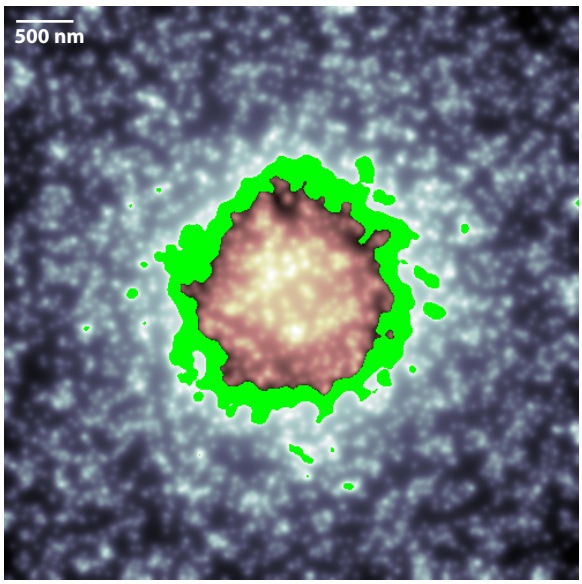

Figure 5-20: Calculated IR including the effects of donor correlations using a $c_{\text{eff}} = 1.5 \times 10^{10}$ cm^{-2}.

defects in the Wigner lattice in the ordered donor layer. Using $T_0 = 120$K give a effective donor concentration of about 1.5×10^{10} cm$^{-}2$. This model is particularly simple to implement: it involves putting in only c_{eff} random donors and replacing the remaining charge in the donor layer with a uniform sheet.

Using this disorder model, the calculated $\nu = 1$ IR is shown in figure 5-20. The ring is now clearly circular and has a much smoother shape. Also, the ring contains quantum dot islands at far fewer tip positions, more consistent with our interpretation of the experimental results.

5.6.3 Moving the Tip: Creating a Simulated SCA Image

As discussed in section 3.2, in a picture where the IR forms a simple ring of constant shape, the intersection of the IR with the fixed hotspot in the 2DES, the SCA images show arc shapes that directly reflect the shape of the IR formed around the tip. This becomes a bit more complicated when we include the effects from disorder distorting the shape of the IR. In particular, one cannot predict the shape of the arcs in the SCA image directly from the shape of the IR shown in figures 5-18 and 5-20 because as we move the tip, the shape if the IR will also change. To correctly predict the

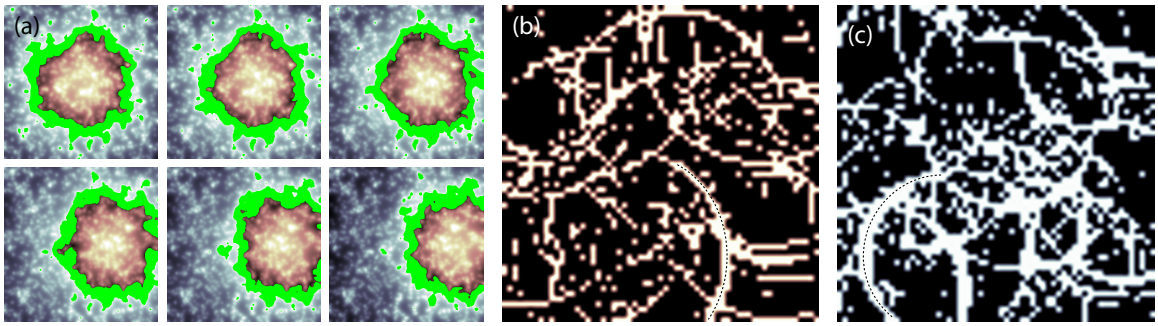

Figure 5-21: By repeating the simulation for a 3×3 μm area with the tip centered at positions on a 50 nm grid, we can produce a 3×3 μm simulated SCA image that is 61×61 pixel, shown in (b). We produce this simulated "image" by identifying tip positions where there is an island in the IR, using an algorithm described in the text. We can also repeat this for a hole-bubble, to produce a simulated hole-bubble SCA image shown in (c). Possible candidates for arcs obeying the electron hole bubble symmetry in (b) and (c) are marked with dashed lines.

shape of the arcs that we see in the images, we would have to perform a series of simulations that determine the locus of tip positions that maintain the intersection of the *changing* IR shape with a given hotspot.

To do this, we have performed a series of simulations of the the IR in a 3×3 μm area where we have moved the tip to different positions on a 50 nm grid, simulating a 61x61 pixel SCA image. These simulations are very time consuming: on a 1GHz desktop computer, each simulation takes 10 minutes to run. To complete simulation for the entire 61×61 grid of tip positions requires 25 days of continuous computation. A subset of the results of such a series of simulations are shown in figure 5-21(a). In the SCA experiment, we directly measure the resistance of the IR. We will not make any attempt to calculate the resistance of the triangular tunnel barrier formed by the calculated IR, nor will we attempt to model the resonant transport through the quantum dot islands. Instead, we will pursue a very simple analysis to extract a prediction of the shape of the arcs in our SCA images. By comparing the shapes of the arcs predicted by the simulations to those seen in the experiment, we may be able to directly infer the nature of the disorder in our sample.

The analysis is as follows. For each simulated image showing the IR at a given tip position, we will perform an image analysis to determine if there is and isolated

$\nu > 1$ or $\nu < 1$ island inside the IR. If there are no islands in the IR, then we will assume that the IR has a large resistance and we will put a "0" in the simulated SCA image to indicate that the central bubble is not charging. If there is at least one island embedded in the IR, we will assume the IR has a low resistance and we will put a "1" in the simulated SCA image.

Unfortunately, such a simple analysis produces a nearly white image, as there are frequently very small islands in the IS (often just a single 10x10 nm pixel). We can improve the results by requiring that the island in the IR has a size beyond a certain threshold to produce resonant tunneling. This thresholding eliminates noise from anomalously small islands that arise in our simulation due to our use of the Thomas-Fermi approximation on such small lengthscales. Such an analysis for a 50 nm threshold island size is shown in figure 5-21(b). Here, we can start to see the signatures of arcs in the simulated SCA image. Furthermore, the arcs do not form close ring, as is observed in the experiment. Figure 5-21(c) shows the same analysis from a set of simulations using a hole bubble. A careful examination shows that some of the partial arcs in the hole bubble images are inverted, as we would expect from the electron-hole bubble symmetry mechanism we proposed based on the experimental data. There is still too much background noise in the image, however, to allow a conclusive comparison.

Ultimately, such an analysis is limited in usefulness by the background noise from the large number of islands present in the rings even with the reduced disorder. It would not work at all on the higher disorder images such as shown in figure 5-18, as these images always display a large number of islands in the ring. An alternative would be to attempt to isolate the effect of a hotspot at a particular position in the sample. For example, the position of a potential hotspot could be chosen by eye and we could perform a similar analysis but only output a bright pixel in the simulated image if there is an island in the IR *and* that island intersects our position of interest. This would produce a simulated SCA image that shows only arcs associated with a single hotspot position. Such an analysis, along with simulation on a finer grid of tip positions, could be useful in predicting the shape of the arcs in the image and

in determining if the partial arcs have the same electron-hole bubble symmetry as observed in the experiment.

Finally, while this simple analysis should be sufficient to predict the shape of the arcs we observe in the SCA images, it is likely that it will not predict the density of the arcs with any degree of accuracy. In particular, simply the presence of an island in the IR will not guarantee a conductance enhancement. The conductance enhancement due to resonant tunneling will depend on the degree to which the tunnel barriers on either side of the island are symmetric [131], as well as quantum confinement and Coulomb blockade effects that we have not accounted for.

5.7 Simulating the incompressible bulk

Aside from applications in simulating the details of our experiments, the software we have developed can also be used to model other aspects of the quantum Hall system. In particular, we have used it to model incompressible strips in the bulk 2DES.

In the nonlinear screening models, the quantized Hall resistance arises due to localization of electrons in the bulk into small puddles by a percolating incompressible strip. Using our simulations, we can predict this localization and visualize the effects of disorder and filling factor on the shape of the incompressible strip.

Some of these results are shown in figure 5-22. At low disorder, the percolating strip is quite wide and occurs only very near to $\nu = 1$. The simulation shows many isolated islands that are small enough to have significant Coulomb blockade energies, as observed experimentally in [116]. At higher disorder, shown in (b), the strip becomes narrower due to the larger mean square disorder gradients, and percolates for a wider range of filling factors. At low magnetic fields, the IS becomes very narrow, as shown in 5-22(c). The narrow incompressible strip has presents much lower tunneling resistance, and the Hall plateaus become narrower. Also, at these low fields, the disorder fluctuations in density Δn_{dis} can become larger than the Landau level degeneracy n_{LL}, and multiple Landau levels are occupied. In this limit, the compressible regions corresponding to different Landau level fillings follow the

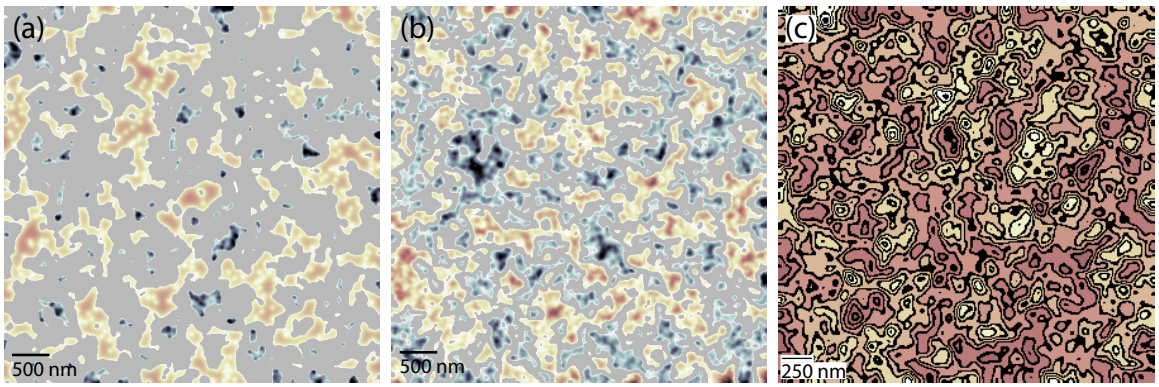

Figure 5-22: Simulations of the incompressible strip that percolates through the bulk at integer filling factor. (a) and (b) show 5×5 μm simulations of the $\nu = 1$ state with correlated (a) and uncorrelated (b) donors and a 50 nm setback. The pink and blue regions are $\nu < 1$ and $\nu > 1$ respectively, and the gray region corresponds to local incompressible $\nu = 1$ state. (c) 3×3 μm simulation with uncorrelated donors showing filling factors at $\nu = 10$. Black regions are incompressible strips at integer filling. The colored areas represent metallic regions of different partially filled Landau levels.

same paths as the drift trajectories in the single particle models. This suggests that in this regime, the transport follows the same phenomenology as predicted by the single particle models, as suggested by Cooper *et al.* [52] and later by Ilani *et al.* [116].

5.8 Conclusions

We began with a very modest plan of modeling the electrostatics of our tip in order to obtain estimates of the capacitive signals we expect to observe in our experiment. We were able to model the capacitance versus distance curves for our tips and the signal levels from the gate remarkably accurately. The results provide very useful insight into the optimal size and shape of the tip for our experiment. They also corroborate well with the empirical evidence we have gathered from experience with different sized tips discussed in chapter 2. Comparison with the simulations provides a method of quantitatively determining the size of the tip *in situ* purely from the capacitance measurements we perform in our scanning experiment.

Incorporating the simple physics of the self-consistent screening model developed

for the quantum Hall effect [47] has allowed us to predict the size and width of incompressible strips that would exist in the experiments from chapter 3 in the absence of disorder. The lever arm reduction of the voltage appearing across the incompressible strp was obtained, along with the value of the capacitance of the bubble to the tip and its surroundings. We found that the bubble's capacitance to the bulk dominated over the other contributions. The bubble's calculated self capacitance was found to be very close to the order of magnitude estimates from chapter 3.

Extending our simulation to 3 dimensions, we simulated the incompressible ring in the presence of disorder from remote ionized donors, allowing us to directly visualize the effect of disorder on the ring. We found evidence from these results that donor correlations play a role in our high mobility heterostructure, and the simulations allow us to directly see the fluctuations that lead to the hotspot islands in the incompressible strip. Work has been started on simulating the effect of the disorder on the arcs seen in the SCA images, and through comparison with these results, we will be able to infer quantitative details concerning the nature of disorder in high mobility heterostructures.

Chapter 6

Future Research Directions

In this thesis, we ahve studied transport through a ring shaped region of incompressible states in the quantum Hall effect. We characterized transport through incompressible regions formed from orbital energy gaps at $\nu = 2$ and $\nu = 4$ as well as at exchange-enhanced spin gaps at $\nu = 1$ and $\nu = 3$. In all cases, transport was dramatically enhanced by resonant transport through Coulomb blockaded quantum dot islands induced by disorder. The existance of these islands and the shape of the arcs we observed provided a unique characterization of disorder in the high mobility 2DES. Measuring the relative tunneling resistance at different filling fractions characterized the magnitude of the micrscopic energy gaps in the quantum Hall effect.

A natural extension of these results would be to study the fractional quantum Hall effect [151, 152, 153]. As shown in figure 6-1, at low temperatures the 2DES displays a staggering number of fractional quantum Hall states at high magnetic fields. These states arise due to the effects of strong correlations between interacting electrons when only the first or the second orbital Landau levels are partially filled. Just as we did for the orbital and exchange-enhanced gaps in the integer quantum Hall effect, we could use our tip to create an incompressible ring formed by the gaps from fractional states. At 300 mK, such an incompressible strip was found to be too leaky. Study of fractional quantum Hall incompressible rings will require larger magnetic fields and lower temperatures.

At lower temperatures with more than two orbital Landau levels filled, it appears

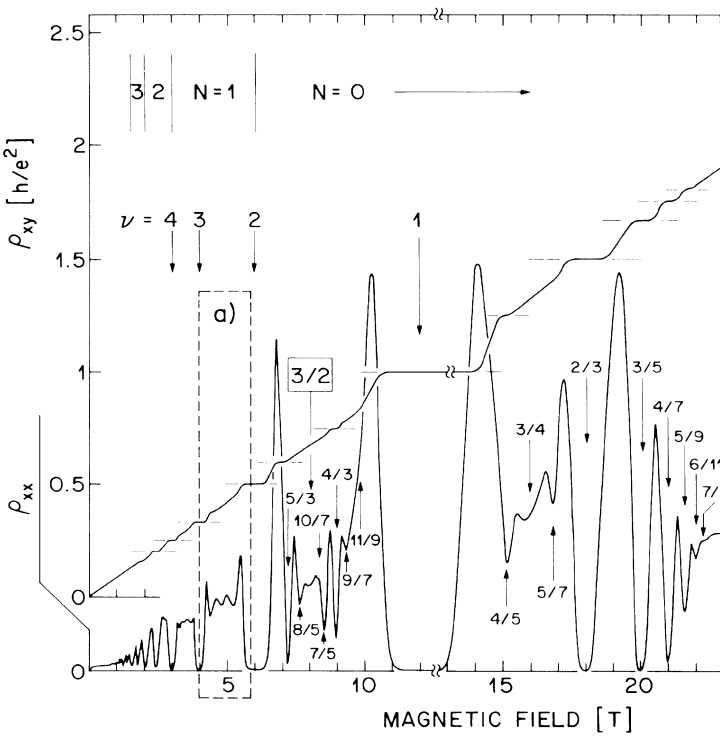

Figure 6-1: The fractional quantum Hall effect in a sample with a mobility of 1.3×10^6 cm^2/Vs and at a temperature of 150 mK. Reproduced from Willett *et al.* [151].

that electron interactions do not create the correlations that lead to the fractional quantum Hall states. Instead, they are believed to create electron crystals (charge density waves) [127], as shown in figure 6-2(a). At 1/4 and 3/4 filling of a spin splig Landau level, this produces a Wigner-crytal-like lattice of clumped electrons, referred to as the "bubble" phase. At half filling, a "stripe" phase is predicted. There is significant experimental evidence for the bubble phase in the form of the reentrant integer quantum Hall effect [128, 154] (see figure 6-2(b)) and in microwave resonance experiments (cite), as well as for the stripe phase in the form of anisotropic transport measurements at half filling of higher Landau levesl [155]. Reentrant phases have also been observed in the first orbital Landau level [102], shown in figure 6-2(c). The origin of these states remains unexplained. All of these exotic phases involve highly resistive states of the 2DES that occur at specific filling fractions. Similar to work we have already done, we could use our microscope to induce a ring shaped region of such a states, and to probe it's local conductance. For example, we could start

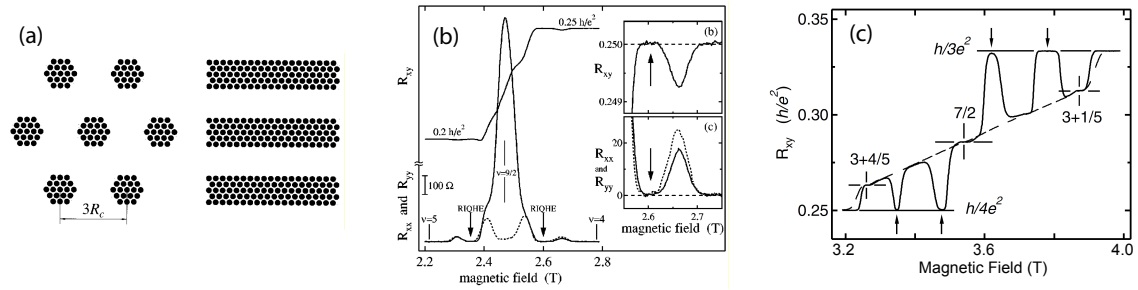

Figure 6-2: (a) Predictions of the bubble and strip phases of electrons in higher Landau levels. Adapated from Fogler *et al.* [127]. (b) Transport measurements shown the reentrant and anisotropic phases in higher Landau levels taken at 50 mK. The sample has a moblity of 1.1×10^7 cm^2/Vs and a density of 2.7×10^{11}. Adapted from Cooper *et al.* [154]. (c) New insulating states in the first orbital Landau level. The dashed line shows data taken at 50 mK and the solid line shows data taken at *approx* 15 mK. Adapated from Eisenstein *et al.* [102].

with $\nu = 4.6$ in the bulk and apply a voltage to induce a region of $\nu = 4.9$ under the tip. These two regions would be separated by a ring shaped region at $\nu = 4.75$. This would allow use to probe and image the resistance of a micrscopic region of bubble-phase electron crystal.

Ultimately, this technique can be applied to any system where the conductance properties vary peridically with the electron density. Moving away from the 2DES, a natural candidate is the 2D hole system (2DHS) in GaAs. Holes in GaAs have a much higher effective mass, which increases the strength of electron interactions relative to quantum kinetic energies[1]. Finally, the technique is not limited to GaAs based materials. In particular, the recently discovered quantum Hall effect in graphene [156, 157] has received a lot of interest due to the peculiar band structure of graphene. The electrons in graphene obey a Dirac-like equation of motion and display an intriguing half-integer quantization of the Hall resistance. Our technique could easily be applied to study localized states in the quantum Hall effect in graphene. Such measurements would provide a unique characterization of disorder in these materials, something that is currently very poorly understood, as well as a local probe of the nature of localiation of Dirac fermions in this exotic quantum Hall effect.

[1]For example, the exchange-enhanced spin gap in holes is much than the oribital gaps. This is reversed from the situation in the 2D electron system

Appendix A

Measuring the Input Noise of the Capacitance Bridge

During the operation of the bridge, we do not need to know either the gain nor shunt capacitance in order to calibrate our capacitance measurements, as this can be done using the known value of the reference capacitor. However, to optimize the sensor design, a knowledge of the shunt capacitance as well as the absolute value of the input voltage noise are required.

In our experiment, we use a bias transistor as our reference capacitor. The source-drain capacitance of a pinched-off FHX45X transistor was measured directly against a 590 fF reference capacitor. This reference capacitor was independently calibrated using a General Radio type 1615A hand-operated capacitance bridge. The source-drain capacitance at 4K was measured as 106 fF. The measurement was also sensitive to whether or not the metal plane under the GaAs chip mount was grounded or not. Ungrounding this metal plane lead to a measured capacitance value of $\sim$120 fF. This suggests that the source drain capacitance of the bias transistor is dominated by the electrode and/or the channel capacitance, and that the contribution from the capacitance from the source lead wire bond to the center point of the bridge was about $\sim$20 fF.

The bias transistor is convenient because it requires one less wire to the sensor. It is also useful for performing gain measurements: unbiasing the gate of the bias tran-

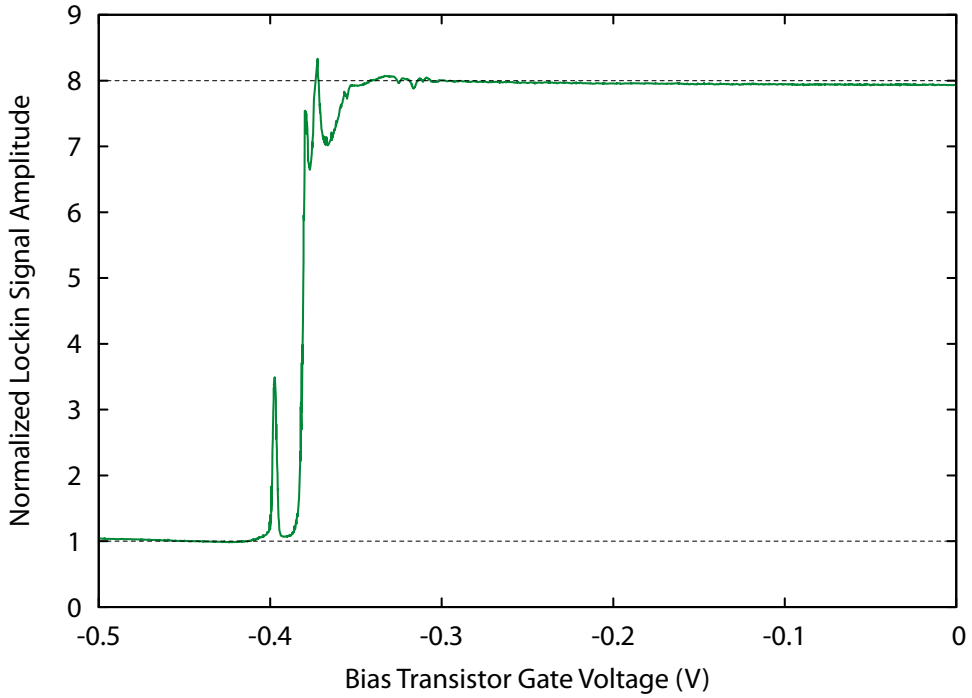

Figure A-1: A measurement of the lockin signal with a small AC voltage applied to the bias transistor source as the bias transistor is pinched off. The ratio of the lockin signal before and after pinch off is equal to the ratio of the total capacitance at the center point of the bridge to the bias transistor source-drain capacitance. For this transistor mount, the total center point capacitance was 800 fF. The spikes in the signal during pinch off are due to resonant tunneling through localized states in the short channel.

sistor, we can apply a known AC excitation directly to the gate of the measurement transistor and directly measure the total amplifier gain. It also provides a simple method of measuring the shunt capacitance. To do this, we apply a small AC excitation to the source of the bias transistor and monitor the lockin signal as the bias transistor is pinched off. The ratio of the amplitude of the lockin signal before and pinch off is equal to the ratio of the total center point capacitance to the reference capacitance. An example of such a measurement is shown in figure A-1.

Once the gain of the amplifiers is known, the input noise can be calculated by measuring the noise at the lockin amplifier using its internal noise mode and then dividing by the gain. This will directly give an input noise in $\mathrm{nV}/\sqrt{\mathrm{Hz}}$ at the frequency that the lockin is set to.

Performing a frequency sweep using the lockin amplifier would be an exception-

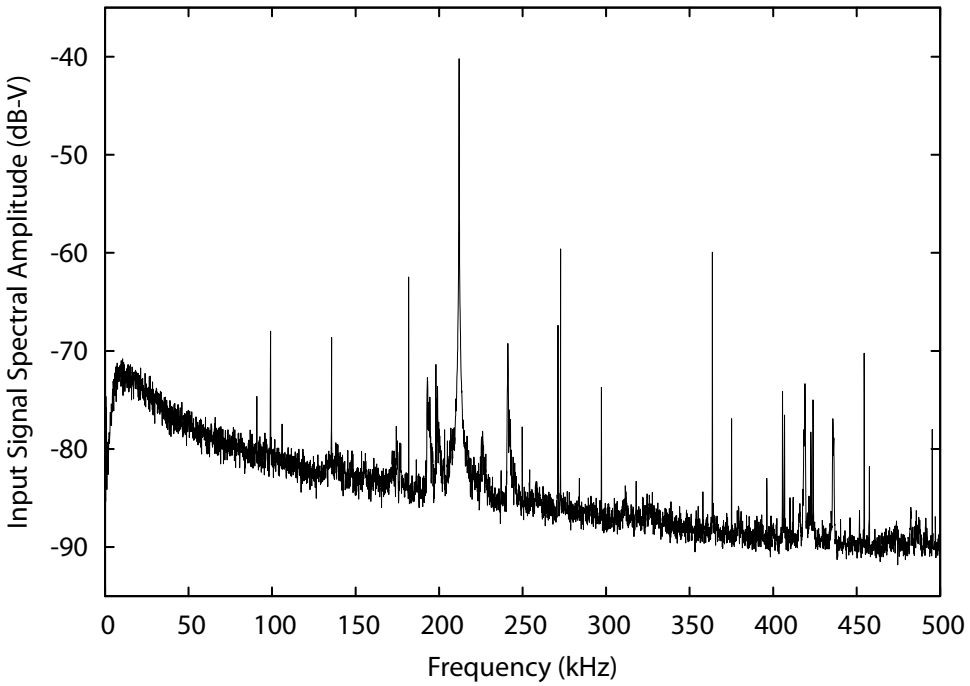

Figure A-2: A broadband noise spectrum measured using the FFT mode of the TDS744. The vertical scale shows the amplitude of the FFT in dB relative to a 1V signal per frequency bin.

ally slow process: lockins are inherently very narrow band instruments designed for optimal out-of-band noise rejection. As such, they are not terribly well suited for measuring broadband noise. A much more efficient way to measure the noise spectrum is to digitize a time trace of the amplified signal and then take a Fast Fourier Transform (FFT). This can be done conveniently using the TDS744 digital oscilloscope to measure the signal from the lockin "Monitor Output" connector, which gives a buffered copy of the broadband signal after the lockin input amplifier. The TDS744 should be set to "HighRes" mode, which will oversample the signal and average the oversampled point. This prevents high frequency noise from being aliased down into our measurement window. The math mode of the TDS744 should be configured to take the FFT of the time trace and then to average the amplitude of the FFTs of subsequent time traces. The frequency resolution is given by $2 * \pi/\Delta t$, where Δt is the spacing between points in the time trace. This is determined by a combination of the time base of the oscilloscope (ms/division) and the record length (number of points per time trace). We typically use a 15,000 point record length.

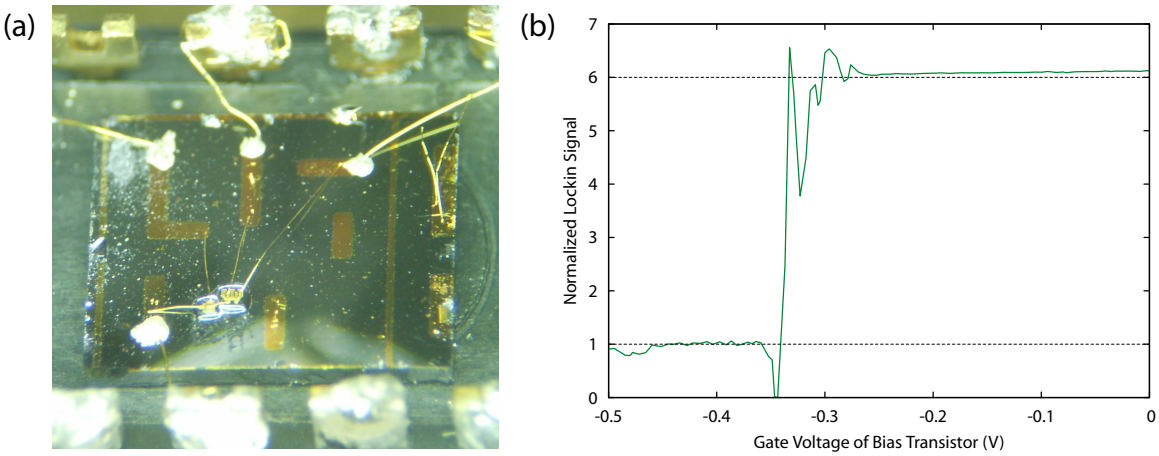

Figure A-3: (a) The transistor setup used to measure the minimum possible center point bridge capacitance C_T. (b) A pinch off measurement to determine the ratio of the C_T to the bias transistor source-drain capacitance. The measurement shows that the minimum possible capacitance is about 600 fF. The mount fabrication and capacitance measurement was performed by Eric Lin.

The result of such a measurement is shown in figure A-2. The units on the vertical scale are "dB-V per frequency bin". This corresponds to the total integrated FFT amplitude in one frequency division relative to a 1V sine-wave signal. We should be able to convert this to directly to a noise reading in $\mathrm{nV}/\sqrt{\mathrm{Hz}}$ by dividing by the square root of the spacing of the points in frequency. For some reason, this does not seem to work. Nonetheless, the trace provides a quantitative measure of the relative noise magnitudes at different frequencies, and can be calibrated to units of $\mathrm{nV}/\sqrt{\mathrm{Hz}}$ by normalizing to a value at one frequency measured using the lockin noise mode.

As a final note, an absolute minimum possible shunt capacitance for a configuration using these transistors was obtained by Eric Lin by measuring the shunt capacitance of a bias and measurement transistor with no tip, shown in figure A-3. For this setup, a total bridge capacitance of 600 fF was measured. This suggests the smallest possible shunt capacitance possible using wire-bonded transistors is around 600 fF. It also suggests that the added shunt capacitance from the tip is on the order of 200 fF.

Appendix B

Transconductance Calculations and Noise Considerations for the HEMT Amplifier

The charge sensor in our experiement uses a High-Electron Mobility Transistor (HEMT) to convert AC charge on its gate into a voltage at the input of our lock-in amplifier. In order to better understand hwo the parameters of the HEMT affect this measurement, we derive in this appendix the gain of the circuit in terms of the properties of the HEMT field effect transistor.

B.1 Properties of a FET

A field effect transistor (FET) consists fo a channel whose resistance is controlled by an external gate voltage, as shown in figure B-1(a). Typcial I-V curves of a FET are shown in figure B-1(c). At low source-drain voltages, the drain current is proportional to the source-drain voltage, and the FET acts like a variable resistor. This is called the linear regime. At larger source-drain voltages, the current increases sublinearly, and eventually saturates. The source-drain current after saturation is set only by the gate voltage.

A common and useful small signal model for a FET is shown in figure B-1(d).

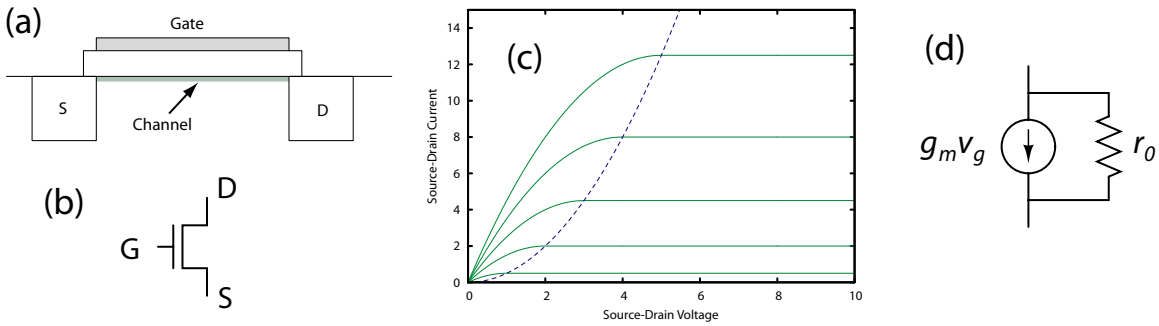

Figure B-1: (a) The layout of a typical field field effect transistor and (b) the schematic symbol used. (c) I-V curves for an ideal FET. The dotted line shows the saturation current for the quadratic model. (d) A common model of a FET using a current source in parallel with an output resistance.

The FET is modelled as an ideal current source in parallel with a ouput resistance r_o. The current source provides a small signal current given by $g_m v_g$, where g_m is called the transconductance, and is defined by:

$$g_m(V_g, V_d) = \left.\frac{\partial I_d}{\partial V_g}\right|_{V_d}$$

In general, the transconductance depends on both the DC gate voltage and the DC drain voltage. The output resistance r_o is given by:

$$r_o(V_g, V_d) = \left.\frac{\partial V_d}{\partial I_E}\right|_{V_g}$$

It too will depend in general on both the gate voltage and the drain voltage. This model becomes particularly simple in the saturated regime. After saturation, the output resitance $r_0 \to \infty$ and the FET can be considered an ideal (small signal) current source. Also, in saturation the transconductance depends only on the gate voltage. This model is also very useful when we are not in saturation, although we have to keep in mind that r_o and g_m will depend on V_g and V_d. In the next section, we will calcuate the I-V curves of a FET using a simple model. From these, we will obtain expressions for the transconductance and output resistance in the linear and saturated regimes as a function of the gate and drain voltage, as well as the physical properties of the transistor.

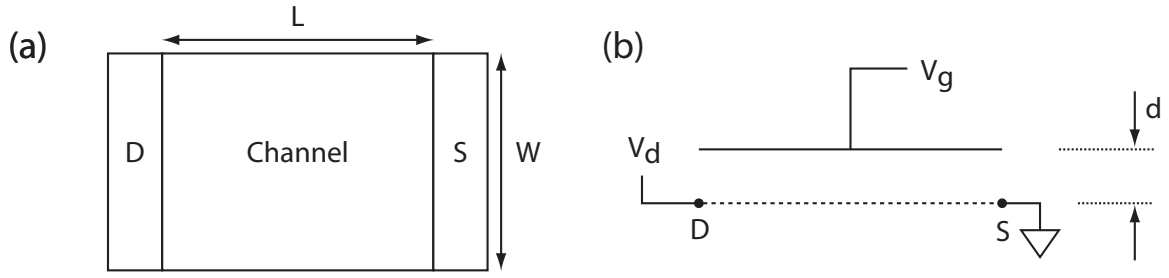

Figure B-2: Dimensions of the FET. (a) Top view. (b) Side view, showing separation of the channel from the gate.

B.2 Modelling the FET

Our derivation wil be based on an analysis of a MOSFET given in [158] . We will consider a channel of width W and length L shown in figure B-2(a). The gate will be sepaarted from the channel by a distance d by a insulator with dielectric constant ϵ. Applying a voltage V_SD across the source and the drain, a current will flow between the source and the drain given by:

$$I_{SD} = V_{SD}/R_{SD} = G_{SD}V_{SD}$$

where G_{SD} is the total conductance of the channel. We will consider first the linear regime, where $V_D << V_G^D$, where V_G^D is the gate voltage required to fully deplete the channel. In this case, the density across the channel can be considered approximately constant. We will take the conductivity of the layer to be linearly proportional to the electron concentration:

$$\sigma = ne\mu$$

In particular, this assumes that the mobility μ of the 2D layer is independent of density. In the linear regime, the conductivity of the channel is constant, and the total conductance is given by:

$$G = \frac{\sigma W}{L} = \frac{ne\mu W}{L}$$

The electron density in the channel is determined by the gate voltage through the capacitance to the gate:

$$n = n_0 + \frac{1}{e}\frac{\epsilon V_G}{d} = \frac{\epsilon}{ed}(V_G - V_G^D)$$

where $V_G^D = -\frac{ed}{\epsilon}n_0$. We then have:

$$I_D = \frac{\mu\epsilon}{d}\frac{W}{L}(V_G - V_G^D)V_D$$

and the transconductance

$$g_m = \frac{\mu\epsilon}{d}\frac{W}{L}\ V_D \tag{B.1}$$

and the output resitance

$$r_o = \frac{d}{\epsilon\mu}\frac{L}{W}\frac{1}{V_G - V_G^D}$$

At higher currents, the local voltage $V_C(x)$ in the channel due to the voltage drop from source to drain will now be significant enough to modify the local charge density $n(x)$ in the channel due to the capacitance to the gate. We will consider an infinitessimal section of the channel of length dx. By conservation of current, the current through this section must be equal to I_D. We can relate the current through this section to the drop dV_C

$$I_{SD} = \frac{n(x)e\mu W}{dx}\ dV_C(x)$$

The local density at position x of the channel is now given by

$$n(x) = \frac{\epsilon}{ed}(V_G - V_G^D - V_C(x))$$

This gives the relation

$$I_D dx = \frac{\epsilon\mu}{d}W(V_G - V_G^D - V_C(x))dV_C(x)$$

The drain current is constant across the channel. Integrating:

$$I_D \int_0^L dx = \frac{\epsilon\mu}{d} W \int_0^{V_{DS}} (V_G - V_G^D - V_C) dV_C$$

gives

$$I_D = \frac{\epsilon\mu}{d}\frac{W}{L}\left[(V_G - V_G^D)V_{DS} - \frac{(V_{DS})^2}{2}\right] \qquad V_{DS} < V_G - V_G^D$$

As we increase the drain voltage, the current does not increase as quickly as for a simple resistor because portions of the channel are at a lower electron density and have a lower conductivity. Once we reach the point where $V_{DS} > V_G - V_G^D$, a narrow depletion region forms near the drain. This region has a very high resistance. As we increase the drain voltage further, the width of this region self-consistenly adjusts itself to accomodate the extra voltage drop, keeping the current at a constant value.

Before saturation, the transconductance has the same form as in the linear regime:

$$g_m = \frac{\mu\epsilon}{d}\frac{W}{L}\ V_D$$

while the output resistance has increased:

$$r_o = \frac{d}{\epsilon\mu}\frac{L}{W}\frac{1}{V_G - V_G^D - V_{DS}}$$

After saturation, $r_o \to \infty$ and V_D is replaced by $V_G - V_G^D$ in the transconductance expression.

The only assumption we have made that may not hold for at HEMT transistor[1] is that the mobility μ is independent of density. In the 2DES at low temperatures, simple models (see [131]) predict that the mobility varies as a power law $\mu \sim n^{1.5}$. In the linear regime, this simply means that in the expression for the transconductance, μ depends on V_G. In the non-linear regime, this will lead to additional terms in the integration accouting for the fact that the mobility also varies with the gate voltage. The model would no longer be quadratic, but the corrections would be simple to

[1] Aside from effects from extremely short channels

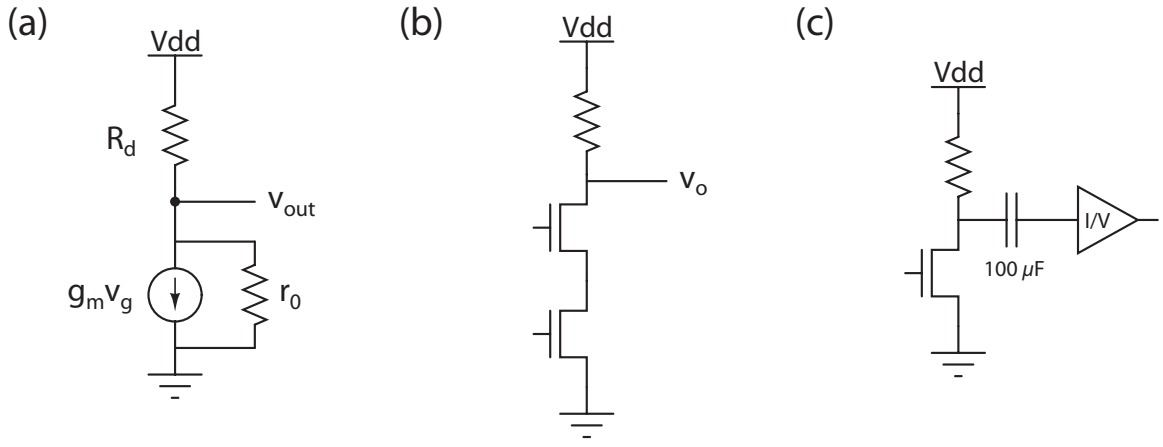

Figure B-3: (a) Model of a common-source amplifier. (b) Eliminating the effect of the output resistance r_o by placing a second transistor in "cascode" with the first, which acts as a low-impedence current to voltage converter. The increases the voltage gain and the bandwidth if there is a large capacitance at the drain of the first transistor (such as a cable leading out of a cryostat). (c) A similar solution using an AC coupled current amplifier. Note that the coupling capacitor must be very large so that its AC impedence is smaller that the 50 ohm input of the current amplifier.

include.

B.3 Amplifier Design

These expression can easily be applied to predict the gain of a common-source voltage amplifier shown in figure B-3(a). In the amplifier, a drain resistor is used to convert the FET current into an output voltage v_o. In this case, the voltage gain is given by the drain current multiplied by the parallel resistance of R_d and the FET output impedence r_o:

$$\frac{v_o}{v_g} = g_m \left(\frac{1}{\frac{1}{R_d} + \frac{1}{r_o}} \right)$$

Note that if we are not in the saturated regime, the voltage gain is reduced because the transistor current source is now driving a lower impedence resistor formed from the parallel combination of R_d and r_o. Effectively, some of the current is "leaking out" through the low output impedence of the FET. The situation can be remedied by instead using a current-readout method. This can be done either by including a second FET in "cascode" with the HEMT [159, 160] shown in figure B-3(b), or

by directly using an AC coupled current amplifier shown in figure B-3(c). For the cascode, biasing the circuit can be tricky [160]. The current amplifier is easier to setup, although constructing a stable, low-noise, wide bandwidth current amplifier can be difficult. A design by Oliver Dial using an Analog Devices current-input op-amp was used occasionally in our experiment. Both of these techniques eliminate the effects of the small output resistance r_o on the gain.

The common-source amplifier shown in B-3(a) will also suffer from a poor bandwidth if there is a large capacitance from the cable connected to its drain, since this capacitor must charge up through the impedence provided by the parallel combination of R_d and r_o. By providing a AC low impedence point at the drain and effectively measuring currents rather than voltages, the designs in B-3(b) and (c) also significantly increase the bandwidth of the amplifier.

B.4 Charge Transconductance

In our experiment, we are fundamentally concerned not with voltage amplificatoin, but instead with amplifying a signal proportional to the charge on the gate. For this, we will define a charge transconductance:

$$e_m = \frac{\partial I_D}{\partial q_G} = \frac{\partial I_D}{\partial V_G}\frac{\partial V_G}{\partial q_G} = \frac{g_m}{C}$$

Using the $C = \epsilon WL/d$ and expression B.1 for g_m gives

$$e_m = \frac{\mu}{L^2}\ V_{DS} \tag{B.2}$$

The charge transconductance is independent of the width of the channel, but depends strongly on the channel length.

For the operation of the capacitance bridge, we will consider the situation shown in figure B-4. Here we have a charge q that is distributed across a the gate of the transistor and a capacitance C_0. C_0 represents the sum of all the capacitances at the

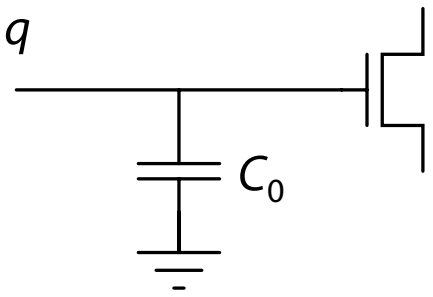

Figure B-4: The amplifier shown with the capacitance C_0 from the bridge and a charge q.

centerpoint of the bridge except for that of the gate of the measurement transistor:

$$C_0 = C_{sample} + C_{ref} + C_{stray}$$

We are interested in the drain current modulation i_d for a given q at the center of the bridge. This charge q will generate a voltage v given by:

$$v = \frac{q}{C_G + C_0}$$

where C_G is the transistor gate capacitance. Using $i_d = g_m v$ and expression B.1 for the transconductance gives:

$$\frac{i_d}{q} = \frac{C_G}{C_0 + C_G}\frac{\mu V_{DS}}{L^2}$$

Note from this expression that increasing C_G by making the channel wider but keeping the same channel length will always result in a larger modulation of the drain current for a given input q. For a given C_0 imposed by experimental limitations (stray capacitance of wire bonds, sample capacitance, etc), we should always use a transistor with a gate length L as short as possible but with a gate width W such that C_G is comparable to or greater than C_0. In particular, it means that cleaving the measurement transistor will actually decrease the charge amplification. This can be understood physically from the expression B.2 for the charge transconductance e_m. Since e_m is independent of channel width, increasing the FET input capacitance by using a wider channel will result in a larger fraction of the charge q being put on the

transistor gate.

In practice, there is a limit to how wide the channel is made on commercially avialable HEMTs. The effective channel width can always be made wider by combining multiple HEMTs in parallel, although one has to be careful that the wire bonds are kept short in order to prevent adding stray capacitance.

B.5 Noise

In the previous section, we showed that the charge amplification will always increase if we use transistor with a wider channel. However, this does not neccessarily mean that our charge *sensitivity* will increase since this also depends on how the noise of the transistor changes.

Fortunately the $1/f$ noise generated by a FET is generally inversely proportional to the number of carriers in the channel, or equivalently the area of the channel (see [161, 73] and section VIII.4 of [72]). This suggesets that the wider channel will not only increase the charge amplification, but also decrease the noise, resulting in an even stronger enhancement of the sensitivity. Noise, however, is not a perfect science, and systematic experiments would be needed to substantiate these claims.

Appendix C

Images Taken with a Smashed Tip

In this appendix, we include some images from an earlier cooldown that were taken with a smashed tip. It was with this smashed tip that we first observed the resonances. However, due to the irregular shape of the tip, the incompressible ring had a very irregular shape, making it difficult to interpret the data. The tip from this run showed a capacitance "upturn" of about 3 fF and showed a gate smear of about 3 μm. These both suggest that the tip was very, very large, likely having a flattened end with a diameter of possibly as large as 5 μm.

During this run, we frequently touched the surface during recondensation. After the tip had touched the surface, a "donut" shaped perturbation of the electron density was seen, presumably due to the deposition of charge into surface states. This charge would spread outwards and eventually discharge over a period of about 12 to 24 hours. Curiously, on re-inspection the edges of the "donut" often seem to correlate with shapes seen in the filaments in the images, suggesting the possibility that before it discharged the donut may have been an indication of the shape of the flat end of the tip.

The images will include only brief captions describing the magnetic field and the approximate tip voltage they were taken at.

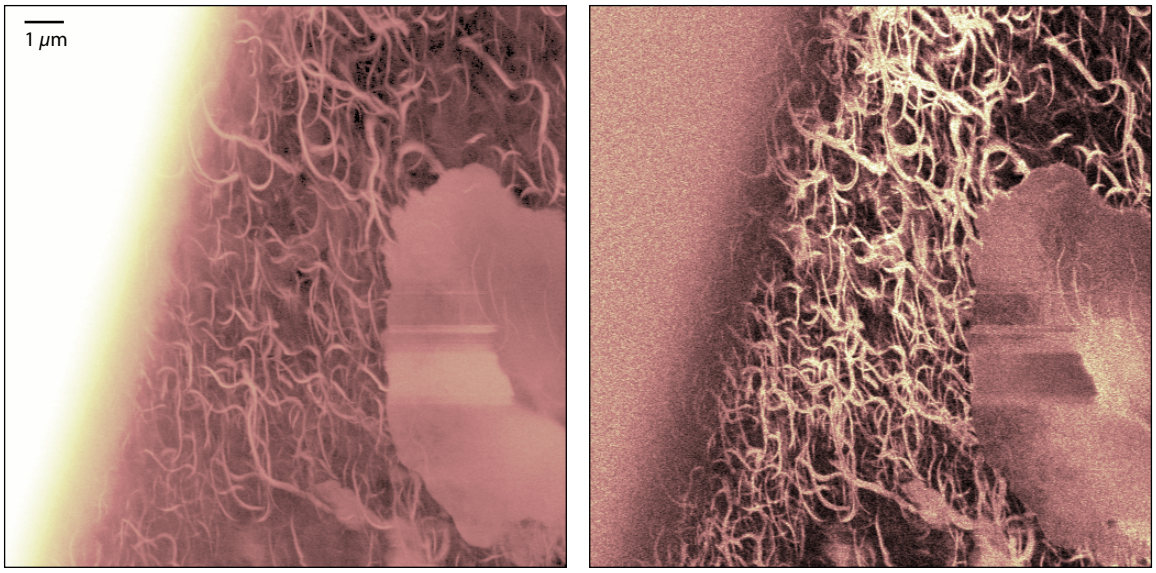

Figure C-1: 14×14 μm in-phase and lagging phase electron bubble images at 6.9T and -1.25V. The charge perturbation from touching the surface is also shown.

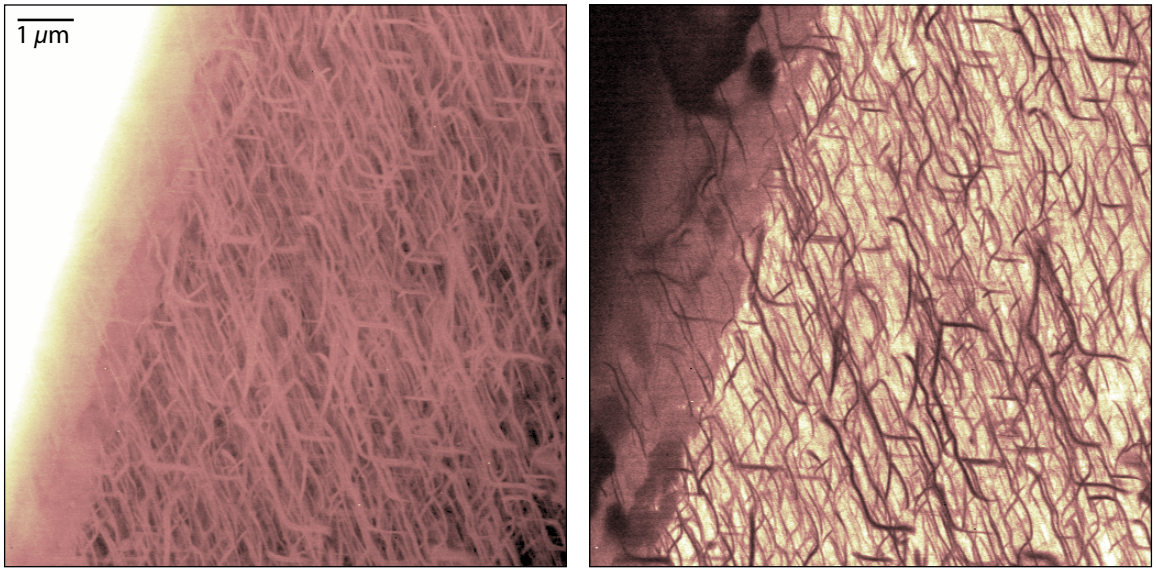

Figure C-2: 10×10 μm in-phase and lagging phase electron bubble images at 5.5T and -0.75V.

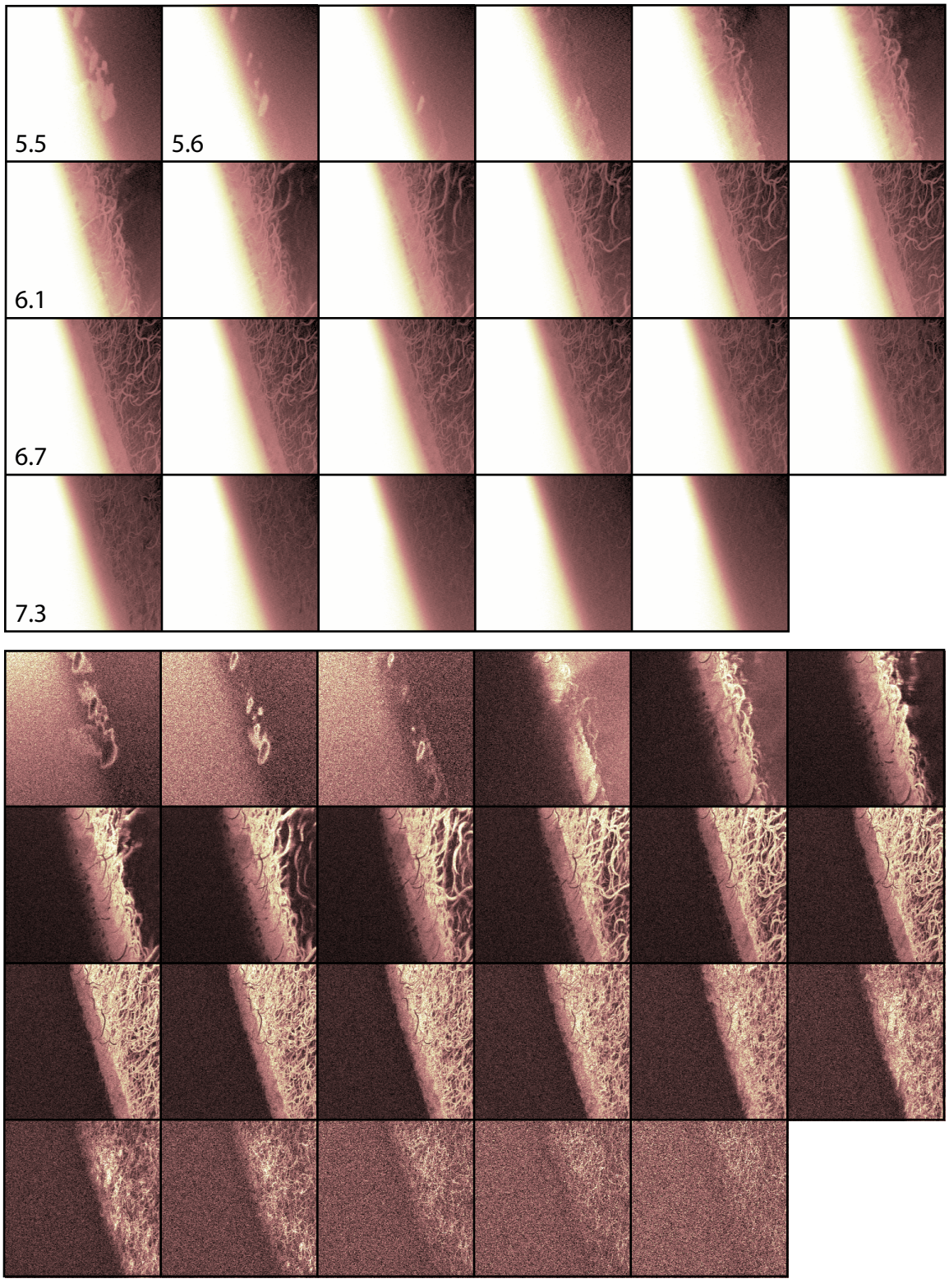

Figure C-3: 10×10 μm electron bubble magnetic field sweep from 5.5 to 8.0 in 0.1T steps at a tip voltage of +1.25V.

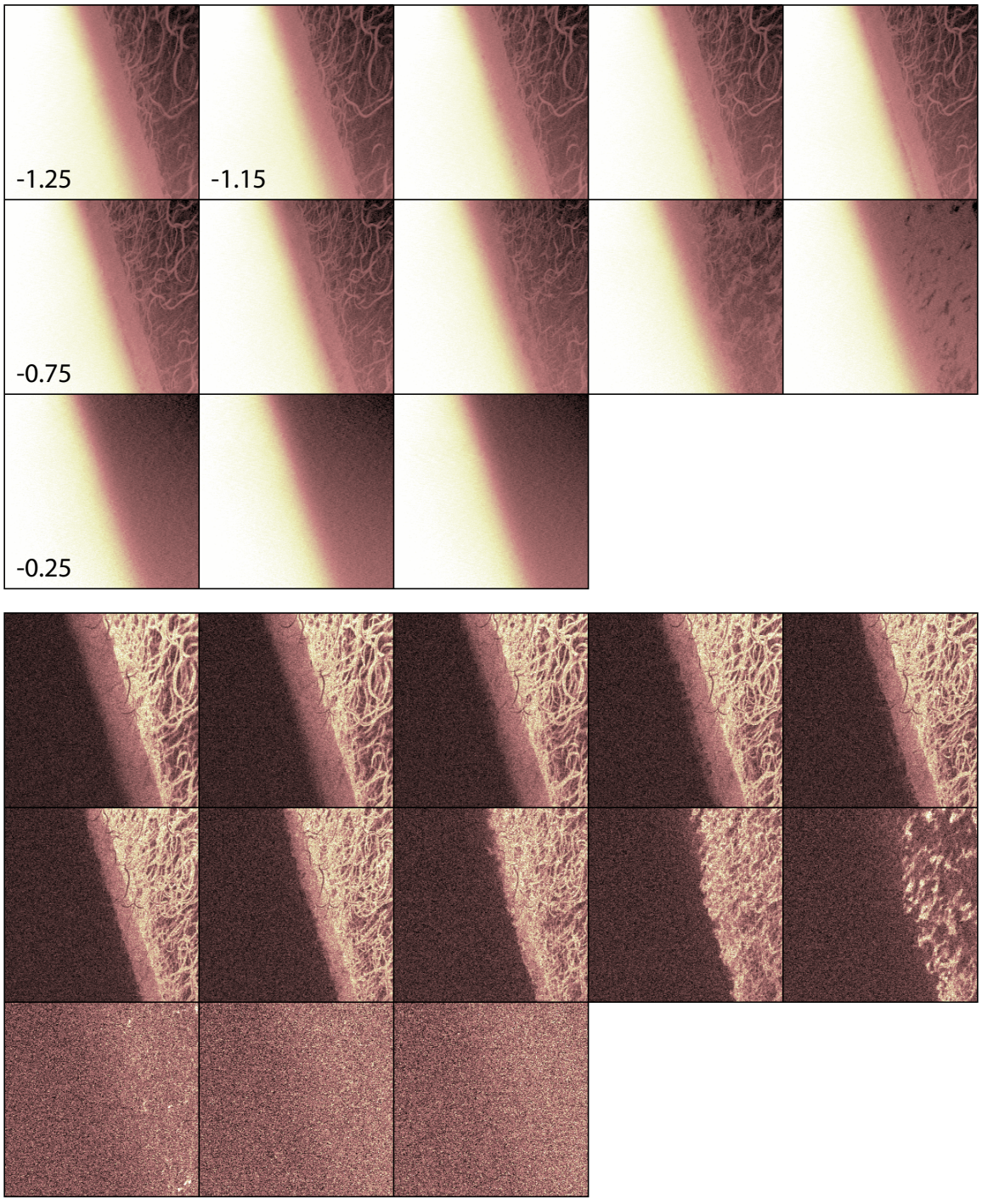

Figure C-4: 10×10 μm electron bubble tip bias voltage sweep from +1.25 to +0.05 V at 6.9T.

Figure C-5: 10×10 μm $\nu = 2$ hole bubble tip bias voltage sweep from -2.25 to -1.00 V at 2.6T. A "donut" charge perturbation is visible in the images.

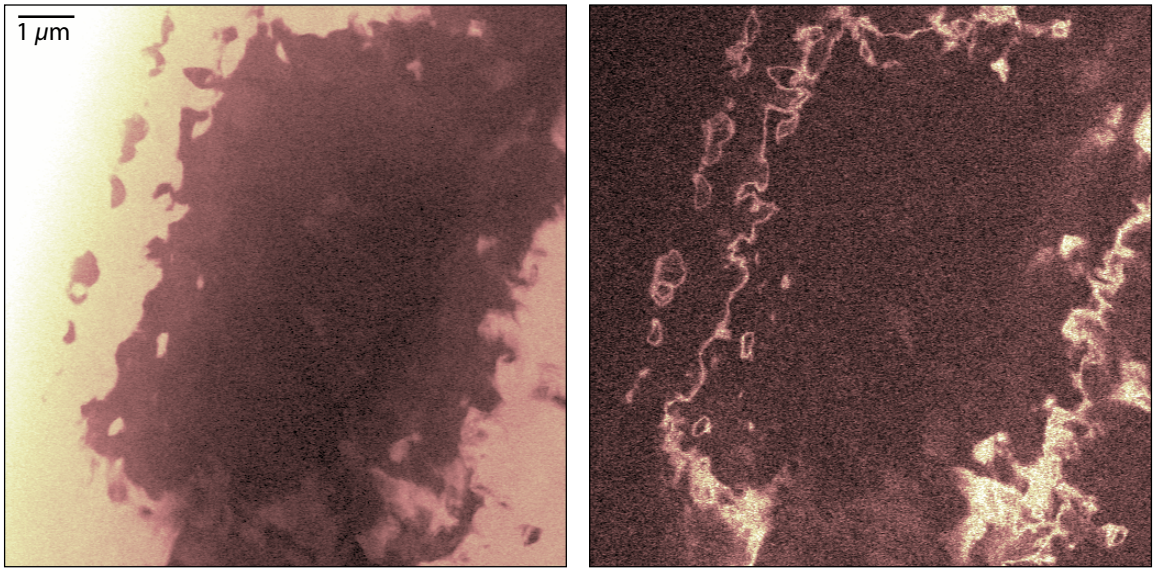

Figure C-6: 10×10 μm in-phase and lagging phase images at 6.4T and 0.25V (near null) with a 5 mV excitation. Features in the image are far sharper that we expect from the electrostatic resolution of the tip determined from the smearing of the gate edge. Similar over-sharp features were seen using an etched tip that had not touched the surface.

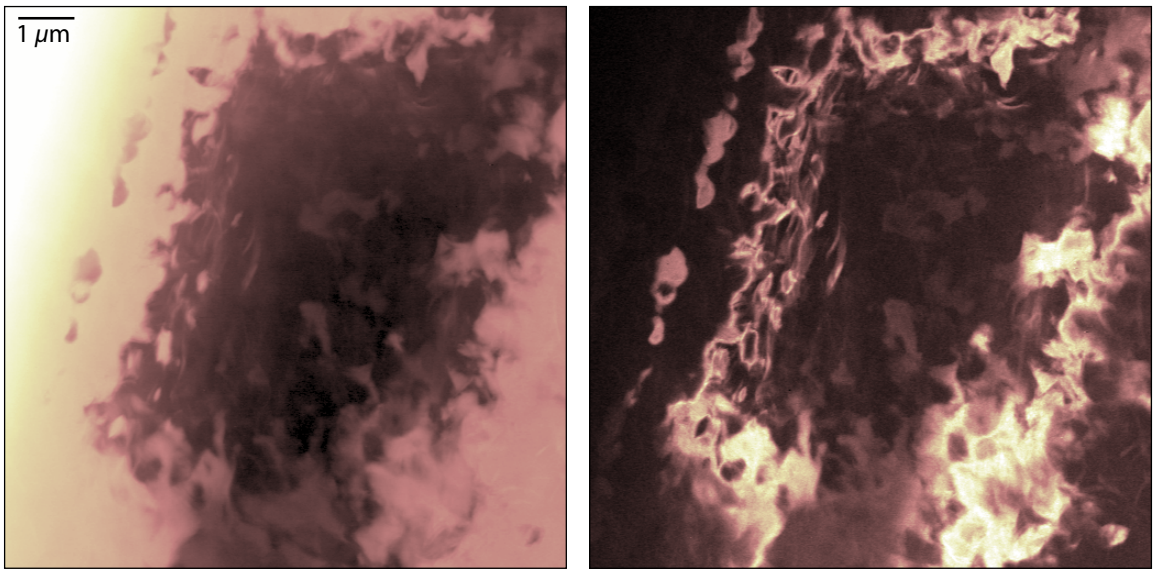

Figure C-7: 10×10 μm in-phase and lagging phase images at 6.4T and 0.25V (near null) with a 10 mV excitation. Compared to the 5 mV images, the sharp edges are smeared slightly, although they are still much sharper than the electrostatic resolution.

Appendix D

Depleting the Sample with a Global Backgate

Since the backgate in our experiment consists of a metal film evaporated on the back of the insulating intrinsic GaAs substrate, we need to apply several hundred volts to it to achieve a significant density change. To calibrate this, we perform magnetocapacitance traces as a function of the backgate voltage. These results are shown in figure D-1. There are a couple of things that are peculiar about these measurements. While the magnetocapacitance dips varied linearly with voltage over much of the backgate voltage range, near zero voltage it curved and came in flat. This suggests that there is a layer below the 2DEG between it and the backgate that needed to be depleted before we could gate the 2DES. In addition, as we start to deplete the sample and come out of this curved region, the depth of the MC dips increases dramatically. This indicates that at the lower densities, the charging of the sample is decreasing in Hall plateaus. This could be related to a change in the density under the gate relative to the bulk 2DES, producing changes in the bulk charging as discussed in section 2.6.

A second strange behavior was that after stepping the backgate voltage, it took several minutes for the density to stabilize, as shown in figure D-2. This suggests that the space charge layer below the 2DES was charging and discharging very slowly. This limited our ability to sweep the bias voltage quickly. This limited us to steps in bias

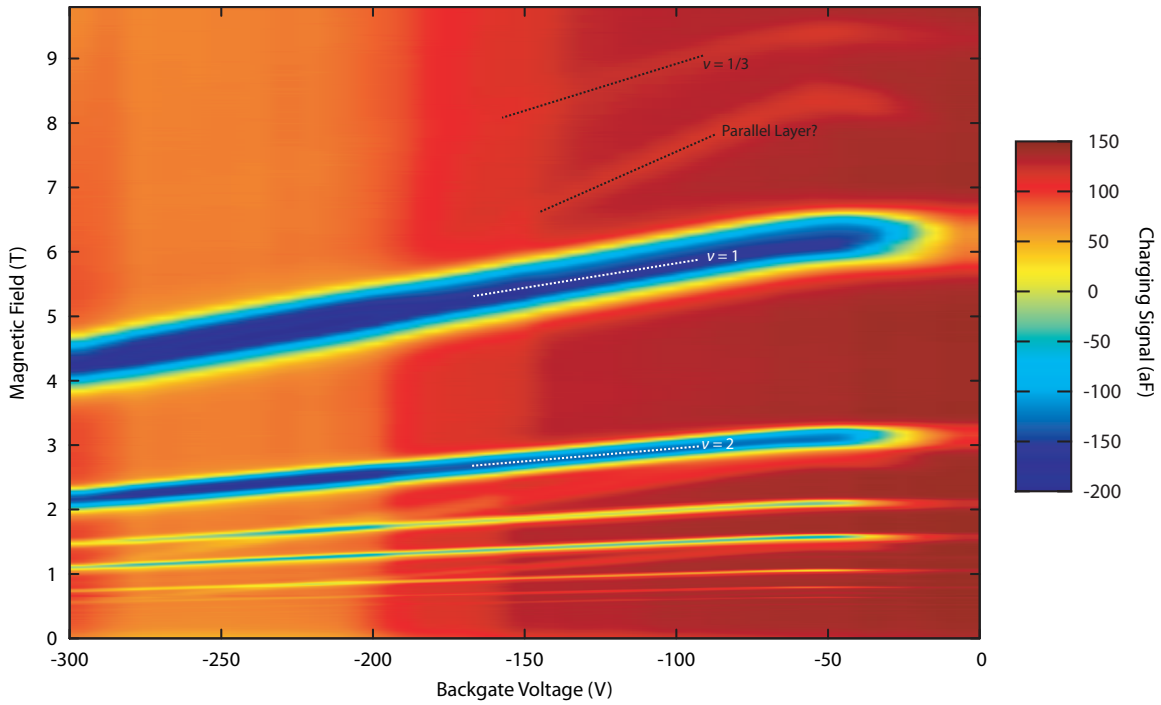

Figure D-1: A color-scale plot of the in-phase charging signal as a function of magnetic field and backgate voltage. The traces were taken before walking in, with the tip about 1 mm from sample.

voltage followed by sweeps in magnetic field for the data shown in figure D-1, which is very time intensive and uses considerably more helium, since the magnet was sweeping continuously.

Finally, a careful examination of the data in figure D-1 shows a second set of Landau fans. This can be seen more clearly in a numerical derivative of the data, shown in figure D-3. The peaks in this second Landau fan have a steeper slope with backgate voltage, suggesting the presence of a second 2D layer forming below our 2DES when we apply a backgate voltage. Since it was not between the tip and the 2D layer of interest, it did not significantly affect our capacitance measurements.

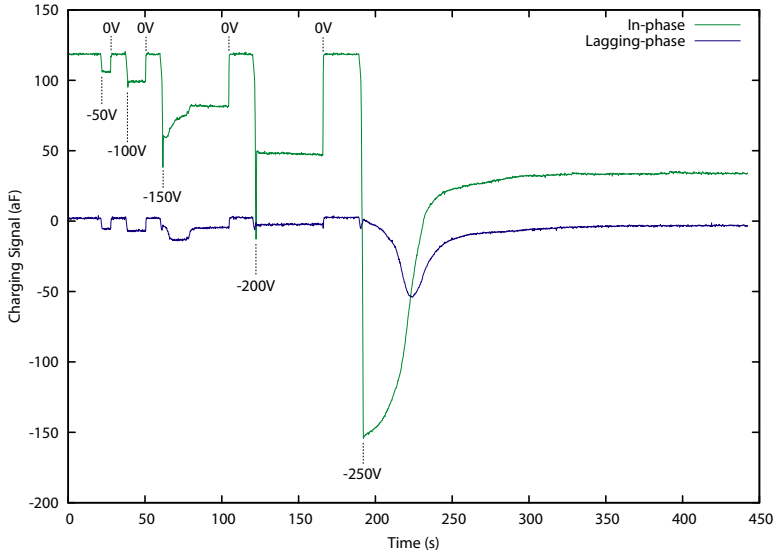

Figure D-2: Charging signals as a function of time after stepping the backgate voltage at zero magnetic field. The backgate initially at 0V, and was stepped at different times to the voltages indicated in the plot. Curiously, stepping the backgate to negative voltages resulted in much longer relaxation times that returning it to 0V.

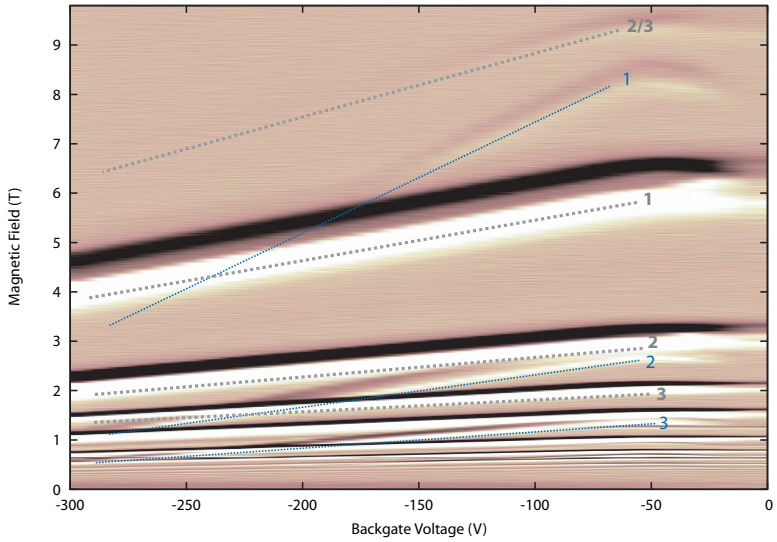

Figure D-3: The derivative of the magnetocapacitance data, taken in the vertical (magnetic field) direction. A second set of Landau fans are visible upon applying the backgate voltage. The fact that the second set of peaks has a steeper slope suggests that they arise from a second 2D layer formed behind the 2DES.

Appendix E

Distributed RC Network

We will start with a single RC, as shown in figure E-1(a). The charge on the capacitor C is determined by the voltage V_1, which is given by a voltage divider between the capacitor and the resistor:

$$\frac{V_1}{V} = \frac{Z_C}{Z_C + R}$$

where Z_C is the complex impedence of the capacitor:

$$Z_C = 1/i\omega C$$

The total charge on the capacitor as a function of the frequency of the applied voltage is then:

$$\frac{Q_T^*(\omega)}{Q_T(0)} = \frac{1}{1 + R/Z_C} \tag{E.1}$$

To calculated the total charge on all of the capacitors in the two-element RC circuit, we will need to find expressions for V_1 and V_2 in figure E-1(b). V_2 is determined by a voltage divider between R and Z_2:

$$\frac{V_2}{V} = \frac{1}{1 + R/Z_2}$$

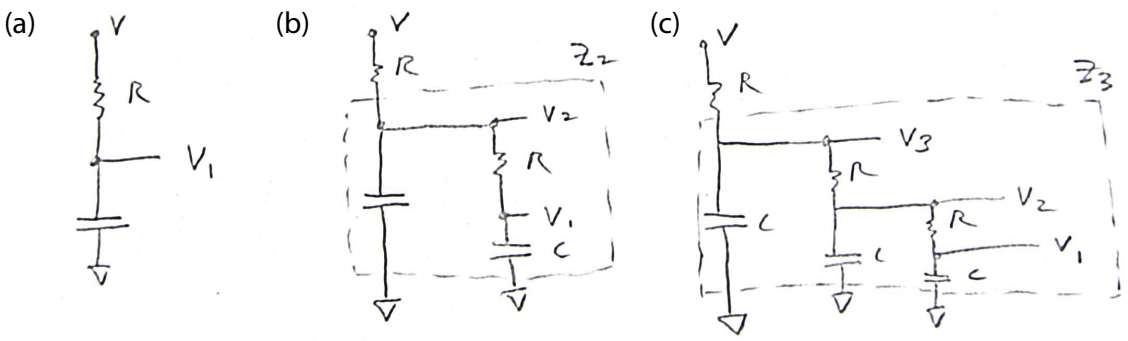

Figure E-1: Schematics for (a) 1 element RC network, (b) 2 element RC network, and (c) 3 element RC network.

Z_2 is given by the parallel combination of the capacitor C on the left branch and the series RC on the right branch:

$$\frac{1}{Z_2} = \frac{1}{Z_C} + \frac{1}{R + Z_C}$$

V_1 is determined from V_2 using the same divider as the single element case:

$$\frac{V_1}{V} = \frac{1}{1 + R/Z_2} \cdot \frac{1}{1 + R/Z_C}$$

The total charge $Q_T = CV_1 + CV_2$ is then:

$$\frac{Q_T^*(\omega)}{Q_T(0)} = \frac{1}{1 + R/Z_2}\left(1 + \frac{1}{1 + R/Z_C}\right) \tag{E.2}$$

Repeating this for the three element case, Z_3 will be given by:

$$\frac{1}{Z_3} = \frac{1}{Z_C} + \frac{1}{R + Z_2}$$

and we will have:

$$\frac{Q_T^*(\omega)}{Q_T(0)} = \frac{1}{1 + R/Z_3}\left[1 + \frac{1}{1 + R/Z_2}\left(1 + \frac{1}{1 + R/Z_C}\right)\right] \tag{E.3}$$

The continuum limit was calculated by F. Stern [162] for a 1D channel, and for a circular annulus or disc by Goodall *et al.* [91]. It turns out that the cicular ring is

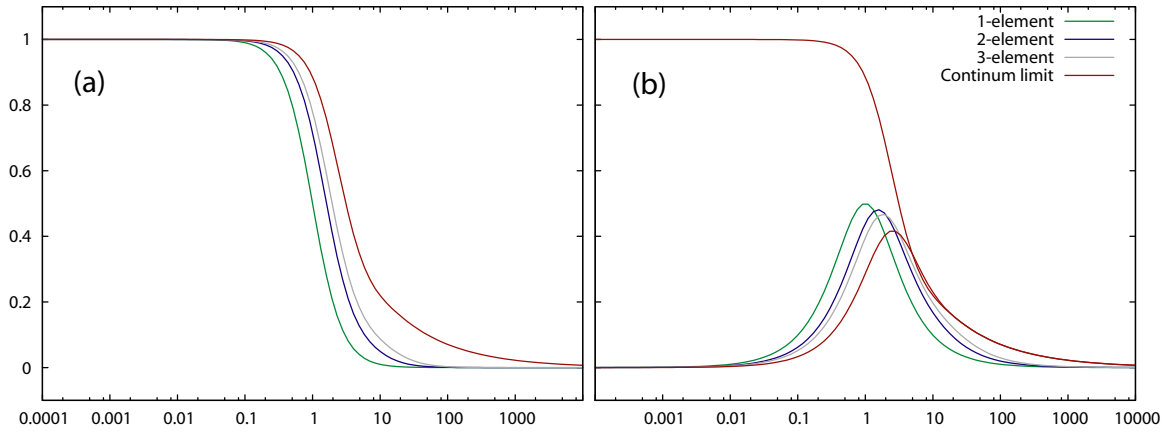

Figure E-2: In-phase (a) and lagging-phase (b) components of the total charge on the capacitors. In the discrete element models, elements were chosen so that $\sum C = 1$ and $\sum R = 1$. In the continuum model, we took $\epsilon L^2/\sigma_{xx} d = 1$. In (b), the real compenent was also plotted for the continuum model. This is to demonstrate the interesting fact that in the high frequency limit of this model, the two curves show the same assymptotic behavior.

equivalent to the 1D case, and the two caculations give the same result. The reason is that for a cicular disc, the increase in the capacitance of a differential radial element at larger radii is exactly cancelled by the decrease in its resistance, so that the product $dC(r) \cdot dR(r)$ remains constant. In this case, the charging signal is given by:

$$\frac{Q_T^*(\omega)}{Q_T(0)} = \tanh\left(\sqrt{\frac{i\omega\epsilon L^2}{\sigma_{xx} d}}\right) \tag{E.4}$$

Here, ϵ/d is the capacitance per unit area to the gate and L is the length of the 1D channel. For a annular ring or disc, L is the difference of the outer and inner radius.

These three functions are plotted in figure E-2. The effect of the distributed RC is to distort the curves giving them a high frequency tail, and to lower the peak value of the lagging-phase signal slightly to a value of about 0.42.

Bibliography

[1] A. B. Fowler, F. F. Fang, W. E. Howard, and P. J. Stiles. Magneto-oscillatory conductance in silicon surfaces. *Physical Review Letters*, 16, 1966. doi:10.1103/PhysRevLett.16.901.

[2] Tsuneya Ando, Alan B. Fowler, and Frank Stern. Electronic properties of two-dimensional systems. *Reviews of Modern Physics*, 54, 1982. doi:10.1103/RevModPhys.54.437.

[3] K. v. Klitzing, G. Dorda, and M. Pepper. New method for high-accuracy determination of the fine-structure constant based on quantized Hall resistance. *Physical Review Letters*, 45, 1980. doi:10.1103/PhysRevLett.45.494.

[4] M. A. Paalanen, D. C. Tsui, and A. C. Gossard. Quantized Hall effect at low temperatures. *Physical Review B*, 25, 1982. doi:10.1103/PhysRevB.25.5566.

[5] NIST Hall Effect Measurements Web Page. Available from: `http://www.eeel.nist.gov/812/hall.html`.

[6] A Hartland. The quantum Hall effect and resistance standards. *Metrologia*, 29, 1992. doi:10.1088/0026-1394/29/2/006.

[7] F. Piquemal and G. Genevès. Argument for a direct realization of the quantum metrological triangle. *Metrologia*, 37, 2000. doi:10.1088/0026-1394/37/3/4.

[8] Klaus von Klitzing. The quantized Hall effect. *Reviews of Modern Physics*, 58, 1986. doi:10.1103/RevModPhys.58.519.

[9] R. Dingle, H. L. Störmer, A. C. Gossard, and W. Wiegmann. Electron mobilities in modulation-doped semiconductor heterojunction superlattices. *Applied Physics Letters*, 33, 1978. doi:10.1063/1.90457.

[10] A. Y. Cho. Growth of periodic structures by the molecular-beam method. *Applied Physics Letters*, 19, 1971. doi:10.1063/1.1653775.

[11] Paul Ioannis Glicofridis. *Subsurface Charge Accumulation Imaging of the Quantum Hall Liquid*. PhD thesis, Massachusetts Institute of Technology, 2001. Available from: `http://electron.mit.edu/theses/`.

[12] L. P. Rokhinson, B. Su, and V. J. Goldman. Peak values of conductivity in integer and fractional quantum Hallect. *Solid State Communications*, 96, 1995. doi:0.1016/0038-1098(95)00442-4.

[13] R. B. Laughlin. Quantized Hall conductivity in two dimensions. *Physical Review B*, 23, 1981. doi:10.1103/PhysRevB.23.5632.

[14] B. I. Halperin. Quantized Hall conductance, current-carrying edge states, and the existence of extended states in a two-dimensional disordered potential. *Physical Review B*, 25, 1982. doi:10.1103/PhysRevB.25.2185.

[15] G. Ebert, K. von Klitzing, C. Probst, E. Schuberth, K. Ploog, and G. Weimann. Hopping conduction in the landau level tails in GaAs-$A_xGa_{1-x}As$ heterostructures at low temperatures. *Solid State Communications*, 45, 1983. doi:10.1016/0038-1098(83)90441-6.

[16] A. Briggs, Y. Guldner, J. P. Vieren, M. Voos, J. P. Hirtz, and M. Razeghi. Low-temperature investigations of the quantum Hall effect in $In_xGa_{1-x}As$-InP heterojunctions. *Physical Review B*, 27, 1983. doi:10.1103/PhysRevB.27.6549.

[17] B. Tausendfreund and K. von Klitzing. Analysis of quantized Hall resistance at finite temperatures. *Surface Science*, 142, 1984. doi:10.1016/0039-6028(84)90311-X.

[18] I. V. Kukushkin and V. B. Timofeev. Activation gaps in the energy spectrum and influence of disorder under fractional quantum Hall effect in silicon mosfet. *Surface Science*, 170, 1986. doi:10.1016/0039-6028(86)90954-4.

[19] R. G. Clark, R. J. Nicholas, A. Usher, C. T. Foxon, and J. J. Harris. Odd and even fractionally quantized states in GaAs-GaAlAs heterojunctions. *Surface Science*, 170, 1986. doi:10.1016/0039-6028(86)90953-2.

[20] G. S. Boebinger, A. M. Chang, H. L. Stormer, and D. C. Tsui. Magnetic field dependence of activation energies in the fractional quantum Hall effect. *Physical Review Letters*, 55, 1985. doi:10.1103/PhysRevLett.55.1606.

[21] G. S. Boebinger, A. M. Chang, H. L. Störmer, D. C. Tsui, J. C. M. Hwang, A. Cho, C. Tu, and G. Weimann. Activation energies of fundamental and higher order states in the fractional quantum Hall effect. *Surface Science*, 170, 1986. doi:10.1016/0039-6028(86)90951-9.

[22] G. S. Boebinger, H. L. Stormer, D. C. Tsui, A. M. Chang, C. M. Hwang, A. Y. Cho, C. W. Tu, and G. Weimann. Activation energies and localization in the fractional quantum Hall effect. *Physical Review B*, 36, 1987. doi:10.1103/PhysRevB.36.7919.

[23] R. G. Clark, J. R. Mallett, S. R. Haynes, J. J. Harris, and C. T. Foxon. Experimental determination of fractional charge e/q for quasiparticle excitations in the fractional quantum Hall effect. *Physical Review Letters*, 60, 1988. doi:10.1103/PhysRevLett.60.1747.

[24] R. J. Nicholas, R. J. Haug, K. v. Klitzing, and G. Weimann. Exchange enhancement of the spin splitting in a GaAs-$Ga_xAl_{1-x}As$ heterojunction. *Physical Review B*, 37, 1988. doi:10.1103/PhysRevB.37.1294.

[25] A. Usher, R. J. Nicholas, J. J. Harris, and C. T. Foxon. Observation of magnetic excitons and spin waves in activation studies of a two-dimensional electron gas. *Physical Review B*, 41, 1990. doi:10.1103/PhysRevB.41.1129.

[26] Y. Katayama, D. C. Tsui, and M. Shayegan. Experimental study of $\sigma_{xx}(t)$ for quasiparticle charge determination in the fractional quantum Hall effect. *Physical Review B*, 49, 1994. doi:10.1103/PhysRevB.49.7400.

[27] A. Schmeller, J. P. Eisenstein, L. N. Pfeiffer, and K. W. West. Evidence for skyrmions and single spin flips in the integer quantized Hall effect. *Physical Review Letters*, 75, 1995. doi:10.1103/PhysRevLett.75.4290.

[28] X. L. Hu, F. W. Van Keuls, Y. Carmi, H. W. Jiang, and A. J. Dahm. Screening of the Coulomb gap. *Solid State Communications*, 96, 1995. doi:10.1016/0038-1098(95)00401-7.

[29] F. W. Van Keuls, X. L. Hu, H. W. Jiang, and A. J. Dahm. Screening of the Coulomb interaction in two-dimensional variable-range hopping. *Physical Review B*, 56, 1997. doi:10.1103/PhysRevB.56.1161.

[30] D. R. Leadley, R. J. Nicholas, J. J. Harris, and C. T. Foxon. Critical collapse of the exchange-enhanced spin splitting in two-dimensional systems. *Physical Review B*, 58, 1998. doi:10.1103/PhysRevB.58.13036.

[31] D. Shahar, M. Hilke, C. C. Li, D. C. Tsui, S. L. Sondhi, J. E. Cunningham, and M. Razeghi. A new transport regime in the quantum Hall effect. *Solid State Communications*, 107, 1998. doi:10.1016/S0038-1098(98)00157-4.

[32] A. Urbina, C. DíazPaniagua, A.F. Brana, and F. Batallán. Hopping conductivity and activated transport in $In_xGa_{1-x}As$ quantum wells. *The European Physical Journal B*, 24, 2001. Available from: `http://www.edpsciences.org/articles/epjb/abs/2001/24/b01294/b01294.html`.

[33] H. P. Wei, A. M. Chang, D. C. Tsui, and M. Razeghi. Temperature dependence of the quantized Hall effect. *Physical Review B*, 32, 1985. doi:10.1103/PhysRevB.32.7016.

[34] Shinji Kawaji and Junichi Wakabayashi. Experiments on scaling relation of conductivities in silicon MOS inversion layers in strong magnetic fields. *Journal of the Physical Society of Japan*, 56, 1987. doi:10.1143/JPSJ.56.21.

[35] H. P. Wei, D. C. Tsui, M. A. Paalanen, and A. M. M. Pruisken. Experiments on delocalization and university in the integral quantum Hall effect. *Physical Review Letters*, 61, 1988. doi:10.1103/PhysRevLett.61.1294.

[36] H. P. Wei, S. W. Hwang, D. C. Tsui, and A. M. M. Pruisken. New results on scaling in the integral quantum Hall effect. *Surface Science*, 229, 1990. doi:10.1016/0039-6028(90)90825-S.

[37] S. Koch, R. J. Haug, K. v. Klitzing, and K. Ploog. Experiments on scaling in $Al_xGa_{1-x}As/GaAs$ heterostructures under quantum Hall conditions. *Physical Review B*, 43, 1991. doi:10.1103/PhysRevB.43.6828.

[38] H. P. Wei, S. Y. Lin, , D. C. Tsui, and A. M. M. Pruisken. Effect of long-range potential fluctuations on scaling in the integer quantum Hall effect. *Physical Review B*, 45, 1992. doi:10.1103/PhysRevB.45.3926.

[39] S. Koch, R. J. Haug, K. v. Klitzing, and K. Ploog. Experimental studies of the localization transition in the quantum Hall regime. *Physical Review B*, 46, 1992. doi:10.1103/PhysRevB.46.1596.

[40] S. W. Hwang, H. P. Wei, L. W. Engel, D. C. Tsui, and A. M. M. Pruisken. Scaling in spin-degenerate landau levels in the integer quantum Hall effect. *Physical Review B*, 48, 1993. doi:10.1103/PhysRevB.48.11416.

[41] H. P. Wei, L. W. Engel, and D. C. Tsui. Current scaling in the integer quantum Hall effect. *Physical Review B*, 50, 1994. doi:10.1103/PhysRevB.50.14609.

[42] Wanli Li, G. A. Csthy, D. C. Tsui, L. N. Pfeiffer, and K. W. West. Scaling and universality of integer quantum Hall plateau-to-plateau transitions. *Physical Review Letters*, 95, 2005. doi:10.1103/PhysRevLett.94.206807.

[43] N. F. Mott. Conduction in non-crystalline materials. III. Localized states in a pseudogap and near extremities of conduction and valence bands. *Philosophical Magazine*, 19, 1969.

[44] Vinay Ambegaokar, B. I. Halperin, and J. S. Langer. Hopping conductivity in disordered systems. *Physical Review B*, 4, 1971. doi:10.1103/PhysRevB.4.2612.

[45] A L Efros and B I Shklovskii. Coulomb gap and low temperature conductivity of disordered systems. *Journal of Physics: Condensed Matter*, 8, 1975. doi:10.1088/0022-3719/8/4/003.

[46] Bodo Huckestein. Scaling theory of the integer quantum Hall effect. *Reviews of Modern Physics*, 67, 1995. doi:10.1103/RevModPhys.67.357.

[47] A. L. Efros. Non-linear screening and the background density of 2deg states in magnetic field. *Solid State Communications*, 67, 1988. doi:10.1016/0038-1098(88)91177-5.

[48] A. L. Efros. Density of states of 2d electron gas and width of the plateau of iqhe. *Solid State Communications*, 65, 1988. doi:10.1016/0038-1098(88)90077-4.

[49] A. L. Efros. Homogeneous and inhomogeneous states of a two-dimensional electron liquid in a strong magnetic field. *Physical Review B*, 45, 1991. doi:10.1103/PhysRevB.45.11354.

[50] A. L. Efros, F. G. Pikus, and V. G. Burnett. Density of states of a two-dimensional electron gas in a long-range random potential. *Physical Review B*, 47, 1993. doi:10.1103/PhysRevB.47.2233.

[51] D. B. Chklovskii, B. I. Shklovskii, and L. I. Glazman. Electrostatics of edge channels. *Physical Review B*, 46, 1992. doi:10.1103/PhysRevB.46.4026.

[52] N. R. Cooper and J. T. Chalker. Coulomb interactions and the integer quantum Hall effect: Screening and transport. *Physical Review B*, 48, 1993. doi:0.1103/PhysRevB.48.4530.

[53] Dmitri B. Chklovskii and Patrick A. Lee. Transport properties between quantum Hall plateaus. *Physical Review B*, 48, 1993. doi:10.1103/PhysRevB.48.18060.

[54] D. B. Chklovskii, K. A. Matveev, and B. I. Shklovskii. Ballistic conductance of interacting electrons in the quantum Hall regime. *Physical Review B*, 47, 1993. doi:10.1103/PhysRevB.47.12605.

[55] M. M. Fogler and B. I. Shklovskii. Resistance of a long wire in the quantum Hall regime. *Physical Review B*, 50, 1994. doi:10.1103/PhysRevB.50.1656.

[56] M. Locatelli, G. Lamboley, J. P. Michenaud, and V. Bayot. Easy method to characterize a piezoelectric ceramic tube as a displacer. *Review of Scientific Instruments*, 59, 1988. doi:10.1063/1.1139804.

[57] C. Julian Chen. Electromechanical deflections of piezoelectric tubes with quartered electrodes. *Applied Physics Letters*, 60, 1992. doi:10.1063/1.107348.

[58] Tutorial: Piezoelectrics in positioning. Available from: `http://www.physikinstrumente.com/en/products/piezo_tutorial.php`.

[59] S. H. Pan, E. W. Hudson, and J. C. Davis. ^{3}He refridgerator based very low temperature scanning tunneling microscope. *Review of Scientific Instruments*, 70:1459, 1999. doi:10.1063/1.1149605.

[60] M. Roseman and P. Grutter. Cryogenic magnetic force microscope. *Review of Scientific Instruments*, 71, 2000. doi:10.1063/1.1290039.

[61] K. R. Brown, L. Sun, and B. E. Kane. Millikelvin scanned probe for measurement of nanostructures. *Review of Scientific Instruments*, 75, 2004. doi:10.1063/1.1753104.

[62] J. Rychen, T. Ihn, P. Struderus, A. Herrmann, and K. Ensslin. A low-temperature dynamic mode scanning force microscope operating in high magnetic fields. *Review of Scientific Instruments*, 70, 1999. doi:10.1063/1.1149842.

[63] T. H. Chang, C. H. Yang, M. J. Yang, and J. B. Dottellis. Cryogenic scanning tunneling microscope for quantum dot spectroscopy. *Review of Scientific Instruments*, 72, 2001. doi:10.1063/1.1379608.

[64] Hans J. Hug, B. Stiefel, P. J. A. van Schendel, A. Moser, S. Martin, and H.-J. Guntherodt. A low temperature ultrahigh vaccum scanning force microscope. *Review of Scientific Instruments*, 70, 1999. doi:10.1063/1.1149970.

[65] W. Allers, A. Schwarz, U. D. Schwarz, and R. Wiesendanger. A scanning force microscope with atomic resolution in ultrahigh vacuum and at low temperatures. *Review of Scientific Instruments*, 69, 1998. doi:10.1063/1.1148499.

[66] Chr. Wittneven, R. Dombrowski, S. H. Pan, and R. Wiesendanger. A low-temperature ultrahigh-vacuum scanning tunneling microscope with rotatable magnetic field. *Review of Scientific Instruments*, 68, 1997. doi:10.1063/1.1148031.

[67] K. Besocke. An easily operable scanning tunneling microscope. *Surface Science*, 181:145, 1987. doi:10.1016/0039-6028(87)90151-8.

[68] J. Frohn, J. F. Wolf, K. Besocke, and M. Teske. Coarse tip distance adjustment and positioner for a scanning tunneling microscope. *Review of Scientific Instruments*, 60:1200, 1989. doi:10.1063/1.1140287.

[69] Private discussions with Amir Yacoby and students of Klauss Ensslin.

[70] Misha Brodsky. *Charging of Small Two-Dimensional Electron Puddles*. PhD thesis, Massachusetts Institute of Technology, 2000. Available from: `http://electron.mit.edu/theses/`.

[71] Raymond C. Ashoori. *The Density of States in the Two-Dimensional Electron Gas and Quantum Dots*. PhD thesis, Cornell University, 1991. Available from: `http://electron.mit.edu/theses/`.

[72] Helmuth Spieler. Introduction to radiation detectors and electronics. Lecture Notes - Physics 198, Spring Semester 1998 - UC Berkeley. Available from: http://www-physics.lbl.gov/~spieler/physics_198_notes/.

[73] M. A. Py and H.-J. Buehlmann. Evidence for screening effects on the 1/f current noise in GaAs/AlGaAs modulation doped field effect transistors. *Journal of Applied Physics*, 80, 1996. doi:10.1063/1.362955.

[74] T. P. Smith, B. B. Goldberg, , P. J. Stiles, and M. Heiblum. Direct measurement of the density of states of a two-dimensional electron gas. *Physical Review B*, 32, 1985. doi:10.1103/PhysRevB.32.2696.

[75] Serge Luryi. Quantum capacitance devices. *Applied Physics Letters*, 52, 1988. doi:10.1063/1.99649.

[76] M. Buttiker. Capacitance, admittance, and rectification properties of small conductors. *Journal of Physics: Condensed Matter*, 5, 1993. doi:10.1088/0953-8984/5/50/017.

[77] Kent L. McCormick, Michael T. Woodside, Mike Huang, Mingshaw Wu, Paul L. McEuen, Cem Duruoz, and J. S. Harris Jr. Scanned potential microscopy of edge and bulk currents in the quantum Hall regime. *Physical Review B*, 59, 1999. doi:10.1103/PhysRevB.59.4654.

[78] P. Weitz, E. Ahlswede, J. Weis, K. Von. Klitzing, and K. Eberl. Hall-potential investigations under quantum Hall conditions using scanning force microscopy. *Physica E*, 6, 2000. doi:10.1016/S1386-9477(99)00136-8.

[79] Micheal T. Woodside and Paul L. McEuen. Scanned probe imaging of single-electron charge states in nanotube quantum dots. *Science*, 296, 2002. doi:10.1126/science.1069923.

[80] Romain Stomp, Yoichi Miyahara, Sacha Schaer, Qingfeng Sun, Hong Guo, Peter Grutter, Sergei Studenikin, and Philip Poole andy Sachrajda. Detection of single-electron charging in an individual InAs quantum dot by

noncontact atomic-force microscopy. *Physical Review Letters*, 94, 2005. doi:10.1103/PhysRevLett.94.056802.

[81] J. F. Janak. g factor of the two-dimensional interacting electron gas. *Physical Review*, 178, 1969. doi:10.1103/PhysRev.178.1416.

[82] Tsuneya Ando and Yasutada Uemura. Theory of oscillatory g factor in an mos inversion layer under strong magnetic fields. *Journal of the Physical Society of Japan*, 37, 1974. doi:10.1143/JPSJ.37.1044.

[83] A. H. MacDonald, H. C. A. Oji, and K. L. Liu. Thermodynamic properties of an interacting two-dimensional electron gas in a strong magnetic field. *Physical Review B*, 34, 1986. doi:10.1103/PhysRevB.34.2681.

[84] A. P. Smith, A. H. MacDonald, and G. Gumbs. Quasiparticle effective mass and enhanced g factor for a two-dimensional electron gas at intermediate magnetic fields. *Physical Review B*, 45, 1992. doi:10.1103/PhysRevB.45.8829.

[85] S. L. Sondhi, A. Karlhede, S. A. Kivelson, and E. H. Rezayi. Skyrmions and the crossover from the integer to fractional quantum Hall effect at small Zeeman energies. *Physical Review B*, 47, 1993. doi:10.1103/PhysRevB.47.16419.

[86] H. A. Fertig, L. Brey, R. Côté, and A. H. MacDonald. Charged spin-texture excitations and the Hartree-Fock approximation in the quantum Hall effect. *Physical Review B*, 50, 1994. doi:10.1103/PhysRevB.50.11018.

[87] Jairo Sinova, A. H. MacDonald, and S. M. Girvin. Disorder and interactions in quantum Hall ferromagnets near ν=1. *Physical Review B*, 62, 2000. doi:10.1103/PhysRevB.62.13579.

[88] R. J. Haug, K. von Klitzing, R. J. Nicholas, J. C. Maan, and G. Weimann. The influence of a tilted magnetic field on the fractional quantum hall effect and the exchange enhancement of the spin splitting. *Surface Science*, 196, 1988. doi:10.1016/0039-6028(88)90689-9.

[89] V. T. Dolgopolov, A. A. Shashkin, A. V. Aristov, D. Schmerek, W. Hansen, J. P. Kotthaus, and M. Holland. Direct measurements of the spin gap in the two-dimensional electron gas of AlGaAs-GaAs heterojunctions. *Physical Review Letters*, 79, 1997. doi:10.1103/PhysRevLett.79.729.

[90] A. Yacoby, H. F. Hess, T. A. Fulton, L. N. Pfeiffer, and K. W. West. Electrical imaging of the quantum Hall state. *Solid State Communications*, 111, 1999. doi:10.1016/S0038-1098(99)00139-8.

[91] R. K. Goodall, R. J. Higgins, , and J. P. Harrang. Capacitance measurements of a quantized two-dimensional electron gas in the regime of the quantum Hall effect. *Physical Review B*, 31, 1985. doi:10.1103/PhysRevB.31.6597.

[92] L.A. Tracy, J.P. Eisenstein, M.P. Lilly, L.N. Pfeiffer, and K.W. West. Surface acoustic wave propagation and inhomogeneities in low density two-dimensional electron systems near the metal-insulator transition. arXiv:cond-mat/0507082.

[93] T. Haavasoja, H. L. Störmer, D. J. Bishop, V. Narayanamurti, A. C. Gossard, and W. Wiegmann. Magnetization measurements on a two-dimensional electron system. *Surface Science*, 142, 1983. doi:10.1016/0039-6028(84)90325-X.

[94] J. P. Eisenstein, H. L. Störmer, V. Narayanamurti, and A. C. Gossard. High precision de Haas-van Alphen measurements on a two-dimensional electron gas. *Superlattices and Microstructures*, 1, 1984. doi:10.1016/0749-6036(85)90020-5.

[95] R. T. Zeller, B. B. Goldberg, P. J. Stiles, F. F. Fang, and S. L. Wright. Floating-gate technique applied to two-dimensional systems. *Physical Review B*, 33, 1986. doi:10.1103/PhysRevB.33.1529.

[96] C. L. Jones, A. Usher, M. Elliott, W. G. Herrenden-Harker, A. Potts, R. Shepherd, T. S. Cheng, and C. T. Foxon. The decay of induced eddy currents in a two-dimensional electron system. *Solid State Communications*, 95, 1995. doi:10.1016/0038-1098(95)00296-0.

[97] J. Huels, J. Weis, J. Smet, K. v. Klitzing, and Z. R. Wasilewski. Long time relaxation phenomena of a two-dimensional electron system within integer quantum Hall plateau regimes after magnetic field sweeps. *Physical Review B*, 69, 2004. doi:10.1103/PhysRevB.69.085319.

[98] D.R. Faulhaber and H.W. Jiang. Nonequilibrium magnetization of a two-dimensional electron gas in a static magnetic field. arXiv:cond-mat/0511569.

[99] T. J. Drummond, W. Kopp, R. Fischer, H. Morkoç, R. E. Thorne, and A. Y. Cho. Photoconductivity effects in extremely high mobility modulation-doped (AlGa)As/GaAs heterostructures. *Journal of Applied Physics*, 53, 1982. doi:10.1063/1.330537.

[100] Marshall I. Nathan. Persistent photoconductivity in AlGaAs/GaAs modulation doped layers and field effect transistors: A review. *Solid-State Electronics*, 29, 1986. doi:10.1016/0038-1101(86)90035-3.

[101] R. Fletcher, E. Zaremba, R. Fletcher, E. Zaremba, R. Fletcher, and E. Zaremba. Persistent photoconductivity and two-band effects in GaAs/$Al_xGa_{1-x}As$ heterojunctions. *Physical Review B*, 41, 1990. doi:10.1103/PhysRevB.41.10649.

[102] J. P. Eisenstein, K. B. Cooper, L. N. Pfeiffer, and K. W. West. Insulating and fractional quantum Hall states in the first excited Landau level. *Physical Review Letters*, 88, 2002. doi:10.1103/PhysRevLett.88.076801.

[103] Khaled Karrai and Robert D. Grobber. Piezoelectric tip-sample distance control for near field optical microscopes. *Applied Physics Letters*, 66, 1995. doi:10.1063/1.113340.

[104] Robert D. Grober, Jason Acimovic, Jim Schuck, Dan Hessman, Peter J. Kindlemann, Joao Hespanha, A. Stephen Morse, Khaled Karrai, Ingo Tiemann, and Stephan Manus. Fundamental limits to force detection using quartz tuning forks. *Review of Scientific Instruments*, 71, 2000. doi:10.1063/1.1150691.

[105] M. Todorovic and S. Schultz. Magnetic force microscopy using nonoptical piezoelectric quartz tuning fork detection design with applications to magnetic recording studies. *Journal of Applied Physics*, 83, 1998. doi:10.1063/1.367642.

[106] J. Rychena, T. Ihn, P. Studerus, A. Herrmann, K. Ensslin, H. J. Hug, P. J. A. van Schendel, and H. J. Güntherodt. Force–distance studies with piezoelectric tuning forks below 4.2 K. *Applied Surface Science*, 157, 2000. doi:10.1016/S0169-4332(99)00541-3.

[107] Jaime C. Grunlan, Xinyun Xia, David Rowenhorst, and William W. Gerberich. Preparation and evaluation of tungsten tips relative to diamond for nanoindentation of soft materials. *Review of Scientific Instruments*, 72, 2001. doi:10.1063/1.1370564.

[108] J. P. Ibe, P. P. Bey, Jr., S. L. Brandow, R. A. Brizzolara, N. A. Burnham, D. P. DiLella, K. P. Lee, C. R. K. Marrian, and R. J. Colton. On the electrochemical etching of tips for scanning tunneling microscopy. *Journal of Vacuum Science and Technology A*, 8, 1990. doi:10.1116/1.576509.

[109] J. P. Song, N. H. Pryds, K. Glejbøl, K. A. Mørch, A. R. Thölén, and L. N. Christensen. A development in the preparation of sharp scanning tunneling microscopy tips. *Review of Scientific Instruments*, 64, 1993. doi:10.1063/1.1144140.

[110] Vladimir Weinstein, Michael Slutzky, Aleksandre Arenshtam, and Eshel Ben-Jacob. A method for preparation of PtIr tips for the scanning tunneling microscope. *Review of Scientific Instruments*, 66, 1995. doi:10.1063/1.1145533.

[111] B. L. Rogers, J. G. Shapter, W. M. Skinner, and K. Gascoigne. A method for production of cheap, reliable PtIr tips. *Review of Scientific Instruments*, 71, 2000. doi:10.1063/1.1150523.

[112] G. A. Steele, R. C. Ashoori, L. N. Pfeiffer, and K. W. West. Imaging transport resonances in the quantum hall effect. *Physical Review Letters*, 95, 2005. doi:10.1103/PhysRevLett.95.136804.

[113] K. v. Klitzing, G. Dorda, and M. Pepper. New method for high-accuracy determination of the fine-structure constant based on quantized Hall resistance. *Physical Review Letters*, 45, 1980. doi:10.1103/PhysRevLett.45.494.

[114] N. B. Zhitenev, M. Brodsky, R. C. Ashoori, and M. R. Melloch. New class of resonances at the edge of the two-dimensional electron gas. *Physical Review Letters*, 77, 1996. doi:10.1103/PhysRevLett.77.1833.

[115] Dmitri B. Chklovskii. Comment on "New class of resonances at the edge of the two-dimensional electron gas.". arXiv:cond-mat/9609023.

[116] S. Ilani1, J. Martin, E. Teitelbaum, J. H. Smet, D. Mahalu, V. Umansky, and A. Yacoby. The microscopic nature of localization in the quantum Hall effect. *Nature*, 427, 2004. doi:10.1038/nature02230.

[117] J. K Jain and S. A. Kivelson. Quantum Hall effect in quasi one-dimensional systems: Resistance fluctuations and breakdown. *Physical Review Letters*, 60, 1988. doi:10.1103/PhysRevLett.60.1542.

[118] E. Peled, D. Shahar, Y. Chen, E. Diez, D. L. Sivco, and A. Y. Cho. Near-perfect correlation of the resistance components of mesoscopic samples at the quantum Hall regime. *Physical Review Letters*, 91, 2003. doi:10.1103/PhysRevLett.91.236802.

[119] David H. Cobden, C. H. W. Barnes, and C. J. B. Ford. Fluctuations and evidence for charging in the quantum Hall effect. *Physical Review Letters*, 82, 1999. doi:10.1103/PhysRevLett.82.4695.

[120] A. Simmons, H. P. Wei, L. W. Engel, D. C. Tsui, and M. Shayegan. Resistance fluctuations in narrow AlGaAs/GaAs heterostructures: Direct evidence of frac-

tional charge in the fractional quantum hall effect. *Physical Review Letters*, 63, 1989. doi:10.1103/PhysRevLett.63.1731.

[121] J. A. Simmons, S. W. Hwang, D. C. Tsui, H. P. Wei, L. W. Engel, and M. Shayegan. Resistance fluctuations in the integral- and fractional-quantum-Hall-effect regimes. *Physical Review B*, 44, 1991. doi:10.1103/PhysRevB.44.12933.

[122] Patrick A. Lee. Comment on "Resistance fluctuations in narrow AlGaAs/GaAs heterostructures: Direct evidence of fractional charge in the fractional quantum Hall effect". *Physical Review Letters*, 65, 1990. doi:10.1103/PhysRevLett.65.2206.

[123] Jens Martin, Shahal Ilani, Basile Verdene, Jurgen Smet, Vladimir Umansky, Diana Mahalu, Dieter Schuh, Gerhard Abstreiter, and Amir Yacoby. Localization of fractionally charged quasi-particles. *Science*, 305, 2004. doi:10.1126/science.1099950.

[124] N. C. van der Vaart, M. P. de Ruyter van Steveninck, L. P. Kouwenhoven, A. T. Johnson, Y. V. Nazarov, C. J. P. M. Harmans, and C. T. Foxon. Time-resolved tunneling of single electrons between landau levels in a quantum dot. *Physical Review Letters*, 73, 1994. doi:10.1103/PhysRevLett.73.320.

[125] M. A. Topinka, B. J. LeRoy, R. M. Westervelt, S. E. J. Shaw, R. Fleischmann, E. J. Heller, K. D. Maranowski, and A. C. Gossard. Coherent branched flow in a two-dimensional electron gas. *Nature*, 410, 2001. doi:10.1038/35065553.

[126] Dragana Popović, A. B. Fowler, and S. Washburn. Resonant tunneling and hopping through a series of localized states in a two-dimensional electron gas. *Physical Review Letters*, 67, 1991. doi:10.1103/PhysRevLett.67.2870.

[127] M. M. Fogler, A. A. Koulakov, and B. I. Shklovskii. Ground state of a two-dimensional electron liquid in a weak magnetic field. *Physical Review B*, 54, 1996. doi:10.1103/PhysRevB.54.1853.

[128] M. P. Lilly, K. B. Cooper, J. P. Eisenstein, L. N. Pfeiffer, , and K. W. West. Evidence for an anisotropic state of two-dimensional electrons in high Landau levels. *Physical Review Letters*, 82, 1999. doi:10.1103/PhysRevLett.82.394.

[129] M. Kaplit and J. N. Zemel. Capacitance observations of Landau levels in surface quantization. *Physical Review Letters*, 21, 1968. doi:10.1103/PhysRevLett.21.212.

[130] A. M. Voshchenkov and J. N. Zemel. Admittance studies of surface quantization in [100]-oriented Si metal-oxide-semiconductor field-effect transistors. *Physical Review B*, 9, 1974. doi:10.1103/PhysRevB.9.4410.

[131] John H. Davies. *The Physics of Low-dimensional Semiconductors: An Introduction*. Cambridge University Press, Cambridge, 1998.

[132] D. C. Tsui, A. C. Gossard, G. Kaminsky, and W. Wiegmann. Transport properties of GaAs-$Al_xGa_{1-x}As$ heterojunction field-effect transistors. *Applied Physics Letters*, 39, 1981. doi:10.1063/1.92858.

[133] Kazuhiko Hirakawa and Hiroyuki Sakaki. Mobility of the two-dimensional electron gas at selectively doped n-type $Al_xGa_{1-x}As$/GaAs heterojunctions with controlled electron concentrations. *Physical Review B*, 33, 1986. doi:10.1103/PhysRevB.33.8291.

[134] Rolf Crook, Abi C. Graham, Charles G. Smith, Ian Farrer, Harvey E. Beere, and David A. Ritchie. Erasable electrostatic lithography for quantum components. *Nature*, 424, 2003. doi:10.1038/nature01841.

[135] Nemanja Spasojevic. Electrostatic simulations of interactions between a scanning probe and quantum hall liquid. Undergraduate thesis, Massachusetts Institute of Technology, 2005. Available from: `http://electron.mit.edu/theses/`.

[136] J. D. Jackson. *Classical Electrodynamics*. Wiley, New York, 3 edition, 1999.

[137] S. Teukolsky, W. Vetterling, W. Press, and B. Flannery. *Numerical Recipes in C*. Cambridge University Press, New York, 2 edition, 1993.

[138] James W. Demmel. *Applied Numerical Linear Algebra*. SIAM, Philadelphia, 1997.

[139] A. Weichselbaum and S. E. Ulloa. Potential landscapes and induced charges near metallic islands in three dimensions. *Physical Review E*, 68, 2003. doi:10.1103/PhysRevE.68.056707.

[140] V. G. Burnett, A. L. Efros, and F. G. Pikus. Magnetotransport through antidot and dot lattices in two-dimensional structures. *Physical Review B*, 48, 1993. doi:10.1103/PhysRevB.48.14365.

[141] Available from: `http://koti.welho.com/jfrantz/software/g3data.html`.

[142] Stefan Lányi and Miloslav Hruskovic. The resolution limit of scanning capacitance microscopes. *Journal of Physics D: Applied Physics*, 36, 2003. doi:10.1088/0022-3727/36/5/326.

[143] M. Stopa. Single-mode quantum wires. *Physical Review B*, 53, 1996. doi:10.1103/PhysRevB.53.9595.

[144] M. Stopa. Quantum dot self-consistent electronic structure and the Coulomb blockade. *Physical Review B*, 54, 1996. doi:10.1103/PhysRevB.54.13767.

[145] M. Stopa and Y. Aoyagi. Effect of donor layer ordering on the formation of single mode quantum wires. *Physica B*, 227, 1996. doi:10.1016/0921-4526(96)00342-0.

[146] M. Stopa. Donor ordering and the statistics of quantum dot level spacings and widths from full 3d self-consistent electronic structure. *Superlattices and Microstructures*, 21, 1997. doi:10.1006/spmi.1996.0427.

[147] S Das Sarma and S Kodiyalam. Intrinsic dopant correlations and transport properties of mesoscopic modulation-doped heterostructures. *Semiconductor Science and Technology*, 13, 1998. doi:10.1088/0268-1242/13/8A/019.

[148] R. Grill and G. H. Döhler. Effect of charged donor correlation and wigner liquid formation on the transport properties of a two-dimensional electron gas in modulation δ-doped heterojunctions. *Physical Review B*, 59, 1999. doi:10.1103/PhysRevB.59.10769.

[149] A. L. Efros, F. G. Pikus, and G. G. Samsonidze. Maximum low-temperature mobility of two-dimensional electrons in heterojunctions with a thick spacer layer. *Physical Review B*, 41, 1990. doi:10.1103/PhysRevB.41.8295.

[150] F. G. Pikus and A. L. Éfros. Large-scale potential fluctuations in plane layers with impurities. *Soviet Physics - JETP*, 69, 1989. (english translation).

[151] R. Willett, J. P. Eisenstein, H. L. Störmer, D. C. Tsui, A. C. Gossard, and J. H. English. Observation of an even-denominator quantum number in the fractional quantum Hall effect. *Physical Review Letters*, 59, 1987. doi:10.1103/PhysRevLett.59.1776.

[152] J. P. Eisenstein and H. L. Stormer. The fractional quantum Hall effect. *Science*, 248, 1990. Available from: `http://adsabs.harvard.edu/cgi-bin/nph-bib_query?bibcode=1990Sci...248.1510E`.

[153] Horst L. Stormer, Daniel C. Tsui, and Arthur C. Gossard. The fractional quantum hall effect. *Reviews of Modern Physics*, 71, 1999. doi:10.1103/RevModPhys.71.S298.

[154] K. B. Cooper, M. P. Lilly, J. P. Eisenstein, L. N. Pfeiffer, and K. W. West. Insulating phases of two-dimensional electrons in high landau levels: Observation of sharp thresholds to conduction. *Physical Review B*, 60, 1999. doi:10.1103/PhysRevB.60.R11285.

[155] Yong Chen, R. M. Lewis, L. W. Engel, D. C. Tsui, P. D. Ye, L. N. Pfeiffer, and K. W. West. Microwave resonance of the 2d wigner crystal around integer landau fillings. *Physical Review Letters*, 91, 2003. doi:10.1103/PhysRevLett.90.016801.

[156] K. S. Novoselov, A. K. Geim, S. V. Morozov, D. Jiang, M. I. Katsnelson, I. V. Grigorieva, S. V. Dubonos, and A. A. Firsov. Two-dimensional gas of massless dirac fermions in graphene. *Nature*, 438, 2005. doi:10.1038/nature04233.

[157] Yuanbo Zhang, Yan-Wen Tan, Horst L. Stormer, and Philip Kim. Experimental observation of the quantum hall effect and berry's phase in graphene. *Nature*, 438, 2005. doi:10.1038/nature04235.

[158] Bart Van Zeghbroeck. Principles of semiconductor devices. Course notes for ECEN 5355 - University of Colorado. Available from: `http://ece-www.colorado.edu/~bart/book/book/contents.htm`.

[159] Adrian T. Lee. Broadband cryogenic preamplifiers incorporating GaAs MESFETs for use with low-temperature particle detectors. *Review of Scientific Instruments*, 60, 1989. doi:10.1063/1.1140521.

[160] Björn Starmark. A cryogenic preamplifier using a GaAs field effect transistor input stage. Diploma thesis, Chalmers University of Technology, 1996. Available from: `http://fy.chalmers.se/~starmark/`.

[161] F N Hooge, T G M Kleinpenning, and L K J Vandamme. Experimental studies on 1/f noise. *Reports on Progress in Physics*, 44, 1981. doi:10.1088/0034-4885/44/5/001.

[162] F. Stern. internal IBM technical report, 1972. (unpublished).